The muon content of extensive air showers measured by the Underground Muon Detector of the Pierre Auger Observatory

For the attaiment of the academic degree of

Doctorate in Science

from the KIT-Fakultät für Physik of the
Karlsruher Instituts für Technologie (KIT)
and the Instituto de Tecnología "Prof. Jorge A. Sábato" of the
Universidad Nacional de San Martín (UNSAM)

accepted

Dissertation

of

Lic. Marina Scornavacche

from Ciudad Autónoma de Buenos Aires

Day of the oral examination: 16. 05. 2025
Referee: Prof. Dr. Juan Manuel Figueira
Co-referee: Prof. Dr. Ralph Engel
Supervisors: Prof. Dr. Federico Sánchez, Dr. Darko Veberič

The muon content of extensive air showers measured by the Underground Muon Detector of the Pierre Auger Observatory

Zur Erlangung des akademischen Grades eines

Doktors der Naturwissenschaften (Dr. rer. nat.)

von der KIT-Fakultät für Physik des
Karlsruher Instituts für Technologie (KIT)
und des Instituto de Tecnología "Prof. Jorge A. Sábato" der
Universidad Nacional de San Martín (UNSAM)

angenommene

Dissertation

von

Lic. Marina Scornavacche

aus Ciudad Autónoma de Buenos Aires

Tag der mündlichen Prüfung: 16. 05. 2025
Referent: Prof. Dr. Juan Manuel Figueira
Korreferent: Prof. Dr. Ralph Engel
Betreuer: Prof. Dr. Federico Sánchez, Dr. Darko Veberič

The muon content of extensive air showers measured by the Underground Muon Detector of the Pierre Auger Observatory

Tesis aceptada para optar por el título de

Doctor en Astrofísica

de la KIT-Fakultät für Physik del
Karlsruher Instituts für Technologie (KIT)
y del Instituto de Tecnología "Prof. Jorge A. Sábato" de la
Universidad Nacional de San Martín (UNSAM)

por

Lic. Marina Scornavacche

de Ciudad Autónoma de Buenos Aires

Fecha de la defensa oral: 16. 05. 2025
Director: Prof. Dr. Juan Manuel Figueira
Co-director: Prof. Dr. Ralph Engel
Colaboradores: Prof. Dr. Federico Sánchez, Dr. Darko Veberič

Abstract

Designed to study the highest-energy cosmic rays, the Pierre Auger Observatory is the largest and most precise observatory of its kind. Fully operational for over a decade, it is currently undergoing an upgrade, AugerPrime, to enhance the separation between the electromagnetic and muonic components of air showers produced by cosmic rays. The Underground Muon Detector plays a crucial role in AugerPrime, as it enables a direct measurement of the muonic component—a key sensitive observable for determining cosmic-ray mass composition. Identifying the masses of the incoming cosmic rays could help us solve the mysteries regarding their origin. Additionally, ultra-high-energy cosmic rays are of particular interest to probe particle physics beyond the energy scales of modern colliders. Nevertheless, it is well established that current air-shower simulations fail to reproduce the muon content observed in data. While muon measurements seem to be consistent with simulations up to about $1{\times}10^{16}$ eV, a growing muon deficit in the simulations is observed at higher energies, challenging therefore our understanding of the hadronic interactions at the highest energies.

The Underground Muon Detector is equipped with scintillation modules buried at 2.3 m, providing two complementary methods for muon estimation: binary mode for low particle densities and ADC mode for high particle densities. This thesis focuses on the ADC mode, its calibration, and reconstruction techniques to accurately measure high muon densities close to the shower core impact point and, consequently, determine the muon content in air showers. To enhance data reconstruction, a new algorithm for signal charge estimation is developed. With a better understanding of the signals measured by the detector, we revise the existing calibration strategy. While designed to estimate the charge deposited by individual atmospheric muons, this method introduces a bias favouring inclined, high-energy muons due to the trigger condition requested, which generates a significant bias in muon reconstruction. Additionally, we show that calibrating underground detectors requires careful consideration of the interactions of penetrating particles through matter. Since the ADC mode relies on the charge of the signal determined by the energy deposited by muons in the plastic scintillators, we examine the impact of energy deposition by other shower particles. In particular, we show that delta (knock-on) electrons produced in the surrounding ground as muons traverse the medium significantly affects the charge measurements. To correct for this, a new calibration strategy is proposed that ensures an unbiased muon estimator, applying it to data covering a six-year period.

After significantly improving the muon reconstruction for high particle densities, we develop a combined likelihood method that integrates both binary and ADC acquisition modes to reconstruct the Muon Lateral Distribution Function. This method is validated through full-detector simulations. Finally, we present the first measurement of the muon content in extensive air showers, produced

by cosmic rays of energies between $2{\times}10^{17}$ eV and $1{\times}10^{19}$ eV, obtained using the information of the ADC mode. To interpret the mass composition, dedicated air shower simulations with proton and iron primaries were performed across the full energy range, as composition can only be inferred through comparison with simulations. Our analysis confirms that data reveals a growing muon deficit in air-shower simulations when increasing energy, aligning with findings from other experiments. These results provide a valuable input for improving the high-energy hadronic interaction models that could lead to better mass composition analyses and, ultimately, a deeper understanding of the origin of cosmic rays.

Zusammenfassung

Das Pierre Auger Observatorium, das darauf ausgelegt ist hochenergetische kosmische Strahlen zu untersuchen, ist das größte und präziseste Observatorium seiner Art. Es ist seit über einem Jahrzehnt vollständig in Betrieb und wird derzeit um das AugerPrime Upgrade erweitert, um die Trennung zwischen den elektromagnetischen und myonischen Komponenten der Luftschauer, die durch kosmische Strahlen erzeugt werden, zu verbessern. Der Untergrund Myonen Detektor spielt eine entscheidende Rolle in AugerPrime, da er eine direkte Messung der myonischen Komponente ermöglicht – eine empfindliche Schlüssel-Observable zur Bestimmung der Masse der kosmischen Strahlen. Die Identifizierung der Massen der eintreffenden kosmischen Strahlen könnte uns helfen, die Geheimnisse über ihren Ursprung zu lösen. Darüber hinaus sind ultra-hochenergetische kosmische Strahlen von besonderem Interesse, um die Teilchenphysik jenseits der Energie-Skalen moderner Teilchenbeschleuniger zu untersuchen. Es ist jedoch allgemein bekannt, dass die aktuellen Luftschauer-Simulationen den Myoneninhalt, der in den Daten beobachtet wird, nicht reproduzieren können. Während die Myonenmessungen bis etwa $1{\times}10^{16}$ eV mit den Simulationen übereinzustimmen scheinen, wird bei höheren Energien ein wachsender Myonen-Defizit in den Simulationen beobachtet, was unser Verständnis der hadronischen Wechselwirkungen bei höchsten Energien in Frage stellt.

Der Untergrund Myonen Detektor ist mit Szintillationsmodulen ausgestattet, die in 2,3 m Tiefe vergraben sind, und bietet zwei komplementäre Methoden zur Schätzung von Muonen: den Binärmodus für niedrige Teilchendichten und den ADC-Modus für hohe Teilchendichten. Diese Dissertation konzentriert sich auf den ADC-Modus, sowie seine Kalibrierung und Rekonstruktionstechniken, um hohe Myonendichten in der Nähe des Einschlagpunkts des Schauerkerns genau zu messen und folglich den Myoneninhalt in Luftschauern zu bestimmen. Um die Datenrekonstruktion zu verbessern, wurde ein neuer Algorithmus zur Schätzung des Signals entwickelt. Mit einem besseren Verständnis der vom Detektor gemessenen Signale überarbeiten wir die bestehende Kalibrierung. Obwohl die Methode zur Schätzung der von einzelnen atmosphärischen Myonen hinterlassenen Ladung entwickelt wurde, führt diese Methode aufgrund der angeforderten Triggerbedingungen zu einem Bias zugunsten von geneigten, hochenergetischen Myonen, was einen signifikanten Bias in der Myonenrekonstruktion erzeugt. Darüber hinaus zeigen wir, dass die Kalibrierung von unterirdischen Detektoren eine sorgfältige Berücksichtigung der Wechselwirkungen durchdringender Teilchen durch Materie erfordert. Da der ADC-Modus auf dem Signal basiert, das durch die Energie bestimmt wird, die von Myonen in den Plastikszintillatoren abgegeben wird, untersuchen wir den Einfluss der Energiedeposition durch andere Schauerteilchen. Insbesondere zeigen wir, dass Delta (Knock-on)-Elektronen, die im umgebenden Boden entstehen während die Myonen das Medium durchqueren, die Messungen der Ladung erheblich beein-

flussen. Um dies zu korrigieren, wird eine neue Kalibrierung vorgeschlagen, die einen unbeeinflussten Myonen-Schätzer sicherstellt und auf Daten angewendet wird, die einen Zeitraum von sechs Jahren abdecken.

Nach einer erheblichen Verbesserung der Myonenrekonstruktion für hohe Teilchendichten entwickeln wir eine kombinierte Likelihood-Methode, die sowohl den Binär- als auch den ADC-Erfassungsmodus integriert, um die Laterale-Verteilungsfunktion von Myonen zu rekonstruieren. Diese Methode wird durch vollständige Detektorsimulationen validiert. Schließlich präsentieren wir die erste Messung des Myoneninhalts in ausgedehnten Luftschauern, die von kosmischen Strahlen mit Energien zwischen $2{\times}10^{17}$ eV und $1{\times}10^{19}$ eV erzeugt wurden, unter Verwendung der Informationen des ADC-Modus. Um die Massenkomposition zu interpretieren, wurden spezielle Luftschauer-Simulationen mit Protonen- und Eisen-Primärteilchen über den gesamten Energiebereich durchgeführt, da die Zusammensetzung nur durch Vergleich mit Simulationen abgeleitet werden kann. Unsere Analyse bestätigt, dass die Daten ein wachsendes Myonen-Defizit in den Luftschauer-Simulationen bei steigender Energie zeigen, was mit den Ergebnissen anderer Experimente übereinstimmt. Diese Ergebnisse liefern einen wertvollen Beitrag zur Verbesserung der Modelle für hadronische Wechselwirkungen bei hohen Energien, die zu besseren Analysen der Massenkomposition und letztlich zu einem tieferen Verständnis des Ursprungs der kosmischen Strahlen führen könnten.

Resumen

Diseñado para estudiar los rayos cósmicos de mayor energía, el Observatorio Pierre Auger es el observatorio más grande y preciso de su tipo. Totalmente operativo durante más de una década, actualmente está experimentando una actualización, AugerPrime, para mejorar la separación entre las componentes electromagnéticas y muónicas de las lluvias de aire producidas por los rayos cósmicos. El Detector Subterráneo de Muones desempeña un papel crucial en AugerPrime, ya que permite una medición directa de la componente muónica, un observable sensible clave para determinar la composición de masa de los rayos cósmicos. Identificar las masas de los rayos cósmicos podría ayudarnos a resolver los misterios relacionados con su origen. Además, los rayos cósmicos de ultra alta energía son de particular interés para investigar la física de partículas más allá de las escalas de energía de los colisionadores modernos. No obstante, está bien establecido que las simulaciones actuales de lluvias de aire no logran reproducir el contenido de muones observado en los datos. Mientras que las mediciones de muones parecen ser consistentes con simulaciones hasta alrededor de $1{\times}10^{16}$ eV, se observa un creciente déficit de muones en las simulaciones a energías más altas, lo que desafía nuestra comprensión de las interacciones hadrónicas a las energías más altas.

El Detector Subterráneo de Muones está equipado con módulos de centelleo enterrados a 2.3 m, proporcionando dos métodos complementarios para la estimación de muones: el modo binario para bajas densidades de partículas y el modo ADC para altas densidades de partículas. Esta tesis se centra en el modo ADC, su calibración y las técnicas de reconstrucción para medir con precisión las altas densidades de muones cerca del punto de impacto del núcleo de la lluvia y, en consecuencia, determinar el contenido de muones en las lluvias de aire. Para mejorar la reconstrucción de los datos, se desarrolla un nuevo algoritmo para la estimación de la carga de la señal. Con una mejor comprensión de las señales medidas por el detector, revisamos la estrategia de calibración existente. Si bien fue diseñado para estimar la carga depositada por los muones atmosféricos individuales, este método introduce un bias a favor de muones inclinados de alta energía debido a la condición de trigger requerida, lo que genera un bias significativo en la reconstrucción de muones. Además, mostramos que la calibración de detectores subterráneos requiere una consideración cuidadosa de las interacciones de partículas penetrantes a través de la materia. Dado que el modo ADC se basa en la carga de la señal determinada por la energía depositada por los muones en los centelladores plásticos, examinamos el impacto de la deposición de energía por otras partículas de la lluvia. En particular, mostramos que los delta electrones (electrones knock-on) producidos en el suelo circundante mientras los muones atraviesan el medio afectan significativamente las mediciones de carga. Para corregir esto, se propone una nueva estrategia de calibración que asegura

un estimador de muones sin bias, aplicándola a los datos de un período de seis años.

Después de mejorar significativamente la reconstrucción de muones para altas densidades de partículas, desarrollamos un método de likelihood combinada que integra ambos modos de adquisición binario y ADC para reconstruir la Función de Distribución Lateral de Muones. Este método se valida a través de simulaciones del detector completo. Finalmente, presentamos la primera medición del contenido de muones en lluvias extensas de aire, producidas por rayos cósmicos con energías entre 2×10^{17} eV y 1×10^{19} eV, obtenida utilizando la información del modo ADC. Para interpretar la composición en masa, se realizaron simulaciones dedicadas de lluvias de aire con protones e iones de hierro primarios a través de todo el rango de energías, ya que la composición solo puede inferirse mediante la comparación con simulaciones. Nuestro análisis confirma que los datos revelan un creciente déficit de muones en las simulaciones de lluvias de aire cuando aumenta la energía, consistente con los hallazgos de otros experimentos. Estos resultados proporcionan un valioso aporte para mejorar los modelos de interacción hadrónica a altas energías, lo que podría conducir a mejores análisis de la composición en masa y, en última instancia, a una comprensión más profunda del origen de los rayos cósmicos.

Contents

Chapter I

Cosmic rays

Cosmic Rays (CRs) are charged particles, discovered in the early 20^{th} century, that originate from various extraterrestrial sources. Their energy spectrum spans from less than 1 GeV to approximately 10^{20} eV, making them the most energetic particles known to date. Ultra-High Energy Cosmic Rays (UHECRs) are CRs with energies above $\sim 10^{18}$ eV and they are of particular interest as they provide an opportunity to study hadronic interactions at energies far beyond those achievable with human-made accelerators, such as the Large Hadron Collider (LHC) [1]. While low-energy CRs are mainly produced by coronal ejections from nearby stars, such as our Sun [2], the origins of UHECRs remain uncertain and are an active area of research.

The discovery of cosmic rays is attributed to Viktor Hess. Years earlier, scientists had already measured a source of ionising radiation that caused electroscopes to discharge, initially believing it originated from radioactive elements from the ground of the Earth. In 1912, Hess demonstrated the extraterrestrial origin of this highly penetrating ionising radiation by ascending in a hot-air balloon to an altitude of 5300 m with three electroscopes. He observed that, contrary to previous assumptions, the intensity of ionising radiation increased with altitude rather than decreasing [3]. Hess soon established that this energetic radiation originated beyond the solar system, as he repeated the experiment during solar eclipses and confirmed that the radiation remained unchanged. However, it was hard to discern whether it was caused by photons or massive particles.

In 1925, the concept of "Cosmic Rays" was introduced by Robert Millikan [4]. At the time, gamma rays were considered the most likely candidate, as γ radiation was the most penetrating form of radiation known. However, following the discovery of the dependence of the cosmic-ray flux on the magnetic field of the Earth, predicted by Rossi [5], it was established that these "rays" were, in fact, charged particles. These particles were found to generate secondary particles

in the atmosphere without significant energy loss [6], ultimately leading to the discovery of the muon [7]. These secondary particles, produced by the interaction of very high-energy cosmic rays with atmospheric atoms, propagate towards the ground as an extensive air shower (EAS). The phenomenon was first discovered by Pierre Auger, who initiated the study of extended atmospheric cascades in 1938 [8]. Auger operated detectors spaced 300 m apart at high-altitude sites in the Alps, measuring events in coincidence due to the temporal correlation in the arrival of secondary particles. Based on these observations, he concluded that cosmic radiation must include particles with energies exceeding 10^{15} eV. For a historical review, see Ref. [9].

Nearly two decades of intense research and debate followed Hess's discovery of cosmic rays before it was conclusively established that they are predominantly composed of massive, charged particles, primarily high-energy protons and, to a lesser extent, heavier atomic nuclei [2, 10]. Since nuclei with an atomic mass number A greater than that of iron are less stable, they disintegrate into smaller nuclei during their long journey to Earth. While electrons, photons, and neutrinos can also contribute to cosmic rays, they are far less abundant.

In Section 1.1, we present the cosmic ray flux measurements from various experiments. Section 1.2 provides a brief overview of potential sources and acceleration mechanisms. The development of EAS is examined in Section 1.3 through the Heitler and Matthews models. Finally, Section 1.4 discusses cosmic ray mass composition estimators and the muon deficit observed in simulations across different experiments.

1.1. Cosmic ray flux

The differential cosmic-ray flux, defined as the number of CRs detected per unit energy E, area A, time t, and solid angle Ω, follows a decreasing broken power-law energy spectrum

$$\frac{\mathrm{d}N}{\mathrm{d}E\,\mathrm{d}A\,\mathrm{d}t\,\mathrm{d}\Omega} \propto E^{-\gamma}, \tag{1.1}$$

where the spectral index γ presents small variations to reflect changes in the steepness of the spectrum over the 11 orders of magnitude. Fig. 1.1 presents the differential flux of cosmic rays, scaled by a factor of E^2 to enhance the visibility of these features. The equivalent laboratory energy of the LHC, approximately 10^{17} eV, is illustrated for reference.

The flux of CRs decreases with the energy of the cosmic ray. At the lowest energies of approximately $\sim 10^9$ eV, the cosmic-ray flux reaches a few hundred particles per m^2 per second, while for energies above $\sim 10^{15}$ eV the flux becomes so low that cosmic rays can only be detected indirectly by measuring the extensive

air showers they produce. At the highest energies of $\sim 10^{18}$ eV, UHECRs have a flux of around one particle per km^2 per year. This extremely low flux necessitates the use of extensive detector arrays to collect statistically significant data. These large ground-based observatories exploit the atmosphere as a natural calorimeter, detecting either the secondary particles of the EAS at ground level or the radiation emitted due to their interaction with the atmosphere.

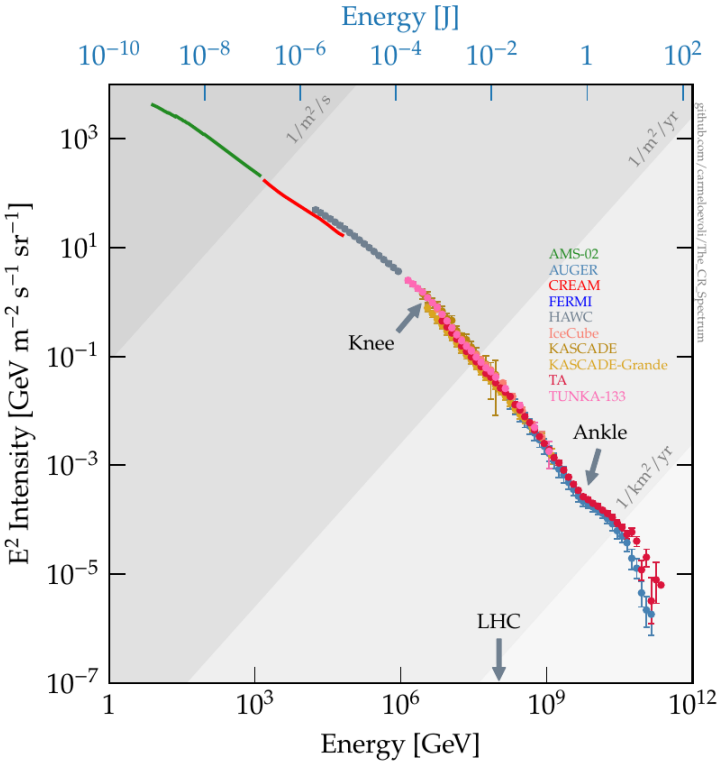

Figure 1.1: Energy spectrum of cosmic measured by different experiments. Image taken from Ref. [11].

In the energy spectrum, there are four significant features at which the spectral index varies. The interpretation of these spectral features still remains an active area of research, as they offer valuable insights into the nature of CR sources. These features are:

- The "knee" above $\sim 10^{15}$ eV, where the flux steepens and the spectral index γ shifts from 2.7 to 3.1. In this energy range, a transition from lighter to heavier elements was observed by the Karlsruhe Shower Core and Array Detector (KASCADE) experiment [12], which is consistent with the hypothesis that galactic supernova remnants (SNRs) reach the maximum energy to which they can accelerate light nuclei, such as protons.
- The "second knee" at $\sim 10^{17}$ eV, where a sudden steepening occurs, produced most likely due to a decrease in the population of heavier elements in the

cosmic ray flux from our galaxy. Similar to the "knee", this feature is also attributed to the maximum acceleration energy of SNRs [13], since at this energy the local galactic acceleration mechanisms are probably not “extreme enough” to accelerate heavier particles such as iron nuclei.

- The “ankle” around 5×10^{18} eV, where there is a sudden hardening of the CR spectrum. Given that at this energy, cosmic rays approach the threshold at which they can escape their galactic boundaries, a possible explanation for the ankle is the transition from the dominance of galactic to extragalactic cosmic rays. Additionally, there is a transition from lighter to heavier elements [14]. The shift to extragalactic sources is further supported by the absence of a directional origin in the galactic plane for cosmic rays at this energy.

- The “supression” above 5×10^{19} eV, where a strong suppression of the energy spectrum is observed and whose nature remains an open question. The steep decrease at the end of the spectrum could indicate that the cosmic ray sources have reached their acceleration limit or could be caused by propagation effects, such as the theoretically predicted Greisen-Zatsepin-Kuzmin (GZK) cut-off for protons or photodisintegration for heavier nuclei. The GZK cut-off was proposed in Refs. [15, 16] after the discovery of the cosmic microwave background radiation (CMB) [17]. It describes that the interaction of the CMB photons with protons of energies above 5×10^{19} eV, leads to energy loss through pion production via the Δ-resonance

$$\begin{aligned} p + \gamma_{\text{CMB}} &\rightarrow \Delta^+ \rightarrow n + \pi^+, \\ p + \gamma_{\text{CMB}} &\rightarrow \Delta^+ \rightarrow p + \pi^0. \end{aligned} \tag{1.2}$$

  Given that this interaction degrades proton energy, protons with energies greater than 5×10^{19} eV are prevented from being observed at distances greater than approximately 100 Mpc. The flux above this energy should then be largely suppressed if cosmic rays originate at cosmological distances, resulting in a sharp decrease in the cosmic ray energy spectrum, known as the GZK cut-off. For primary cosmic rays with mass number $A > 1$ the photodisintegration process via the giant dipole resonance leads to the ejection of one or several nucleons N from the nucleus [18, 19]. To achieve a similar suppression in the flux at high energies, the threshold energy for these processes is typically higher than for protons, as the energy of the primary nuclei is shared between nucleons.

A series of experiments studied the high energy cosmic ray events and con-

tributed to determining their spectrum, such as Haverah Park in England [20], Yakutsk in the USSR [21], KASCADE and Kascade-Grande in Germany [22], AGASA in Japan [23] and Fly's Eye - HiRes in the USA [24, 25]. However, a notorious discrepancy was observed between the spectra reported by the two largest observatories. While High Resolution Fly's Eye (HiRes), a fluorescence telescope, reported a steepening of the spectrum at very high energies, Akeno Giant Air Shower Array (AGASA), a ground-based detector, did not observe a suppression at the highest energies, thus contradicting the expectations from the GZK suppression. If these events had an astrophysical origin, due to the GZK effect they would necessarily need to have a nearby origin (of the order of $\sim 100\,\mathrm{Mpc}$). This conclusion created a tension with the expectation that, in this case, their arrival directions should suffer small deviations and should, therefore, point backwards to identifiable sources, which was not the case. The question about the existence of the GZK cut-off, together with the fact that the sources of the highest energy cosmic rays had not yet been identified, led to the construction of a new, larger observatory: the Pierre Auger Observatory (see Chapter 2). The existence of a suppression of the spectrum at the highest energies was verified by the Pierre Auger Observatory after ten years of operation. However, it is necessary to reconstruct the mass composition at the highest energies to determine whether the cause of the suppression is due to propagation effects or the acceleration limits of the sources.

1.2. Sources and propagation

The mechanisms responsible for accelerating UHECRs remain unknown, as no experiment has yet identified their point sources. However, viable acceleration processes have been proposed by Enrico Fermi [26]. In the second-order Fermi mechanism, a charged particle gains energy through elastic scattering with magnetic irregularities in a moving, magnetised cloud, leading to an energy gain proportional to the square of the velocity of the cloud [27]. While the energy gain per scattering event is relatively small, repeated interactions can lead to a significant energy increase for the particle over time. The faster the cloud moves, the more energy the particle can gain.

Given the small energy gain per scattering event, Fermi suggested a more efficient acceleration mechanism where particles could be accelerated at supernova shock fronts, resulting in an energy gain that scales linearly to the shock wave velocity [28]. This process, known as diffusive shock acceleration or first-order Fermi acceleration, is the most widely accepted mechanism. In this scenario, charged particles gain energy by crossing back and forth through ultra-relativistic shock waves, such as those from supernova remnants, due to magnetic field irregular-

ities on both sides. The first-order Fermi mechanism is more efficient as, during the interactions with the shock front, the particle always exits the shock in the upstream direction, ensuring a continuous energy gain. Considering the escape probability of particles from these systems, Fermi also predicted that cosmic ray energy spectra follows an inverse power law, with theoretical models suggesting a spectral index of $\gamma \sim 2.2$, which is consistent with observations [29].

The challenge of accelerating UHECRs is expressed in the form of the minimum requirement for the accelerators, through what is commonly known as the "Hillas condition" [30]. This condition states that a necessary requirement to accelerate particles to UHECR energies is confinement; particles must remain within the acceleration region, which is ensured if their Larmor radius R_L is smaller than the size of the accelerator R. Therefore, the maximum achievable energy, $E_{\max}$, in a source with a characteristic size R and magnetic field B, is

$$E_{\max} \propto \beta Z e B R, \tag{1.3}$$

where Z is the charge number of the accelerated particle, e the unit charge and β the velocity of the acceleration region. While the confinement condition is necessary, it is not sufficient to guarantee UHECR acceleration. Even if a source passes the Hillas condition, it must still have the required energy budget to produce enough UHECRs to explain the observed flux.

Fig. 1.2 shows the Hillas diagram, which combines the characteristic sizes and magnetic fields of different source classes. The lines in the diagram represent the minimum values of R and B required to confine a proton within the acceleration region, up to the corresponding marked energy (knee, ankle, or GZK), assuming $\beta = 1$. The leading candidates for galactic cosmic-ray sources are supernova remnants (SNRs), while the main candidates for extra-galactic cosmic-ray sources are gamma-ray bursts (GRBs), jets of active galactic nuclei (AGNs), and starburst galaxies [31].

Current research aims to identify potential sources of UHECRs. Neutrinos and, to some extent, photons could serve as tracers since they propagate unaffected by intergalactic magnetic fields, yet their fluxes at ultra-high energies are extremely low [33, 34]. Since hadronic cosmic rays are charged particles, their trajectories experience deviations due to the extragalactic and galactic magnetic fields, with heavier nuclei being deflected more than lighter ones since they carry more charge. Even small magnetic fields can cause deflections that add up significantly during their long propagation towards Earth. An alternative approach is to study the light component of UHECRs, such as protons, as they experience less deflection than heavier nuclei, and could potentially be used to trace UHECR sources after modelling the magnetic fields.

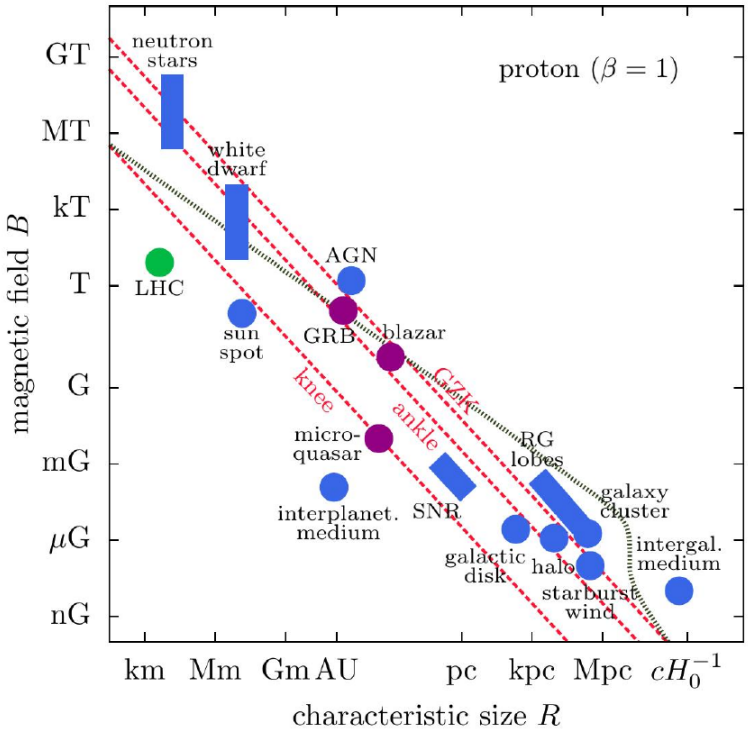

Figure 1.2: Hillas diagram with possible cosmic ray sources depending on their characteristic sizes and magnetic fields. Figure taken from Ref. [32].

1.3. Extensive air showers

The interaction of very high-energy cosmic rays with the atoms of the atmospheric air produce secondary particles that propagate to the ground as an extensive air shower (EAS). The atmosphere acts as an inhomogeneous calorimeter. Detecting these air showers with large ground-based arrays can be accomplished through two primary methods: (i) directly measuring the energy deposits of secondary particles at ground level using surface detectors, or (ii) detecting the fluorescence light emitted by excited nitrogen molecules as the shower propagates through the atmosphere. The longitudinal evolution of the EAS is given by the atmospheric depth X, described by

$$X(h) = \frac{1}{\cos(\theta)} \int_h^\infty \rho(h')\mathrm{d}h', \tag{1.4}$$

where $\rho(h')$ is the air density relative to the height h' above sea level and θ is the zenith angle of the shower, defined between the CR momentum vector and the normal surface vector, to account for the longer path in the atmosphere for an inclined event.

Fig. 1.3 presents the shower model introduced by Heitler and Matthews in

Refs. [35, 36], where the development of the shower is characterised by four distinct components.

Firstly, the hadronic component consists mainly of neutral and charged pions, as well as kaons, neutrons, and some heavier nuclei. This component develops near the core of the shower, with these particles originating from high-energy hadronic interactions during the early stages of the shower's development, subsequently feeding the other components of the shower.

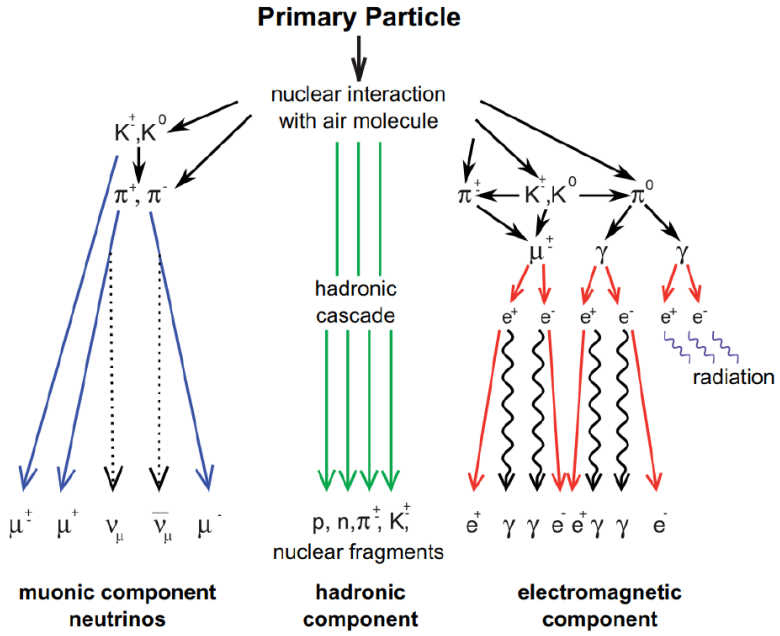

Figure 1.3: Development of an EAS with its different components, according to the Heitler and Matthews model. Figure extracted from Ref. [37].

Secondly, the electromagnetic component consists of photons, electrons, and positrons, which are produced from the decay of secondary mesons and muons. Neutral pions, in particular, decay with a high probability into two photons. When these photons possess sufficient energy, they can produce through pair-production electron-positron pairs. These pairs may subsequently produce photons through bremsstrahlung, which can then produce more electron-positron pairs, thus initiating an electromagnetic cascade. The majority of the secondary particles observed in an EAS, approximately 98%, originates from this electromagnetic component. This component inherits around 90% of the initial energy of the primary, which is quickly absorbed by the atmosphere producing the emission of fluorescence light by the excited nitrogen molecules.

Thirdly, the muonic component is composed by muons and anti-muons that are generated by the decay of charged pions and kaons, constituting less than 2% of the air shower. Charged pions have a longer lifetime compared to neutral pions,

allowing them to undergo multiple interactions before their energy decreases to a limit where their decay into muons and neutrinos becomes more likely than further interactions. The majority of muons reach the ground without further interaction due to their long mean lifetime in the atmosphere ($\sim 2\mu$s). Given that the muonic component is related to the hadronic interactions in the shower, the muonic component serves as a sensitive observable of the mass composition of the cosmic ray, as shown in Section 1.3.2.

Fourthly, the "invisible" component primarily consists of neutrinos, which are produced in the decay of charged mesons such as pions and kaons. Due to their extremely low interaction, neutrinos escape detection in most cosmic-ray experiments, carrying away a small but non-negligible fraction of the total energy of the EAS. The energy lost to this component is generally considered minimal compared to the other components.

1.3.1. Heitler model

In the Heitler model [35], developed in 1944, the evolution of a shower initiated by a photon is governed by electromagnetic processes. In the atmosphere, the photon produces an electron-positron pair via pair production. The electron and positron then produce photons via bremsstrahlung, which can then produce more electron-positron pairs. This process results in an exponential increase of electromagnetic particles in the cascade until a critical threshold energy is reached. The Heitler model explains the main characteristics of an electromagnetic cascade by considering the shower as a binary tree: after traversing an atmospheric layer of thickness λ, defined as the electromagnetic interaction length, each particle produces two new particles, each carrying half the energy of the original particle (see left panel of Fig. 1.4). After n stages, the shower reaches an atmospheric depth X with a total number of particles N, given by

$$N = 2^n = 2^{\frac{X}{\lambda}}. \tag{1.5}$$

In the model hypothesis, the energy is distributed evenly among the N particles, thus the energy per particle is expressed as

$$E = \frac{E_0}{N}, \tag{1.6}$$

where E_0 is the energy of the primary particle. The shower continues developing until the energy of each secondary particle E falls below a critical energy E_c and, consequently, the multiplication process ceases. The critical energy in air is E_c =85 MeV and it represents the minimum energy required to produce new particles.

The shower reaches its maximum size at an atmospheric depth $X_{\max}$ (the depth

where the number of particles is maximal), producing the maximum number of particles $N_{\max}$, expressed as

$$N_{\max} = \frac{E_0}{E_c} = 2^{\frac{X_{\max}}{\lambda}},$$
$$X_{\max} = \lambda \log_2 \left(\frac{E_0}{E_c}\right). \tag{1.7}$$

The maximum amount of particles generated in the shower development is proportional to the energy of the primary cosmic ray and the maximum of the atmospheric depth is proportional to the logarithm of its energy. The Heitler model, despite its simplicity, successfully describes these key features of electromagnetic showers.

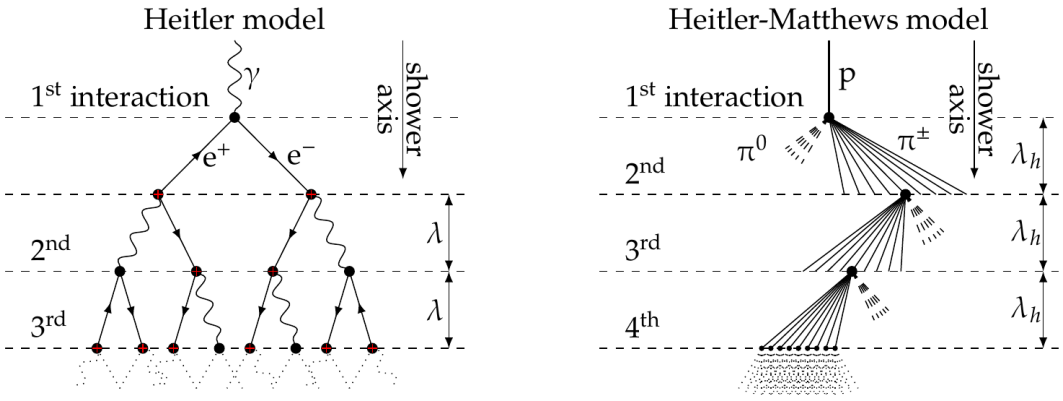

Figure 1.4: Schematics of the shower development for a shower initiated by a photon (left panel) and a proton (right panel), according to the Heitler and the Heitler-Matthews models, respectively.

1.3.2. Heitler-Matthews model

The Heitler model has been generalised by Matthews to showers generated from primary nuclei [36]. The Matthews-Heitler model assumes that pions play a key role for the development of the shower cascade. The process is shown for a proton primary in the right panel of Fig. 1.4. The proton interacts in the atmosphere producing a number of pions. Given that pions are $(\pi^{\pm}, \pi^0)$, the decay ratio is 2:1 (charged:neutral). Neutral pions decay with a high probability into two photons, transferring energy to the electromagnetic cascade, as explained above. Charged pions have a longer lifetime than neutral pions, allowing them to undergo multiple interactions before they decay. The charged pions decay approximately after the hadronic interaction length λ_h, when they reach a critical energy threshold to decay into a muon and a neutrino, originating thus the

muonic component of the shower.

Assuming that each interaction produces N_π pions, after n interactions the average energy of pions, E_π, is given by $E_\pi = E_0/N_\pi^n$. In the framework of the Heitler-Matthews model, the critical energy is fixed to $E_{hc} = 20\,\text{GeV}$ and the maximum number of interactions, $n_{\max}$, is obtained when $E_\pi = E_{hc}$, given by

$$n_{\max} = \frac{\ln\left(\frac{E_0}{E_{hc}}\right)}{\ln N_\pi}. \tag{1.8}$$

In this model, muons are produced only by charged pion decays, thus

$$N_\mu = \left(\frac{2N_\pi}{3}\right)^{n_{\max}}. \tag{1.9}$$

By combining these two equations, we show that the number of muons is related to the primary energy, expressed as

$$\begin{aligned}
\ln N_\mu &= n_{\max} \ln\left(\frac{2N_\pi}{3}\right), \\
&= \frac{\ln\left(\frac{2N_\pi}{3}\right)}{\ln N_\pi} \ln\left(\frac{E_0}{E_{hc}}\right), \\
&= \beta \ln\left(\frac{E_0}{E_{hc}}\right),
\end{aligned} \tag{1.10}$$

where $\beta = \frac{\ln\left(\frac{2N_\pi}{3}\right)}{\ln N_\pi} = 0.85$ in the Heitler-Matthews model. However, air-shower simulations fit better β between 0.85 to 0.92.

From the neutral pions we can derived an equation for the maximum of the atmospheric depth. Given that each interaction produces $N_\pi/3$ neutral pions and each neutral pion decays into two photons, each of these photons, with an energy of $E_0/2N_\pi$, generates an electromagnetic sub-shower. Therefore, we can modify Eq. (1.7) to

$$X_{\max} = X_0 + \lambda \log_2\left(\frac{E_0}{2N_\pi E_c}\right), \tag{1.11}$$

where we assumed that the proton first interacted at X_0.

The superposition principle is used to model air showers initiated by nuclei of atomic mass number A and energy E_0. According to this principle, an air shower produced by this nuclei is equivalent to the sum of A proton showers of energy E_0/A. Therefore, the number of muons can be written as $N_\mu^A(E_0) = AN_\mu^p\left(\frac{E_0}{A}\right)$ and, from Eq. (1.10), we can thus derive

$$\begin{aligned}
\ln N_{\mu}^{A}(E_0) &= \ln A + \ln N_{\mu}^{p}\left(\frac{E_0}{A}\right), \\
&= \ln A + \beta \ln\left(\frac{E_0}{A E_{hc}}\right), \\
&= (1-\beta)\ln A + \beta \ln\left(\frac{E_0}{E_{hc}}\right), \\
&= (1-\beta)\ln A + \ln N_{\mu}^{p}(E_0). \qquad (1.12)
\end{aligned}$$

Moreover, the maximum of the atmospheric depth can be obtained from Eq. (1.11) by replacing E_0 for E_0/A, resulting in

$$\begin{aligned}
X_{\max}^{A}(E_0) &= X_{\max}^{p}\left(\frac{E_0}{A}\right), \\
&= X_{\max}^{p}(E_0) - \lambda \log_2 A.
\end{aligned}$$

In the framework of the Heitler-Matthews model of a cascade, the number of muons N_μ and the maximum of the atmospheric depth $X_{\max}$ are mass composition sensitive observables. Showers initiated by heavier nuclei at the same primary energy are expected to produce more muons and reach their maximum development higher in the atmosphere. Iron primaries are expected to interact earlier in the atmosphere than protons, since the interaction probability increases with the number of nucleons. Additionally, the fluctuations in their first interaction depth are significantly smaller, generating a narrower $X_{\max}$ distribution.

1.4. Mass composition and muon deficit

The energy-dependent mass composition of cosmic rays carries a unique imprint from the origin and propagation of cosmic rays. To accurately determine both the energy and mass of the cosmic ray from air shower measurements, a comprehensive understanding of the hadronic interactions in an air shower is needed. While the fluorescence technique has reduced the model dependence in energy measurements by tracking the longitudinal shower development, significant uncertainties in hadronic interactions still pose a challenge for precise mass determination. In Fig. 1.5, the predictions are shown for the mean logarithmic mass $\langle \ln A \rangle$. As explained above, the two leading observables to infer $\langle \ln A \rangle$ are the depth of the shower maximum $X_{\max}$, illustrated as a yellow band, and the number of muons N_μ produced in the shower, represented as a green band. The width of the bands in Fig. 1.5 arises from two main sources of uncertainty: experimental measurement errors and the larger uncertainties associated with

converting air shower observables into $\langle \ln A \rangle$, which requires air shower simulations with hadronic interaction models. The leading models are tuned to LHC data, such as EPOS-LHC [38] and QGSJet-II.04 [39]. However, inconsistencies between the mass composition measurements derived from the two leading observables ($X_{\max}$ and N_μ) suggest that these models are not correctly describing all aspects of hadronic physics in air showers.

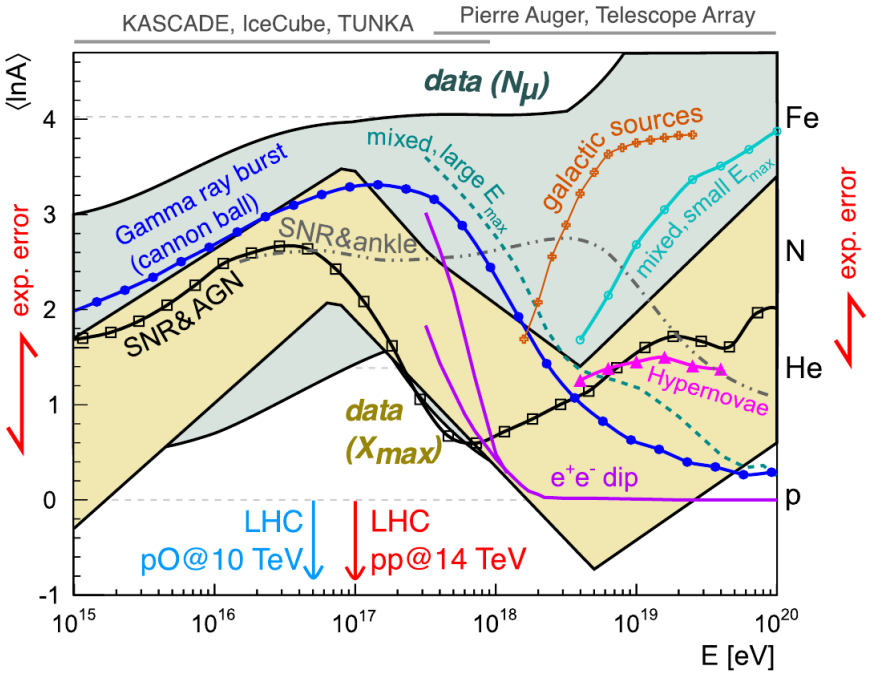

Figure 1.5: $\langle \ln A \rangle$ as a function of the cosmic ray energy E to determine the mass composition. The model predictions are indicated as markers and lines, while the data is represented as bands. At the sides, vertical arrows display the instrumental error of the leading experiments at low and high energies. Figure extracted from Refs. [40, 41].

The correct simulation of muons in air showers is a long-standing problem. Several experiments have reported discrepancies between observed data and theoretical predictions, such as the HiRes/MIA collaboration in the year 2000 and the NEVOD-DECOR experiment in 2010 [40], indicating a persistent muon deficit in simulations.

The muon density at ground level is influenced by various factors, including the cosmic ray energy, the zenith angle of the shower, the lateral distance from the shower axis, and the energy threshold of the muon detectors. As a result, direct comparisons of muon measurements between different experiments are not feasible. Since muon measurements are performed in each experiment under very different conditions and using different techniques, each experiment is compared to air shower simulations by computing the z-scale, defined in Ref. [40] as

$$z := \frac{\ln(N^{\text{data}}_{\mu,\,\text{det}}) - \ln(N^{\text{p}}_{\mu,\,\text{det}})}{\ln(N^{\text{Fe}}_{\mu,\,\text{det}}) - \ln(N^{\text{p}}_{\mu,\,\text{det}})} \tag{1.13}$$

where $N^{\text{data}}_{\mu,\,\text{det}}$ is the measured muon density by the detector, while $N^{\text{p}}_{\mu,\,\text{det}}$ and $N^{\text{Fe}}_{\mu,\,\text{det}}$ are the proton and iron muon densities derived from from full-detector simulations.

The z-scale adopts air shower simulations as a universal reference frame, ranging from $z = 0$ for pure proton showers to $z = 1$ for pure iron showers, assuming there are no discrepancies between real and simulated air showers. However, comparing data to Monte Carlo (MC) ratios instead of just data introduces a complication. This ratio depends on the selection of corresponding air shower simulations, and matching the cosmic-ray energy between simulations and experiments is challenging. In air shower experiments, systematic uncertainties on the energy scales typically range from 10% to 20%. Two otherwise identical experiments with an energy-scale offset of 20% would observe an 18% offset in the data/MC ratios, simply because equivalent measurements are compared to air showers simulated at different (apparent) energies. A cross-calibration of the energy-scales is needed to remove these offsets. Given that the cosmic-ray flux is highly isotropic up to $10^{19.2}$ eV, it can serve as a universal reference. Assuming all deviations in measured fluxes between different experiments arise from energy-scale offsets, then a relative energy-scale ratio can be determined for each experiment so that the all-particle fluxes overlap [42, 43].

The z-scale of different experiments, obtained after applying the energy-scale cross-calibration, is shown in Fig. 1.6 for EPOS-LHC and for QGSJII-04 in the top and bottom panels, respectively. Muon measurements seem to be consistent with simulations up to about $1{\times}10^{16}$ eV. However, at higher energies, a growing muon deficit in the simulations is observed.

The underlying cause of the observed muon deficit remains unclear, with potential explanations ranging from the emergence of new phenomena at high energies to deficiencies in the modelling of hadronic interactions across different energy scales [44]. Identifying the specific phase-space region where this discrepancy arises is crucial, as it would enable improvements in high-energy hadronic interaction models, ensuring they accurately reproduce the observed muon content. Achieving this level of agreement would not only enhance the reliability of these models but also allow for a reduction in the systematic uncertainties associated with mass composition analyses. Consequently, this could lead to a deeper understanding of the origin of cosmic rays.

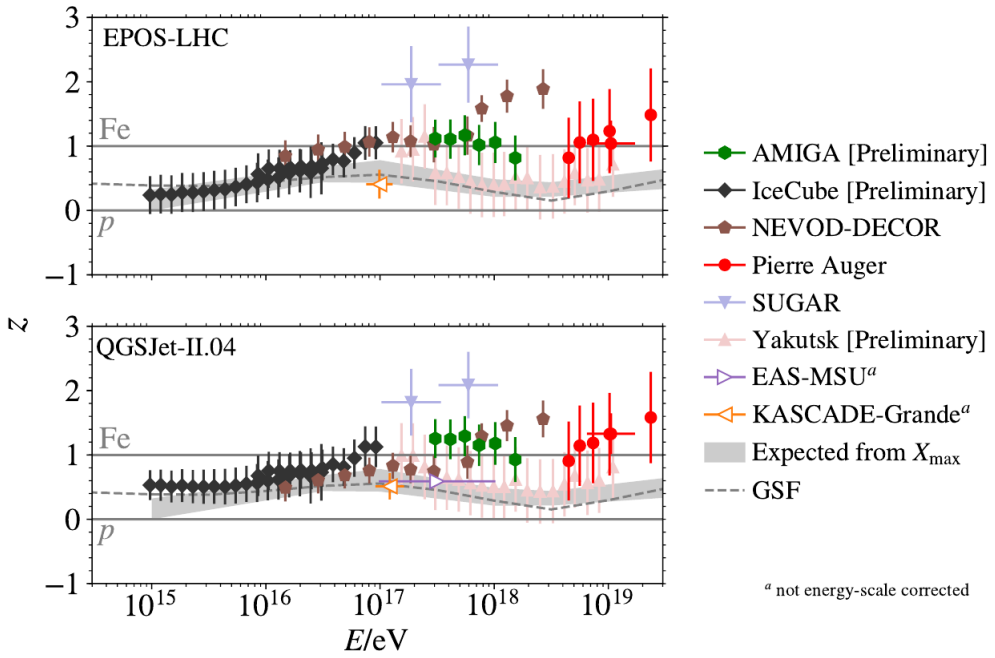

Figure 1.6: z-scale of different experiments, obtained after applying the energy-scale cross-calibration, for EPOS-LHC (top panel) and for QGSJII-04 (bottom panel). The points for KASCADE-Grande and EAS-MSU cannot be cross-calibrated and are only included for comparison. Image taken from Ref. [40].

Chapter II

The Pierre Auger Observatory

The Pierre Auger Observatory is located in the Departments of Malargüe and San Rafael in the Province of Mendoza, Argentina. Built to study the highest-energy cosmic rays, it is the largest and most precise observatory of its kind, covering a total area of approximately 3000 km^2 to detect with adequate statistics the low flux of high-energy cosmic rays. It has been fully operational for over a decade. A key feature of Auger was its *hybrid detection* concept: a surface array of 1660 water Cherenkov detectors is complemented with 27 fluorescence telescopes which overlook the atmosphere above the surface array. Fig. 2.1 and Fig. 2.2 show the schematic of the Observatory with its hybrid detection. Combining data from both detection systems significantly enhances the reconstruction capability beyond what is achievable with a single technique, unlike other experiments that rely solely on surface detection, as utilised by AGASA [23] and Haverah Park [20], or fluorescence detection, as pioneered by Fly's Eye [24] and employed in HiRes [25].

The Observatory is currently undergoing an upgrade dubbed AugerPrime [10]. The purpose of AugerPrime is to improve the sensitivity to mass composition observables, such as the muon content of the air showers. In order to probe the characteristics of cosmic rays above 10^{17} eV, AugerPrime will provide a cleaner separation between the electromagnetic and muonic components of the showers. The Underground Muon Detector (UMD), also referred to as Auger Muons and Infill for the Ground Array (AMIGA), plays a key role in AugerPrime since it is designed to perform a direct measurement of the muon component of the air showers.

In this chapter we present the different detectors that integrate the Pierre Auger Observatory. The main detectors of the baseline design, which are surface detectors and the fluorescence telescopes, are shown in Section 2.1 and Section 2.2, respectively. The detectors that integrate AugerPrime are briefly summarised in

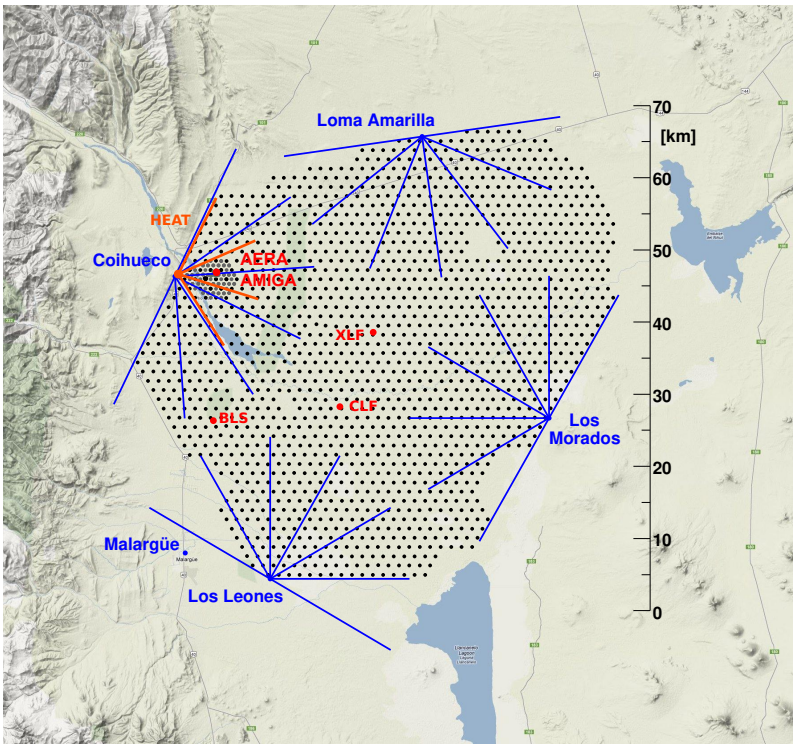

Figure 2.1: Schematic of the Pierre Auger Observatory [45], including a kilometric scale for comparison. Each black dot represent a surface detector, while the fluorescence detectors and their fields of view are illustrated with blue colours. Other detection systems are displayed, including the UMD (alias AMIGA).

Section 2.3 and Section 2.4. As this thesis focuses on the UMD, this detector is explained particularly in depth in Section 2.5.

2.1. Surface Detector

The Surface Detector (SD) is an array of Water-Cherenkov Detectors (WCDs) that provides key information about the arrival times and lateral distribution of the secondary particles of EAS as they reach the ground. The baseline design of the surface array consisted of 1600 WCDs distributed in a triangular grid with 1500 m spacing, ensuring full trigger efficiency for events of energy above $2.5{\times}10^{18}$ eV. In addition to the SD array with a 1500 m spacing, referred to as SD-1500, two denser arrays were deployed. The "Infill array", dubbed as SD-750, is composed of the standard array with additional detectors placed at half the spacing between them, i.e., forming an array with a 750 m distance between detectors. This denser array covers an area of 23.5 km^2 and enables the triggering of smaller showers caused by lower energy cosmic rays, allowing to lower the trigger threshold by one decade in energy and enabling the detection of cosmic rays with full efficiency down to $3{\times}10^{17}$ eV. To access even lower energies, additional detectors were installed at the

Figure 2.2: The *hybrid detection* of the Pierre Auger Observatory, showing a water Cherenkov detector with fluorescence detectors seen in the background.

central point of the 750 m-triangles, forming a 433 m-array, referred to as SD-433, and covering an area of 1.9 km^2. Some positions have been equipped with more than one detector for timing and calibration studies, bringing the total number of detectors in the field to 1660 units.

The WCDs operate by detecting Cherenkov light emitted when relativistic charged particles from air showers travel through water (an electrically polarizable medium) [46, 47]. Electrons, positrons, and muons produce Cherenkov radiation if their speed exceeds the speed of light in water. When high energy photons interact with the water, they can also produce electron-positron pairs and generate detectable Cherenkov emission. While electrons lose energy quickly and penetrate only a few centimetres, muons, due to their greater mass, traverse the entire tank, emitting photons along their path.

Each WCD consists of a 10 m^2 water surface area and a 1.2 m deep tank, holding 12,000 litres of ultra-pure water contained in a liner within the tank. The inner liner, made of reflective Tyvek, ensures uniform Cherenkov light distribution within the water volume, while the black outer layer provides light tightness. A photograph and a schematic of the detector are shown in Fig. 2.3. The SD stations are completely autonomous, self-powered, and use wireless communica-

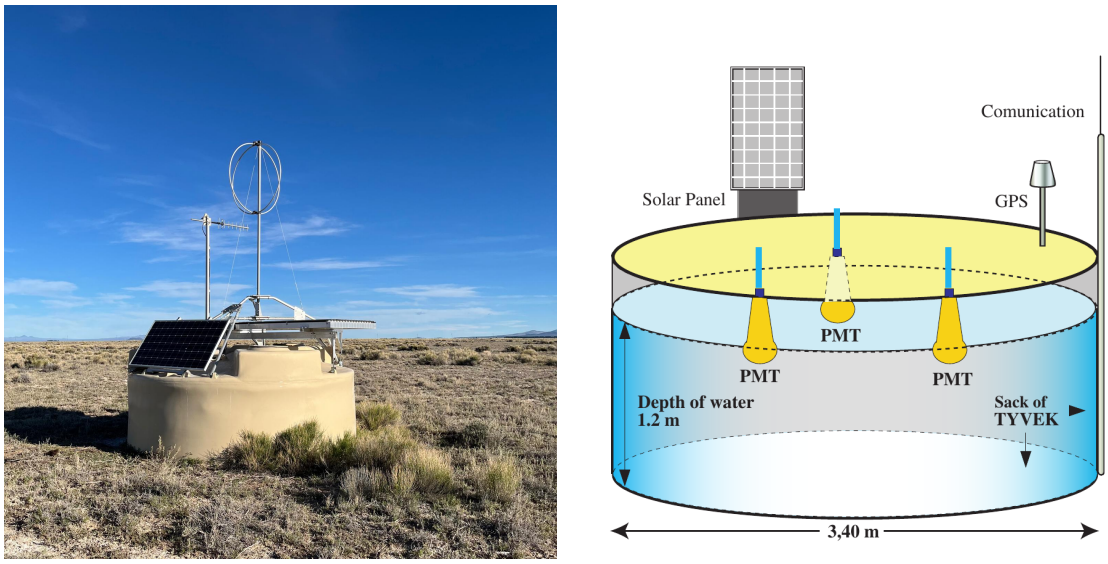

Figure 2.3: (left) Picture of a deployed WCD equipped with the Scintillator Surface Detector and the Radio Detector on top. (right) Schematic view inside a WCD. Image taken from Ref. [48].

tion to interact bidirectionally with the Central Data Acquisition System (CDAS). Each station is equipped with a GPS receiver and antenna for event timing and synchronisation.

Three photomultiplier tubes (PMTs) are used inside each WCD to detect the Cherenkov light produced as particles of the EAS travel through the water. Two signals are obtained from each PMT. The low-gain channel (LG) is connected to the anode of the PMT, while the high-gain channel (HG) to the last dynode and is amplified to provide a signal with 32 times the charge gain of the anode [49]. The analog pulses are read out by the Unified Board (UB), which is mounted atop the WCD and sampled using two 10-bit Flash Analog-to-Digital Converters (FADCs) at a frequency of 40 MHz [46]. The output is a time trace that can be integrated to acquire a signal. As part of AugerPrime, the SD stations will be upgraded with new electronics, replacing the UB electronics with the Upgraded Unified Board (UUB) and increasing thus the data quality by providing faster sampling of analog traces (120 MHz), better timing accuracy, increased dynamic range (12-bit FADC), and enhanced triggers [50].

The detector is calibrated using the "vertical equivalent muon" (VEM), determined by the average charge collected from Cherenkov light produced by a vertical central through-going muon [51]. The total signal recorded by the WCDs, which is a measure of the total energy transferred to Cherenkov light inside the detector, is converted then into VEM units.

The SD data acquisition (DAQ) trigger system is structured hierarchically to reduce the 3 kHz background rate from atmospheric muons without losing physics

events [52]. The lowest trigger levels are T1 and T2, that operate at the local level of each WCD. Two independent trigger modes are implemented as T1:

- Threshold trigger (Thr1): Detects muons in highly inclined showers by requiring all three PMTs to register a signal above 1.75 VEM, reducing the background rate from ~ 3 kHz to ~ 100 Hz.
- Time-over-threshold trigger (ToT): Identifies small signals spread in time, detecting low energy showers with a zenith angle below 60°. By requiring at least two PMTs to detect 0.2 VEM for over 325 ns within a 120-bin window, it efficiently filters out random muon background, reducing the rate to less than 2 Hz.

The T2 trigger reduces the T1 rate to ~ 23 Hz at each WCD. The T3 trigger, determined globally by CDAS, identifies at least three T2-triggered stations clustered in time and space. The total T3 trigger rate is presently of the order of 0.1 Hz. To ensure data quality, two off-line "triggers" are applied: T4, which selects real showers and discards accidental coincidences, and a fiducial cut, which preserve events whose shower core is within an area well enclosed by functioning detectors.

The reconstruction of cosmic ray energy and arrival direction from air showers triggering the surface detector array is based on the signal sizes and start times from individual stations [49]. Showers are reconstructed by fitting signals of the triggered detectors to a lateral distribution function and arrival times to a shower front shape, allowing determination of the shower core impact point, azimuthal and zenith angles, and the lateral spread of the signal as a function of the distance to the shower axis. From the lateral spread of the shower, the signal expected $S(1000)$ is interpolated. The reference distance of 1000 m (from the shower axis) is chosen for the SD-1500 because it minimises the fluctuations in the expected signal. Given the dependence of the atmospheric attenuation with zenith angle, $S(1000)$ is corrected using the Constant Intensity Cut method, which is based on the fact that the flux of cosmic rays above a certain energy is independent of the arrival zenith angle. The zenith angle-corrected value is normalised to a median angle of 38°, S_{38°, and the absolute energy scale for S_{38° is assigned based on hybrid data acquired with the Fluorescence Detector.

2.2. Fluorescence Detector

The Fluorescence Detector (FD) is composed of 24 telescopes, installed in four buildings - Los Leones, Los Morados, Loma Amarilla, and Coihueco - located atop small elevations on the perimeter of the surface array. The FD can directly estimate the energy of the primary particle and the maximum shower depth, as

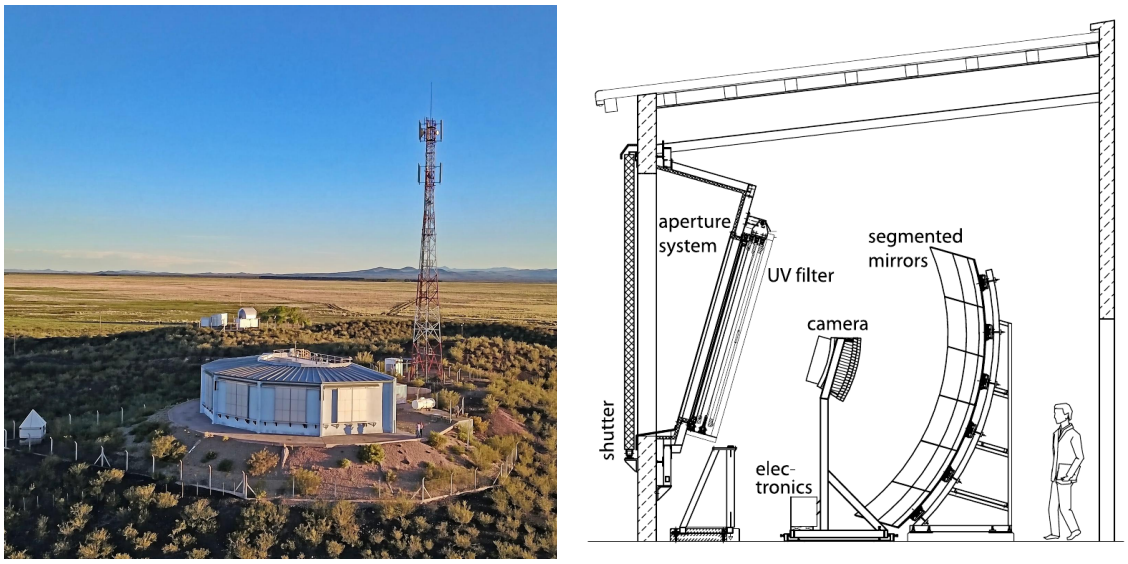

Figure 2.4: (left) Picture of one of the four air fluorescence sites. (right) Schematic view of a fluorescence telescope. Image taken from Ref. [53].

the intensity of fluorescence radiation produced in the atmosphere is directly proportional to the number of particles in the shower. In the left panel of Fig. 2.4, one of the four air fluorescence sites can be observed. Each site is equipped with six telescopes [53], in six independent bays within a building with controlled climate. Each telescope has a field of view from 1° to 31° in elevation and covering 30° in azimuth, facing towards the interior of the array so that the combination of the six telescopes provides 180° coverage in azimuth. Three additional fluorescence telescopes "HEAT" (High Elevation Atmospheric Telescopes) [54] were installed to complement the FD. The objective of the HEAT telescopes is to observe lower energy showers, whose maximum development occurs higher in the atmosphere. To achieve this, the instruments have a field of view with an elevation between 30° and 60°. The field of view of the fluorescence telescopes at the 4 locations of the FD is illustrated in Fig. 2.1 with blue lines, while the view of the HEAT extension at Coihueco is in red. The Central Laser Facility (CLF) and the Extreme Laser Facility (XLF), marked with red dots, are located at the centre of the SD array, at 12 km from each other. They are used for the measurement and monitoring of the atmospheric conditions, firing vertical UV laser pulses which are registered by the FD telescopes in order to determine the light attenuation in the atmosphere.

The goal of the FD telescopes is to track the longitudinal development of EAS by measuring the ultraviolet fluorescence light emitted isotropically (in the ~ 300 - 430 nm range) by the molecules of the atmospheric nitrogen, which become excited as charged particles from the cosmic air showers traverse the atmosphere. The right panel of Fig. 2.4 illustrates an individual FD telescope. The nitrogen fluorescence light enters through a large UV-passing filter window, is collected

by a segmented spherical mirror, with an area of 13 m^2 and 3.4 m radius of curvature, and is focused onto a camera of 440 pixels with photomultiplier light sensors, arranged in a matrix of 22 rows by 20 columns. A shutter system and fail-safe curtains protect the telescope when not in operation or when excessive outside light or weather effects are detected.

The number of emitted fluorescence photons is proportional to the energy deposited in the atmosphere due to electromagnetic energy losses by the charged particles. Once the geometry of the shower is known, the light collected at the aperture as a function of time can be converted to the energy deposited by the shower as a function of the traversed atmospheric depth X. The full longitudinal profile of the energy deposit $\frac{dE}{dX}(X)$ and its maximum at depth $X = X_{\max}$ are estimated by fitting an asymmetric bell-shaped Gaisser–Hillas function to the time profile of photoelectrons detected in the PMTs of the FD cameras, where a log-likelihood fit is used to compare them to the expectation from the Gaisser-Hillas function after folding it with the fluorescence yield (the proportionality between the fluorescence intensity and the energy deposit), atmospheric transmission, lateral distributions and detector response. Finally, the integral over the total longitudinal profile gives the total energy dissipated electromagnetically, which is approximately 90% of the total energy of the primary cosmic ray. The total energy is estimated by correcting for the "invisible energy" carried away by neutrinos. Systematic uncertainties in the energy scale amount to 14%, with the largest contribution of 9.9% arising from the absolute calibration of the telescopes. Other sources of uncertainty include fluorescence yield, atmospheric conditions, profile reconstruction, estimation of invisible energy, and energy scale stability.

While the SD operates continuously throughout the year, the high sensitivity of the cameras limits the working time of the FD to clear, moonless nights, resulting in a duty cycle of approximately ~15%. An EAS detected by both the FD and SD is classified as a "hybrid event", allowing a very precise timing of arrival of the shower, which is required for a precise geometric reconstruction. The events that trigger three or more SD stations are named "Golden hybrid", since an independent reconstruction can be made with the SD alone. To assign the energy to the showers detected with the SD, these high-quality hybrid events are used for cross-calibration, relating the shower size from the SD, S_{38°, to the almost-calorimetric measurement of the shower energy from the FD, E_{FD}. The relation between S_{38° and E_{FD} is well described in Ref. [55].

2.3. Scintillator Surface Detector

The Scintillator Surface Detector (SSD) will be installed above each of the existing WCDs. The SSD consists of a box of 3.8 m × 1.3 m, housing two plastic scintillator

panels, each covering an area of 1.9 m^2, fixed to an aluminium frame mounted on top of the WCD (see Fig. 2.2). The SSD array will measure the lateral footprint of EAS at the surface, with greater sensitivity to the electromagnetic component than to muons. Whereas in a WCD the signal deposited by electromagnetic particles (γ, $e^{\pm}$) is proportional to their energy and the signal from muons is proportional to their track length, in the SSD each particle contributes to the signal essentially one MIP (Minimum Ionising Particle). Given that the SSD and the WCD have different responses to muons and electromagnetic particles, this will allow the disentangling of the different shower components.

2.4. Radio Detector

Extensive air showers are composed of charged particles undergoing acceleration in the atmosphere, thus leading to the generation of radio emission in the frequency range of tens to hundreds of MHz. AugerPrime will also include a radio-detector (RD) covering 3000 km^2, with a radio antenna installed atop each of the 1660 WCDs. Fig. 2.2 presents a deployed WCD equipped with the SSD and the radio antenna. Horizontal air showers produce a large footprint of the radio emission on the ground, covering areas of the order of 100 km^2 for very inclined showers. This has already been confirmed experimentally with the Auger Engineering Radio Array (AERA), which consists of an array of more than 150 radio detector stations distributed over an area of about 17 km^2 and co-located with the infill array [56].

Combining the muon content of the WCD with the electromagnetic energy measured by the RD will allow us to determine the energy dependence of the number of muons in inclined air showers up to the highest energies, as has previously been done with the WCD-FD combination, but achieving an order of magnitude higher event statistics. While the WCD-SSD combination measures the electron-to-muon ratio (e/μ) for vertical showers, the WCD-RD extends this to horizontal showers, increasing the aperture of the Observatory for mass-sensitive investigations.

2.5. Underground Muon Detector

The two denser arrays SD-750 and SD-433 will be equipped with 219 scintillation modules of the UMD located at 73 positions: 61 locations in the first array, and 12 in the latter. Currently, 45 positions (61% of the full UMD array) are in acquisition (see Fig. 2.5). The full UMD array is expected to be completed by end-2025.

In the final design of the UMD, exhibited in the left panel of Fig. 2.6, three modules of 10 m^2 are buried at 2.3 m next to a WCD of the SD-750 and the

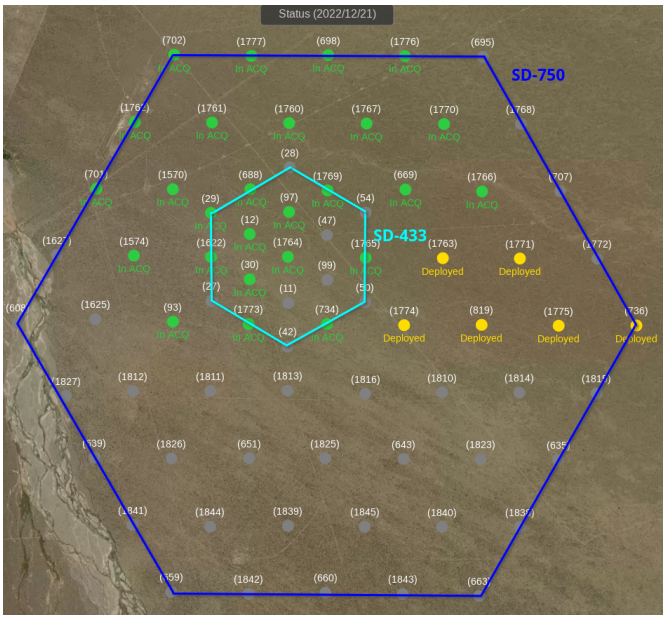

Figure 2.5: Schematics of the WCDs (circles) where UMD positions were deployed (yellow) and are in acquisition (green) in the SD-750 (blue grid) and SD-433 (light blue grid).

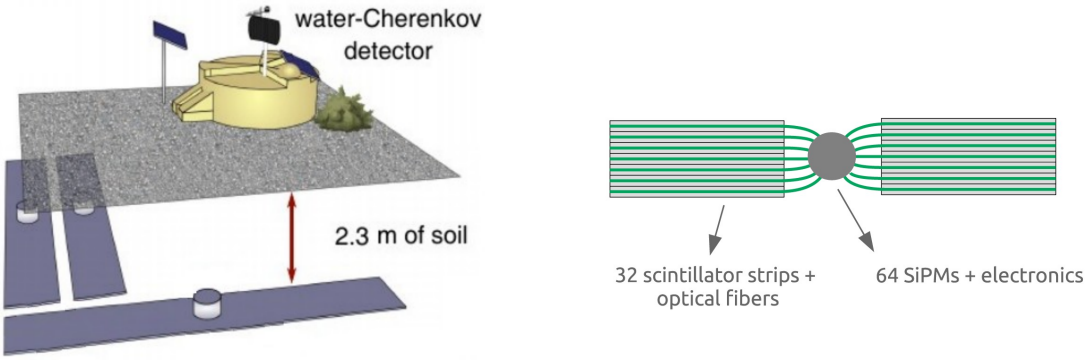

Figure 2.6: (left)Schematicof the final UMD design with three modules of 10 m^2. (right) Schematic of an UMD module.

SD-433 arrays. In the engineering array, 2 modules of 5 m^2 and 2 modules of 10 m^2 were used instead. The UMD modules are located in the vicinity of the WCD, so the same physical point of the shower development can be measured with all AugerPrime detectors (RD+SD+SSD+UMD), in order to perform multi-hybrid analysis and to compare the UMD estimation of the muon content with the one measured by SSD+WCD. Vertical muons must have a minimum energy of approximately 1 GeV to reach the detector, taking into consideration the depth at which the detectors are buried and the density of the soil.

Each module consists of 64 plastic scintillator strips, divided into two identical panels of 32 strips each, containing wavelength shifting (WLS) optical fiber connected to an array of 64 silicon photomultipliers (SiPMs) (see right panel of

Figure 2.7: (Top) Three modules of 10 m^2 deployed in the field. (Bottom) Scintillator module constructed in the assembly building, where we show the scintillation strips (white on the outside) and the WLS optical fibers (green) placed in the cookie.

Fig. 2.6). When a muon impinges the scintillator, the photons produced are collected and propagated along the fibers towards a cookie, which makes the optical connection to the SiPMs. In Fig. 2.7, pictures of a complete deployed station are shown in the top panels, along with a module under construction in the bottom panels. The scintillation strips (white on the outside) can be observed, as well as the WLS optical fibers (green) placed in the cookie.

The scintillation material utilised in the strips is polystyrene doped with fluor and the principle of detection is through fluorescence, given that the impinging muons excite the electrons of the scintillation material, which de-excite by emitting fluorescence photons. The polystyrene base (Dow Styron 663W) absorbs the

incident radiation and emits photons in the ultraviolet spectrum. These photons would attenuate in millimetres if they were not absorbed by a first dopant (2,5-diphenyloxazole or PPO), which emits other UV photons with larger attenuation length. Since the plastic is not transparent for these photons, a second dopant (1,4-bis(5-phenyloxazol-2-yl) benzene or POPOP) is introduced, which absorbs these ultraviolet photons and emits blue photons of approximately 420 nm. Each strip, measuring 4 m long, 4.1 cm wide, and 1.1 cm thick, is covered in the outside with a refractive titanium dioxide (TiO_2) layer to decrease the probability of photons escaping from the strip.

These blue photons produced in the scintillator have a mean attenuation length between 5 cm and 25 cm. Given that the length of the scintillator strip is 4 m long, an WLS optical fiber is used to absorb the blue photons and re-emit them as green photons with $\lambda \sim 500$ nm. The typical time of these green photons is between 3 ns and 10 ns, so they can propagate several meters through the optical fiber until they are collected by the photodetector. The UMD utilizes the Saint-Gobain BCF-99-29AMC multi-clad WLS fibers, which have a ~1.2 mm radius and are coupled to the scintillator strip with optical cement. These fibers are made of a polystyrene core doped with a fluorophore, and cladded with two layers of transparent material with lower refractive indexes than the core. The two layers of cladding material allows ~ 10% of these green photons emitted by the fiber to remain inside the fiber (due to the refractive indexes of the layers) and propagate through the fiber core by total internal reflection. The photons that were not attenuated are able to reach the SiPM and produce signal. Fig. 2.8 shows the schematic of the scintillation strip with the WLS optical fiber (left panel) and of the fiber with the refractive indexes of the core and claddings (right panel).

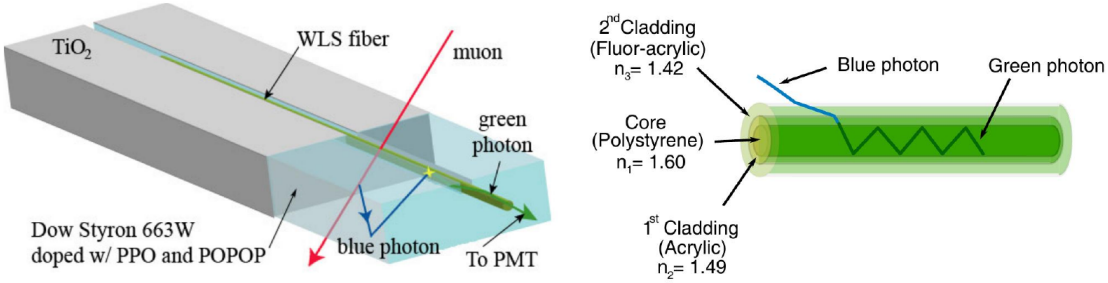

Figure 2.8: (left) Schematic of the scintillation strip with the WLS optical fiber. (right) Schematic of the fiber with the refractive indexes of the core and claddings.

During the engineering array of the UMD, PMTs were used as photodetectors instead of SiPMs. For the full UMD array, the SiPM option was chosen because of their better photodetection efficiency, reduced power consumption and lower cost

[57]. Each SiPM is an array of 1584 avalanche photo-diodes (also referred to as cells) operated in Geiger mode, where the number of triggered cells is referred to as photon equivalents (PE). For a detailed review of the design, characterisation and implementation of the SiPMs for the data acquisition see Refs. [58, 59]. The UMD electronics consist, basically, of: an array of SiPM with its read-out system, a Field-Programmable Gate Array (FPGA) that manages acquisition logic, data transmission and slow control, and an interface for the WCD trigger, monitoring data, and communications [60]. The UMD works as a slave-detector, given that the event acquisition is governed by the SD.

The number of muons in the UMD can be estimated in two complementary ways to extend the dynamic range of the detector: binary mode (or counting) for low particle densities and ADC mode (or integrated signal) for high particle densities [61]. The first relies on the amplitude of the signals, the latter on its charge.

In the binary mode the 64 SiPM signals are handled independently through a pre-amplifier, fast-shaper, and a discriminator. A "1-bit" is produced if the signal goes above the discriminator threshold and "0-bit" otherwise. An example of a simulated single-muon signal [62] is shown in the top panel of Fig. 2.9. This discriminator threshold is set at 2.5 PE to filter most of the SiPM dark current (due to the crosstalk between the SiPM cells). The calibration procedure [60] ensures an equalised response in the whole SiPM array. For each detector unit of 10 m^2, 64 binary traces are produced in each event, where each trace spans 2048 time bins.

The single-muon signal in the binary mode was characterised employing laboratory measurements, showing that the minimum time a signal produced by a single muon above 2.5 PE threshold is 12.5 ns. Since muons deposit wider signals than the background in the binary trace, the criteria to count a muon in the binary mode is to identify a sequence of at least 4 consecutive positive bits, i,e., "1111...". Muons are then identified by applying a time window starting from the first identified match, during which the muon search is inhibited. An optimal inhibition window of 12 samples from the first match was selected in Ref. [63], containing approximately 99% of the muon signals. It was proposed as a compromise between the under-counting due to the strip efficiency and over-counting due to both the detector noise and wide muon signals. In Ref. [64], a new strategy was developed that reconstructs the time structure of the muon signal to a single time-bin resolution. This strategy, known as the *one-bin* strategy, employs the optimal inhibition window of 12 samples as the inhibited time of the detector. Conversely, in Ref. [65], a muon reconstruction was proposed without using the time structure of the muon signal, by employing the strategy known as *infinite* window (the inhibition window is equal to the total 2048 time bins of the

trace). Both strategies perform reasonably well. For a detailed description of the *infinite* window and *one-bin* strategies see Ref. [66].

The sources of bias in the muon reconstruction within the binary mode arise from several factors common to all segmented detectors. These include pile-up, corner-clipping, detector inefficiency, and noise. Strategies to mitigate these effects have been documented in various studies, as can be seen in Refs. [64, 65, 66, 67, 68]. Pile-up occurs when multiple muons strike the same scintillation bar within the time resolution of the detector, leading to an under-counting effect due to their registration as a single muon. Conversely, corner-clipping muons are inclined muons that cross neighbouring adjacent bars and generate signals, causing an over-counting. It can also be produced, to a lesser extent, by a knock-on electron that deviates and activates the adjacent bar. This phenomenon depends on the detector geometry, increasing with the zenith angle and becoming more pronounced when the detector's azimuth angle is more perpendicular to the shower axis. In contrast, detector inefficiency, caused by a muon failing to activate any bar, and noise, measuring spurious muon patterns caused by spontaneous light emission in the scintillator-fiber system, are subdominant and have a negligible impact [60].

The ADC mode depends on the charge of the signal determined by the energy deposited by muons in the plastic scintillator strips. The ADC mode operates by treating the module as a single unit, independent of its internal segmentation. In this mode, the signals from all 64 SiPMs are summed and then amplified through two separate channels using high- and low-gain amplifiers. The amplified signal of each channel is digitised with a sampling interval of 6.25 ns, resulting in a waveform of 1024 time bins. Finally, the integrated charge from the combined signals is calculated and stored (see bottom panel of Fig. 2.9). The low-gain (LG) channel in this mode extends the dynamic range of the detector, allowing it to measure high muon densities near the shower core.

In Ref. [63], an ADC mode based method was proposed to estimate the number of muons by dividing the signal charge by the mean charge deposited by a single vertical muon, extracted from the calibration histograms obtained by the algorithm implemented in Ref. [60]. In this method, the number of muons N_{μ}^{ADC} can be estimated following equation

$$N_{\mu}^{\mathrm{ADC}} = \frac{q_{\mathrm{meas}} \cos\theta}{\langle q_{1\mu}(\theta{=}0)\rangle}, \tag{2.1}$$

where the quantity in the numerator is the total charge per vertical path-length and the quantity in the denominator is the mean charge deposited by vertical muons. Since in the field the zenith angle of each muon impinging on the scintillator θ_{μ} can not be measured, the approximation $\langle\theta_{\mu}\rangle \approx \theta_{\mathrm{shower}}$ is used.

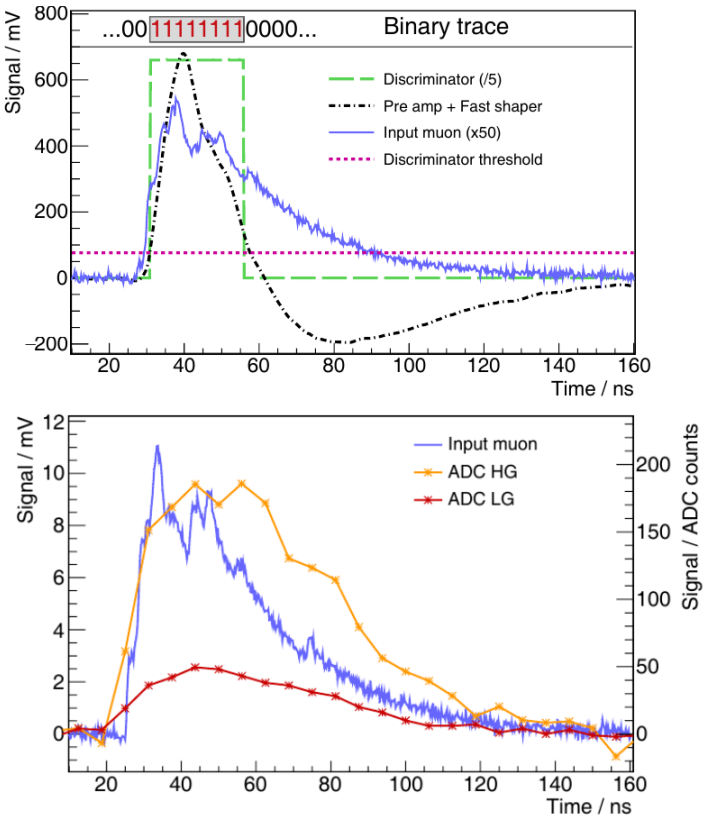

Figure 2.9: Two simulated single-muon signals at 2 m for the binary mode (top) and for the ADC mode (bottom). In the first case, the signal from the SiPM and the discriminator pulse are re-scaled for illustration.

The optimal muon reconstruction for the ADC mode will be developed in the following chapters.

Chapter III

Monitoring the performance of the UMD

Pierre Auger Observatory has implemented several procedures to examine the performance of its different detectors. These procedures are vital to guarantee the attainment of the best possible scientific results. In this chapter we developed, scrutinising the so-called ADCT1 files, a set of new tools to complement existing monitoring tools of the UMD (see Ref. [69]). We introduce monitoring tools for the UMD to ensure good performance of the modules and a rapid response detecting malfunctioning of a module.

The ADCT1 files contain daily measurements of the ADC mode, obtained with a two-folded condition: an individual muon pattern in the binary traces of a whole module and a T1 trigger from the WCD.

When a T1 trigger is received, the algorithm looks for a muon pattern over a window around the position of the T1, denoted as "Signal+Noise" window. The muon pattern consists of a sequence between four and twelve "1"s on only one scintillator strip, while having zero "1"s on all the other scintillator strips. If the muon condition is fulfilled, a signal+noise charge is obtained by integrating the ADC trace over a 200-ns window. Similarly, if a muon pattern condition over the "Noise" window is fulfilled, a noise charge, that accounts for the optical fiber/scintillator noise, is obtained by integrating the ADC trace over a 200-ns window located far from the "Signal+Noise" window. The signal charge is then obtained by subtracting the noise charge from the signal+noise charge. An in-depth exploration of the UMD former calibration of the ADC mode can be found in Section 5.2.1.

Since these files are dependent on the T1 trigger of the WCD, the T1 trigger rate is examined in Section 3.1. The number of events recorded, corresponding to instances when the muon pattern condition is satisfied, is presented in Section 3.2.

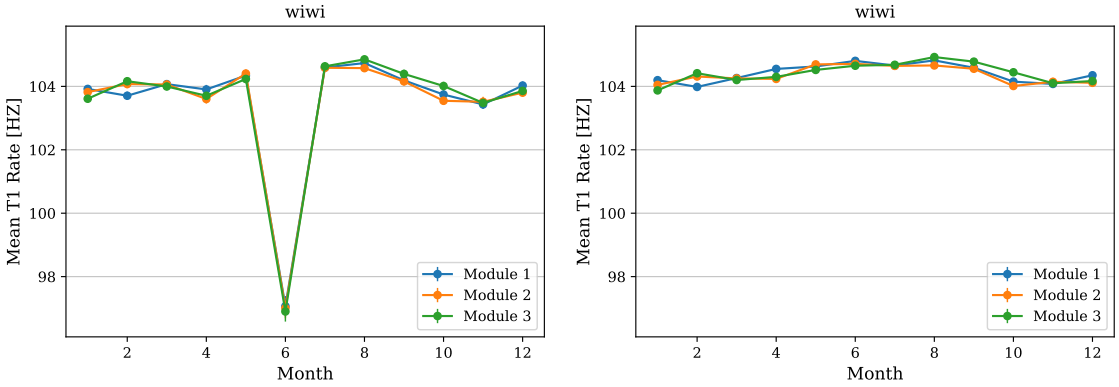

(a) Raw data

(b) Clean data

Figure 3.1: Rate of the T1 trigger for station Wiwi. In the clean data, periods with lack of communication were excluded.

The average charge and baseline values measured in the ADC mode are discussed in Section 3.3. Section 3.4 details the tools used for monitoring module operations, which have been integrated into the UMD shift procedure. Finally, the number of ones detected in the binary mode is analysed in Section 3.5.

The files analysed in the subsequent sections (excluding Section 3.5) correspond to 77 modules and a 1-year period during 2021. In Section 3.5, the analysed files are from a ten-day period in September 2023. During the data selection process, we excluded entries with negative charge estimations, as these often indicated inaccuracies in the charge calculation, potentially arising from errors in baseline estimation, integration window settings, and other related factors. Furthermore, certain stations were omitted from the analysis due to specific issues, which included the introduction of new electronics (refer to Section 3.4).

3.1. T1 TRIGGER RATE FROM THE ASSOCIATED WCD

As the UMD trigger is not autonomous and the ADCT1 data depends on the first-level trigger T1 from the associated WCD, we conducted a year-long study to assess the stability of the T1 trigger. This hardware parameter undergoes continuous monitoring, given that each T1 event is transmitted to the UMD electronics, and its data is stored in plain text files, which are distinct from the ADCT1 files.

Fig. 3.1 illustrates the T1 trigger rate for station Wiwi. In Fig. 3.1a, a decrease in the average T1 rate in June can be observed, coinciding with the recording of numerous "Zeros" in the monitoring files. These "Zeros" indicate a lack of communication between the WCD and UMD. As a result, periods with communication issues were excluded from the analysis, as depicted in Fig. 3.1b.

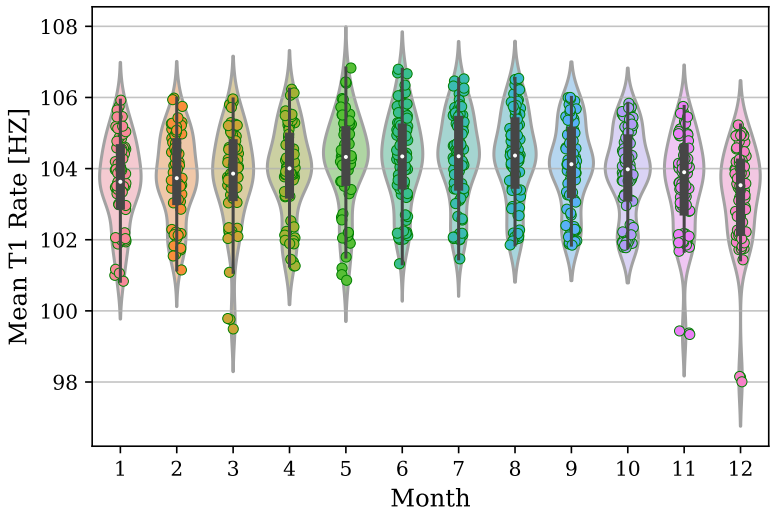

Figure 3.2: The means of the T1 trigger rate for each module are displayed using various colours to represent different months. The distribution of each monthly data is illustrated with a violin plot, where each coloured dot represents one module. The white dot in the centre of the box represents the median of the distribution. The lower and upper edges of the box exhibit the first quartile Q_1 and third quartile Q_3, so the length of the box symbolizes the interquartile range IQR = $Q_3 - Q_1$. The length of the black line that extends out of the box represents the lower/upper adjacent values defined as $Q_1 - 1.5\,\text{IQR}$ and $Q_3 + 1.5\,\text{IQR}$, respectively.

After data cleaning, the T1 trigger rate was calculated for each module over the whole array in Fig. 3.2. The installation of the new UUB electronics in December resulted in a reduced trigger rate in Constanza module 2 and Toribio module 2 and module 3. For this reason, these particular data points were excluded from the analysis.

A seasonal modulation of approximately 1% in the T1 trigger rate can be appreciated in Fig. 3.2, showing that the trigger rate remains notably stable and sufficiently high, approximately at 104 triggers per second. This high rate ensures a substantial amount of data for the ADCT1 files.

3.2. Number of events

The number of times muon pattern condition is fulfilled in the two different windows ("Signal+Noise" and "Noise") were calculated for each individual module across the entire array. The number of "Signal+Noise" events is illustrated in the left panels of Fig. 3.3, while the number of "Noise" events is presented in the right panels. The top plots correspond to modules with an area of $10\,\text{m}^2$, whereas the bottom plots represent modules with an area of $5\,\text{m}^2$. As expected, the modules with a smaller detection area ($5\,\text{m}^2$) exhibit fewer events in both windows. For every "Noise" event, there are approximately ten times as many "Signal+Noise"

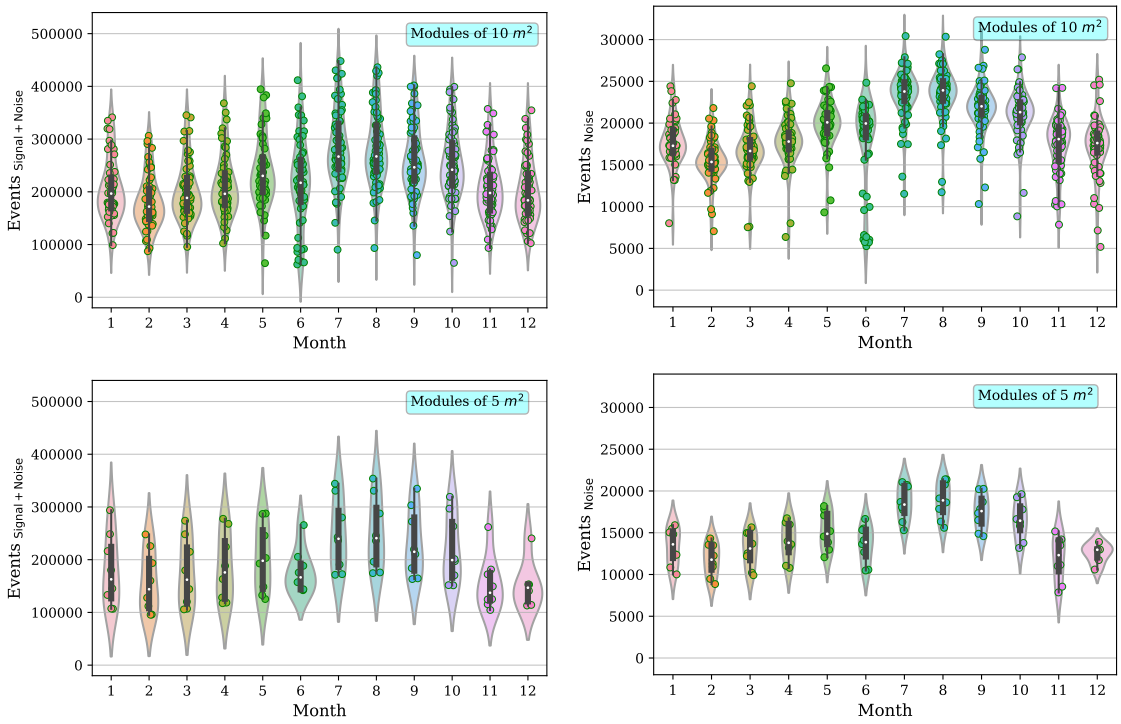

(a) "Signal+Noise" window

(b) "Noise" window

Figure 3.3: Number of events per module for the modules of 10 m^2 (top) and 5 m^2 (bottom).

events. Monitoring this event rate for each module serves as a verification of the module's operational status (see Section 3.4).

Fig. 3.4 illustrates the annual variation in the number of events for all the 10 m^2 modules (dotted lines) and all the 5 m^2 modules (dashed lines). Each curve was calculated by averaging the curves obtained for individual modules, so that each module was normalised by its annual mean. There is a seasonal modulation in the number of events in both windows, characterised by a winter increase of approximately 20 to 30%. It is important to mention that June stands out as an exception due to certain periods of communication disruption, as discussed in Section 3.1.

In Ref. [63], both SiPM gain and temperature were measured over an eight-month period with a temperature range of ~10 to ~30°C (since the UMD are buried 2.3 m deep the overall temperature variation is only ~20°C). The corresponding gain variation was approximately ~0.2%/°C. Further studies are required in order to rule out any potential impacts arising from temperature variations in the observed seasonal modulation.

The literature has documented the variation in muon flux as a function of temperature (of up to ~8%) in Ref. [70, 71]. Change of the muon flux can occur because of the change of pion and kaon decay probability (meson effect) or be-

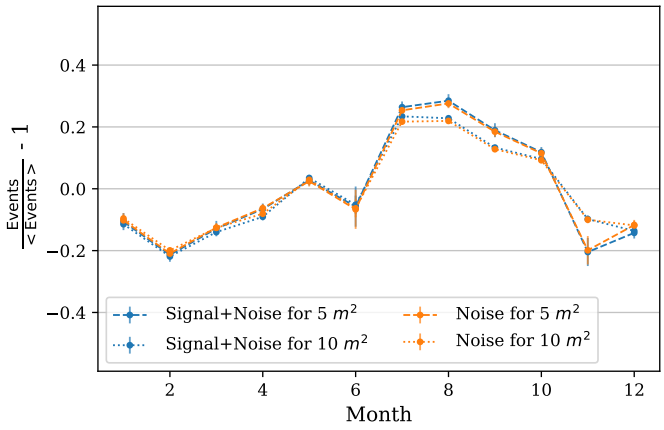

Figure 3.4: Annual variation in the number of events. To compute the calculation, each module was normalized by its annual mean.

cause of the change of muon decay probability (muon effect). If the temperature increases, the atmosphere expands, density of air decreases and the probability of the interaction of mesons (kaons and pions) at unit of geometric path becomes smaller, hence decay probability becomes higher. If the temperature increases and the atmosphere expands, the geometric path from generation level to registration point becomes longer, so higher number of muons will decay. The relation between absolute values of these effects depends on E_{min} (threshold energy of the muon detector). In case of low threshold energies, the absolute value of the muon effect is greater than the value of meson effect, and the sign of the total effect is negative. Hence, for low threshold energies the muon flux is less during summer. In case of high threshold energies, the muon effect degrades (muons have not enough time to decay in the atmosphere) and the sign of the total effect becomes positive (increasing the muon flux during summer). To introduce corrections for temperature and pressure effects, it is necessary to know differential temperature coefficient and barometric coefficient [71].

3.3. Mean charge and baseline in the ADC mode

An example of the charge estimation procedure of the ADC mode, using events recorded in the ADCT1 files, is presented in Fig. 3.5 for module 1 of station Luisa in July. We obtained the charge histogram from "Signal+Noise" events (red) and the charge histogram from "Noise" events (blue), where the first contains approximately ten times more events than the latter. From the signal events, we calculated the mean muon charge, resulting in $\langle q \rangle = 399.6 \pm 1.3$ in a.u.. For noise events, the mean muon charge was determined as $\langle q \rangle = 145.8 \pm 0.9$ in a.u.. By subtracting the histograms of both sets, we effectively eliminated the noise component, resulting in a mean muon charge of $\langle q \rangle = 434.9 \pm 1.4$ in a.u..

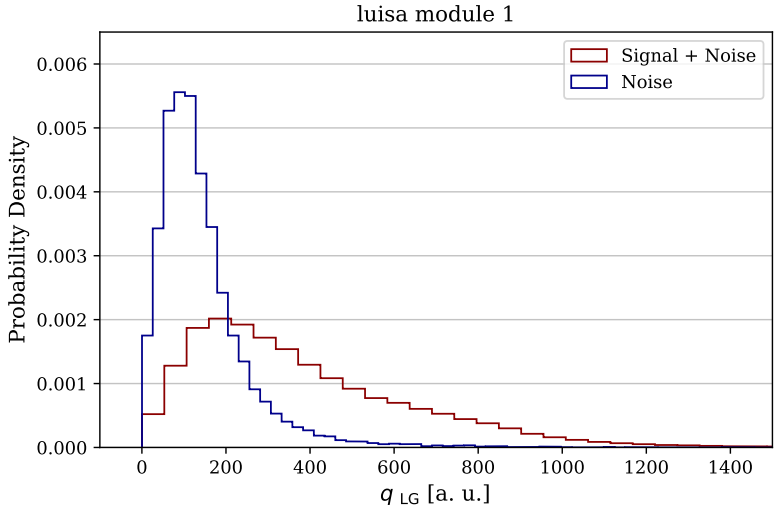

Figure 3.5: Charge histograms for the LG channel of Luisa module 1 in July.

In Fig. 3.6, we present the annual progression of the mean charge obtained from ADCT1 files for module 3 of station Kathy Turner (on the left panels) and module 1 of station Toune (on the right panels) for both the LG channel (in red) and the HG channel (in green). The charge estimation method from ADCT1 files is thus stable, even under temperature variations. Additionally, an ageing-related effect of approximately 1% is observed.

The monthly mean charge was calculated for each module and plotted in Fig. 3.7 for the LG (left panels) and the HG (right panels) channels, where the modules of 10 (5) m^2 are on the top (bottom) of each figure. The mean of the monthly means was computed for both channels. For the LG channel, the charges obtained were $\langle q \rangle = 384.7 \pm 2.7$ in a.u. for the modules of 10 m^2 and $\langle q \rangle = 388.3 \pm 3.8$ in a.u. for the modules of 5 m^2,[1] whereas for the HG channel these values were $\langle q \rangle = 1515.2 \pm 9.7$ in a.u. and $\langle q \rangle = 1530.2 \pm 14.2$ in a.u., respectively. From Fig. 3.7, it can be concluded that the charge remains stable throughout the year for modules of 10 m^2. However, for 5 m^2 modules, a slight variation of approximately 3% is observed for both channels over the course of the year.

The baseline is determined by calculating the average signal at the beginning of the trace, specifically between 62.5 ns and 1312.5 ns. The baseline of each channel was analysed to study its stability. The monthly mean baseline values were computed for each module and are represented in Fig. 3.8 for the "Signal+Noise" window (blue) and for the "Noise" window (orange). The yearly mean baseline values obtained for the LG and HG channels were (8223.9±0.2) ADC and (8223.9± 0.1) ADC, respectively.

[1]These values are consistent with those reported in Ref. [72] for 21 modules in April 2020.

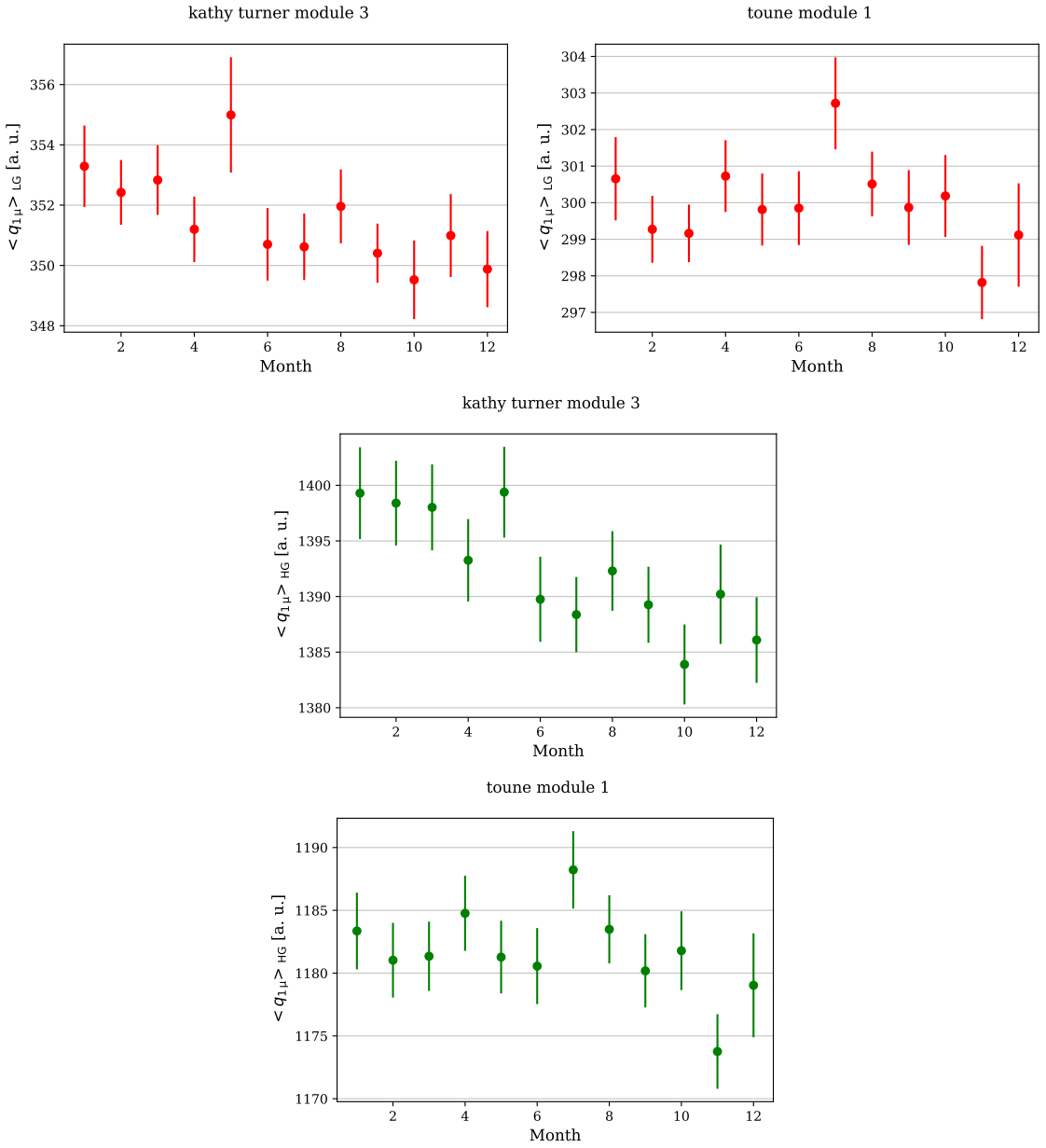

Figure 3.6: Mean charge from ADCT1 files for the LG (red) and the HG (green) channels of Kathy Turner module 3 (left) and Toune module 1 (right).

3.4. Incorporating tools to the UMD shifts

The algorithm for extracting data serves as a valuable tool for monitoring module operations and swiftly detecting any issues in detector performance. By analysing the files, data loss can easily be identified, which can be attributed to various factors such as a module or station being offline, communication glitches, or software issues. This capability allows for rapid response and maintenance to ensure the continued integrity of the detector system.

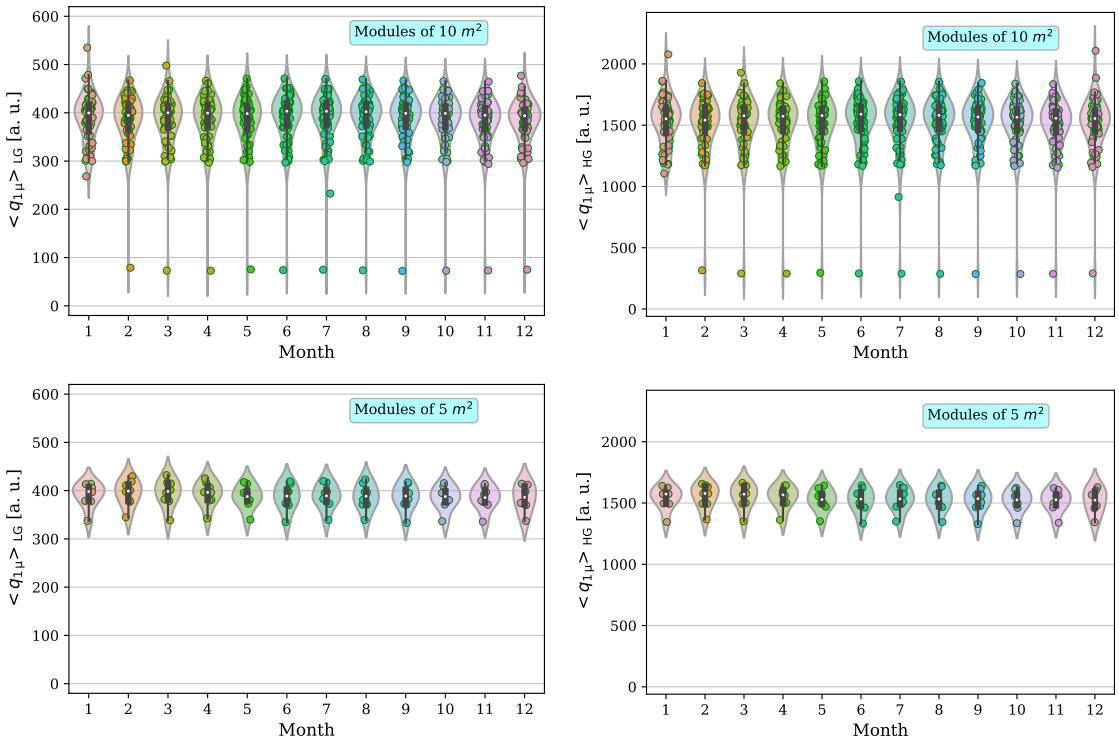

(a) LG channel **(b)** HG channel

Figure 3.7: Mean charge from ADCT1 files of both ADC channels for modules of 10 m^2 (top) and 5 m^2 (bottom).

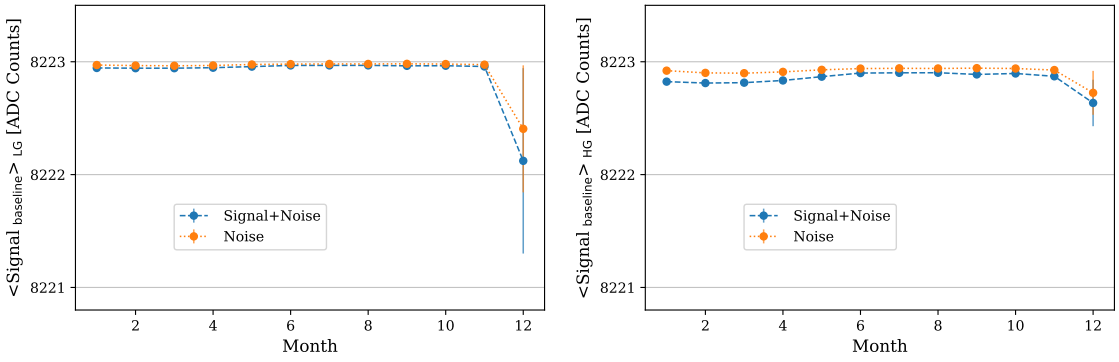

(a) LG channel **(b)** HG channel

Figure 3.8: Average signal of the baseline for the LG and HG channels of the ADC.

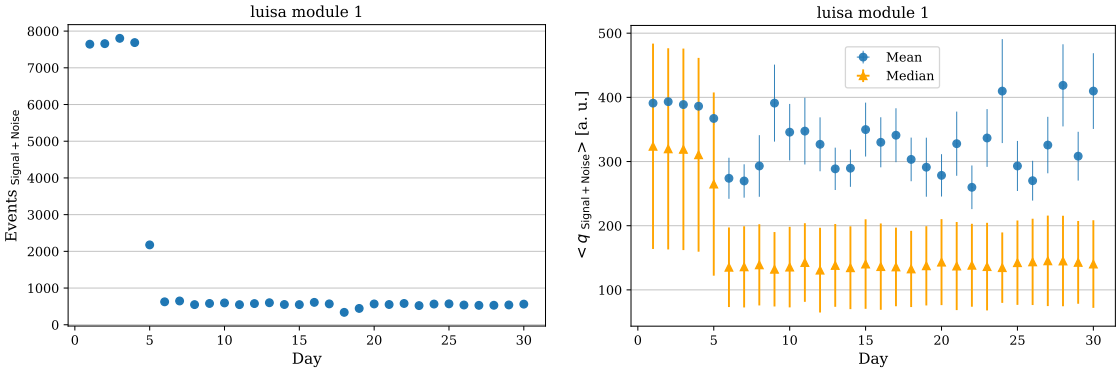

Figure 3.9: Number of events (left) and charge (right) in the "Signal+Noise" window for the LG channel of Luisa module 1 in November.

An illustrative example is presented in Fig. 3.9 for module 1 of station Luisa. In this figure, we examine the number of events (left) and the charge (right) obtained within the "Signal+Noise" window on a daily basis throughout the month of November. Notably, the installation of the new UUB electronics on 05 November is associated with a decrease in both of these parameters.

The charge histograms obtained for module 1 of station Luisa in December are displayed in Fig. 3.10. In this graph, in contrast to Fig. 3.5, both histograms overlap. It is notable that the number of events in the "Signal+Noise" window (15635) is comparable to the number of events in the "Noise" window (15390), even though, as mentioned in Section 3.2, the rate should ideally be around 10. The installation of UUB in Luisa resulted in a shift of around 20 bins in the bin where the accumulation of "1" is maximised for events triggered by a T1-Thr1 condition (aka, the effective "latch" bin). When the "latch" bin is not properly set, the algorithm fails to detect muons in the binary trace, as it attempts to locate them within a time window uncorrelated with the T1 trigger. Consequently, the number of events in both windows becomes similar, resulting in histograms dominated by noise. This shift in the "latch" bin also occurred in other stations that underwent UUB installations in December (Toune, Constanza, and Toribio). This shift in the "latch" bin led to the failure of the ADC charge estimation procedure.

A novel code developed based on the findings of this work was integrated into the UMD shift procedures, significantly enhancing the speed and efficiency for identification of potential issues. Every two weeks, heatmaps similar to those in Figs. 3.11 and 3.12 are generated during the UMD shifts. For each module, two different variables from the files are examined: the number of events per module area and the median charge deposit, both within the "Signal+Noise" window of the LG channel. During these shifts, the shifter is responsible for reporting the following conditions:

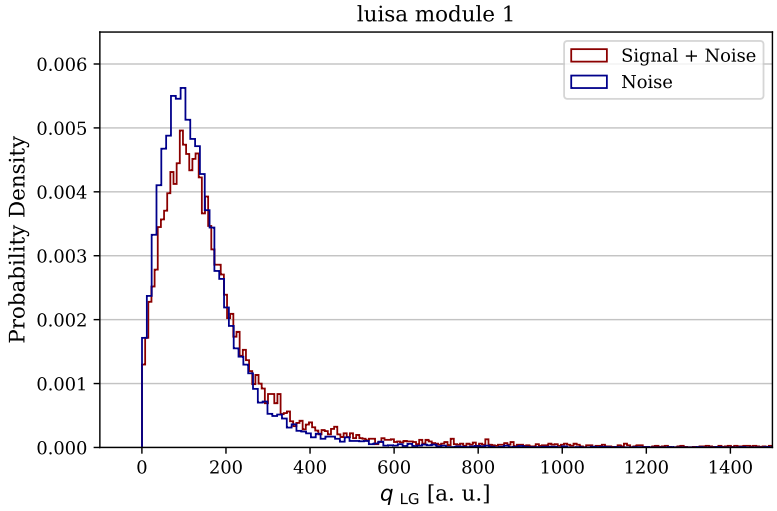

Figure 3.10: Charge histograms for the LG Channel of Luisa module 1 in December.

1. Grey days: days with no data available
2. Number of events per module area less than 200
3. Decreases in the number of events per module area of more than 50% compared to the previous day
4. Decreases in the median charge of more than 50% compared to the previous day
5. Black stations: stations that did not produce any file during the shift

For instance, in Figs. 3.11 and 3.12, Constanza would be reported for having fewer than 200 events per module area and for experiencing changes of more than 50%, both in terms of the median charge and the number of events per module area.

3.5. Number of ones in the binary mode

The information about the number of "1"s in the binary traces produced for each event was incorporated into the daily ADCT1 files in September 2023. The following studies were conducted during ten days of September.

In Fig. 3.13, the charge obtained by the ADC mode with the LG channel is compared to the number of "1"s obtained by the binary mode. It is observed that the charge increases at a faster rate than the number of "1"s, the latter eventually reaching a plateau with an average of ~9. When the energy deposit in the scintillator increases the photons reaching the SiPM tend to mostly pile up.

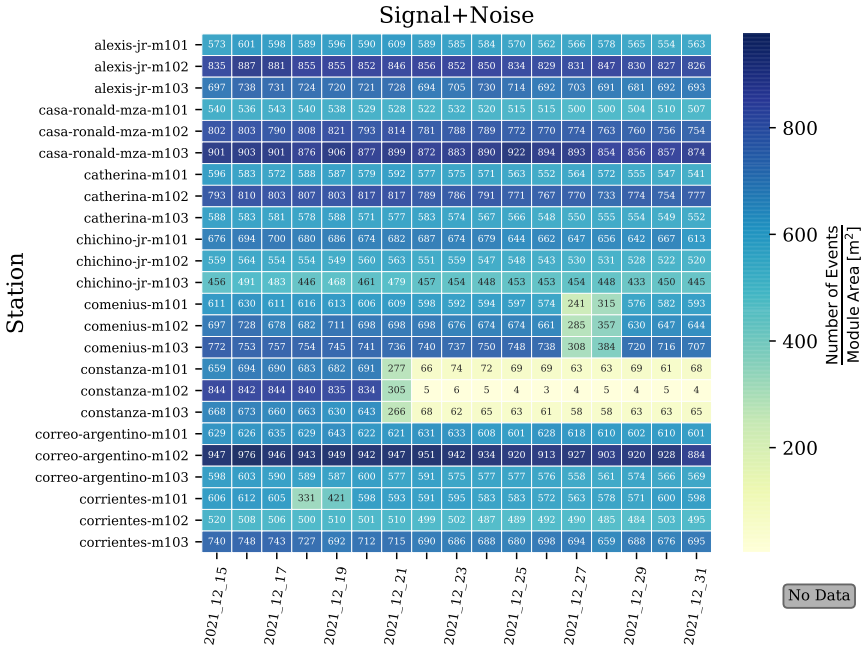

Figure 3.11: Heatmap of the number of events per module area in December.

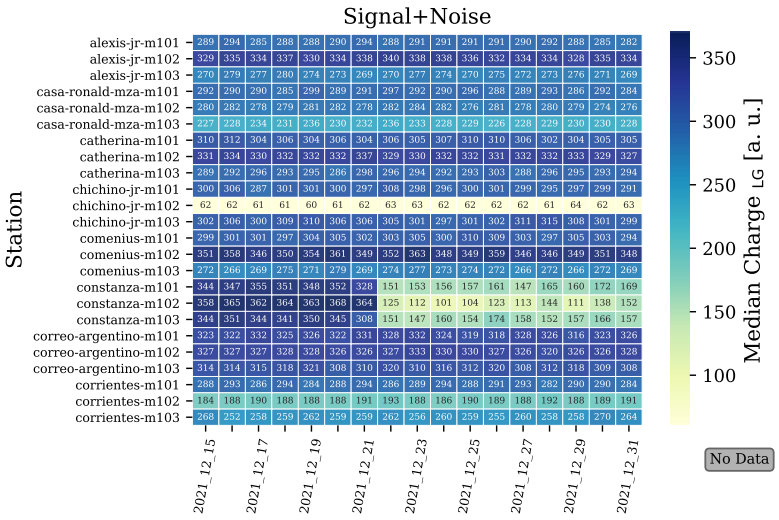

Figure 3.12: Heatmap of the median charge of the LG Channel in December.

The ADC is more sensitive to this effect than the binary since the pile up increases the area of the signal (charge) more than its time over threshold (number of "1"s).

In Fig. 3.14, we illustrate the probability distribution of number of "1"s obtained by the binary mode in the "Signal+Noise" window (orange histogram) and in the "Noise" window (blue histogram). The resulting histogram from subtracting both is displayed in black. The maximum number of "1"s produced are 11, as expected from the selection criteria requested. The probability obtained

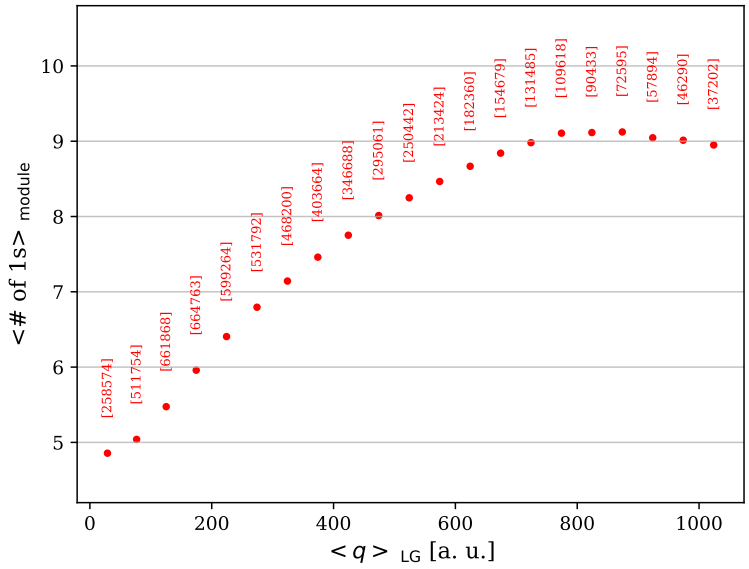

Figure 3.13: Number of "1"s per module obtained in the binary traces as a function of the charge in the LG channel.

with noise events decreases with the number of "1"s, in agreement with measurements performed in the laboratory using a muon telescope to select vertical muons [60]. The histogram obtained from signal events exhibits a broader distribution with a peak at six. A higher noise rate in the field can account for making the distribution wider towards a lower-than-average number of ones. The wider distribution towards values with higher-than-average number of ones will be further analysed in Section 5.2.2.

3.6. Summary

We analysed the ADCT1 files of the ADC channel in the field during a 1-year period in 2021. We observed a seasonal modulation in the number of recorded events, with approximately a 30% increase in events during the winter months. The modulation occurred in spite of the T1 trigger rate from the associated WCD remaining stable. We have also obtained the recorded charges in ADCT1 events. For the LG channel, the mean charges obtained were $\langle q \rangle = 384.7 \pm 2.7$ in a.u. for the modules of $10\,\mathrm{m}^2$ and $\langle q \rangle = 388.3 \pm 3.8$ in a.u. for the modules of $5\,\mathrm{m}^2$. For the HG channel the values were $\langle q \rangle = 1515.2 \pm 9.7$ in a.u. and $\langle q \rangle = 1530.2 \pm 14.2$ in a.u., respectively. The values reported are consistent with those reported in Ref. [72] for 21 modules in April 2020. Additionally, the mean charges of both LG and HG channels remained consistent throughout the year, with only a marginal variation of around 3% observed for the $5\,\mathrm{m}^2$ modules.

Furthermore, from the analysis of the ADCT1 files we developed a set of

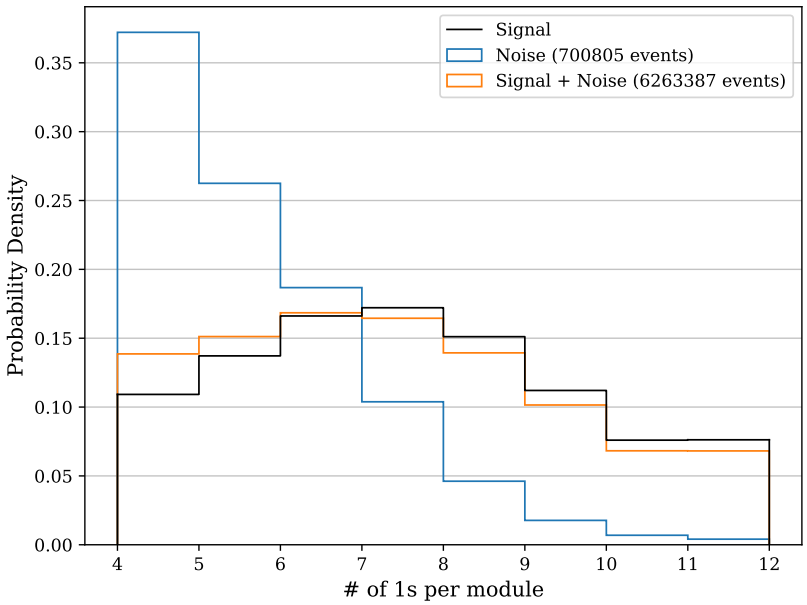

Figure 3.14: Number of "1"s in the binary traces obtained for the "Signal+Noise" window (orange), for the "Noise" window (blue) and for the resulting histogram from subtracting both (black)

new monitoring tools that have been integrated into the UMD shifts to inspect the detector performance and to examine the quality of the data acquired on a daily basis. Two observables were found to be sensitive to changes in the overall behaviour of the modules: the number of events and the median from the charge estimation.

Finally, we incorporated in the files the information about the number of "1"s produced in the binary traces in September 2023. The ADCT1 files will prove to be a valuable resource in the future for conducting long performance or efficiency studies.

Chapter IV

Improved reconstruction of the ADC signal in the UMD

A comprehensive analysis of three years of data (2020, 2021, 2022) was conducted to enhance the data reconstruction of the ADC mode. In this work, two modules were developed and implemented in Offline [73]: the `MdADCGlitchCleaner` and the `MdADCChargeCalculator`. The first is described in Section 4.1 and the latter in Section 4.2. Glitches, defined as single-bin jumps in the ADC traces produced by a wrongly optimised FPGA firmware, are present in the data of the low-gain channel until October of 2023 when a modified version of the electronics firmware solved the problem. The `MdADCGlitchCleaner` module successfully identifies and removes an average of 5000 glitches per UMD module during the three year analysed. With the `MdADCChargeCalculator` module we introduce a new algorithm to estimate the signal charge and we compare it to the previous algorithm implemented in the `MdMuonIntegrator` module. In Section 4.3, the comparison of the data reconstruction between the previous module `MdMuonIntegrator` and the `MdADCChargeCalculator` module is presented.

4.1. MdADCGlitchCleaner module

A glitch is defined as a noisy jump of a single time bin in the ADC trace which does not correspond to any real signal. Glitches are present in the ADC traces of the LG channel due to software issues arising from the FPGA programming. These glitches do not affect the UMD binary signals. UMD engineers worked to update the firmware and managed to solve the glitches in October of 2023. However, several years of data have been stored with glitches and this motivated to develop algorithms to cope with this issue.

To this aim, the module `MdADCGlitchCleaner` was developed and imple-

mented in Offline. The underlying idea is to find an algorithm that identifies and removes sudden jumps without losing real signal pulses. The strategy employed consists of calculating, for each time bin of the trace, the mean m and standard deviation σ of the amplitude signal considering the first A time bin neighbours. If the amplitude of a given time bin exceeds the mean amplitude of its neighbours (m) by n times the standard deviation (σ), it is identified as a glitch and the amplitude of that particular time bin is substituted with the mean amplitude of the first two neighbouring time bins. For this analysis, the values of A and n were optimised to $A = 6$ and $n = 30$. After removing glitches from the trace, a new 'deglitched' trace is generated, and stored for subsequent analysis.

In Fig. 4.1, an example of a trace with glitches is illustrated. In the top panel, the raw trace is displayed, where a jump in the amplitude of the trace is clearly observed at time bin 512. In the bottom panel, the 'deglitched' trace (obtained with the algorithm of first neighbours explained above) is illustrated. Not being able to properly remove the glitch could have led to a significantly inaccurate estimation of the charge, given that the amplitude of the glitch is evidently larger than the peak of the distribution.

In Fig. 4.2, we built a histogram indicating the time bins where glitches were identified during the three years data analysis. As observed from the histogram, glitches can be found in any time bin of the ADC trace. However, the two positions most likely to have glitches are located at 0 and 512 in the ADC trace. It is important to highlight that the proposed algorithm successfully removed glitches between the time bins 600 and 800, where the majority of muon signals arrive. The amplitude of the glitches can be as substantial as 16000 ADC Counts, potentially resulting in a notably inaccurate charge estimation if the raw trace is utilised. Additionally, failing to effectively eliminate glitches between the time bin 1 and 210 could result in inaccurate baseline estimations.

Glitches were detected in most of the UMD modules deployed in the field, with an average of approximately 5000 glitches per UMD module during the three year data analysis. Approximately ~8% of the traces analysed contained glitches. In these glitchy traces, there were found on average 2 glitches per trace.

Although the `MdADCGlitchCleaner` module successfully identifies and removes glitches, given that the strategy depends on the neighbouring time bins, the algorithm might fail to identify a glitch if there are several glitches in consecutive time bins or if the jump of the glitch in amplitude is very low compare to its neighbours. Compensating this latter effect is not possible with this strategy since setting a very low value of n may lead to the identification of false glitches near the maximum amplitude of the signal. In Fig. 4.3, an example of a trace with survival glitches is illustrated. Although the algorithm identified 4 glitches in the trace, 2 survival glitches are present in 2 consecutive bins around the time bin 230.

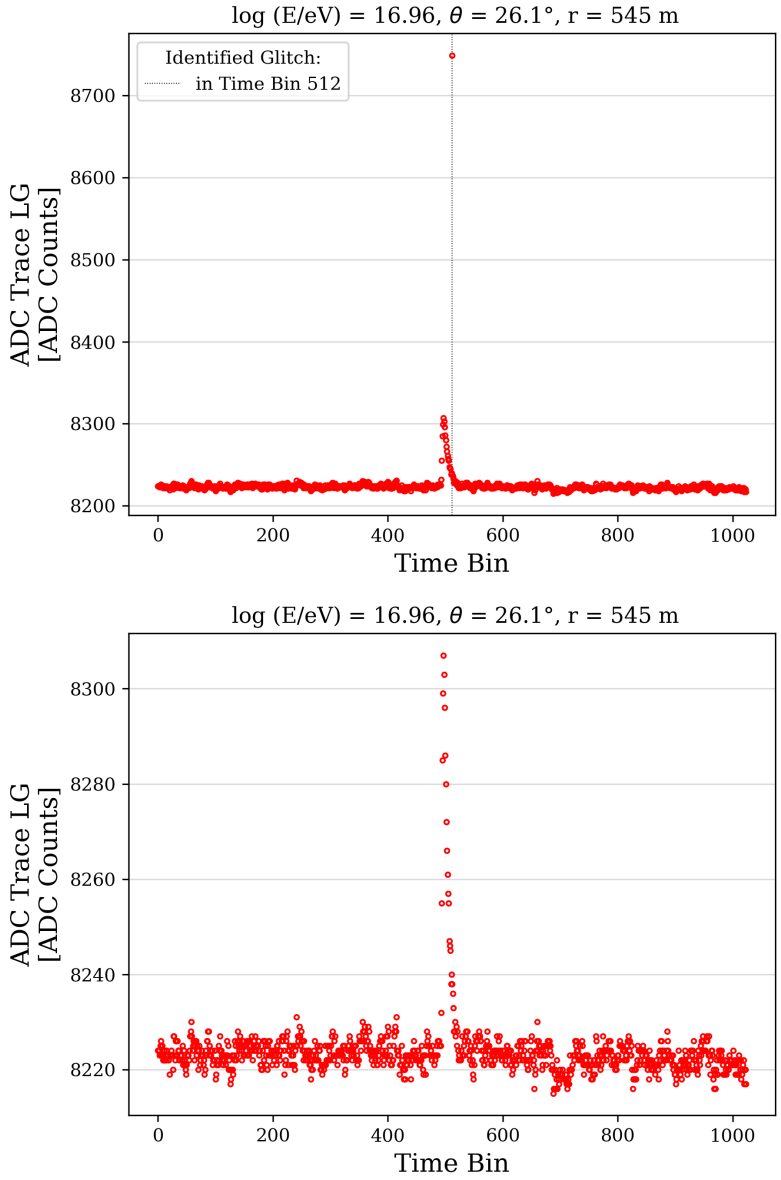

Figure 4.1: Example of a raw trace with glitches (top panel), and the same trace after glitch removal (bottom panel), resulting in a new 'deglitched' trace used for computing the charge estimate.

The algorithm fails to identify glitches in approximately 10% of cases. As it will be explained below, the `MdADCChargeCalculator` module implements a strategy to mitigate the contribution of these survival glitches to the reconstructed charge. Despite these strategies, some glitches still persist and could potentially affect the charge estimation. However, these glitches represent less than 0.4% of the total events, and their contribution is minimal due to their very low amplitude.

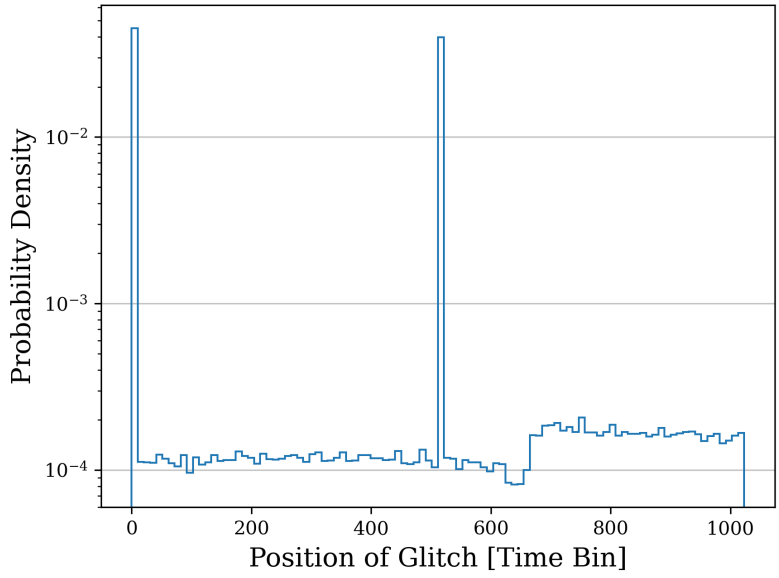

Figure 4.2: Histogram illustrating the glitches identified in the three year data analysis. The time bins 0 and 512 in the ADC trace clearly have a higher incidence of glitches.

4.2. MdADCChargeCalculator module

The previous implementation in Offline to estimate the charge of an ADC trace was optimised with simulations. Nevertheless, in simulations the baseline of the ADC trace remains very stable, and the noise is quite simplified. On top of that, data traces exhibit undershoot, a characteristic not replicated in the simulated traces. To address both issues, a new algorithm was developed. The strategy to compute the charge implemented previously was integrating between the first leading muon and the last muon identified by the binary mode irrespective of the waveform of the trace. Reconstructing data with this strategy results in summing over the undershoot of the trace, which can lead to artificial negative values. To mitigate this, a strategy with several integration windows was developed in the `MdADCChargeCalculator` module.

4.2.1. Multiple window strategy

To compute the charge of a signal, the first step is to correctly estimate the baseline. For the ADC trace, the baseline is determined by calculating the average signal at the beginning of the trace, specifically between the time bins 1 and 210. The time intervals for computing the baseline estimation are selected in a region where no signals from particles of the extensive air shower are expected. However, in ~2.5% of the total traces analysed a pattern compatible with a muon pattern in the binary traces was detected before time bin 210. In those cases, the baseline is

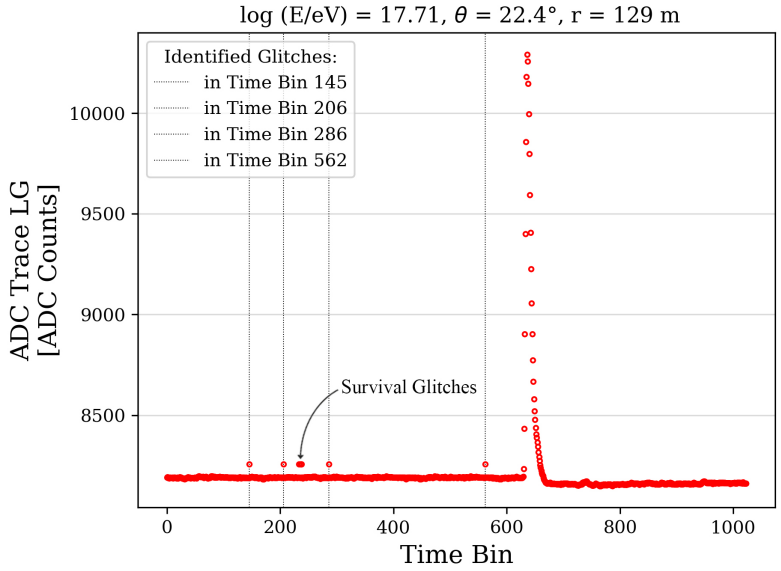

Figure 4.3: Example of a trace with 4 identified glitches and 2 survival glitches.

determined by averaging the signal up to the point where the muon pattern was identified.

After the estimation of the baseline, the following step is to find the appropriate number of windows and their widths. To this aim, the binary reconstruction is used as this acquisition mode provides the arrival time of individual muons. To illustrate the rationale behind the proposed algorithm, two simplified examples are shown in Fig. 4.4 for the case of two muons arriving to the UMD. In the first example of Fig. 4.4a, both muons arrive very close in time producing a single pulse in the ADC trace. Once the leading muon is identified in the binary mode, the integration window is defined around this time bin and spans where the trace is over two standard deviations above the baseline (see Fig. 4.4). In the case of Fig. 4.4a, this procedure leads to only one integration window. However, in the second example of Fig. 4.4b, the muons arrive quite spare in time, producing two distinct pulses in the ADC. After computing the first integration window with the leading muon identified in the binary, the algorithm checks if another muon pattern is present in the binary trace after the end of the first integration window. If so, the process defines a second window and determines its width with the same logic described above. The procedure is iterated until no muon patterns are found in the binary mode.

In data, the algorithm is much more complicated that this simplified example. Firstly, as the binary and ADC electronics are built in different architectures, there are signal delays between ADC and binary modes and the muon signal starts later in the ADC mode (see for example Fig. 4.5). Secondly, and most importantly, two conditions are requested to define the integration window: the

maximum amplitude of the trace within the integration window has to be higher than t times the standard deviation from the baseline and the integration window has to have a minimum width w of time bins. The two conditions minimise the effect of integrating pulses from thermal noise, while the second condition also helps with the survival glitches. Noise of 1 or 2 single-photoequivalent pulses in the SiPM might produce signals in the ADC mode of amplitudes higher than 2 standard deviations from the baseline for several consecutive bins. The minimum width w of time bins required is related to the minimum width that a muon might produce (obtained from simulated traces). The maximum amplitude of the trace t is a compromise: selecting a very high value may complicate the identification of the integration window for low muon densities, as they deposit less energy, but conversely utilising a very low value may lead to the integration of noise signals. In our analysis, we utilised $w = 5$ and $t = 5$.

In Fig. 4.5, two examples are presented. The ADC traces of the LG and HG channels are shown in red and green, respectively. The baseline estimate is represented as a dark horizontal line, while the integration windows are illustrated as blue vertical lines. The number of integration windows employed to estimate the charge are 3 and 4, respectively. In the bottom panel of each figure, the binary mode is presented. The binary trace of each scintillator Id is plotted as black dots. The first and last muon pattern identified in the binary traces of all 64 scintillators, dubbed as leading muon and last muon, are indicated as vertical lines, with the colours violet and light blue. The time delay binary-ADC (due to the electronics) is clearly observed between the identification of the leading muon in the binary trace (violet line) and the first integration window in the ADC trace (blue line). The length of the binary trace in the bottom panel spans 2048 time bins, while the length of the ADC trace in the two top panels is confined to 1024 time bins.

4.2.2. Rejection of anomalous data

During the data analysis, we encountered events with flat traces in the LG channel and a positive number of reconstructed muons in the binary, as can be seen in Fig. 4.6. In this example, the muon reconstruction with the binary mode is $N_{\mu}^{\text{Bin}} \approx 272$. In the third panel, muon patterns are observed in the binary traces, while in the second panel, the HG channel is saturated. The trace of the LG channel in the first panel is evidently inconsistent with the measurements and should be classified as anomalous data. Events like these are likely related to a malfunction of the UMD module and should be excluded from any physics analysis. In the `MdADCChargeCalculator` module, we implemented a function to classify a UMD module measurement as anomalous data if the charge in the LG channel is null and the number of reconstructed muons in the binary mode is higher than 5. The UMD module is consequently classified as rejected and is not

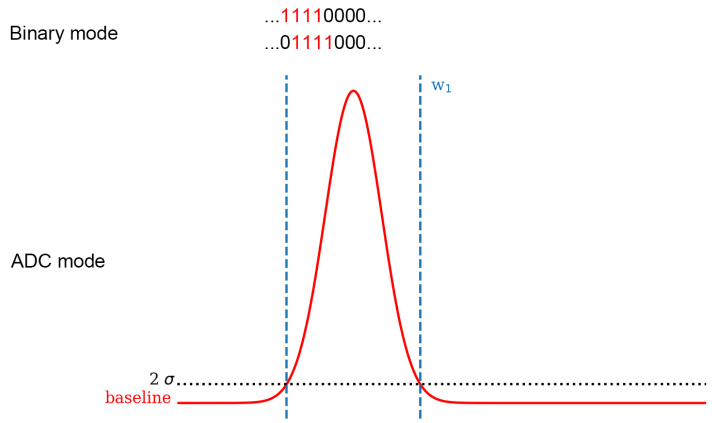

(a) Two muons arriving close in time.

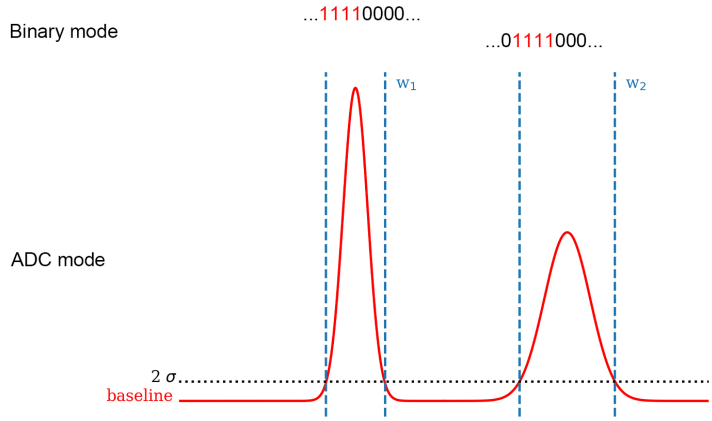

(b) Two muons arriving separate in time.

Figure 4.4: Schematics of the UMD modes when two muons arrive to the detector in two different scintillator strips. In the top panel, both muons arrive very close in time in the binary mode, resulting in only one integration window in the ADC mode. In the bottom panel, the muons arrive quite spare in time, generating two different integration windows.

included in the reconstruction of the muon lateral distribution function (MLDF). These events are very infrequent, representing less than 0.1% of the total traces in the three year data analysis.

4.3. Comparison with the previous reconstruction algorithm

The reconstruction of the ADC mode in the modules `MdMuonIntegrator` and `MdADCChargeCalculator` varies significantly in data. In Fig. 4.7, an example of an event reconstructed with both ADC algorithms is presented. In the top panel, the estimation of the charge was computed with the previous algorithm coded in `MdMuonIntegrator`, whereas in the bottom panel the new `MdADCChargeCalculator` was utilised. The baseline is illustrated as a dark horizontal line, while the in-

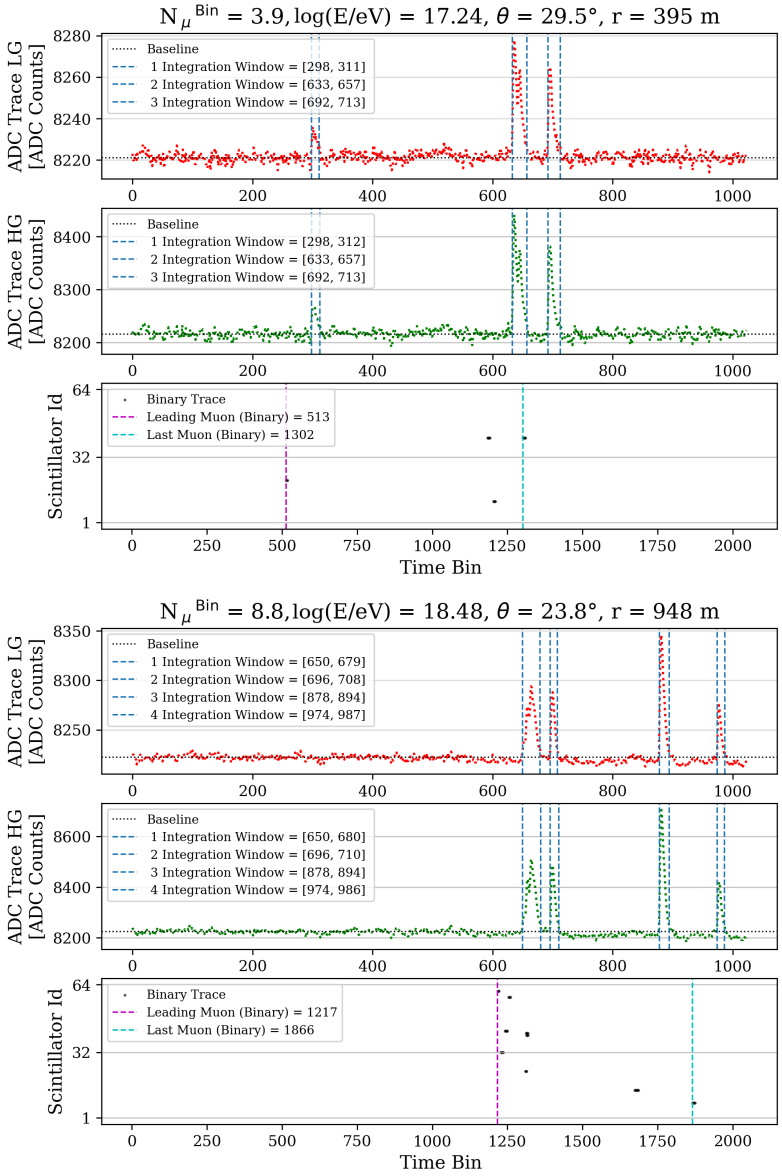

Figure 4.5: Traces exemplifying muon reconstructions in the binary mode with $N_{\mu}^{\text{Bin}} \approx 4$ and 9. For each example, the ADC mode is displayed in the top two panels, while the binary mode is shown in the bottom panel.

tegration windows are represented with blue vertical lines. It is worth noting that the strategy implemented in `MdMuonIntegrator` defines a single window of ~1906 ns, which clearly includes the pronounced undershoot. The strategy proposed in this work, on the other hand, defines two smaller windows of ~175 ns and ~50 ns respectively. An inset figure in the top panel illustrates the undershoot after the first peak. The charge estimations were $q = 37647$ in a.u. and $q = 63025$ in a.u. respectively, showing the importance of getting rid of the undershoot while integrating.

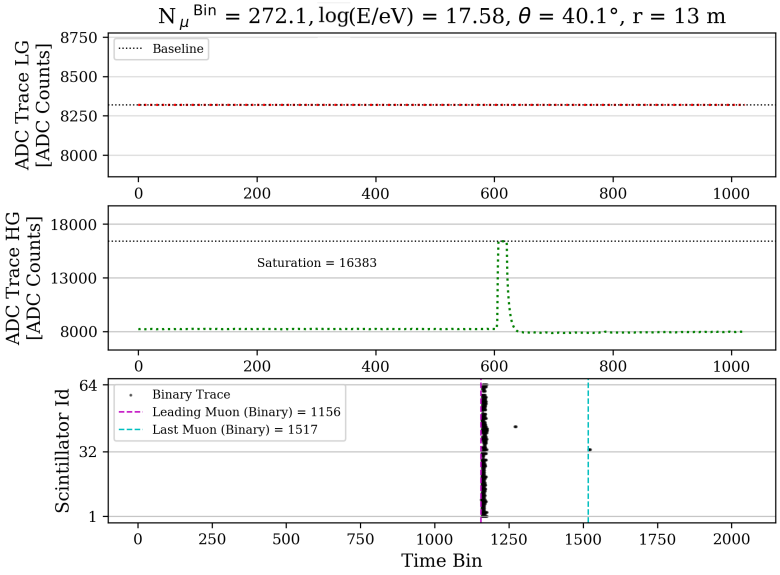

Figure 4.6: (Left) Example of a trace classified as anomalous data during the data analysis. The muon reconstruction with the binary mode is $N_{\mu}^{\text{Bin}} \approx 272$ and the HG channel is saturated. However, the trace of the LG channel remains flat.

In Fig. 4.8, we present the number of reconstructed muons in the binary mode as a function of the vertical equivalent charge q_{vert} measured with the ADC mode. The vertical equivalent charge is obtained from the measured charge and the zenith angle of the shower, following the equation $q_{\text{vert}} = q_{\text{meas}} \cos\theta_{\text{shower}}$. The red circles represent the data reconstruction in Offline with the previous module `MdMuonIntegrator`, whereas the dark stars represent the analysis conducted with the `MdADCChargeCalculator` module presented in this work. Each data point corresponds to the reconstruction performed by an individual UMD module over the three-year data period. UMD modules that encountered saturation in the binary mode or in the ADC mode were excluded from the analysis. More data points are represented in the analysis conducted with the `MdADCChargeCalculator` compared to the previous module `MdMuonIntegrator`, given that the previous algorithm failed to compute the charge estimation of the ADC mode for about 13% of the total cases analysed.

Both reconstructions perform very different. Firstly, the undershoot plays a key role in the new reconstruction. In the previous reconstruction, the charge was integrated between the first leading muon and the last muon identified in the binary, resulting in the summation of undershoot. This led to the reconstruction of negative charge values, reaching as low as $q_{\text{vert}} \approx -250000$ in a.u.. The previous algorithm calculated negative charge values $q_{\text{vert}} < 0$ in 3.5% of all traces analysed, while the new algorithm reduces this proportion to 0.002%. Secondly, in the previous reconstruction, glitches are not eliminated from the traces. This re-

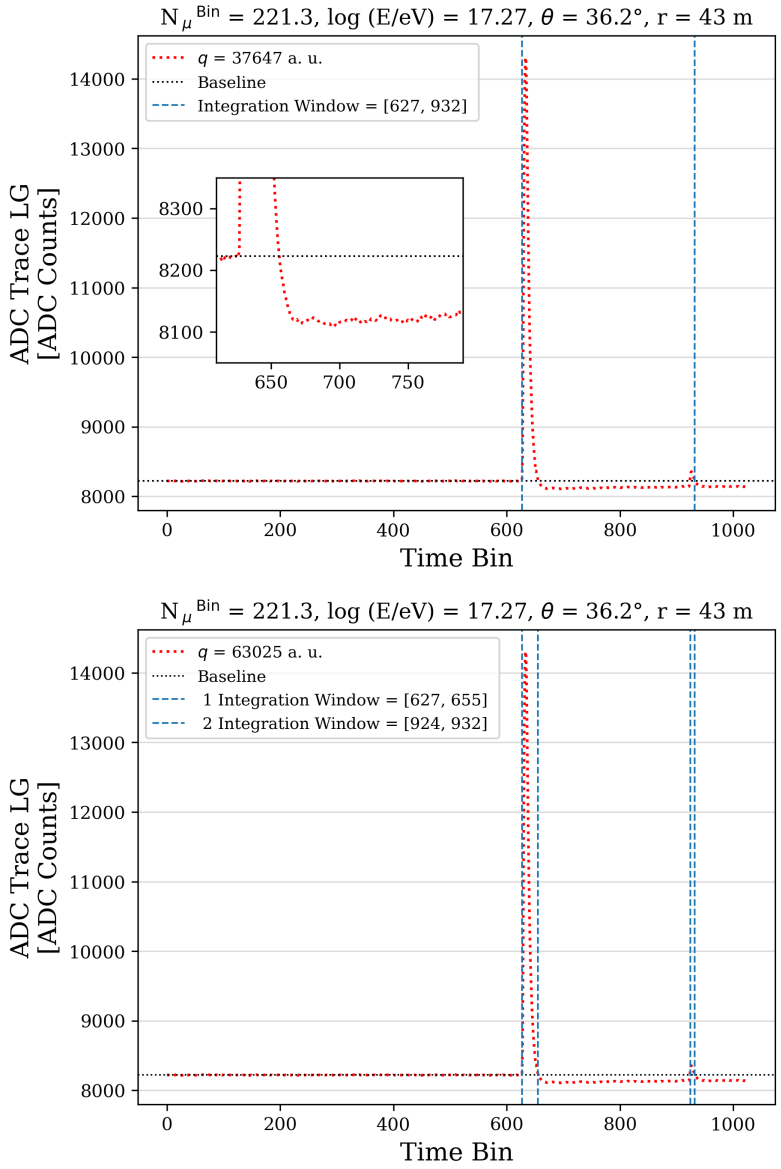

Figure 4.7: Example of a trace where the charge estimation was conducted with the previous module `MdMuonIntegrator` (top panel) and with the `MdADCChargeCalculator` module (bottom panel).

sults in data points with low muon densities in the binary mode but exceptionally high charge values appearing as outliers in the bottom right of Fig. 4.8. Thirdly, in the previous reconstruction, several traces were reconstructed with low values of charge around $q_{\text{vert}} \approx 10^2$ in a.u.. The outliers meeting the conditions $N_{\mu}^{\text{Bin}} > 10$ and $q_{\text{vert}} < 600$ in a.u. were 13 times more with the previous algorithm than with the new algorithm. This arises from inaccurately calculating the charge, either due to difficulty in locating the integration region or from summing the undershoot, given that the undershoot not only produces negative charge values

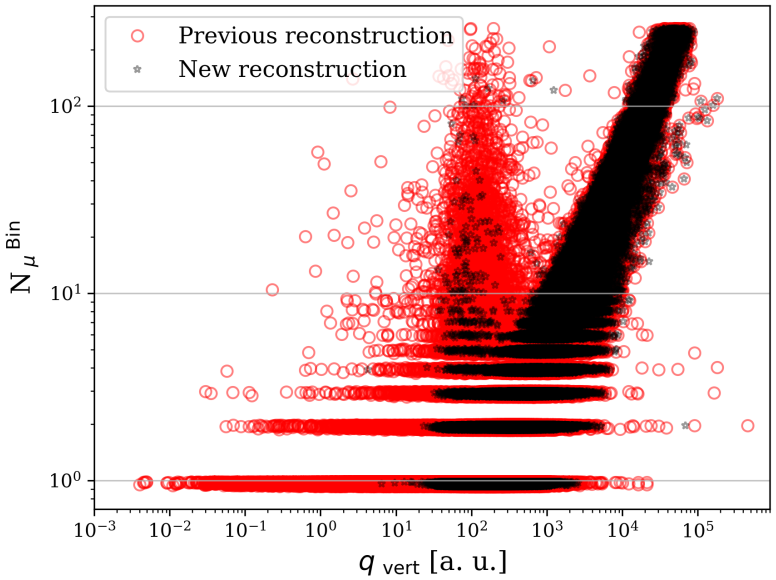

Figure 4.8: Data reconstruction of the binary mode (y-axis) as a function of the ADC mode (x-axis) for the three year analysis. The ADC mode was reconstructed with the LG channel using the previous algorithm (red circles) and the new algorithm (black stars).

but also contributes to a reduction in the measured charge. Fourthly, upon examining the spread of distributions for low muon densities, the new reconstruction results in a narrower charge distribution compared to the previous reconstruction. The analysis was also conducted for the HG channel, resulting in the same conclusions.

4.4. Summary

We exhibited the effectiveness of the `MdADCGlitchCleaner` module to identify the glitches within the LG channel and to remove them by generating a new 'deglitched' trace to estimate the number of muons. We showed that glitches might be found in any time bin of the ADC trace, in particular between the time bins 600 and 800, where the majority of muons arrive. However, the two positions most likely to have glitches are located at 0 and 512 in the ADC trace. Glitches were detected in most of the UMD modules deployed in the field, with an average of approximately 5000 glitches per UMD module during the three year data analysis. Approximately ~8% of the traces analysed contained glitches.

In the `MdADCChargeCalculator` module, we developed an algorithm to estimate the charge of the ADC trace based on integrating several windows, since employing multiple integration windows helps to mitigate the risk of summing over the undershoot of the trace and to prevent negative reconstructions of muons. By comparing the data reconstruction between the binary mode and the ADC mode,

we exhibited that the `MdADCChargeCalculator` module improves the charge estimation of the ADC mode, minimising the appearance of outliers obtained with the previous module `MdMuonIntegrator`. The baseline estimate is accurately computed in the `MdADCChargeCalculator` module for the first integration window. However, in cases where there are additional integration windows, these pulses overlap with the undershoot of the trace, which can be significant for high muon densities. The undershoot induces a decrease in the baseline, an effect not accounted for. A possible improvement would be to enhance the baseline estimation in the algorithm for the cases of more than one integration window and high muon densities.

For the development of the algorithms, we conducted a comprehensive analysis of three years of data (2020, 2021, 2022) and incorporated the periods found of bad data in the `MdModuleRejectorAG` module, marking them as rejected to ensure high quality data for any subsequent analyses. Moreover, we included in the `MdADCChargeCalculator` module a function to classify a UMD module measurement as anomalous data, subsequently excluding it from the reconstruction of the MLDF, given that we encountered events where traces from the LG channel exhibited clear inconsistencies with the measurements of the HG channel and the binary reconstruction. These events occurred very infrequent, representing less than 0.1% of the total traces analysed.

Chapter V

Calibration of the ADC mode with single atmospheric muons

In this chapter, we study the existing calibration strategy. To calibrate the ADC mode in the field, an algorithm was implemented in the electronics to select individual atmospheric muons detected in parallel to the shower data acquisition [74, 60]. This calibration is performed using atmospheric muons that generated a T1 trigger (from the associated WCD) and looks for an exclusive single-muon signature in the 64 binary traces (i.e., between four and twelve "1"s on only one scintillator strip).

Single muon simulations were conducted in $\overline{\text{Off}}\underline{\text{line}}$ in Section 5.1. In Section 5.1.1, the dependencies of the ADC mode and binary mode on the energy and zenith angle of the injected muon are presented. To examine the existing calibration strategy, muons were simulated in Section 5.1.2 following the energy and zenith angle distributions of atmospheric muons, to determine the mean charge deposited in the ADC mode. To ensure comparability with field data, the simulated muons were required to satisfy the same triggering condition in the buried UMD modules as requested in the field. Furthermore, we compare the results to simulations of single vertical muons, since the mean charge deposited by vertical muons is used in the muon reconstruction of the ADC mode proposed in Ref. [63] (see Section 2.5).

In Section 5.2, an in-depth study of the calibration method implemented in data, known as 'ADCT1 files' or 'online calibration', is presented. The algorithm is described in detail in Section 5.2.1. In Section 5.2.2, asymmetries between the halves of modules are reported, generated by the trigger dependence with the WCD. These results strongly suggest that the T1 trigger involved in the calibration procedure introduces a bias towards inclined muons with higher energies. This conclusion aligns with other results summarised in Section 5.2.2. To further

investigate this, in Section 5.2.3, we conduct Offline simulations of single muons detected in coincidence by the WCD and its corresponding UMD station, comparing the results with data. Using the differential energy flux, we estimate the expected muon rate of these muons in Section 5.2.4 and contrast it with the rate of vertical muons reaching the UMD after receiving a WCD trigger. Finally, in Section 5.2.5, we introduce a method to determine the mean charge deposited by a vertical muon using T3 shower events from 2021, showing the bias in muon reconstruction on shower events between the binary and ADC modes and comparing it to the bias found employing the ADCT1 files.

5.1. Single muon simulations in the UMD

Single muon simulations were performed in Offline varying the energy of the muon, angle and position of injection, using the `ParticleInjector` module. The muon was always injected from the ground towards the UMD in order to study not only the muon signal produced, the contribution from knock-on electrons and positrons generated in the soil. Additionally, the `onlyMuons` attribute in the `G4StationSimulator` module was utilised for comparison purposes. When this attribute is activated, knock-on electrons and positrons are deliberately omitted, i.e., they are not injected into the UMD scintillator.

In Fig. 5.1, three UMD modules, each with an area of 10 m^2, are shown adjacent to the WCD. The trajectories of single muons are visualised for a vertically incident muon (left panel) and a muon with a zenith angle of 45° (right panel), both injected at the centre of one-half of the module. The red trajectory represents the muon, while the green trajectories correspond to the knock-on electrons and positrons produced in the soil.

5.1.1. Dependencies with zenith angle and energy

Since the detector response varies depending on the position where muons are injected, due to optical-fiber attenuation, simulations were performed with muons originating from a fixed position at ground level. Each muon was injected towards a UMD module, aiming to strike the middle of the left half of the module with an azimuth angle of $\Delta\varphi_m = 90°$. This configuration, in which the muon enters transversely through the centre of scintillator Id 16, maximises the effect of corner-clipping muons.

The passage of muons through a given material determines a loss of their energy and a deflection of their incident direction. These effects are primarily due to collective results of two processes, inelastic collisions with the atomic electrons and elastic scattering from nuclei. Other processes, such as emission of Cherenkov

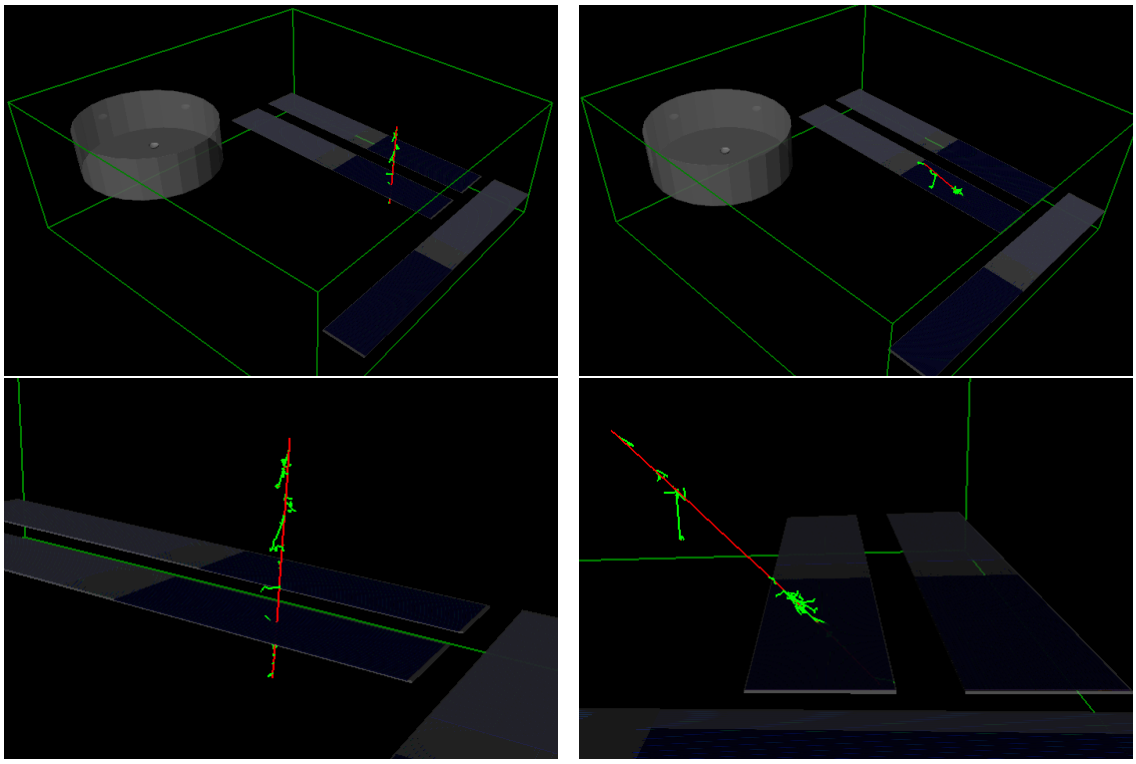

(a) Vertical Muon **(b)** Muon at 45°

Figure 5.1: Trajectories for a single muon of 3 GeV injected from the ground to the detector (red) and the corresponding knock-on electrons/positrons from the soil (green).

radiation, bremsstrahlung and nuclear reactions, can give contributions in specific energy ranges [75].

The energy loss produced by the soil is displayed in Fig. 5.2 for a vertical muon (orange) and a muon at 45° (green). For muons injected at ground level with energies exceeding 10 GeV, the energy loss can be considered negligible. However, a vertical muon injected with 1 GeV loses approximately ~ 90% of its energy, while a muon at 45° with the same initial energy is unable to reach the detector.

Since the energy threshold for muons to penetrate the soil is approximately 0.9 GeV, simulations were conducted for initial energies ranging from 1 up to 200 GeV in 1 GeV increments, with 100 muons simulated at each energy. These simulations were performed for various zenith angles: 0°, 10°, 20°, 30°, and 45°.

In Fig. 5.3, the scintillator Ids are plotted based on the type of particle reaching the detector: injected muons (top panels) and electrons (bottom panels). Two scenarios are analysed: a vertically incident muon (left panels) and a muon with a zenith angle of 45° (right panels). As shown in the top figures, for energies below 25 GeV, a fraction of muons were scattered, striking neighbouring bars, approximately 12% for vertical muons and 30% for muons at 45°. As the energy

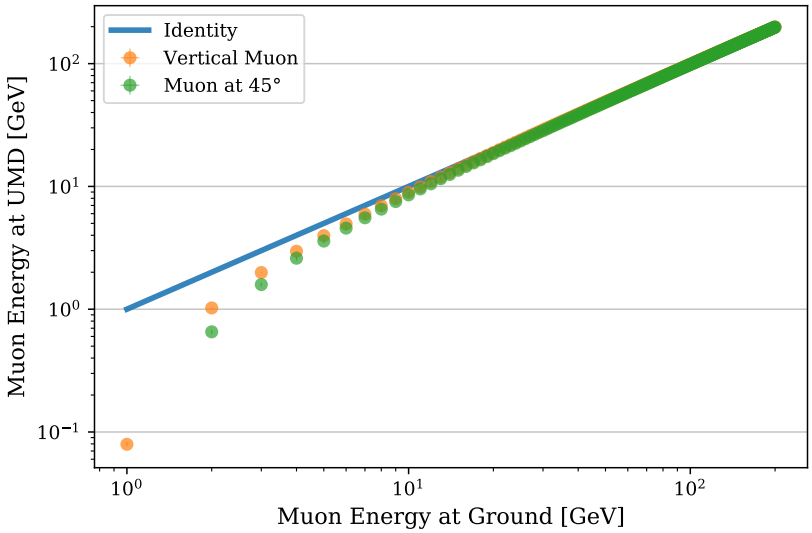

Figure 5.2: Muon energy at the UMD as a function of the muon energy at ground.

increased, the muon followed an almost straight trajectory through the soil. For a muon at 45°, the energy required to maintain a nearly straight trajectory was higher than that for a vertical muon due to the longer path length in the soil. Notably, as seen in the bottom figures, higher-energy muons generated a greater number of electrons and positrons in the soil.

The charge deposited in the ADC mode for the LG channel was analysed in Fig. 5.4 for a vertically incident muon (left panel) and a muon with a zenith angle of 45° (right panel). The charge was normalised by the charge deposited by a 2 GeV muon, as indicated by the blue markers. Additionally, the mean number of electrons and positrons contributing to the UMD signal (also normalised to the values at 2 GeV) is represented by green markers. The charge exhibited an increase as a function of muon energy, reaching up to approximately 25% for 180 GeV muons, while the normalised number of "1"s in the binary trace rose by about 6%. This stronger energy dependence observed in the ADC mode is attributed to the larger number of knock-on electrons and positrons from the soil reaching the UMD and depositing energy.

Finally, the dependence of the detector response on the zenith angle was analysed for both ADC and binary modes. To quantify this dependence, the normalised response was defined as

$$A_{\text{norm}}(E_{\text{i}}, \theta) = \frac{\langle A(E_{\text{i}}, \theta)\rangle}{A_0} \quad \text{and} \quad A_0 = \frac{\langle A(E_1, 0°)\rangle + \langle A(E_2, 0°)\rangle}{2}, \tag{5.1}$$

where A represents either the charge in the LG channel or the mean number of "1"s in the binary mode, summed over all scintillators. Figure 5.5 illustrates

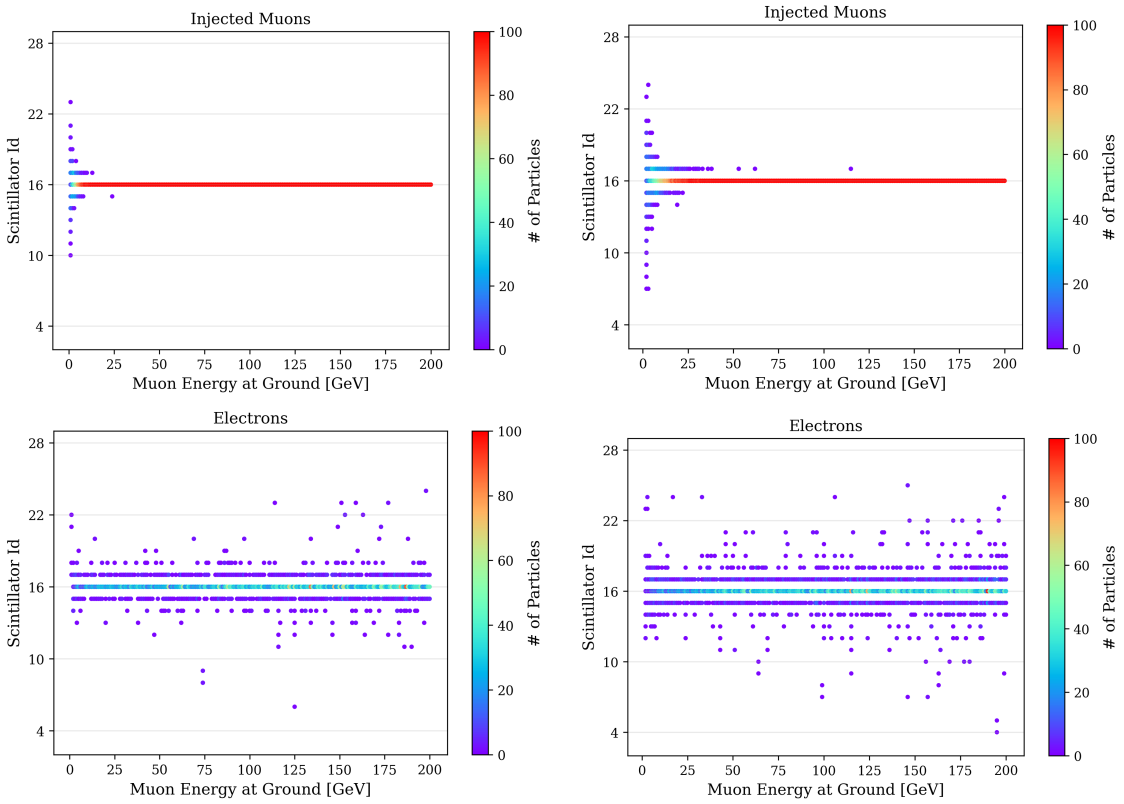

Figure 5.3: Scintillator Id as a function of the particle type that reached the detector. Left and right panels correspond to muons with zenith angles of 0° and 45°, respectively.

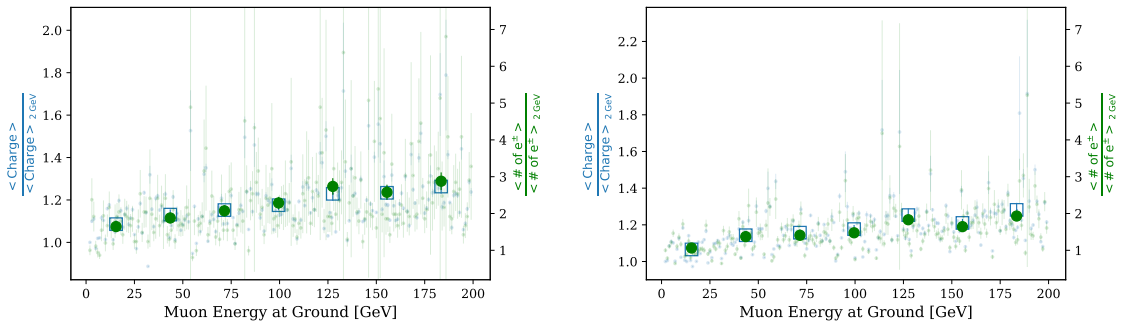

(a) Vertical Muon

(b) Muon at 45°

Figure 5.4: Mean charge (blue) and mean number of electrons/positrons (green) normalised by the value produced by a 2 GeV muon. The profile distributions are plotted as darker markers.

these dependencies for two energy bins: a low-energy bin, $E_1 = [1, 26]$ GeV, and a high-energy bin, $E_2 = [175, 200]$ GeV. An inverse cosine function was fitted to the data, confirming that the charge follows this dependence with the zenith angle, whereas the mean number of "1"s increases at a significantly slower rate. This difference arises because inclined muons travel longer paths through the

scintillator strips, resulting in greater energy deposition. The ADC mode is much more sensitive to this effect than the binary mode, as it directly depends on the deposited charge (energy), whereas the binary mode relies on the width of the signals exceeding the discriminator threshold. Additionally, the contrast between the two energy bins reinforces that the ADC mode exhibits a stronger energy dependence than the binary mode due to the increased production of secondary electrons and positrons in the soil for higher-energy muons.

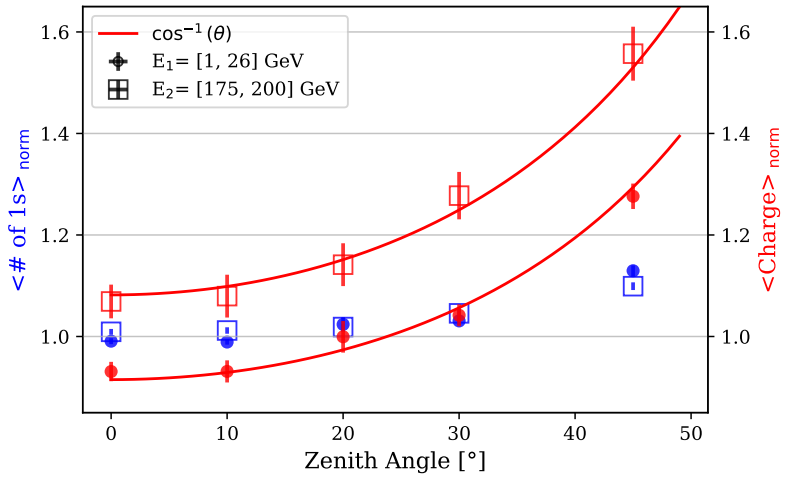

Figure 5.5: Dependence of the detector response on the zenith angle for both ADC (red) and binary modes (blue) for two energy bins: $E_1 = [1, 26]$ GeV and $E_2 = [175, 200]$ GeV.

5.1.2. Atmospheric muons

The atmospheric muons exhibit a $\cos^2(\theta)$ dependence on the zenith angle θ [76]. When this intensity is projected onto a finite flat detector area (such as the UMD) at ground level, the resulting distribution of muons follows a $\cos^3(\theta)$.

For the energy dependence, we used the secondary particle spectrum from Corsika simulations in Malargüe [77]. The energy spectrum of muons was fitted with a log-normal distribution, as shown in the left panel of Fig. 5.6. The energy of the muon is log-normally distributed $E \sim \text{Lognormal}(\mu, \sigma^2)$, meaning that the logarithm of the energy is normally distributed with mean μ and variance σ^2. The fitted values from the model were $\mu = (2.578 \pm 0.003)$ GeV and $\sigma = (1.229 \pm 0.001)$ GeV. Most atmospheric muons at ground level have energies up to 50 GeV. The cumulative probability, shown in the right panel of Fig. 5.6, indicates that 98.7% of the spectrum is contained below 200 GeV. While there could be muons with energies up to 4000 GeV, they are extremely unlikely.

We simulated random single muons based on these distributions using the rejection sampling algorithm. The muons were injected following uniform distributions for both the azimuth angle φ and the injection position within the

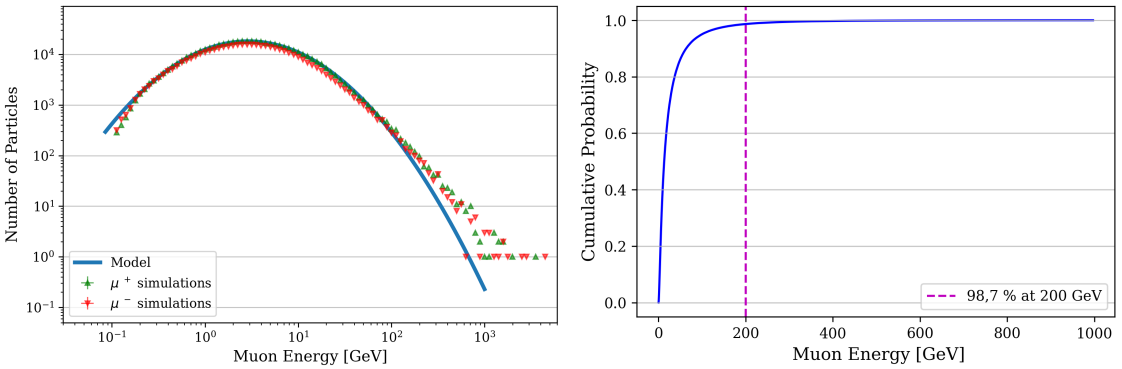

Figure 5.6: (left) Energy spectrum of muons from Corsika simulations in Malargüe, fitted with a log-normal distribution. (right) Cumulative probability of the model.

module, ensuring the accurate reproduction of light attenuation effects in the fiber. A total of 20,000 simulations were performed from the ground towards the UMD module, with 95.90% of the muons successfully reaching the UMD module and generating a signal.

In Fig. 5.7, the two complementary modes in the UMD (binary and ADC) were compared, where the charge collected across all scintillators was plotted against the number of "1"s in the binary trace (summed over all scintillators). The number of events in each bin is indicated in red brackets, with a minimum of 30 events per charge bin required. The charge increased at a faster rate than the number of "1"s, as the ADC mode is sensitive to the area under the signal, while the binary mode is mainly sensitive to the width. As the energy deposited in the scintillator rises, the photons reaching the SiPM tend to pile up, causing the area to increase more significantly than the width of the signal.

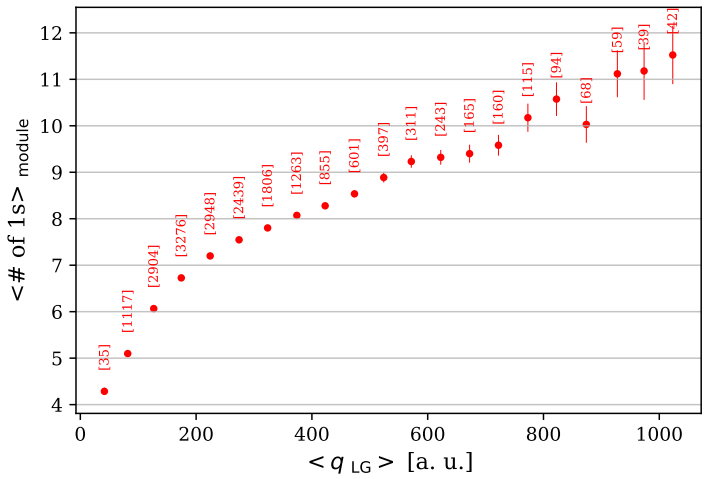

Figure 5.7: Comparison of the ADC mode (x-axis) and the binary mode (y-axis).

In Fig. 5.8, we present the charge histograms for the LG and HG channels of the ADC. The mean charge deposited by atmospheric single muons was recorded as $\langle q \rangle = 272.0 \pm 1.3$ in arbitrary units (a.u.) for the LG channel and $\langle q \rangle = 1038.4 \pm 5.0$ in a.u. for the HG channel. When the `onlyMuons` attribute was activated in the `G4StationSimulator` module, preventing the injection of knock-on electrons/positrons into the scintillator, these values were 7% lower. These results are consistent with those reported for UMD laboratory data [72], where the setup consisted of only four scintillator bars stacked on top of each other. In the lab, no electrons/positrons were produced from the soil (since the setup was not buried), and no clipping muons occurred due to the design.

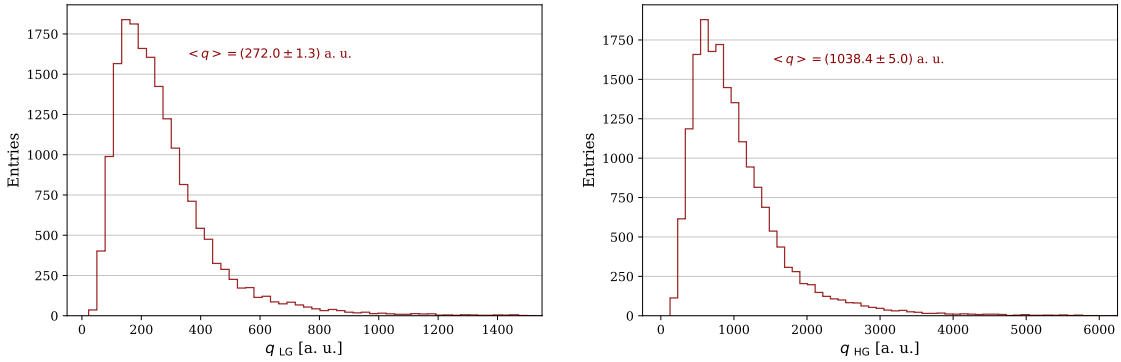

(a) LG channel **(b)** HG channel

Figure 5.8: Charge histograms of atmospheric muons in the LG and HG channels of the ADC mode.

To compare the charge histograms with the online calibration, the simulated muons were required to satisfy the same selection criteria as those used for the binary channel in the field. Specifically, the single muon events had to contain more than 4 and less than 12 consecutive "1"s on a single scintillator strip in the binary trace. The selection criteria was passed by 95.35% of the muons, while 4.63% exceeded the condition. In 5.9, the charge of the LG channel was analysed in relation to the selection criteria applied to the binary trace. A stable charge was observed when the minimum number of "1"s required in the binary trace was varied up to six, indicating that most muons produced at least six "1"s. If the minimum was set above seven, less than 50% of the events met the selection criteria. In Fig. 5.10, the number of "1"s in the binary trace is shown as a function of the particle type reaching the scintillator strips. Of the simulations, 81.2% produced 'Muons' and 18.8% produced both 'Muons and Electrons'. The mean number of "1"s for 'Muons' was $\langle \#1s \rangle = (6.94 \pm 0.01)$, while for 'Muons and Electrons' the value was $\langle \#1s \rangle = (9.18 \pm 0.05)$.

Finally, the charge histograms of ominidirectional atmospheric muons from Fig. 5.8 are compared to the results of vertical muons, since the mean charge de-

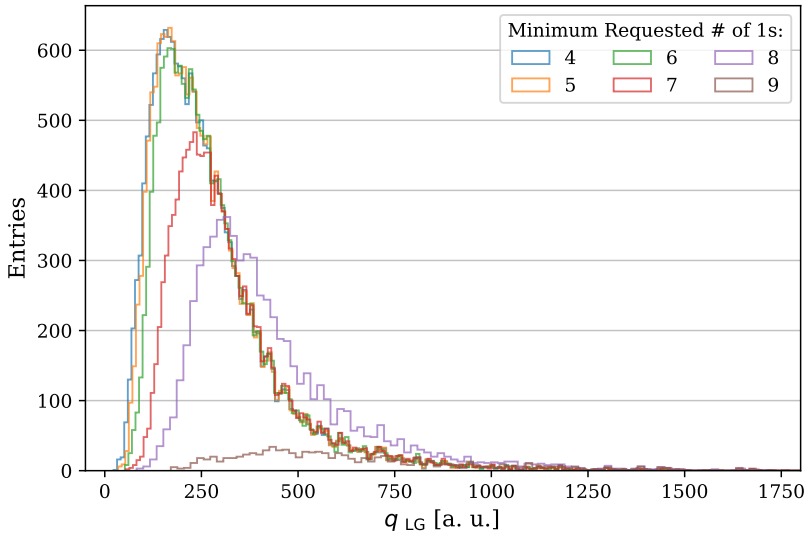

Figure 5.9: Charge histogram obtained for the LG channel as a function of the minimum requested number of "1"s in the binary trace.

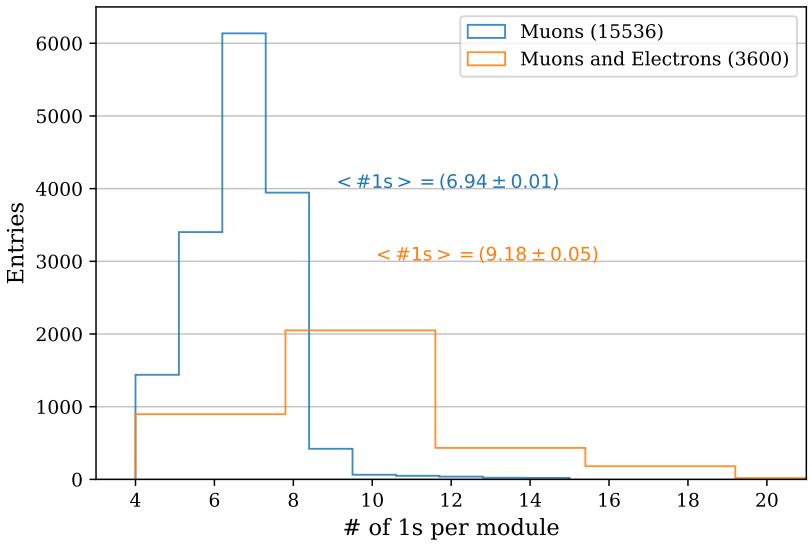

Figure 5.10: Ones produced in the binary trace as a function of the particle type impinging on the scintillators. The cases where only muons generated signal are plotted in blue, while the cases where the electrons/positrons from the soil reached the scintillators are plotted in orange.

posited by vertical muons is used in the muon reconstruction of the ADC mode proposed in Ref. [63] (see Section 2.5). The bias of the muon reconstruction using vertical muons will be analysed in Section 6.1. To study this, 5000 single vertical muons were simulated following the energy distribution outlined earlier. The charge histograms for vertical muons are shown in blue in Fig. 5.11. The mean charge was $\langle q \rangle = 250.3 \pm 2.5$ in a.u. for the LG channel and $\langle q \rangle = 955.5 \pm 9.5$ in a.u.

for the HG channel. The charge for vertical muons is 8% lower than the charge obtained for omnidirectional atmospheric muons (orange histogram). Assuming that the online calibration is measuring these ominidirectional atmospheric muons, the contribution to the muon reconstruction, as proposed in Ref. [63], from inclined muons is not negligible.

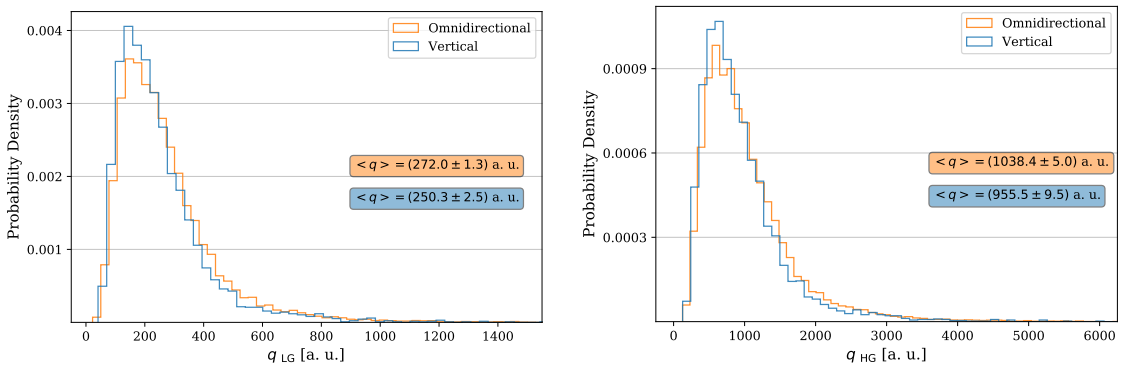

(a) LG channel **(b)** HG channel

Figure 5.11: Charge histograms produced by vertical muons (blue) compared to the charge histograms produced by ominidirectional atmospheric muons (orange).

5.2. Single muons in data with T1 events

5.2.1. ADCT1 files

An algorithm is implemented in the electronics to extract the calibration histograms [60] of the ADC channel. The histograms are built for each channel (LG/HG) selecting individual muons with the binary mode. The schematics of the files can be seen in Fig. 5.12. The algorithm runs parallel to the shower acquisition when a UMD module receives a local trigger T1 from the WCD. The algorithm looks for an exclusive single-muon signature in the 64 binary traces, which consists of a sequence between four and twelve consecutive "1"s on only one scintillator strip, while having zero "1"s on all the other scintillator strips. This muon criteria was based on laboratory measurements: the lower limit of consecutive "1"s was set to reject more than 95% of the SiPM noise with less than 1% of muon signal loss, while the upper limit was set to select about 99% of the single-muon signals, avoiding biases in the muon charge estimation due to shower events with several particles (see Ref. [60]).

Fig. 5.13 shows the sum of binary channel traces (top panel) and the overlap of ADC traces (bottom panel) for 360,000 background events which correspond to the equivalent of one hour of T1 events. When a T1 trigger is received, the algorithm looks for a muon pattern in the binary channel over a window around

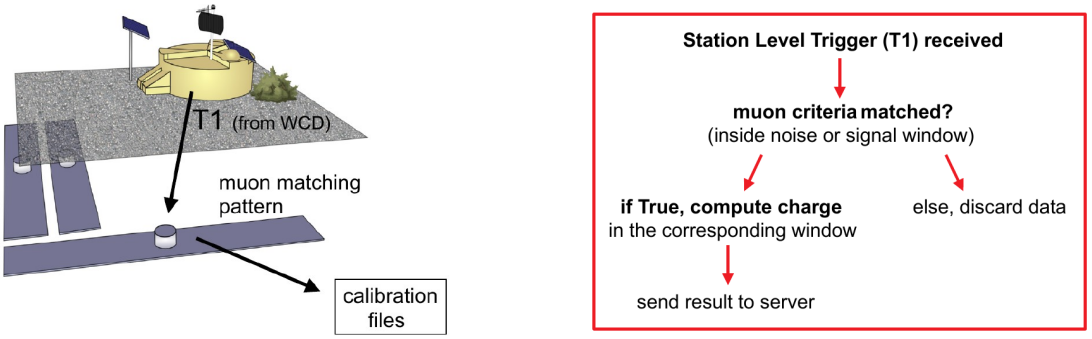

Figure 5.12: Schematics of the ADC online calibration.

the position of the T1 (represented by dotted orange lines in the top panel). If the muon condition is fulfilled, a signal-plus-noise charge is obtained by integrating the ADC trace over a 200-ns window established by including a well-known time shift between the binary and the ADC channels (dotted orange lines in the bottom panel) [74]. The span of the integration window was defined as 3 standard deviations from the mean width of the pulse obtained with laboratory data, where the mean width refers to the number of time bins with an amplitude above two times the standard deviation of the baseline. Similarly, if a muon pattern condition over the noise window is fulfilled, a noise charge, that accounts for the optical fiber/scintillator noise, is obtained by integrating the ADC trace over a 200-ns window located far from the signal-plus-noise window (black lines in the bottom panel). The signal charge is then obtained by subtracting the noise charge from the signal-plus-noise charge.

The online calibration of the ADC mode is stored daily in plain text files called ADCT1 files (one per module) [78] containing 9 columns with the information of the time of the event, the window where the event fell, the scintillator Id where the muon arrived and the charge and baseline computed. The ADC traces are not stored, so the two parameters used for the charge calculation (integration window and delay ADC-Binary) need to be fine tuned for each module periodically.

5.2.2. ASYMMETRIES BETWEEN HALVES OF THE MODULES

In this section we selected data from nine stations: Franquito, Correo Argentino, Luisa, Peter Mazur, Norberto Wilner, Pea, Casa Ronald, Wiwi, and Mora. These stations were selected because the modules at each of these stations share a consistent orientation in the field, as illustrated in Fig. 5.14.

We studied the distribution of the number of events as a function of the scintillator Id in Fig. 5.15, selecting four months of data from June to October of 2021. It is important to note that the number of events within each window is predominantly influenced by distinct factors. Within the "Noise" window, the

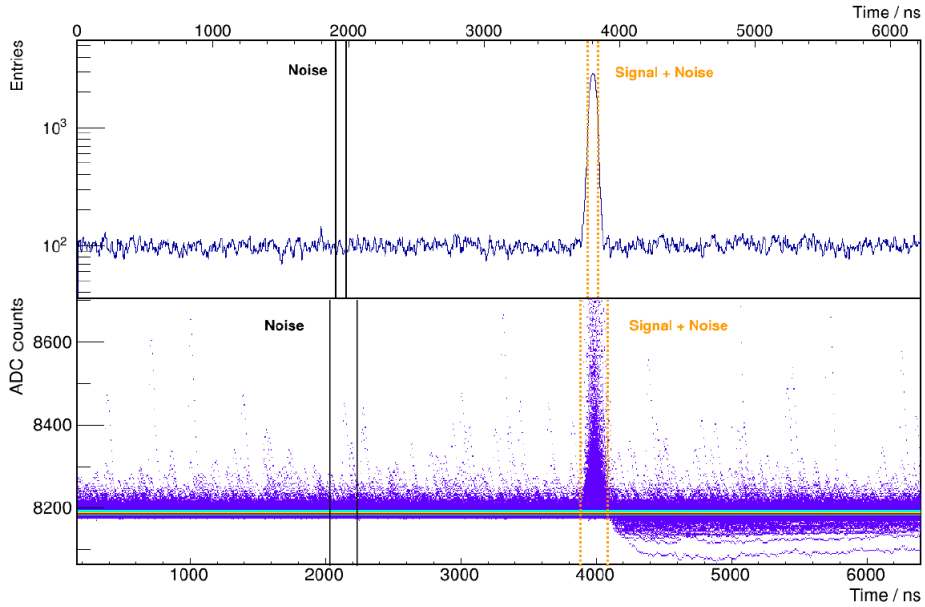

Figure 5.13: Traces from the binary channel (top) and the ADC (bottom), for 360000 events after a T1 trigger is received. The x-axis is shifted because of the ADC-binary delay.

distribution is primarily influenced by the attenuation of light occurring within the fiber. The scintillator strips employed in the UMD measured 4 m long, so the optical fiber length associated to a particular strip can be denoted as 4 m + x, where x is the manifold length defined as the length of the fiber from the end of the bar to the SiPM. Fig. 5.16 presents an analysis of the number of events as a function of the manifold length for each module. More events are generated in the scintillator strips associated with shorter fibers compared to those with longer fibers, due to the greater light attenuation in the longer fibers. In the "Signal + Noise" window, a clear pattern is observed in the three modules: more muons were detected closer to the WCD. This observation contrasts with the expectation of a more uniform distribution of events throughout the module if the incoming muons were omnidirectional, considering only the light attenuation effects. Moreover, in the "Signal + Noise" window more events are evidently observed in the scintillator strips located at the edges of each module, i.e., scintillators with Ids 1, 32, 33, and 64. The ratios between the halves of the module are plotted in Fig. 5.17, illustrating the differences in both the number of events (left) and the charge (right). Interestingly, the farther half of the modules recorded a higher charge, approximately 5% more, while the closer half registered a greater number of events, approximately 33% more. This shows that in the ADC online calibration procedure the number of muons arriving at the buried detector are not uniformly distributed and the charge they deposit is neither constant nor symmetrical across both halves of the module. To illustrate, consider the scenario of a coincident muon generating signals in both the WCD and the UMD,

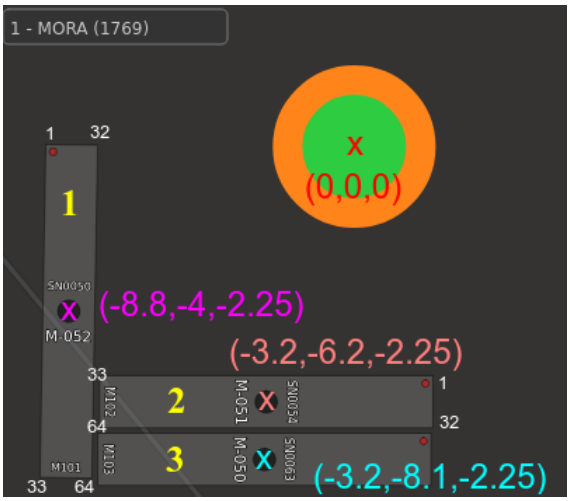

Figure 5.14: Schematics of station Mora in the field. The module Id is illustrated in yellow. The crosses indicate the centre of each module and its position (in meters) in the coordinate system xyz. The centre (0,0,0) is located in the centre xy of the WCD at the ground. The red dot in each module indicates the first scintillator Id.

aiming to reach the farther half of module 1 (scintillators 33 to 64) as shown in Fig. 5.14. In order to trigger the UMD after activating the WCD, this muon would need to arrive at a larger zenith angle than a muon arriving to the closer half of module 1 (scintillators 1 to 32). The larger angle of arrival leads to a more extensive path length within the scintillator, resulting in a higher charge being deposited. Moreover, the probability of a muon arriving at the closer half of module 1 (scintillators 1 to 32) is significantly higher than that of arriving at the farther half (scintillators 33 to 64). There are two primary reasons for this. Firstly, the closer half subtends a larger solid angle with respect to the WCD, making it more likely to register coincidental muons. Secondly, larger zenith angles for atmospheric muons are less probable compared to smaller angles. Additionally, muons with larger zenith angles are less likely to fulfil the muon selection criteria (see Section 5.2.3). The significantly higher number of events in the strips located at the edges of each module, as shown in Fig. 5.15, are an evident footprint of inclined muons. The muon selection criteria, which requires signal on only one scintillator strip, imposes a cut in the events that produce corner-clipping signals in the adjacent bars. Given than the scintillator strips located at the edges do not have an adjacent bar, less corner-clipping signals are discarded resulting in a selection bias. These results strongly suggest that the T1 trigger involved in the procedure introduces a bias towards inclined muons.

This conclusion aligns with results previously presented in Ref. [79], where an extensive analysis with T3 shower events was performed showing that the charges in the ADC calibration files were compatible with showers from inclined events ($51.7° < \theta < 65°$). Moreover, the mean charge of the ADC mode and the number

of "1"s in the binary traces, obtained in the monitoring of the calibration data reported in Section 3.3 and Section 3.5, are not in agreement with the simulations from Section 5.1.2 and with other studies performed in Refs. [80, 60].

In Refs. [80, 60], laboratory measurements were reported using a muon telescope set at 2.5 m from the SiPM to select vertical muons. The mean charge obtained for the LG channel in Ref. [80] was $\langle q \rangle = 235 \pm 2$ in a.u.. In Section 5.1.2, single muon simulations of vertical atmospheric muons were performed in Offline and the mean charge reported was $\langle q \rangle = 250.3 \pm 2.5$ in a.u. for the LG channel in a 10 m^2 module. However, the values reported in Section 3.3 for the calibration data were much higher, corresponding to $\langle q \rangle = 384.7 \pm 2.7$ in a.u. for the modules of 10 m^2 and $\langle q \rangle = 388.3 \pm 3.8$ in a.u. for the modules of 5 m^2. In Section 3.5, the histogram of the number of "1"s in the binary traces from signal events measured in data exhibits a broader distribution that the one reported in the laboratory [60]. A higher noise rate in the field can account for making the distribution wider towards a lower-than-average number of "1"s. The wider distribution towards values with higher-than-average number of "1"s could be explained by events corresponding to muons detected in coincidence by the WCD and the UMD (i.e., arriving with relative large zenith angles) since they will have a deposited charge on the UMD module higher than that expected for vertical muons (as selected in the laboratory by means of a muon telescope). Moreover, this could also explain the higher mean charge values reported in data.

5.2.3. Comparison with simulations of single muons in coincidence on both detectors WCD+UMD

We performed simulations of single muons in coincidence on both detectors (WCD+UMD), in order to study muons that produce both the T1 trigger in the WCD and the signal in the UMD. The simulation is done in a way that the muon may or may not be injected into each module, according to the following procedure: A muon is randomly created with its energy and position over the WCD following those from an expected flux of atmospheric muon, and with an isotopic arrival direction; then full end-to-end propagation and detector simulation are performed using Offline [73], employing the `ParticleInjector` module to inject the muon into the WCD. Considering the geometry of both detectors, we examined the energy and angles required for a muon to arrive at any of the three modules. Based on this analysis, energy, zenith angle, and azimuth angle cuts were implemented to optimise simulation time. The energy distribution of background muons, as presented in Section 5.1.2, was utilised, setting a minimum required energy of 1.5 GeV.

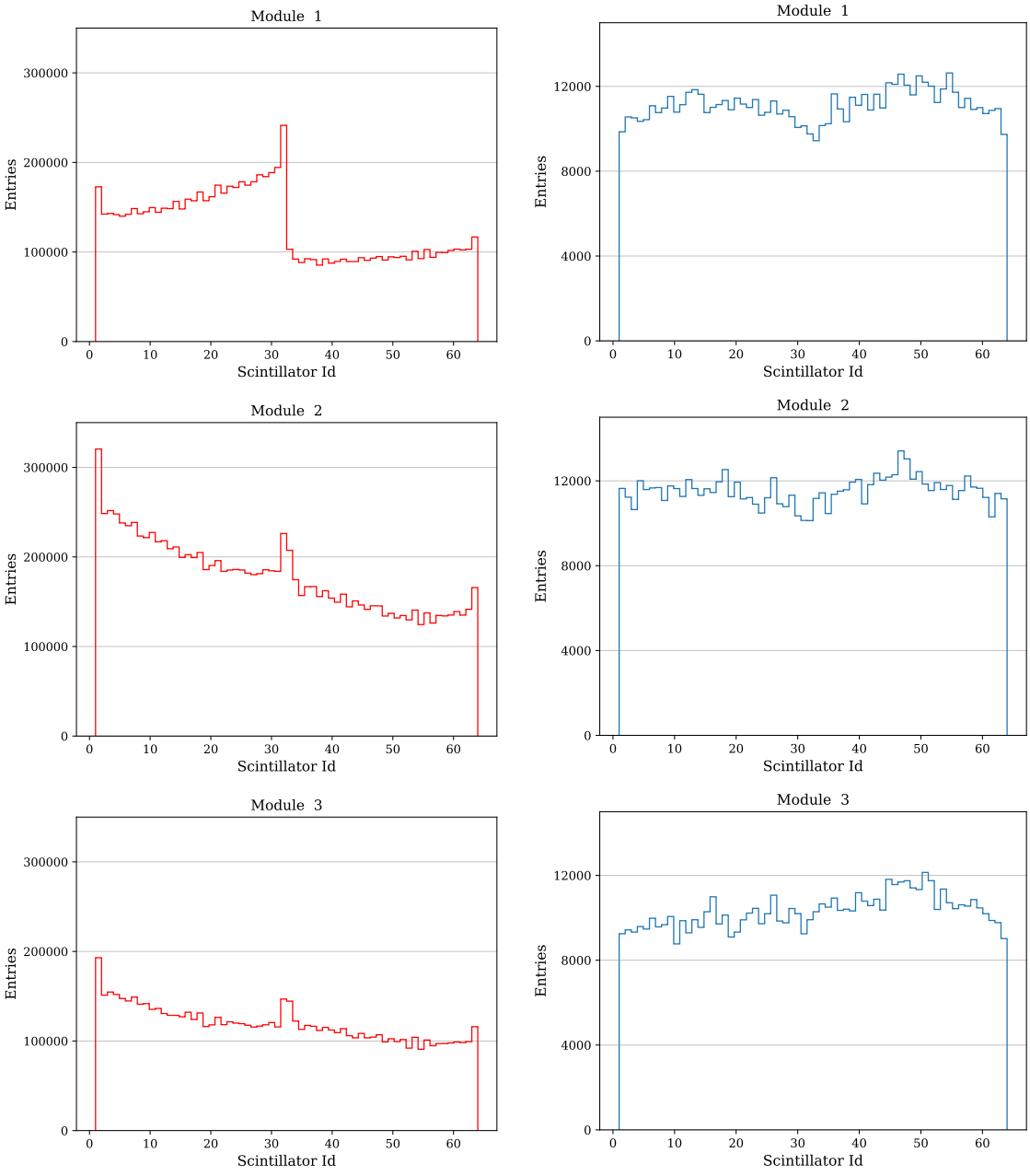

(a) "Signal + Noise" window

(b) "Noise" window

Figure 5.15: Distribution of the number of events for module 1 (top), module 2 (middle) and module 3 (bottom), taken by the UMD online calibration procedure during 4 months.

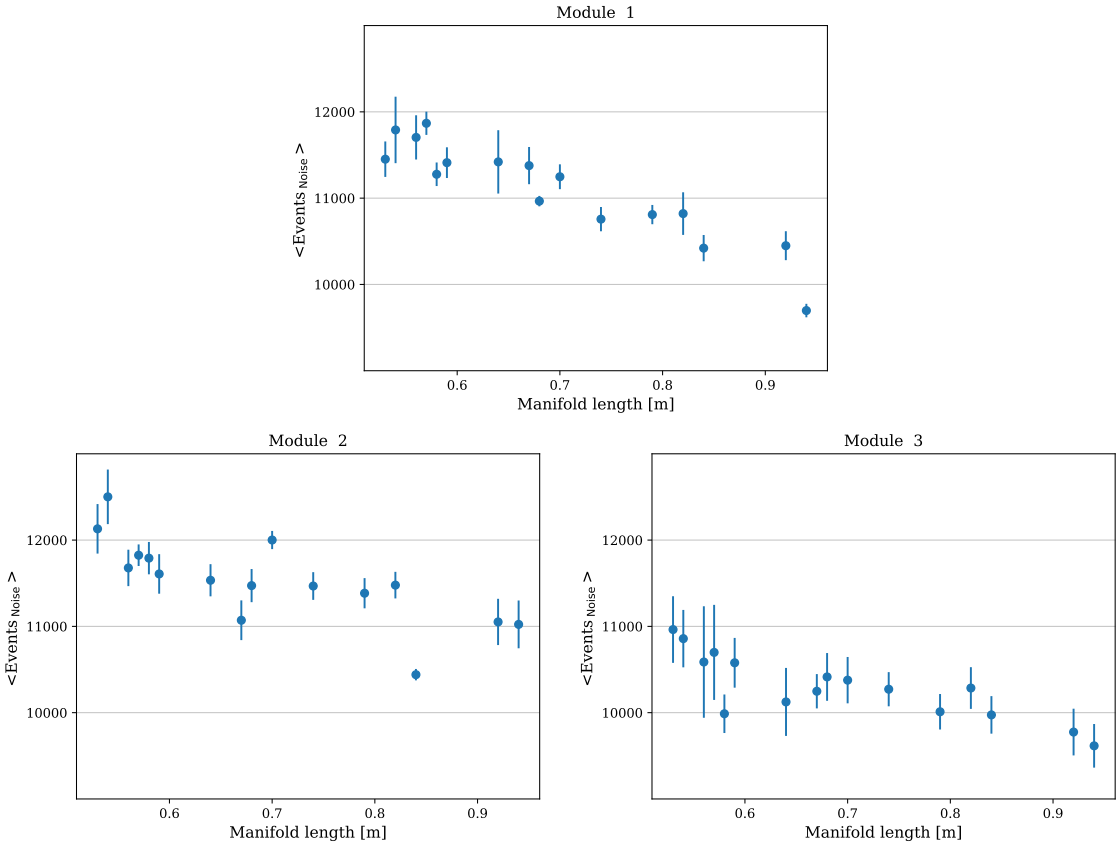

Figure 5.16: Events in the "Noise" window as a function of the manifold length for module 1 (top), module 2 and 3 (bottom), during 4 months of data.

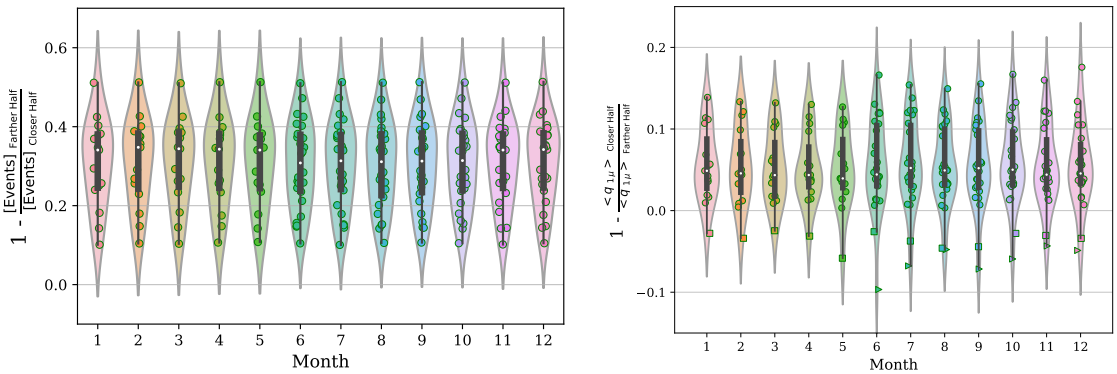

Figure 5.17: Comparison of the number of events (left) and the mean charge (right) between the halves of module with respect to the WCD position.

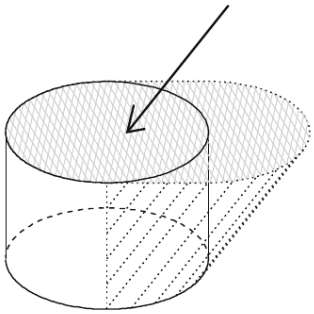

Figure 5.18: Effective area (hatched) of a detector receiving a flux directed along the arrow: top area + projection of the lateral area onto an horizontal plane.

Simulation strategy

To randomly generate the point of injection on the WCD, we have to take into consideration the area seen by a muon with incoming direction θ_μ, which is referred to as the effective area A_{eff} [81]. For an incoming muon with $\theta_\mu = 0$ (vertical muon), the cylinder area can be divided in three. The top area corresponds to the area of a circle with a radius of r: πr^2; while the side area is the area of a rectangle with a height of h and a base of $2r$: $2rh$. To extend this concept to any θ_μ, we need to consider the projections of both areas. The effective area A_{eff} then depends on θ_μ according to the following

$$A_{\text{eff}}(\theta_\mu) = A_{\text{top}} + A_{\text{side}} = \pi r^2 \cos\theta_\mu + 2rh \sin\theta_\mu. \tag{5.2}$$

This area can be seen as the shadow produced by a station on the ground when it is "illuminated" by a beam of muons with a certain direction (see Fig. 5.18).

The simulation strategy to generate the point of injection on the WCD was built following the same idea implemented to generate random injections in the `CachedShowerRegenerator` module of $\overline{\text{Off}}\underline{\text{line}}$. Once the incoming muon θ_μ is generated, we calculate $A_{\text{eff}}(\theta_\mu)$ (with $R = 1.78\,\text{m}$ and $H = 1.2\,\text{m}$ for the WCD). A uniformly distributed random value of area A_{rand} is generated between 0 and the effective area A_{eff}. If $A_{\text{rand}} < A_{\text{top}}$, the muon is injected uniformly at random across the top of the WCD. If the condition is false, the muon is injected uniformly at random across the side of the WCD.

In Fig. 5.19 the positions where the muons were injected into the WCD are plotted based on the module they arrived at. For each module, the distribution of the muons is primarily concentrated on the opposite edge of the cylinder facing the module, as well as on the top.

In the online calibration, the selection of the 200 ns "Signal + Noise" window in the ADC trace is around the position of the Thr1 [74]. Since the WCD was not forced to trigger, we performed around 2.3×10^6 random simulations of single

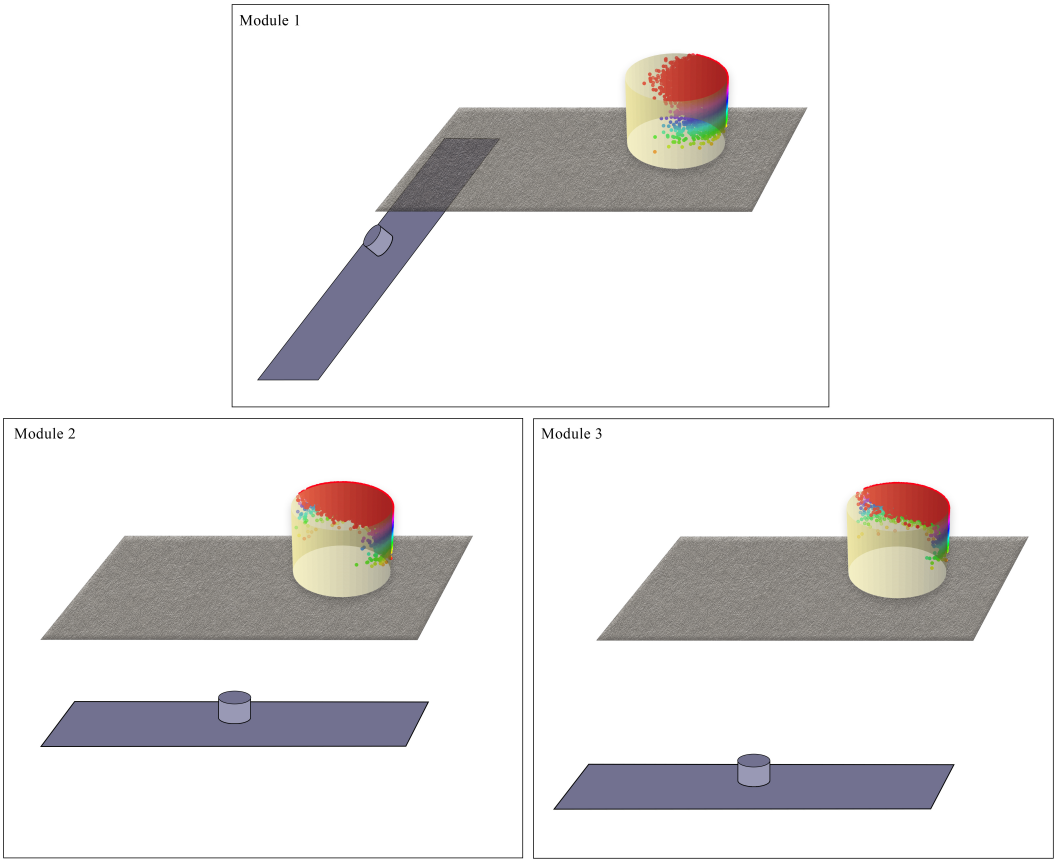

Figure 5.19: Muon injection positions that triggered a T1 signal in the WCD and generated a signal in the UMD for module 1 (top), module 2 (bottom left), and module 3 (bottom right).

muons. Approximately 13% of these simulated muons generated a trigger signal in the WCD. The trigger produced in the WCD was Thr1 ~99.8% of the times, while ToT was ~0.2%. Moreover, ~13% of the muons producing signal in the WCD were able to reach the UMD modules. And in addition to that, only half fulfil the muon selection criteria of having between four and twelve "1"s on only one scintillator strip and zero "1"s on the others (~1% of the total 2.3×10^6 simulations). The trajectory of a muon being detected in coincidence by both WCD and UMD module is shown in Fig. 5.20, where the red trajectory corresponds to the muon, while the green trajectories are travelled by knock-on electrons/positrons.

Zenith angles and energies for muons reaching the UMD

We studied the dependencies of zenith angle and energy for muons that reached the UMD after generating a signal in the WCD. In Fig. 5.21 the zenith angle distributions are plotted as a function of the scintillator Id where the muon arrived. It is important to note that the three modules exhibit distinct zenith

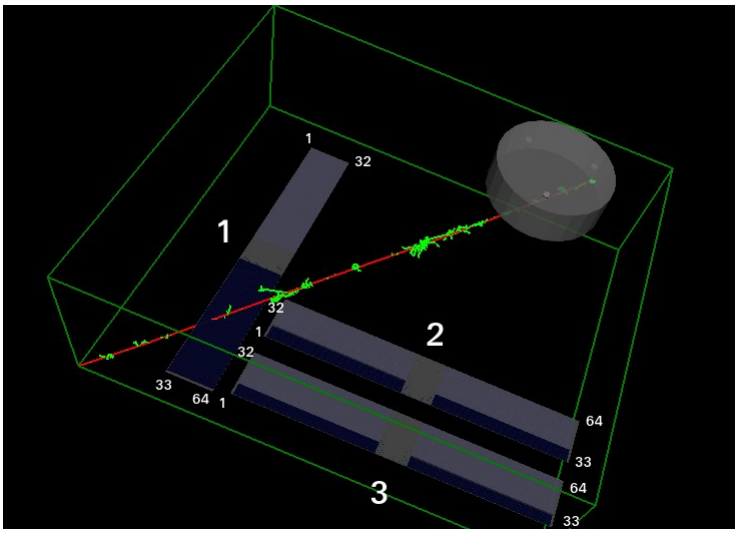

Figure 5.20: Trajectory of a single muon (red) in coincidence passing through the WCD and module 1. The knock-on electrons/positrons from the soil are plotted in green. The module and the scintillator Ids of each module are indicated in white.

angle distributions since they are not equidistant from the WCD. The farthest scintillators from the WCD belong to the second half of module 1 (scintillators Ids 33 to 64), as illustrated in Fig. 5.20. Consequently, the largest zenith angle distributions are observed in this half, with a maximum value of the median of ~75° for the farthest scintillator, which is scintillator 33.

The zenith angle distributions of the three modules are in agreement with their respective distances from the WCD. For instance, smaller angles are observed for module 2 compared to module 3, which is parallel to module 2 but farther.

In Fig. 5.22 the energy distributions of muons are displayed for the three modules. The muons arriving at the module have energies ranging from 3 GeV up to 3000 GeV, with a median energy of around 20 GeV. These energies are significantly higher than the mean energy of atmospheric muon distributions (approximately 3 GeV) since longer trajectories are expected for inclined muons in coincidence. The highest minimum energies of around 5 GeV are observed for the farthest scintillators from the WCD: scintillators Ids 33 to 64 of module 1. Additionally, we encounter the lowest minimum energies of around 3 GeV for the closest scintillators from the WCD: scintillators Ids 33 to 64 of module 2. The energy loss rates of muons in water vary with muon energy, with values of approximately 2.1 MeV/cm for a 1 GeV muon, 2.5 MeV/cm for a 10 GeV muon, and 6.0 MeV/cm for a 1000 GeV muon [75]. For instance, a 10 GeV muon crossing the WCD from top to ground through opposite edges would experience a maximum energy loss, resulting in a track length of about 376 cm. This translates to an energy loss of approximately 940 MeV during its passage through the WCD. The majority of the energy loss is produced through the soil. The soil shielding imposes an energy

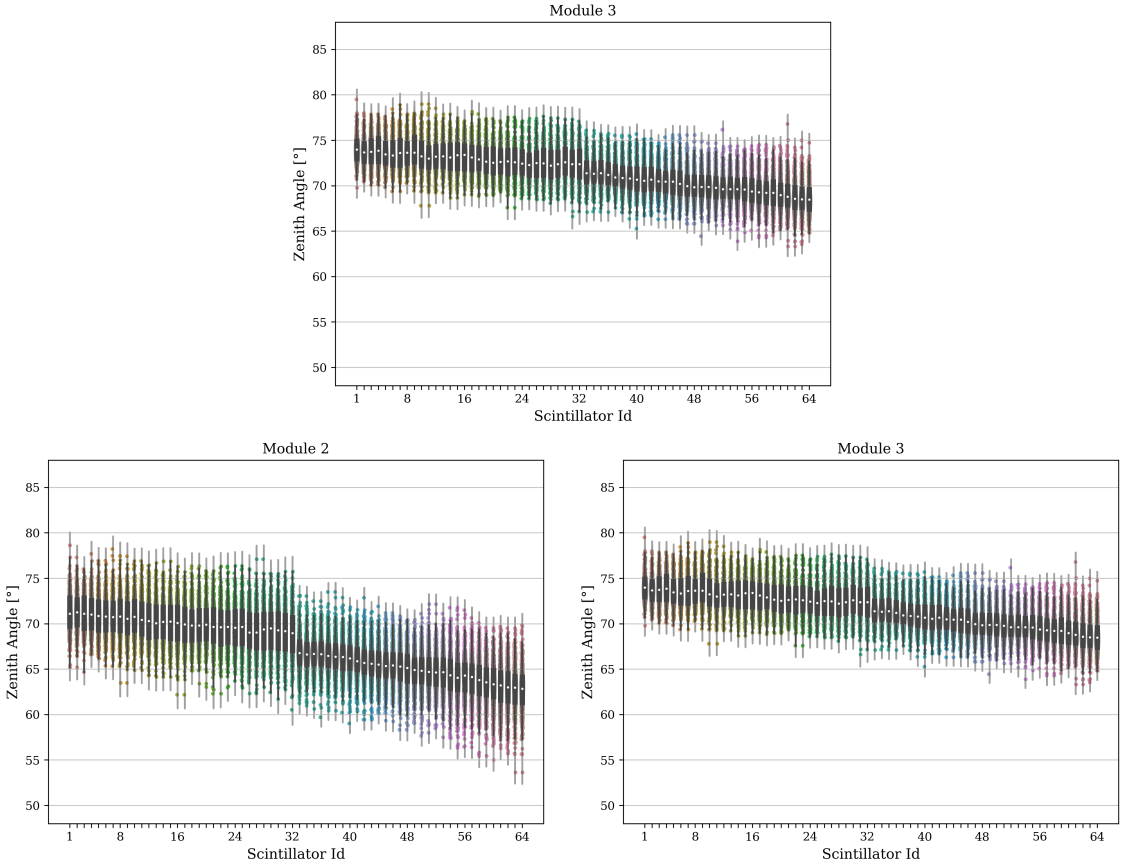

Figure 5.21: Muon zenith angle as a function of the scintillator Id where the muon arrived, for module 1 (top), module 2 (bottom left), and module 3 (bottom right).

threshold on muons attempting to reach the UMD. A muon must have a minimum energy of 1 GeV at the ground to arrive at the UMD with approximately 0.1 GeV (see Section 5.1.1). The distance from the centred at ground of the WCD to the farthest edge of module 1 (edge of scintillator Id 33 in Fig. 5.20) is approximately 13.7 m. To arrive to the farthest edge of the UMD modules, a muon must have a minimum energy at ground of around 6 GeV.

Charge histograms

The charge histograms obtained for the three UMD modules and both channels of the ADC are presented in Fig. 5.23. The mean charge deposited by muons in coincidence were (for the LG and HG channels respectively): $\langle q \rangle = 605.3 \pm 4.7$ in a.u. and $\langle q \rangle = 2319.4 \pm 18.0$ in a.u. (module 1), $\langle q \rangle = 604.6 \pm 2.9$ in a.u. and $\langle q \rangle = 2314.0 \pm 11.3$ in a.u. (module 2), $\langle q \rangle = 704.1 \pm 5.2$ in a.u. and $\langle q \rangle = 2697.8 \pm 19.8$ in a.u. (module 3). These values are significantly higher than those reported in Section 5.1.2 for omnidirectional atmospheric muons, which were $\langle q \rangle = 272.0 \pm 1.3$ in a.u. for the LG channel and $\langle q \rangle = 1038.4 \pm 5.0$ in a.u. for

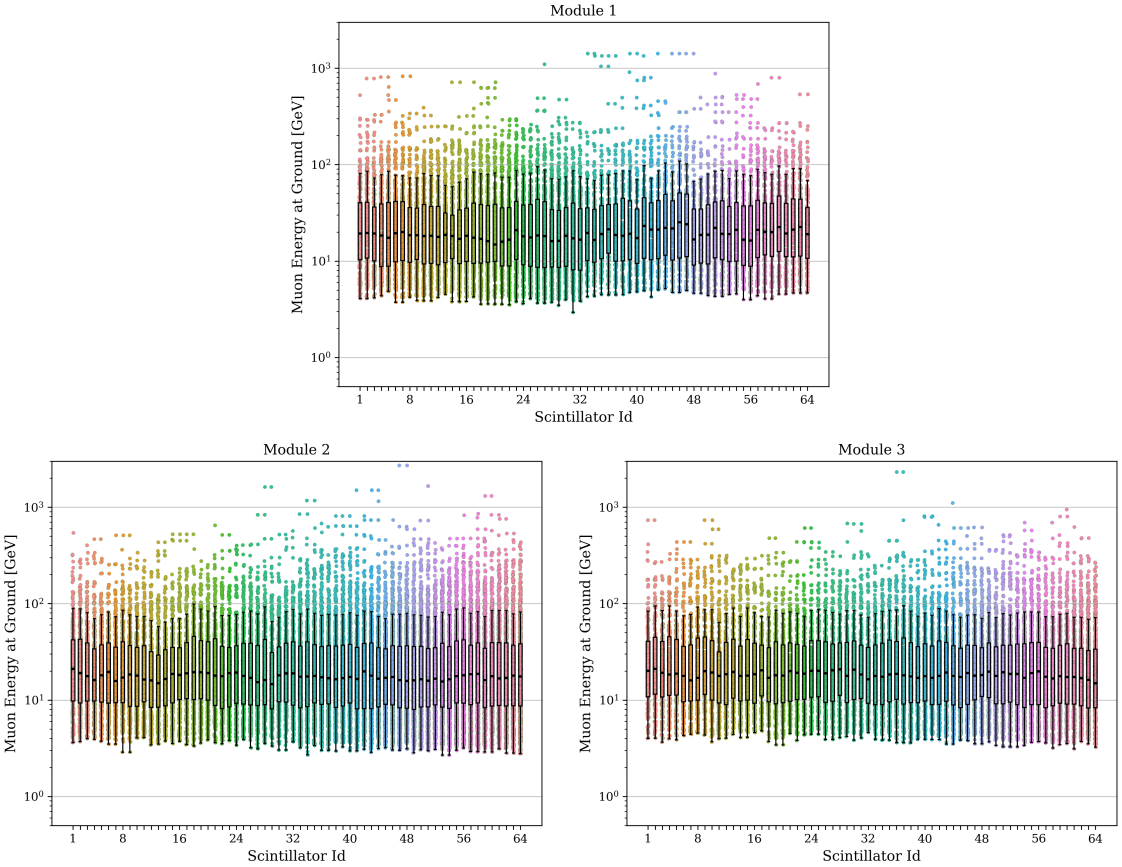

Figure 5.22: Muon energy as a function of the scintillator Id where the muon arrived, for module 1 (top), module 2 (bottom left), and module 3 (bottom right).

the HG channel. This discrepancy is due to the muons in coincidence having larger zenith angles, resulting in more energy deposition in the scintillator strip due to their inclined trajectory. Additionally, these muons have higher energies, producing more knock-on electrons/positrons in the soil that can also deposit energy in the scintillator strip.

Only ~40% of the muons that reached module 1 were able to satisfy the muon selection criteria of having between four and twelve "1"s on only one scintillator strip and zero "1"s on the others. For modules 2 and 3, the percentages were ~56% and ~43% respectively. The muon selection criteria imposed a cut in the events of corner-clipping muons since those kind of events generated signals in adjacent bars. The corner-clipping muon probability depends on the zenith angle of the muon, increasing for higher angles. Consequently, the condition requested for the muon selection was more likely to be fulfilled in the module that was closer to the WCD, which is module 2, given that the muons reaching this module had smaller zenith angles (see Fig. 5.21).

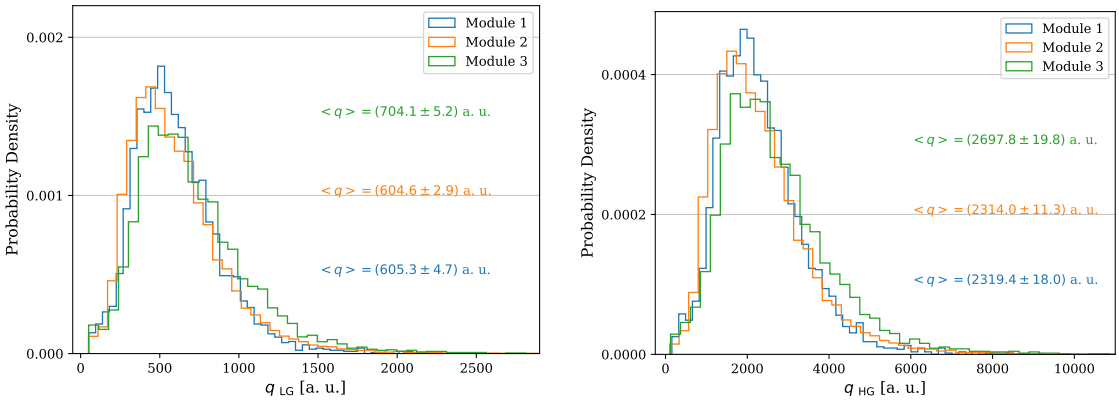

(a) LG channel **(b)** HG channel

Figure 5.23: Charge histograms for both ADC channels in module 1 (blue), module 2 (orange) and module 3 (green).

Comparison between simulations and data

In order to compare with simulations, we selected data from stations with the same orientation, as explained in Section 5.2.2. The number of events as a function of the scintillator Id, as shown in Fig. 5.15 (left), was compared to ones obtained from simulations of coincidence muons in Fig. 5.24.[1]

The scintillators Ids located on the edge of the modules consistently exhibit more events than their neighbouring bars. As detailed in Section 5.2.2, the muon selection criteria, specifically requiring signals on only one scintillator strip, introduces a selection bias. In the case of non-edge bars, corner-clipping muons leave muon signals in two adjacent bars and are therefore excluded. However, this exclusion does not apply to the bars at the edges, as they lack a neighbouring bar, resulting in a higher number of events in these edge bars. The number of events shows a clear pattern in both data and simulations, with an increase of events closer to the WCD.

The closer half of the modules in simulations registered a greater number of events, approximately 50% more, and the farther half recorded a higher charge, approximately 22% more. Although these values were higher than the ones reported with data in Section 5.2.2, approximately 33% and 5% respectively, they follow the same tendency.

5.2.4. COMPARISON WITH THE EXPECTED RATE OF ATMOSPHERIC MUONS

We compared the rate expected for a single inclined muon in coincidence in both the UMD and the WCD, denoted as $R_{\text{inclined}}^{\text{UMD+WCD}}$, to the rate of vertical muons in the UMD after receiving a WCD trigger, dubbed as $R_{\text{vert}}^{\text{UMD+WCD}}$. These calculations

[1]It was taken into account that some stations in the field have their scintillators Ids reflected when compared to simulations.

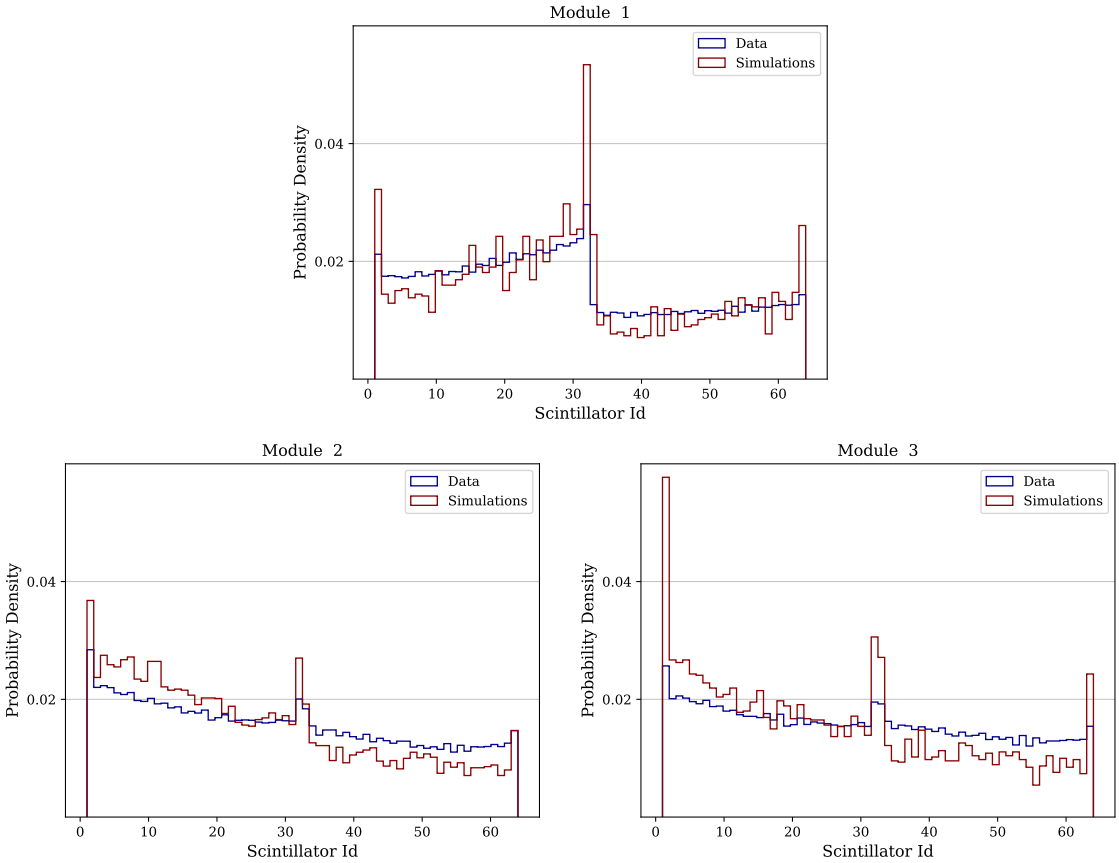

Figure 5.24: The number of events in simulations compared to data for module 1 (top), module 2 (bottom left) and module 3 (bottom right).

were performed using the differential energy flux of atmospheric muons derived from parametric models, which were based on the approximate calculation of the ground-level high-energy mu meson intensities presented in Ref. [82].[2]

The differential energy flux $j(E)$ is displayed in Fig. 5.25 for zenith angles $\theta = 20°$ and $\theta = 75°$. We performed curve fitting to the data, illustrated by the dashed lines, for each zenith angle. We then computed the numerical integral in energy $J = \int_{E_0}^{E_{\max}} j(E)\,\mathrm{d}E$ from the fit where the boundaries were $E_{\max} = 10^3\,\mathrm{GeV}$, $E_0 = 1\,\mathrm{GeV}$ for vertical muons and $E_0 = 3\,\mathrm{GeV}$ for muons in coincidence (see Fig. 5.22). We calculated the integration in the differential solid angle

$$\tilde{J} = \frac{\mathrm{d}N}{\mathrm{d}t\,\mathrm{d}A} = \int J\,\mathrm{d}\Omega \approx J(\hat{\theta}) \int_{\theta_\mathrm{i}}^{\theta_\mathrm{f}} \sin\theta\,\mathrm{d}\theta \int \mathrm{d}\phi. \tag{5.3}$$

For vertical muons, the azimuth angle $\Delta\phi = 2\pi$ was used. For muons in coincidence, we computed the differential solid angle subtended between the WCD and module 3 since the differential flux of $\theta = 75°$ was considered (see

[2] Acknowledgments to Diego Melo for providing this data.

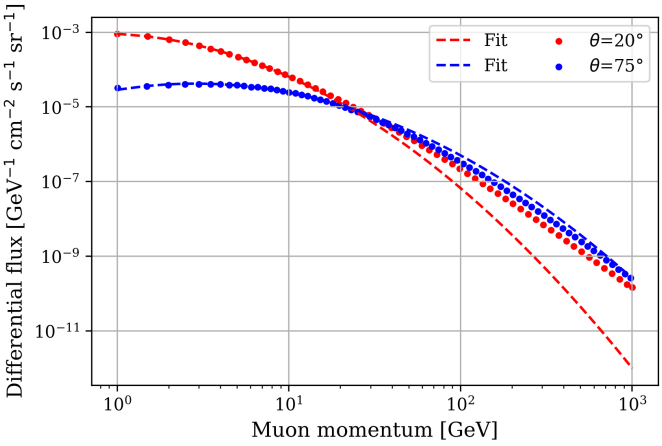

Figure 5.25: Differential energy flux for zenith angles $\theta = 20°$ and $\theta = 75°$.

Fig. 5.21). The azimuth angle subtended was roughly estimated with $\Delta\phi \approx 0.35$. Given than $J(\hat{\theta} = 20°)$ and $J(\hat{\theta} = 75°)$ were employed, we considered $\theta_i = 0$ and $\theta_f = 40°$ for vertical muons and $\theta_i = 67°$ and $\theta_f = 83°$ for muons in coincidence. Since the flux $\tilde{J}$ does not depend on x or y, we obtained $\tilde{\tilde{J}} = dN/dt = \int \tilde{J}\, dA = \tilde{J}\, A$, where A is the 10 m^2 area of a module.

The rate obtained for vertical muons was $r_{\text{vert}}^{\text{UMD}} \approx 435$ Hz, while for muons in coincidence was $r_{\text{inclined}}^{\text{UMD+WCD}} \approx 6$ Hz. However, different considerations have to be taken into account for these rates. To estimate the rate of vertical muons that could arrive to the UMD when the WCD was triggered, the following rate was calculated

$$R_{\text{vert}}^{\text{UMD+WCD}} = r_{\text{vert}}^{\text{UMD}}\, r_{\text{T1}}^{\text{WCD}}\, \tau, \tag{5.4}$$

where $r_{\text{T1}}^{\text{WCD}} = 100$ Hz [52] (see Section 3.1) and $\tau = 200$ ns (the integration window in the UMD after the trigger is received). To compute the detection rate, the efficiency of fulfilling the muon selection criteria in the binary trace of the UMD must be taken into account. This efficiency in simulations, reported in Section 5.1.2, was approximately ~90%. The final rate obtained was $R_{\text{vert}}^{\text{UMD+WCD}} = 0.008$ Hz.

For the single inclined muon in coincidence, the detection rate is also dependent on the efficiency of the WCD, the probability of reaching the UMD and the muon condition requested in the binary trace of the UMD. In simulations, the efficiency was ~1% (see Section 5.2.3). Based on rough estimates, the rate for single inclined muons in coincidence was calculated to be $R_{\text{inclined}}^{\text{UMD+WCD}} = 0.06$ Hz.

The values reported in Section 3.2 for data indicate rates of ~0.08 Hz for signal events and ~0.008 Hz for noise events. However, our calculations show that the vertical muons reaching the UMD after a T1 trigger from the WCD ($R_{\text{vert}}^{\text{UMD+WCD}} = 0.008$ Hz) are insufficient to account for the observed data rate of approximately 0.08 Hz. The rough estimate of $R_{\text{inclined}}^{\text{UMD+WCD}} = 0.06$ Hz is in agreement with the

rate reported for data. It is likely that a combination of various contributions is arriving at the UMD, with a clear bias towards more inclined and energetic muons, influenced by the trigger dependence with the WCD, the geometry of the detectors and the muon selection criteria.

5.2.5. COMPARISON WITH T3 SHOWER EVENTS

The number of muons reconstructed with the ADC mode can be estimated by the following equation

$$N_{\mu}^{\mathrm{ADC}} = \frac{q_{\mathrm{meas}} \cos\theta}{\langle q_{1\mu}(\theta{=}0)\rangle}, \tag{5.5}$$

where the measured charge is multiplied by the geometry dependence on zenith angle and then divided by the mean charge deposited by a vertical muon. Since in the field the zenith angle of each muon impinging on the scintillator θ_{μ} can not be measured, the approximation $\langle\theta_{\mu}\rangle \approx \theta_{\mathrm{shower}}$ is used. We define the vertical equivalent charge q_{vert} as the charge equivalent deposited by vertical muons, described by $q_{\mathrm{vert}} = q_{\mathrm{meas}} \cos\theta_{\mathrm{shower}}$.

In this study, we determined the mean charge deposited by a vertical muon $\langle q_{1\mu}(\theta{=}0)\rangle$ based on T3 shower events recorded in the year 2021. Two example are displayed in Fig. 5.26 for module 1 of station Comenius (top panels) and for module 3 of station Norberto W. (bottom panels). The LG and HG channels are represented in red and green colours, respectively. A comparison between the ADC mode reconstruction (y-axis) and the binary mode reconstruction (x-axis) is illustrated. Given that the dataset from T3 shower events contain showers of different zenith angles, the definition of the vertical equivalent charge q_{vert} is employed. For the binary mode reconstruction, corrections for pile-up and corner-clipping were applied, as detailed in Refs. [64, 68].

To estimate the charge deposited by a single vertical muon in a single module, we performed a linear fit to the mean of the distributions plotted in the x-axis. The binary mode is employed up to 10 reconstructed muons per $10\,\mathrm{m}^2$ given that the bias of the binary mode is minimal in that range and there is a significantly large statistical dataset for each module to compute the means of the distributions on the x-axis.

The mean charges obtained for all the modules are displayed in Fig. 5.27. The modules of $10\,\mathrm{m}^2$ are shown in the top panels, whereas the modules of $5\,\mathrm{m}^2$ are presented in the bottom panels. The LG and HG channels are represented in the left and right panels, respectively. The average of each histogram is displayed as a dark dashed line. The mean charge for the LG channel was $\langle q\rangle = 216 \pm 10$ in a.u. for the modules of $10\,\mathrm{m}^2$ and $\langle q\rangle = 209 \pm 3$ in a.u. for the modules of $5\,\mathrm{m}^2$. These values computed from T3 shower events demonstrate stronger accord with laboratory measurements [80] than the values from the ADCT1 files reported

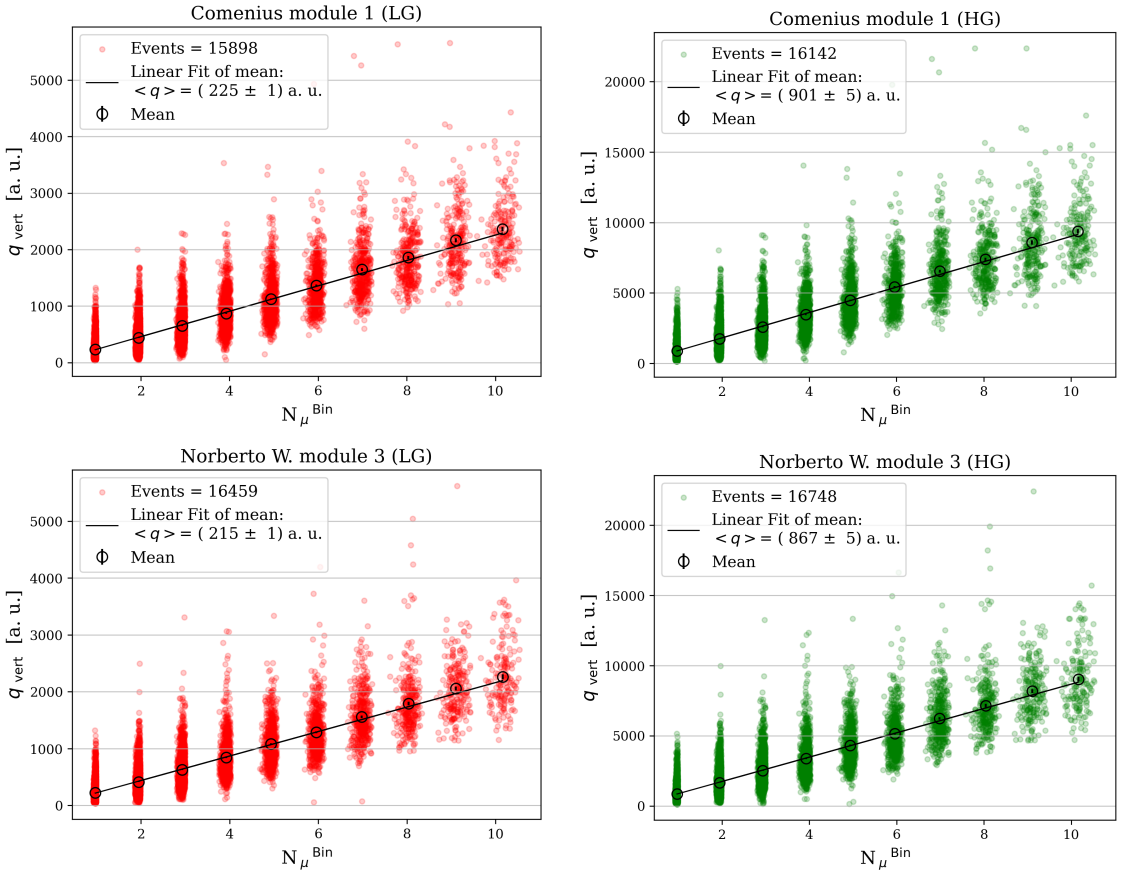

Figure 5.26: Examples of the procedure to estimate the charge deposited by a single vertical muon employing T3 shower events. Module 1 of station Comenius is displayed in the top panels and module 3 of station Norberto W. is presented in the bottom panels.

in Section 3.3. The mean charge reported in Ref. [80] for the LG channel was $\langle q \rangle = 235 \pm 2$ in a.u., employing a muon telescope set at 2.5 m from the SiPM to select vertical muons.

Finally, we present in Fig. 5.28 the bias of the number of reconstructed muons using the LG channel of the ADC mode (N_μ^{ADC}) with respect to the number of reconstructed muons using the binary mode (N_μ^{Bin}), for all the modules used in the study. The bias, displayed as a function of N_μ^{Bin}, was computed up to $N_\mu^{\mathrm{Bin}} = 100$ given that the binary mode reconstruction is optimal in that regime and can thus serve as a reliable estimator. The study, conducted for the year 2021, employed two different methods to estimate the charge deposited by a single muon: the ADCT1 files (orange dots) and the T3 shower events (blue dots). The bias observed in the reconstruction conducted with the ADCT1 files is evidently worse. At lower densities, the bias in the reconstruction using the ADC mode can reach up to 45%. From the comparison with the binary mode it can be concluded that the mean charges derived from the ADCT1 files are unreliable estimators for

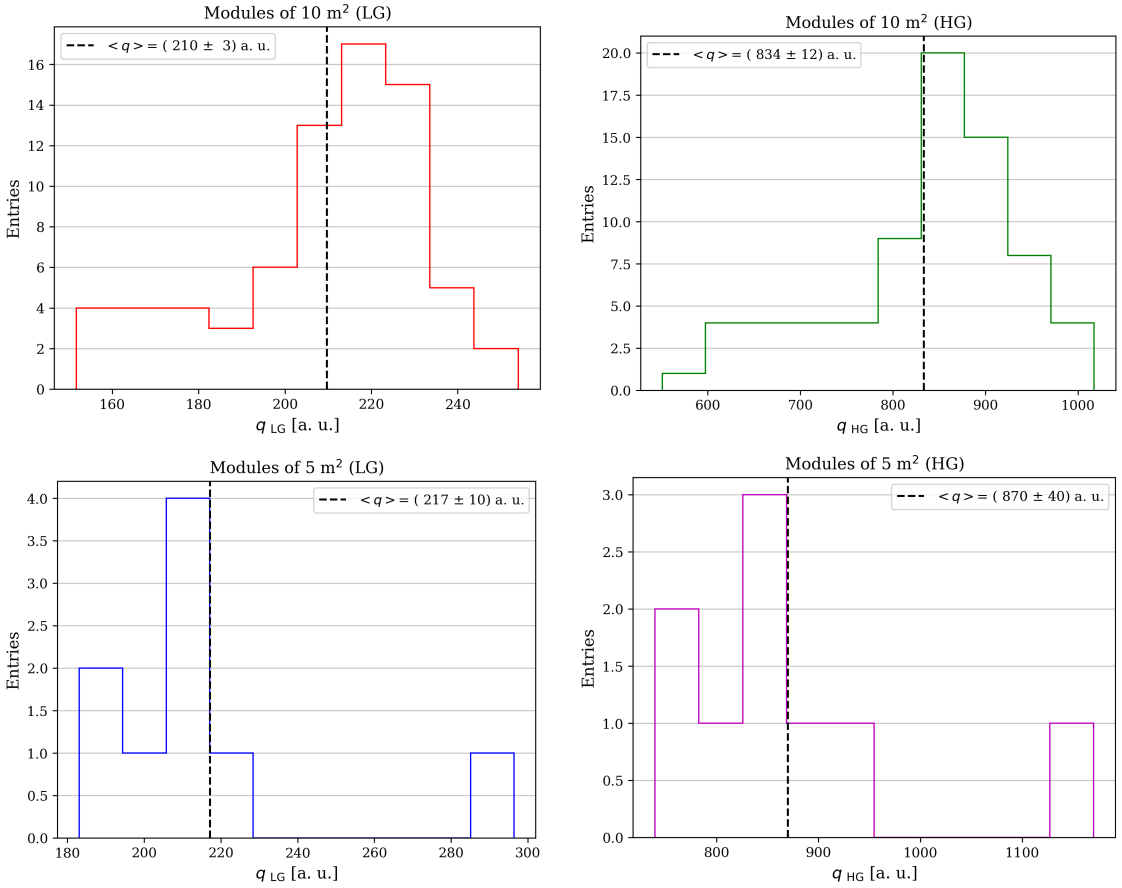

Figure 5.27: Histograms illustrating the mean charges obtained for all the modules of 10 m^2 (top panels) and 5 m^2 (bottom panels). The average is represented as a dark dashed line.

determining the number of reconstructed muons with the ADC mode, as they do not accurately represent the charge deposited by individual vertical muons. Both methods report an increasing bias of approximately 10% within the considered N_μ range. This finding is related to the increase of the energy deposited by knock-on electrons. A comprehensive analysis of this phenomenon will be conducted in Chapter 6 and Chapter 7.

5.3. SUMMARY

This chapter provides a comprehensive analysis of the online calibration strategy designed to estimate the charge deposited by individual atmospheric muons.

We examined the calibration of the ADC mode through single muon simulations. By injecting single muons into the UMD, we studied the number of "1"s in the binary traces, the charge in the ADC mode, and their dependencies on the energy and zenith angle of the muon. We demonstrated that the geometry dependence on the zenith angle is more pronounced in the ADC mode than in

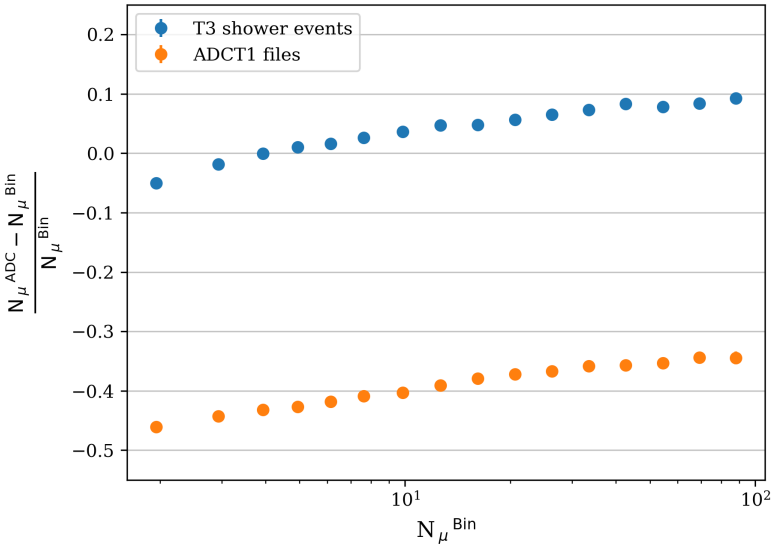

Figure 5.28: Bias in the muon reconstruction between the binary mode and the ADC mode. Two methods were used to compute the charge deposited by a single muon in the LG channel of the ADC mode: the ADCT1 files, displayed in orange, and the T3 shower events, shown in blue.

the binary mode, as the ADC mode is more sensitive to the area under the signal (related to the energy deposited), while the binary mode is more sensitive to the signal width. Additionally, we showed that the ADC mode is also dependent on the energy of the muon, with more energetic muons producing more electrons/positrons in the soil, thereby generating greater charge.

We conducted simulations based on the distributions of ominidirectional atmospheric muons to compare with the online calibration of the ADC mode using T1 events in the field. Furthermore, we performed simulations where knock-on electrons/positrons were deliberately excluded and showed they align well with the UMD laboratory data [72], where no electrons/positrons were expected since the setup was not buried. Finally, we performed simulations of single vertical muons and compared them to the results of ominidirectional atmospheric muons. The mean charge deposited by vertical muons, as proposed in Ref. [63], will be used in Section 6.1 to study the bias in muon reconstruction of the ADC mode.

The T1 trigger requested from the associated WCD in the calibration procedure was found to generate asymmetries between the halves of modules. The farther half of the modules with respect to the WCD recorded a higher charge, approximately 5% more, while the closer half registered a greater number of events, approximately 33% more. Moreover, more events are evidently observed in the scintillator strips located at the edges of each module. This constitutes an evident footprint of inclined muons. Consequently, the calibration procedure introduces a bias towards inclined muons with energies higher than ~2.5 GeV.

We have presented a summary of studies performed with (i) laboratory measurements of vertical muons, (ii) single muon simulations of omnidirectional atmospheric muons, and (iii) shower events. We have shown that the mean charge of the ADC trace and the number of "1" in the binary traces from the calibration procedure do not align with these results.

Simulations of muons detected in coincidence by the WCD and the UMD were performed and compared to the data. We showed that these muons in coincidence could explain the patterns observed in data for the number of events, although the mean charges obtained in simulations were higher. Furthermore, we showed from rough estimations of the differential energy flux that the rate expected of inclined muons in coincidence is an order of magnitude higher than the rate of vertical muons that arrived to the UMD after receiving a WCD trigger. The data could be explained by a combination of various muon distributions, with a clear bias towards more inclined and energetic muons, influenced by the trigger dependence with the WCD, the geometry of the detectors and the muon selection criteria.

We conducted an analysis with T3 shower events recorded in the year 2021 and presented a method to calibrate the ADC mode from the comparison with the binary mode at low densities. We compared the bias in the muon reconstruction with the binary and ADC modes in a regime where the binary mode can be a reliable estimator. We showed that the bias can reach up to 45% when reconstructing up to 100 muons with the online calibration, in contrast to 10% with the T3 shower events. However, we reported that both methods exhibit a bias that is not flat but rather increases by approximately 10% within this range. Chapter 6 and Chapter 7 will provide a comprehensive analysis of this phenomenon.

We conclude than the mean charges obtained in the ADC online calibration are not good estimators of the charge deposited by vertical muons, and therefore, should not be used to estimate the number of muons in the ADC reconstruction. Nevertheless, the calibration files serve as a useful tool for monitoring the performance of the modules, as shown in Section 3.4.

Chapter VI

The effect of knock-on electrons in the reconstruction of the ADC mode

To interpret the readings of underground muon scintillation detectors that are used for the study of extensive air showers, it is necessary to consider the transmission of different particles that reach the observation level through the ground and to take into account showers of secondary particles in the ground that also induce signals in underground muon detectors [83].

In an inelastic collision with atoms, an energetic charged particle transfers energy to the electrons bound in orbitals. When the energy transferred to the electron is higher than its ionisation energy, the electron is ejected from its atomic orbital. The term knock-on electron is utilised for electrons that are ejected from their orbit and additionally have sufficient kinetic energy to travel a significant distance from its point of ejection [84]. Collectively, these electrons are defined as δ-rays when they have sufficient energy to produce secondary interactions and ionise further atoms in areas distant from the primary particle beam. The production of knock-on electrons by underground cosmic-ray muons has been documented in several studies, for example in Refs. [85, 86]. The higher the energy of the muon at the ground, the greater is the energy transferred to the electrons, enabling them to traverse longer distances and enhancing their chances of reaching the underground scintillators. In certain situations knock-on electrons may prevent the accurate determination of the number of muons that hit an underground detector.

The different bias sources in the binary mode have been documented in various studies, as can be seen in Ref. [64, 68]. The effect produced by knock-on electrons is among one of the bias sources since, if they deposit enough energy to activate adjacent scintillation bars to the one impinged by the incident muon, they can produce an overcounting of the number of muons reaching the detector. This

counting bias is mitigated by the so-called 'corner-clipping correction' [68]. The potential influence of the energy deposited by knock-on electrons on the ADC detection mode remains unexplored.

In this chapter, we present an analysis of the energy deposited by the different types of particles reaching the UMD and its impact on muon reconstruction. In Section 6.1 we show that by calibrating the ADC mode with single vertical muon charges, a bias in the muon reconstruction is introduced. Section 6.2 and Section 6.3 aim to explore the source of this bias, studying in Section 6.2 the zenith angle of muons impinging on the UMD and in Section 6.3 the energy deposited in the scintillators.

6.1. Bias in muon reconstruction

Monte-Carlo simulations of proton showers were performed (simulated with the hadronic interaction model EPOS-LHC) at energies of $10^{17.5}$, 10^{18}, and $10^{18.5}$ eV and zenith angles of 0, 12, 22, 32, and 38 degrees. The secondary particles of the shower that reached ground level were propagated through the soil and the energy deposition in the UMD was calculated using Geant4 [87]. The response of the detector was simulated in Offline [73]. Saturated modules were excluded from the analysis.

The number of muons in the binary mode can be estimated considering the different bias sources caused by pile-up, corner clipping, knock-on electrons and the inhibition window selection [64]. In this study the pile-up and corner-clipping corrections, detailed in Ref. [64, 68], and the one-bin strategy from Ref. [64] were employed. The bias in muon reconstruction using the binary mode is presented in Fig. 6.1. The region where the absolute value of the bias is below 5% is represented with two horizontal dashed lines. The bias is within this range for muon densities up to 200 muons per 10 m^2 module and can reach up to 20% for densities of approximately 300 muons per 10 m^2 module. Beyond this point, i.e., for higher densities, the binary mode saturates.

In the ADC mode the number of muons can be estimated by

$$N_{\mu}^{\mathrm{ADC}} = \frac{q_{\mathrm{meas}} \cos\theta}{\langle q_{1\mu}(\theta{=}0)\rangle}, \tag{6.1}$$

where the measured charge is multiplied for the geometry dependence on zenith angle and divided by the mean charge deposited by a vertical muon. The approximation $\langle\theta_{\mu}\rangle \approx \theta_{\mathrm{shower}}$ is employed, considering that in the field it is not feasible to measure the zenith angle of each muon impinging on the scintillator. To calculate $\langle q_{1\mu}(\theta{=}0)\rangle$, we utilised the average of the charge histogram derived from simulations of individual vertical muons obtained in Section 5.1.2.

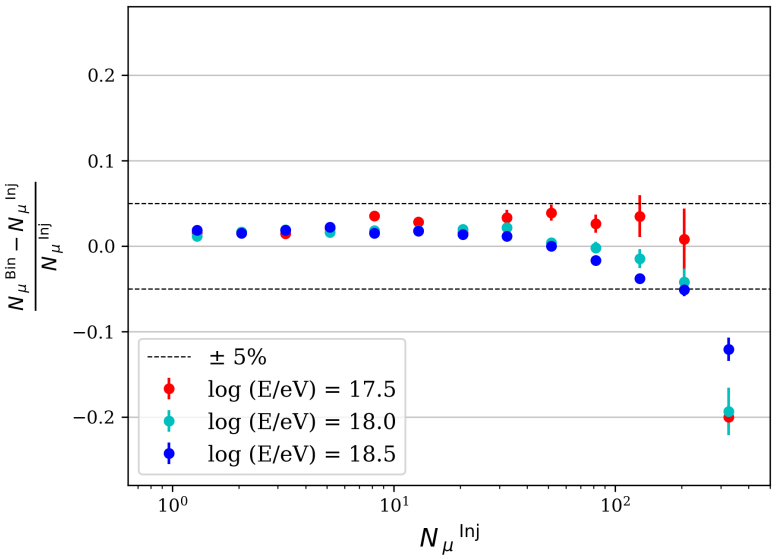

Figure 6.1: Bias obtained in the muon reconstruction with the binary mode as a function of the number of injected muons per 10 m^2 module.

In Fig. 6.2, the bias in muon reconstruction employing the LG channel of the ADC mode is displayed. Two horizontal dashed lines indicate the region where the absolute value of the bias is below 5%. The reconstruction bias for events with less than 5 muons in a 10 m^2 module is under 5%, suggesting that for such low muon densities Eq. (6.1) and the estimated value of the average charge deposited by individual vertical muons perform reasonably well. The figure reveals a concerning trend: reconstruction bias increases with muon density for all considered energy bins. This implies that the bias becomes more severe closer to the shower axis, reaching up to 20% for $10^{17.5}$ eV energy showers with muon densities of around 300 muons per 10 m^2 module. The subsequent sections aim to explore the source of this bias.

6.2. ZENITH ANGLE OF MUONS

The difference between the average zenith angle of the muons impinging on each module $\langle\theta_\mu\rangle$ and the zenith angle of the shower θ_{shower} is displayed in the left panels of Fig. 6.3 for the three energies bins of $10^{17.5}$ eV (top), 10^{18} eV (middle) and $10^{18.5}$ eV (bottom). In the right panels, the bias introduced by the approximation $\cos\langle\theta_\mu\rangle \approx \cos\theta_{\mathrm{shower}}$ in Eq. (6.1) is illustrated. Across all energy bins, the difference $\langle\theta_\mu\rangle - \theta_{\mathrm{shower}}$ is higher for vertical showers, reaching a maximum of approximately 14° and resulting thus in a maximum bias of up to 4% for low muon densities in the more energetic showers. This difference $\langle\theta_\mu\rangle - \theta_{\mathrm{shower}}$ decreases with the distance to the shower core, with biases dropping to less than

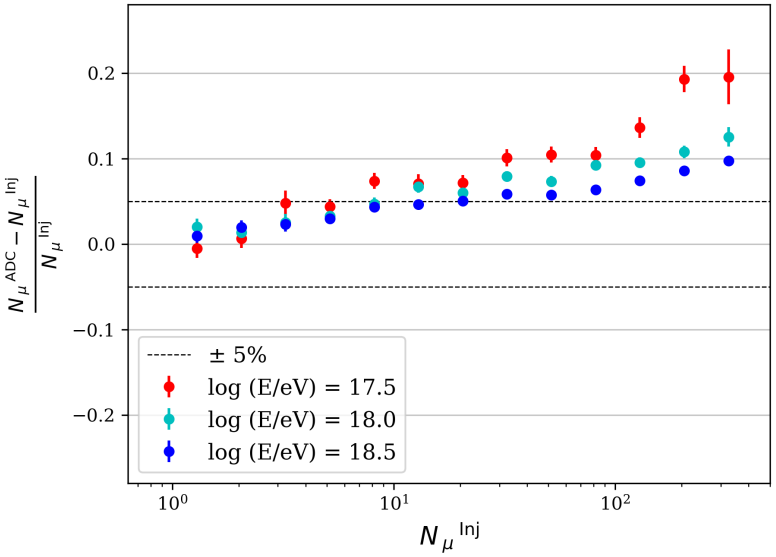

Figure 6.2: Bias obtained in the muon reconstruction with the ADC mode as a function of the number N_μ^{inj} of injected muons per 10 m^2 module.

2% for muon densities of about 300 muons per 10 m^2 module. Consequently, the bias observed in Fig. 6.2, reaching up to 20% for muon densities of about 30 μ/m^2, cannot be attributed to the approximation $\cos\langle\theta_\mu\rangle \approx \cos\theta_{shower}$ in Eq. (6.1).

6.3. Energy deposited in the UMD

In Fig. 6.4, the average energy of muons arriving to a UMD module, obtained as an average across all zenith angle bins, is depicted as a function of the number of injected muons per 10 m^2 module (left panel) and as a function of the distance to the shower core (right panel). As can be seen, more energetic muons correspond to higher muon densities, since the muon energy increases closer to the shower axis. For a fix muon density, the average energy of muons rises as the energy of the shower decreases. In the following analysis, we present how this increase in muon energy influences the energy deposited in the UMD scintillators.

The total energy deposited on the UMD scintillators per injected muon per vertical-path length was calculated as

$$\frac{E_{deposited}^{total}\cos\langle\theta_\mu\rangle}{N_\mu^{Inj}}, \tag{6.2}$$

where the term $\cos\langle\theta_\mu\rangle$ corrects for the fact that more inclined muons traverse a longer path within the scintillator than vertical muons, leading, of course, to higher energy deposition. Fig. 6.5 and Fig. 6.6 were constructed using the

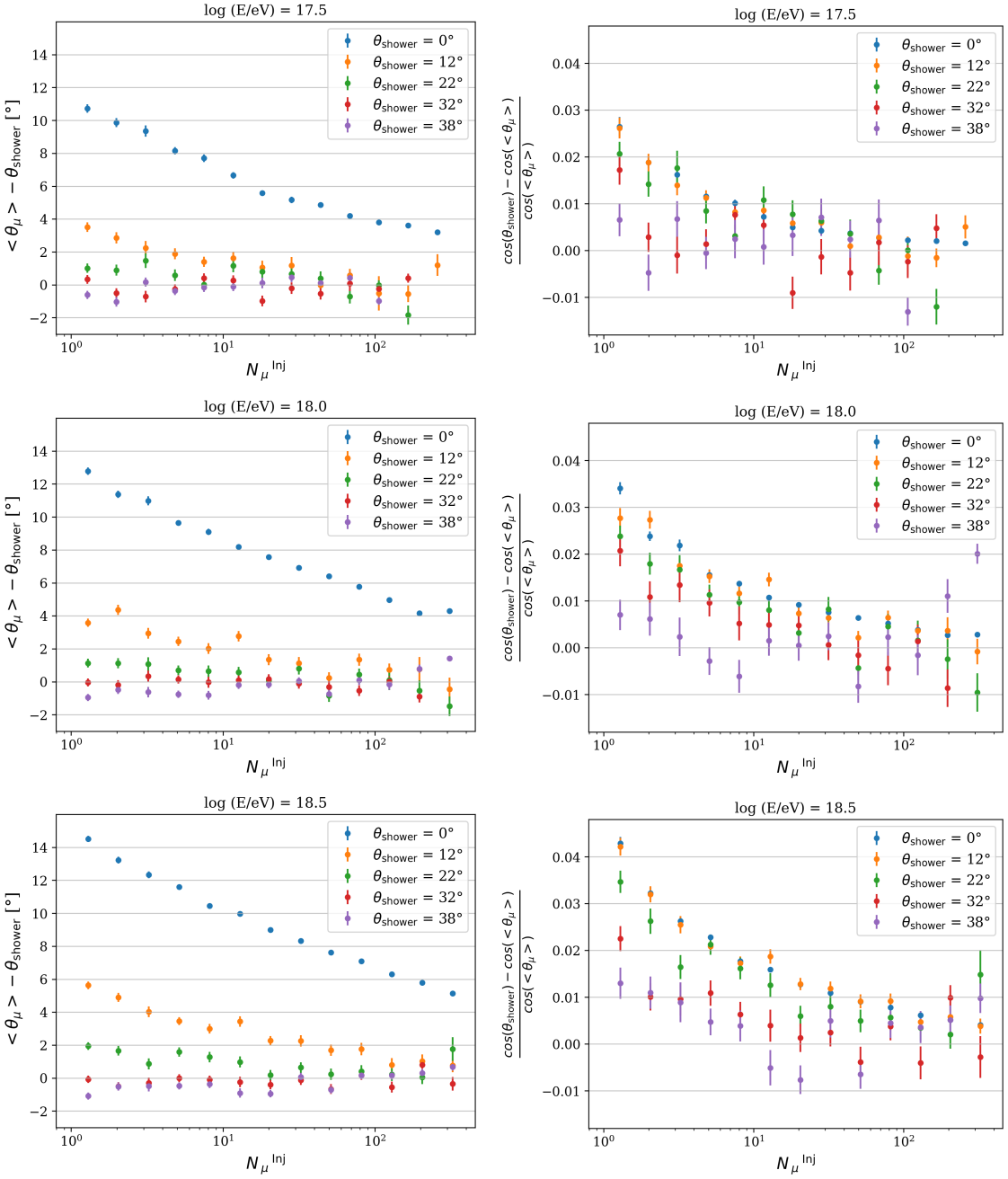

Figure 6.3: (left) Difference between the average zenith angle of muons and the zenith angle of the shower, $\langle\theta_\mu\rangle - \theta_{shower}$, as a function of the number N_μ^{inj} of injected muons per $10\,m^2$ module. (right) Bias introduced in the ADC reconstruction from the approximation $\cos\langle\theta_\mu\rangle \approx \cos\theta_{shower}$ as a function of the number of injected muons per $10\,m^2$ module.

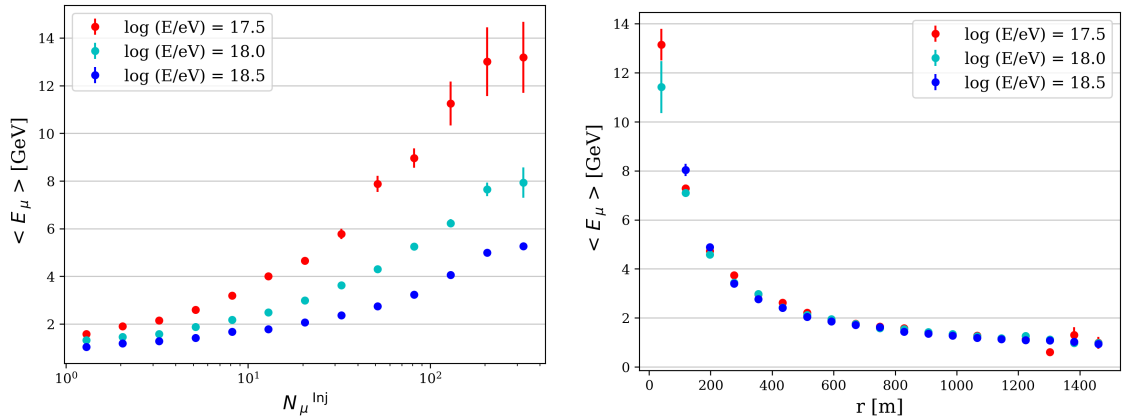

Figure 6.4: (left) Average energy $\langle E_\mu \rangle$ of muons arriving at the UMD as a function of the number N_μ^{inj} of injected muons per 10 m^2 module. (right) Average energy $\langle E_\mu \rangle$ of muons arriving at the UMD as a function of the distance r to the shower core.

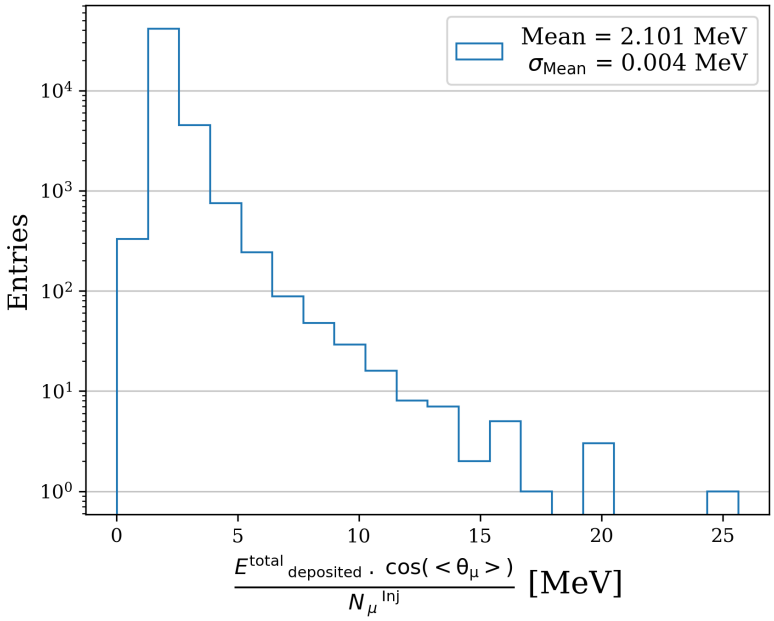

Figure 6.5: Histogram of the total energy deposited per muon per vertical-path length in the UMD scintillators.

complete dataset with the restriction of excluding saturated modules. In Fig. 6.5, an histogram of the total energy deposited per muon per vertical-path length is shown, resulting in an average deposited energy of (2.101 ± 0.004) MeV. The y-axis is displayed in log-scale to emphasise cases where events deposited up to 12 times the average energy.

The energy deposited per muon per vertical-path length is depicted in Fig. 6.6 as a function of the average muon energy. The energy deposited exclusively by muons is represented with blue circles, whereas the total energy deposited

is displayed with orange circles. A dashed line indicates the average energy deposited per muon per vertical-path length of 2.101 MeV. Firstly, it can be noted that when a muon arrives at the UMD with less than ~0.3 GeV, the average energy deposited per muon rises rapidly as muon energy decreases. For muon energies lower than this threshold, the behaviour as a minimum ionising particle ceases and, consequently, the muon energy-loss rate exhibits a rapid rise as expected in the low energy range of the Bethe regime [88], generating an average energy deposited of up to 10 MeV. Secondly, the average total energy deposited reaches a minimum of approximately 1.8 MeV for muon energies of around 0.3 GeV. Above this point, as the muon energy increases, the total energy deposited per muon per vertical-path length exhibits a rapid increase, reaching a ~35% larger value for a muon energy of 20 GeV. However, as can be seen, the energy deposited per muon per vertical-path length by exclusively muons remains nearly constant in the same energy range. Therefore, the observed rise in total energy deposition indicates the involvement of additional particles beyond muons (mainly knock-on electrons, as it will be shown below) in the contribution to the energy deposition in the scintillators.

In the ADC-mode detector, the measured total charge depends on the total energy deposited in the scintillators. Eq. (6.1) assumes that the total charge produced per muon per vertical-path length is constant. However, as shown in Fig. 6.6, the total energy deposited in the scintillators, and then also the total charge measured by the ADC-mode detector, depend on the muon energy. Therefore, if Eq. (6.1) is used, the reconstructed number of muons will present a bias, which will depend on the muon density (since the muon density depends on the muon energy as shown in Fig. 6.4). This explains the dependence of the bias on the muon density when Eq. (6.1) is used in the reconstruction, shown in Fig. 6.2.

Fig. 6.7 presents the average number of particles per module that were identified in the UMD scintillators as a function of the distance to the shower core for the three energy bins $10^{17.5}$ eV, 10^{18} eV and $10^{18.5}$ eV. The particles that are most likely to arrive are $\mu^{\pm}$, γ, $e^{\pm}$, $p^{\pm}$, $\nu_{\mu}^{\pm}$ and $\nu_{e}^{\pm}$. Any other particle observed is categorised as "Other". In the performed simulations, we observed "Other" particles such as π^{+} and K^{+} (along with their corresponding antiparticles), K_{L}^{0}, K_{S}^{0} and $\bar{\Lambda}$. The number of particles increases close to the shower core, as expected. A crucial question to address is whether arriving electrons at the UMD were knock-on electrons, produced in the soil due to the passage of muons, or punch-through electrons, belonging to the electromagnetic component of the air shower. Then, we compare these results with simulations where only muons were allowed to be injected into the ground.

In Fig. 6.8, the fraction of the energy deposited is displayed for the differ-

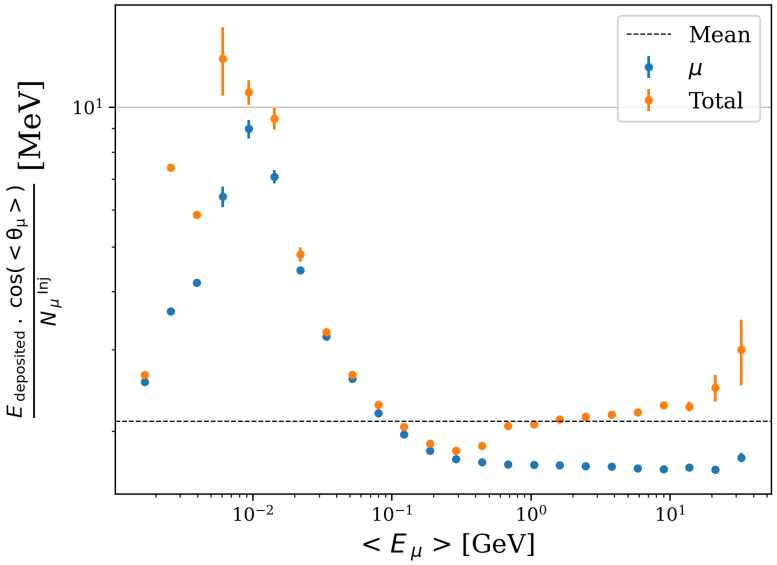

Figure 6.6: Energy deposited per muon per vertical-path length as a function of the average energy of muons arriving at the UMD. Two cases are displayed: the energy deposited by exclusively muons (blue) and the total energy deposited by all the particles (orange).

ent types of particles as a function of the number of injected muons per module. The simulations where all particles were injected into the ground and propagated through the soil are displayed with filled circles, while the simulations where only muons were injected are depicted with unfilled rectangles. This analysis was conducted including the saturated modules, with the aim of illustrating the impact of other particles beyond the scope of our muon measurements. A dashed vertical line indicates the maximum number of injected muons that the ADC mode measured without saturating. Once this limit is reached, the ADC saturates and no muon reconstruction can be performed. In our regime of muon measurements, several conclusions can be drawn. Firstly, upon comparing both sets of simulations, we observe that the energy-deposit fractions for muons (blue), electrons (violet), and photons (orange) are quite similar, therefore punch-through electrons and photons reaching the UMD are negligible and electrons and photons depositing energy into the UMD originated from the passage of muons through the soil. It is worth noting that, as expected, no protons or particles categorised as "Other" (e.g., π^+ and K^+) were found when only muons were injected and, consequently, these are punch-through particles arriving at the UMD which do not belong to the muon component of the shower. Secondly, upon analysing the energy deposited when all particles were injected (filled circles), we can deduce that the main contributions primarily come from muons and electrons, where electrons can contribute up to around 23% of the total energy deposited near the shower axis. Photons have a negligible contribution to the total energy deposit.

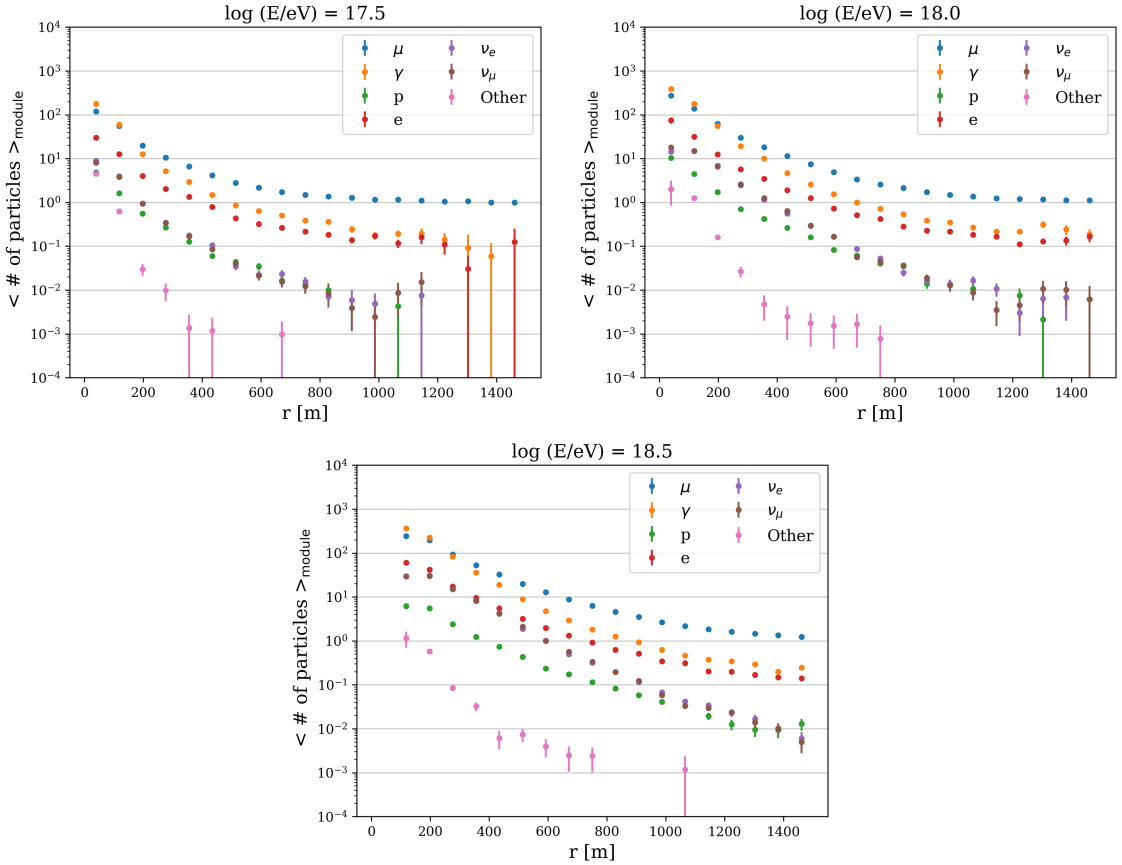

Figure 6.7: Average number of particles per 10 m^2 module that were identified in the UMD scintillators as a function of the distance to the shower core for the three energy bins of log(E/eV)=17.5, 18 and 18.5.

Excluding muons, the primary contribution comes from knock-on electrons, but protons and other particles also play a role, especially near the shower core where their contribution can reach up to 8% for $10^{17.5}$ eV showers. This contribution becomes less significant for higher energy showers within the range of our muon measurements.

Fig. 6.9 illustrates the relative contamination between electrons and muons as a function of the number of injected muons per 10 m^2 module. The ratio of particles is shown in blue, while the ratio of energy deposited is depicted in green. Filled circles represent simulations where all particles were injected on the ground and propagated through the soil, whereas unfilled rectangles depict simulations where only muons were injected. As in Fig. 6.8, a dashed vertical line denotes the maximum number of injected muons measured by the ADC mode before saturation. In our regime of muon measurements, the relative contamination observed in both studies is similar, suggesting that the contamination from punch-through electrons is negligible. Hence, we can conclude that there is a relative

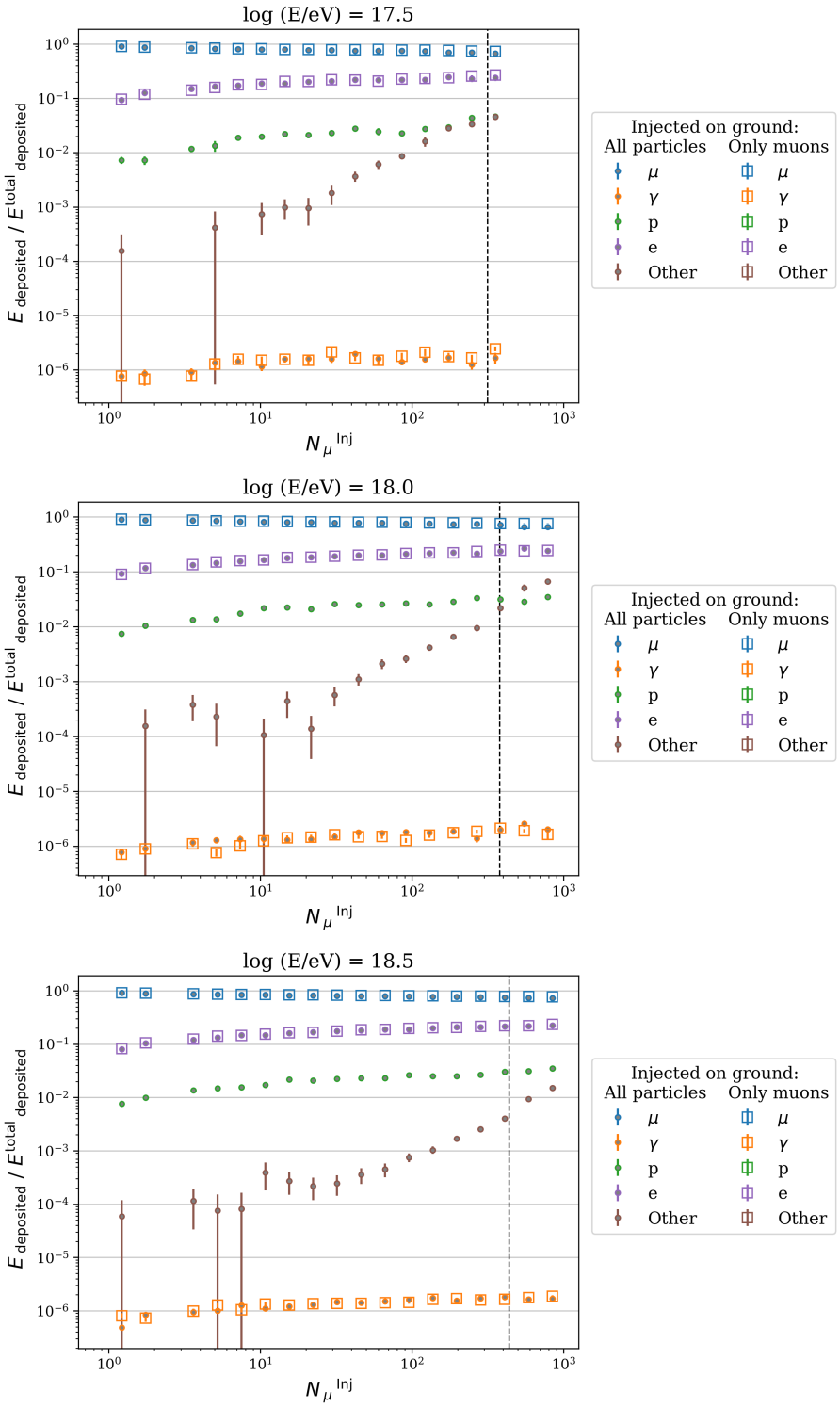

Figure 6.8: Fraction of energy deposited by the different types of particles as a function of the number of injected muons per 10 m^2 module, for the two sets of simulations: all particles injected into the ground (filled circles) and only muons (unfilled rectangles). A dashed line denotes a rough estimate of the ADC saturation.

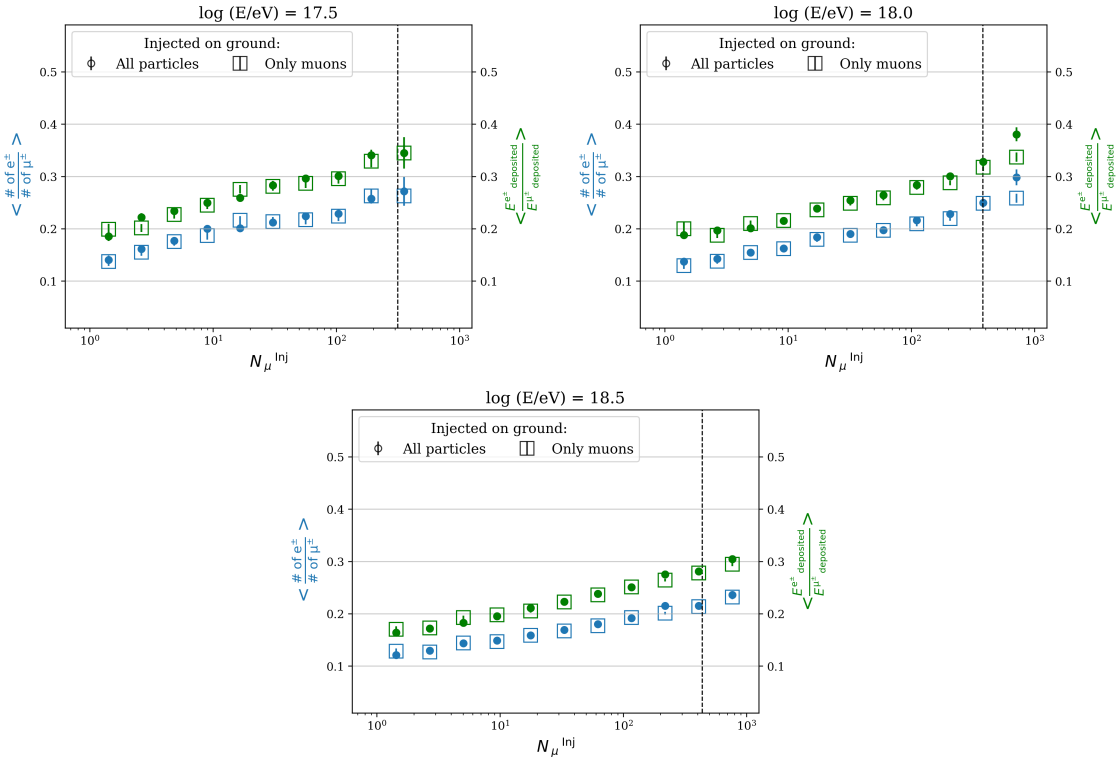

Figure 6.9: Relative contamination between electrons and muons as a function of the number of injected muons per 10 m^2 module. A rough estimate of the ADC saturation is represented with a dashed vertical line. Simulations where all particles were injected on ground and propagated through the soil are displayed by full circles, whereas the simulations where only muons were injected are depicted with unfilled rectangles.

contamination caused by knock-on electrons due to the passage of muons through the soil. The contamination by electrons increases near the shower core for all three energy bins. For instance, in low energy showers, for 300 injected muons there were on average 84 electrons depositing 34% of the energy deposited by muons.

In Fig. 6.10, we present the fraction of energy deposited by particles other than muons. In the left panel, this fraction is exhibited as a function of the number of injected muons per 10 m^2 module. We observe that the fraction of energy deposited by other particles rises with the muon densities, reaching up to 31% of the total energy for low energy showers. This effect is more pronounced for less energetic showers, since (as can be seen in Fig. 6.4) at the same muon density they tend to have more energetic muons. For each bin of the number of injected muons, we calculated the bias in the ADC reconstruction as a function of the fraction of energy deposited by particles excluding muons. In the right panel, we show that the bias in the ADC mode increases in accordance with the increase in energy deposited by other particles. To cope with this issue, a new calibration

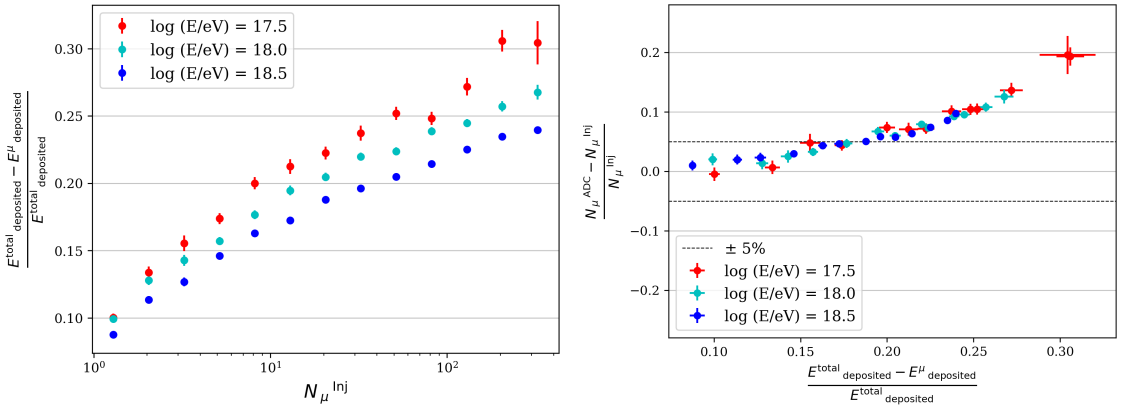

Figure 6.10: (left) Fraction of energy deposited by particles excluding muons as a function of the number N_{μ}^{inj} of injected muons per 10 m^2 module. (right) Bias in the muon reconstruction of the ADC mode as a function of the fraction of the energy deposited by particles other than muons.

method will be introduced in Chapter 7.

6.4. SUMMARY

Calibrating the ADC-mode detector with the average charge from single vertical muons and using Eq. (6.1) for reconstruction introduce a bias in the reconstructed muon density. This bias depends on the muon density and can reach up to 20% for densities of ~30 muons/m^2 in proton showers of $10^{17.5}$ eV. The bias cannot be attributed to the approximation of the zenith angle of the muons to that of the shower axis. The bias increases with the muon density due to the fact that as the muon densities increases by getting closer to the shower axis, the muon energies also increase, and muons of higher energies produce larger total energy depositions per muon per vertical-path length. The rise in the total energy deposit per muon per vertical-path length with increasing muon energy is primarily a consequence of the observed growth of the energy deposition from other particles alongside the muon. At a fixed muon density the bias is more notorious for lower energy showers, since muons reaching the detector are more energetic.

We study the energy deposition of the particles alongside the muons, and particularly whether the arriving electrons at the UMD were primarily knock-on or punch-through electrons, by comparing simulations where all particles were injected on ground with simulations where only muons were injected on ground and propagated through the soil. Within the range where the ADC-mode detector is not saturated, besides muons, knock-on electrons dominate the energy deposition, although protons and other particles like π^+ and K^+ can also contribute slightly. The largest contribution of these particles to the energy

deposition was observed for the lowest energy showers of $10^{17.5}$ eV and at the highest muon density of ~30 μ/m^2, where 23% of the total energy is deposited by knock-on electrons and 8% by protons and other particles, mainly π^+ and K^+.

Chapter VII

Improved calibration of the ADC mode

In Chapter 6, it was shown that the main source of bias in the ADC mode is due to the energy deposited in the UMD scintillators by knock-on electrons produced from the interaction of muons with the surrounding soil of the UMD module. In this chapter, we propose a method to calibrate the low-gain channel of the ADC mode to reduce the effect of contamination by knock-on electrons.

In Ref. [63], it was proposed an ADC mode based method to estimate the number of muons impinging a $10\,\mathrm{m}^2$ UMD module, N_μ^{ADC}, by means of

$$N_\mu^{\mathrm{ADC}} = \frac{q_{\mathrm{meas}}\cos(\theta_{\mathrm{EAS}})}{\langle q_{1\mu}\rangle}. \tag{7.1}$$

In this expression, the quantity in the numerator, $q_{\mathrm{vert}} = q_{\mathrm{meas}}\cos(\theta_{\mathrm{EAS}})$, is the total charge per vertical path-length in the event, with q_{meas} the measured charge in a $10\,\mathrm{m}^2$ UMD module and θ_{EAS} the zenith angle of the EAS. The quantity in the denominator, $\langle q_{1\mu}\rangle$, is the mean charge deposited by vertical muons. In Ref. [63], $\langle q_{1\mu}\rangle$ was obtained by a calibration procedure using single muons and it was taken into account as an independent quantity on the kinetic energy of the impinging muons. However, as we have shown in Chapter 6, $q_{1\mu}$ has a significant direct dependence on the kinetic energy of the impinging muon due to the energy deposition on the detector by knock-on electrons, which are more likely to be produced and are more energetic as the kinetic energy of the muon increases. Since in an EAS the average kinetic energy of the muons and the muon density are correlated, considering $q_{1\mu}$ as an independent quantity on the kinetic muon energy (or the muon density), as done in Ref. [63], introduces a bias in the reconstructed muon density that can reach up to 20% for densities of ~30 muons/m^2.

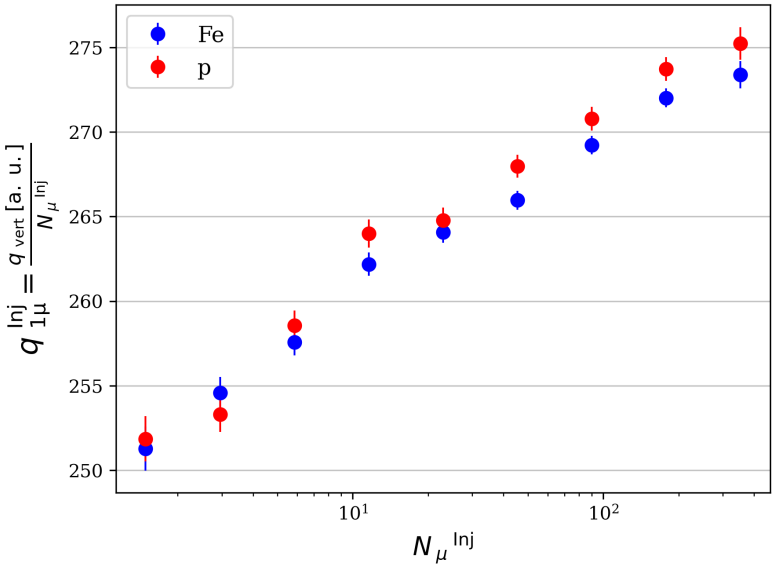

Figure 7.1: Charge deposited per muon as a function of the number of injected muons per $10\,\mathrm{m}^2$ module.

In this chapter, we propose a method to reduce the bias in N_μ^{ADC}, where the mean charge deposited per muon per vertical path-length, required in the denominator of Eq. (7.1), is no longer a constant but a parametrised value. This strategy is developed in Section 7.1 with simulations and applied to data in Section 7.2.

7.1. Calibration method

We performed simulations in Offline [73] of 1800 proton EASs and 1800 iron EASs of energy $1{\times}10^{17.5}\,\mathrm{eV}$, $1{\times}10^{18}\,\mathrm{eV}$ and $1{\times}10^{18.5}\,\mathrm{eV}$ and zenith angle $\theta = [0, 12, 22, 32, 38]°$. The showers were simulated with the hadronic interaction model EPOS-LHC. Saturated modules were excluded from the analysis.

From these simulations, $q_{1\mu}$ can be obtained by means of

$$q_{1\mu} = \frac{q_{\mathrm{vert}}}{N_\mu} \tag{7.2}$$

for each $10\,\mathrm{m}^2$ module of the UMD. In Fig. 7.1, $q_{1\mu}^{\mathrm{Inj}}$ as obtained by using in the denominator of Eq. (7.2) the actual (monte-carlo) number of muons injected in a $10\,\mathrm{m}^2$ module (N_μ^{Inj}), is illustrated as a function of N_μ^{Inj}, for the two different primaries. It is important to note that, as explained above, the charge deposited per muon is not constant, but a function that increases with the muon densities due to mainly the effect of the knock-on electrons.

The proposed calibration method involves estimating $q_{1\mu}$ based on a measur-

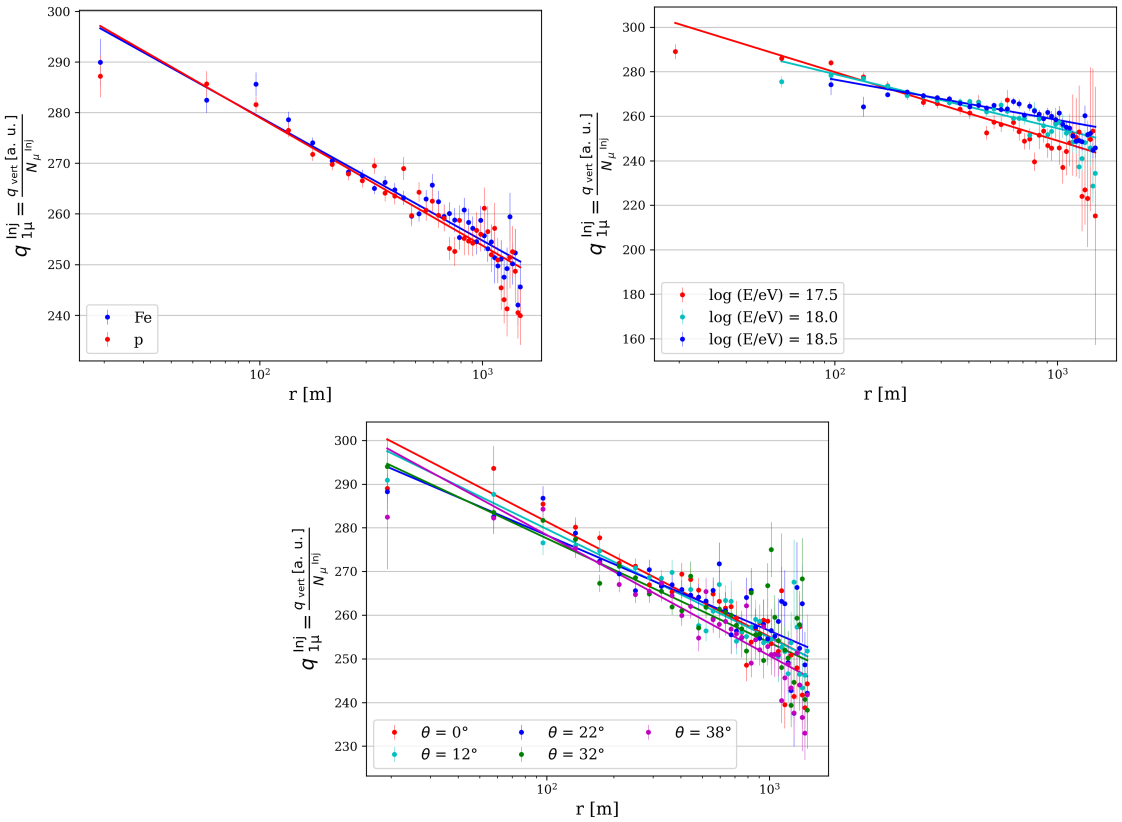

Figure 7.2: Charge deposited per muon per vertical path-length in a 10 m^2 module as a function of the distance to the shower axis, discriminating by primary (a) mass, (b) energy, and (c) zenith angle.

able quantity (m) that correlates with muon energy and is accessible even in high muon-density regions, particularly near the EAS axis where the ADC mode is intended to be used. The strategy is to obtain $q_{1\mu}$ by using Eq. (7.2) with: (1) q_{meas} from the ADC mode of the UMD, (2) $\cos(\theta_{\text{EAS}})$ from the geometry reconstruction of the surface detector (SD), and (3) the reconstructed number of muons from the binary mode of the UMD, N_μ^{Bin}, in the low muon-density regime ($N_\mu^{\text{Bin}} < 70$) where the binary mode is not saturated and has a negligible bias (see Chapter 6). Within this low-density regime, we will establish a parametrisation between $q_{1\mu}$ and the chosen observable m. This relationship will then make possible to estimate by extrapolation $q_{1\mu}$ at higher muon densities, where the binary mode saturates, but the ADC mode continues working in the linear range and m is still available. Then, the number of muons N_μ^{ADC} in a high-muon density event can be reconstructed by using Eq. (7.2). We propose using the distance to the shower axis as m, since it is related to the particle density.

The charge deposited per muon $q_{1\mu}^{\text{Inj}}$ is shown in Fig. 7.2 as a function of the distance to the shower axis r[m] for (a) the two different primaries, (b) three different

energy bins and (c) five different zenith angle bins. As can be seen, $q_{1\mu}$ exhibits a logarithmic dependence on r[m] and, therefore, the chosen parametrisation was

$$q_{1\mu}(r) = A \log_{10}(r/\mathrm{m}) + B \tag{7.3}$$

with A and B fitting parameters. The solid lines represent the obtained fits, which performed very similar, showing that the proposed method has no significant dependence on the mass, the energy (less than 4%) and the incidence zenith angle of the primary (less than 2%).

The reconstructed charge per muon per vertical path-length, $q_{1\mu}^{\mathrm{Rec}}$, obtained by using in the denominator of Eq. (7.2) the reconstructed number of muons from the simulations of the binary mode of the UMD (N_{μ}^{Bin}), is displayed as a function of r[m] in Fig. 7.3, for the low muon-density regime where the binary mode works properly, and without discriminating by primary mass, energy and zenith angle. A cut was imposed on the number of muons measured by a 10 m^2 module of the UMD of ~70 muons, as the binary mode reconstruction is optimal within this range (see Section 6.1). Additionally, a minimum distance of r=100 m to the shower core was required to avoid poor distance reconstruction from stations that are too close to the core and therefore cannot serve as reliable estimators, as shown in Section 8.1. This quality cut proved particularly useful for data reconstruction. The solid line in Fig. 7.3 represents the global parametrisation obtained by fitting the expression in Eq. (7.3) to the whole simulated data set, with parameters $A = (-27.43 \pm 1.14)$ a.u. and $B = (332.61 \pm 3.12)$ a.u.. This global parametrisation was used to obtain N_{μ}^{ADC}, the reconstructed number of muons by the ADC mode of the UMD, in both the low and high muon-density regimes, by means of Eq. (7.1).

The resulting reconstruction bias using the strategy developed in this work is shown by filled circles in Fig. 7.4 for different (a) masses, (b) energies, and (c) zenith angles. On the other hand, the bias calculated employing the strategy used in Ref. [63], i.e., estimating the number of muons with Eq. (7.1) and calibrating the ADC mode detector with the average charge deposited by single vertical muons, is represented by unfilled circles. As can be seen, the calibration method proposed in this work effectively reduces the bias in calculating the number of muons across all cases examined. When discriminating by primary, energy and zenith angle the bias is consistently less than 5% and, as expected, it does not show a significant dependence on mass, energy, zenith angle, and the number of injected muons.

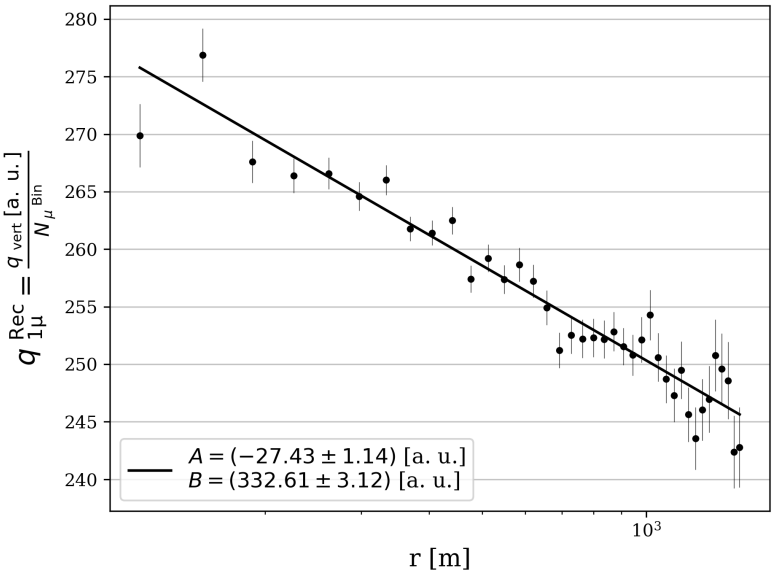

Figure 7.3: Charge deposited per muon using the reconstructed number of muons in a 10 m^2 module of the binary mode as a function of the distance to the shower axis.

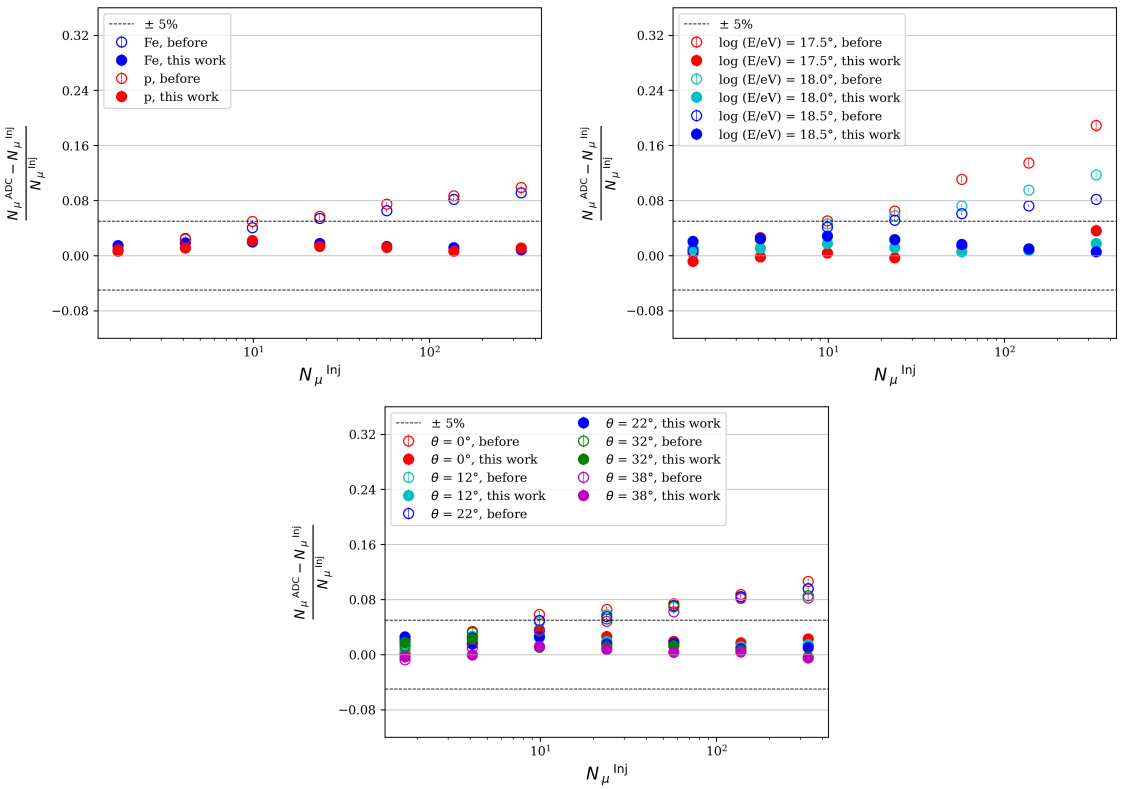

Figure 7.4: Bias in muon reconstruction of the ADC mode. The filled dots were obtained with the calibration method presented in this work, whereas for the unfilled dots the previous method was used.

7.2. Applying the calibration method to data

7.2.1. Phase I

The calibration was performed in 76 modules of $10\,\mathrm{m}^2$ and 7 modules of $5\,\mathrm{m}^2$. The data utilised correspond to Phase I, i.e. acquired using the former electronics (UB), spanning the years 2019 through 2022 (see Section 2.1). Each module was calibrated individually. Since the installation of the upgraded electronics (UUB) started at the end of 2020, events with stations containing UUB were rejected, utilising the `RejectUUBStations` flag in the `SdEventSelector` module in Offline. Given that the UMD modules deployed in 2022 were installed at the end of the year, they were not in acquisition in this data set. Therefore, all the modules analysed to compute the calibration had at least one year of data. The following stations were excluded for particular issues: 1776 module 103, 1622 module 103 and 1764 module 106. As is customary for the UMD, the EASs reconstructed were required to have energies larger than $1{\times}10^{17.3}$ eV and zenith angles smaller than 45°. A quality cut was implemented to exclude events from the analysis in which the ADC mode reconstructed null or negative charge values (see Section 4.2.2).

In Fig. 7.5, four examples of the calibration method are shown for station 1760 module 102, station 1761 module 103, station 1765 module 103 and station 1773 module 101, using the reconstructed binary mode as explained above. The charge deposited per muon increases due to the energy deposition of the knock-on electrons, reproducing the effect observed in simulations.

In Fig. 7.6, the coefficients A and B of the parametrisation are exhibited for the 76 modules of $10\,\mathrm{m}^2$. The average values for these parameters were $A = (-28.8 \pm 0.9)$ in a.u. and $B = (284.1 \pm 3.9)$ in a.u. for the 76 modules of $10\,\mathrm{m}^2$, while for the 7 modules of $5\,\mathrm{m}^2$, the values were $A = (-27.1 \pm 1.0)$ in a.u. and $B = (277.3 \pm 4.3)$ in a.u.. The coefficients obtained from simulations for the $10\,\mathrm{m}^2$ modules are represented as dark vertical lines. The coefficient A from simulations closely matches the value obtained from the data, whereas the coefficient B does not. Since the increase in Eq. (7.3) of the charge deposited per muon with the particle density is related to the coefficient A, the effect of the knock-on electrons in the data is accurately reproduced in the simulations. The coefficient B in simulations is 17% larger than in data. Since this parameter is the intercept of the parametrisation in Eq. (7.3), it suggests that the efficiency in data is lower than in simulations. To compare data and simulations, we computed the average vertical equivalent charge deposited by single muon events. In Fig. 7.7, we present a histogram illustrating the average obtained for each UMD module for the 76 modules of $10\,\mathrm{m}^2$. The average charge deposited in single muon events was $\langle q \rangle = (211.2 \pm 2.3)$ in a.u. for the 76 modules of $10\,\mathrm{m}^2$ and $\langle q \rangle = (207.6 \pm 3.8)$ in a.u. for the 7 modules of $5\,\mathrm{m}^2$. The value in simulations, reported in Section 5.1.2,

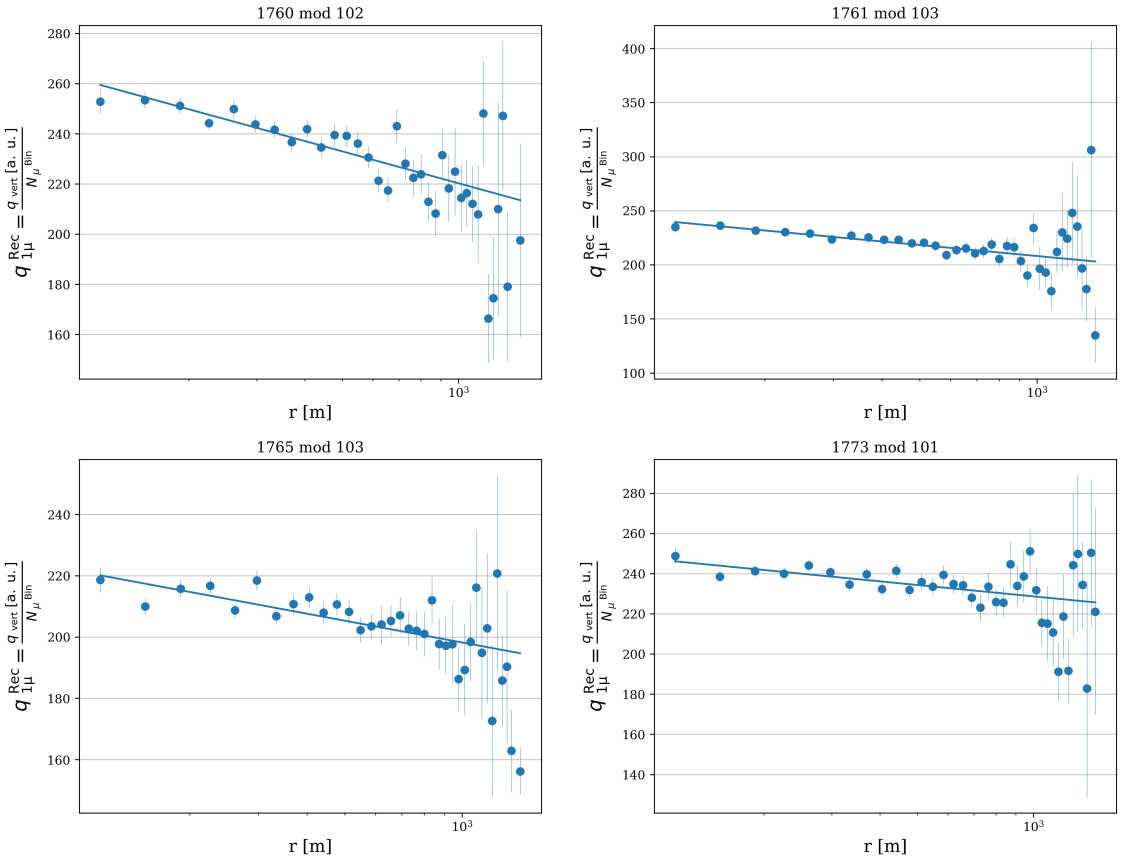

Figure 7.5: Four examples of the calibration method performed in data.

is illustrated as a dark vertical line. The charge deposited by single muon events is also 18% lower in data than in simulations, suggesting that further analysis needs to be performed in the code of the UMD simulation to ensure reproducing the efficiency observed in data.

We present in Fig. 7.8 the bias in the number of reconstructed muons using the ADC mode (N_μ^{ADC}) compared to the number of reconstructed muons using the binary mode (N_μ^{Bin}), for all the modules used in the study. The bias, displayed as a function of N_μ^{Bin}, was computed up to $N_\mu^{\mathrm{Bin}} = 70$ given that the binary mode reconstruction is optimal within this range and can thus serve as a reliable estimator. The bias obtained in this work is represented in blue, whereas the bias obtained with the previous calibration method (ADCT1 files) is presented in orange. Please refer to Section 5.2.1 for a detailed description of the previous method. The bias with the new calibration method remains flat within the considered N_μ range, whereas an increasing bias of approximately 10% is observed in the previous method, showing the importance of accounting for the energy deposited by knock-on electrons.

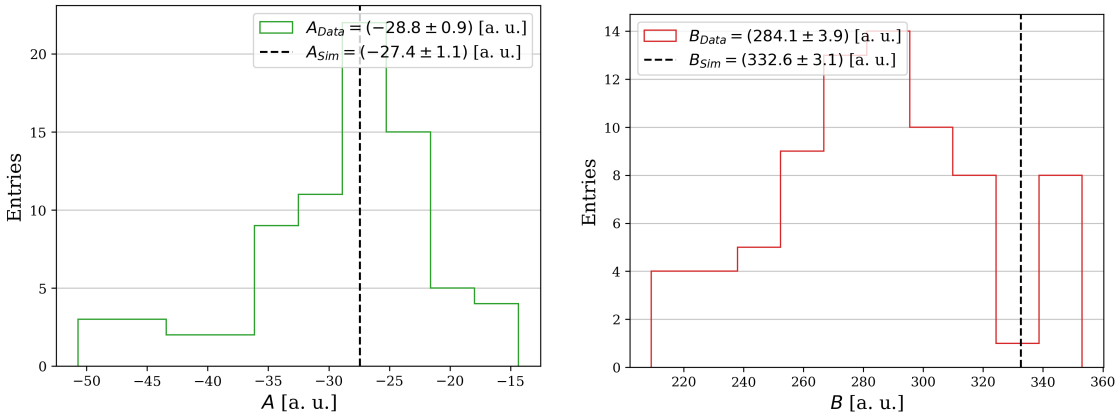

Figure 7.6: Coefficients A and B obtained for the 76 modules of 10 m^2 during the four-year data analysis.

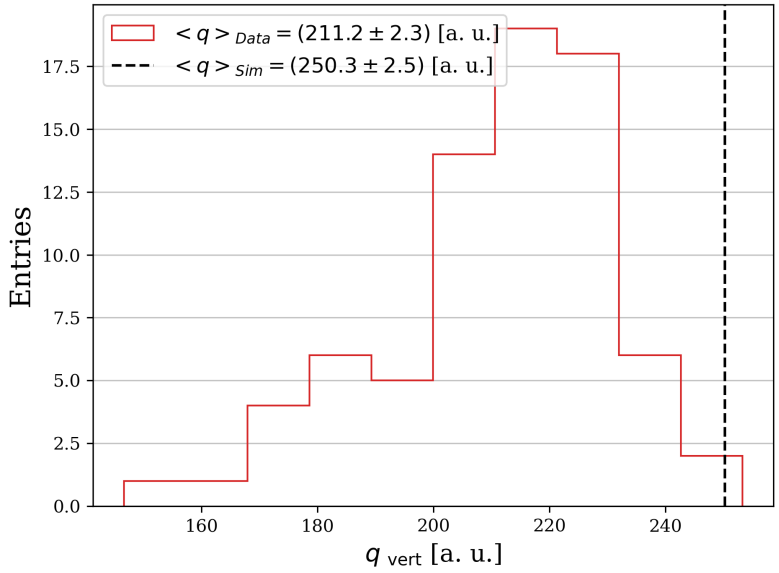

Figure 7.7: Histogram of the vertical charge measured in single muon events.

Stability of the calibration method

In Fig. 7.9, the average number of events per module is illustrated for the stations in acquisition during the four year period. Between the years 2018 and 2019, UMD modules were deployed in 16 stations, whereas in 2020 the process had to be interrupted due to the covid pandemic. In the year 2021, 6 more stations were deployed. To study the stability of the calibration method, we selected the stations 93, 1574, 1764, 1570, 688 and 1773. Two calibration curves can be obtained for these 18 modules given that there is enough data to perform the fits in two different periods: 2019-2020 (first period) and 2021-2022 (second period).

In Fig. 7.10, an example is exhibited for station 1570 module 103 to show

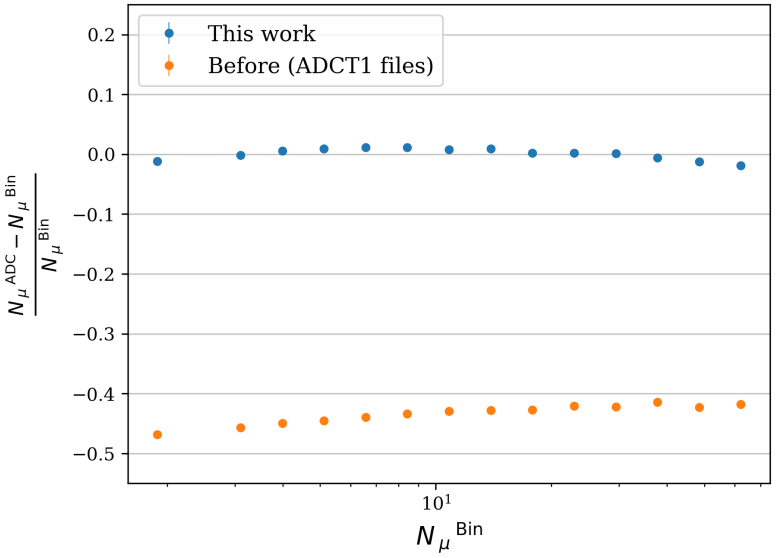

Figure 7.8: Bias in the muon reconstruction between the ADC and binary modes.

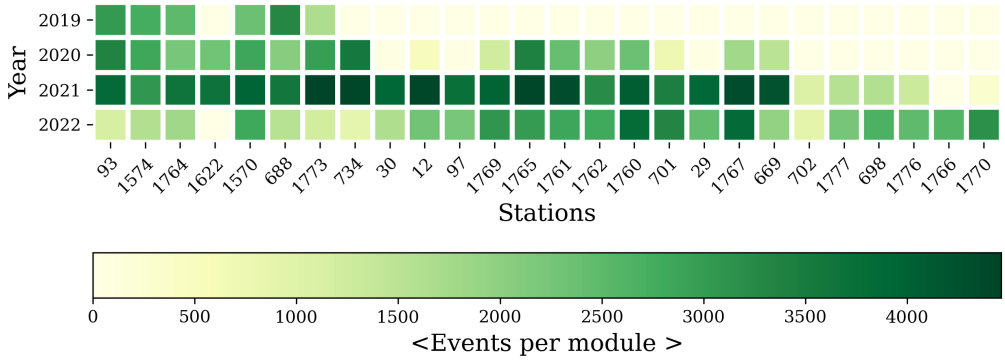

Figure 7.9: Average number of events per module for the stations in acquisition during the four year period.

the calibration stability. The calibration curve obtained with the four year data is illustrated in blue, whereas the curves performed with the data of the first and second periods are represented in red and light blue, respectively. A long-term performance effect can be observed, showing that in the second period smaller values of charge are being measured. An ageing rate of -2.5% per year was already reported for the charge of the ADC mode in Ref. [89], using the ADCT1 files to measure the charge of single muon events. Moreover, this long-term performance effect is similar to the one reported in Ref. [90] for comparable scintillator detectors. It should be accounted for as a systematic uncertainty when analysing any physics results from Phase I.

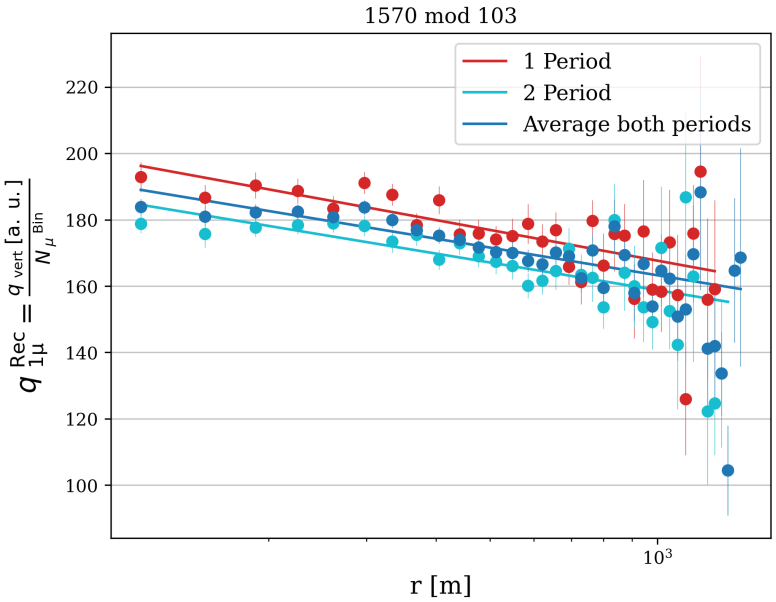

Figure 7.10: Calibration performed during different data periods. The first period contained data from 2019 and 2020, whereas the second period from 2021 and 2022. The curve obtained with the four year data is illustrated in blue.

7.2.2. Phase II

The data used correspond to Phase II, i.e. acquired using the new electronics (UUB), between 2023 and September of 2024 (see Section 2.1). The calibration was carried out on 99 modules of 10 m^2 and 6 modules of 5 m^2. The same quality cuts applied for Phase I were implemented. The following stations were excluded due to specific issues: 710 module 103, 695 module 103, 1772 modules 101 and 102. The average values of the parametrisation coefficients A and B were $A = (-26.1 \pm 0.9)$ in a.u. and $B = (275.7 \pm 3.9)$ in a.u. for the modules of 10 m^2.

In Fig. 7.11, the calibration curves obtained for Phase II are exhibited in orange colours, for station 1767 module 101, station 1761 module 101, station 1764 module 103 and station 1574 module 102. For comparison, the calibration curve from Phase I is displayed in blue. As mentioned earlier, a long-term performance effect is also observed between Phase I and Phase II. In Fig. 7.12, the relative bias of the calibration curve at r=450 m between Phase II and Phase I was calculated. For Phase II, the average measured charge at r=450 m is approximately -5%.

7.3. Summary

The method proposed to calibrate the LG channel of the ADC mode consists of parametrising the charge deposited per muon per vertical path-length using the binary mode and the distance to the shower core for low muon densities.

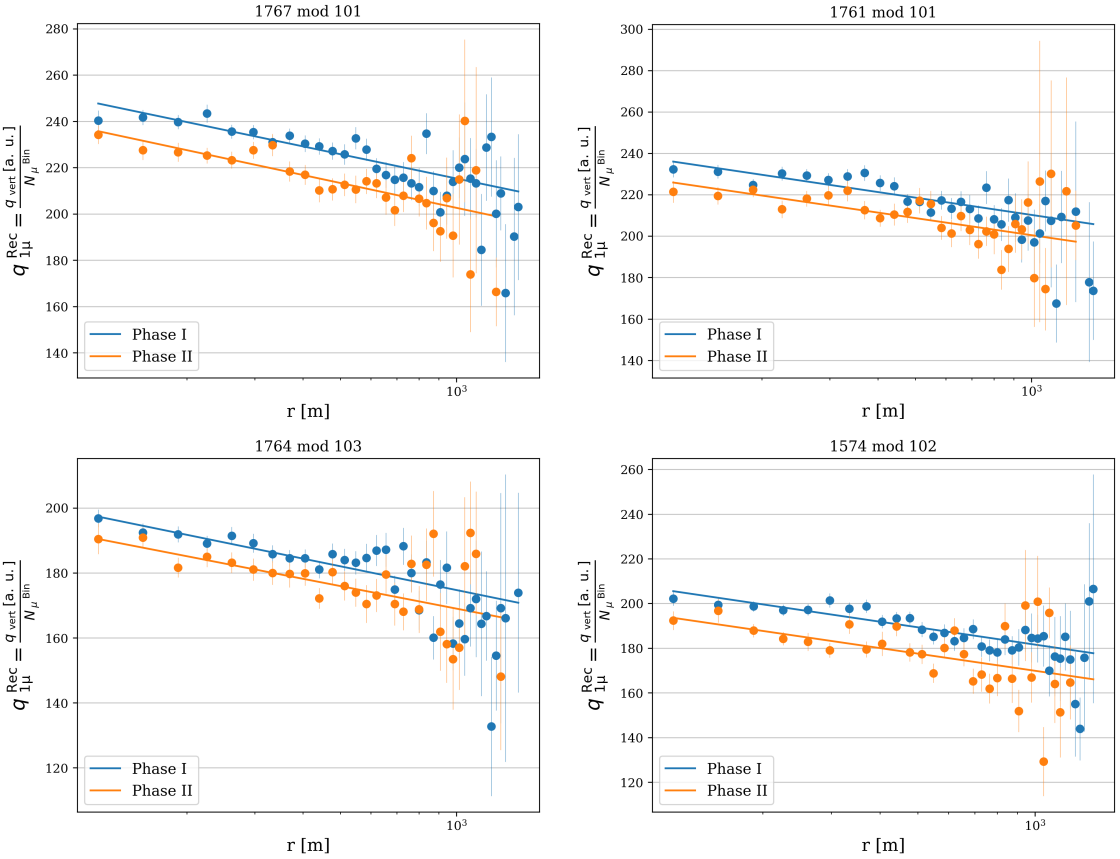

Figure 7.11: Four examples of the calibration curves obtained for Phase II (orange) and Phase I (blue).

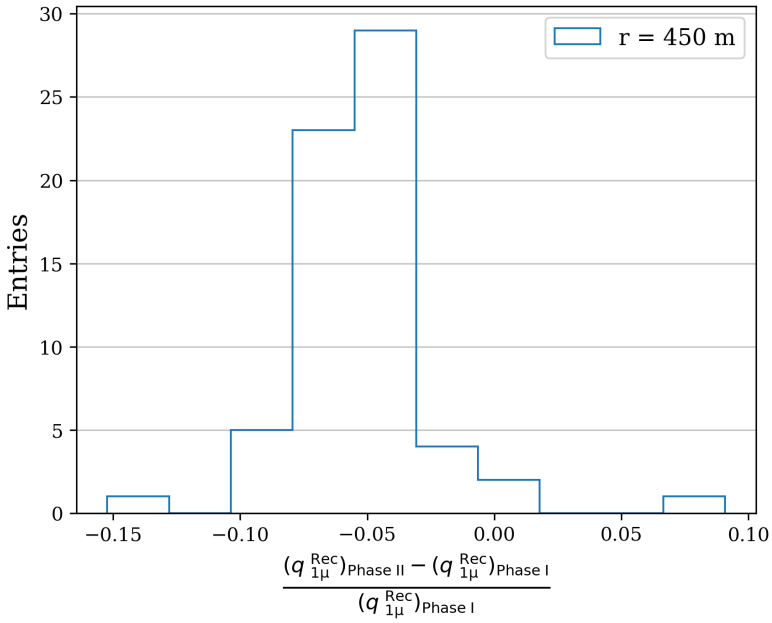

Figure 7.12: Relative bias of the calibration curve evaluated at r=450 m between Phase II and Phase I.

This parametrised curve can then be used to calculate the charge per muon per vertical path-length at high muon densities by extrapolation. The strategy is independent on the zenith angle and the primary of the shower, and it has a negligible dependence of less than 4% on the energy. The method is shown to improve the bias in muon reconstruction using the ADC mode, reducing the effect of the increase in the energy deposition produced by the contamination of the knock-on electrons. The bias obtained for iron and proton EASs is less than 5% for energies of $1{\times}10^{17.5}$ eV, $1{\times}10^{18}$ eV and $1{\times}10^{18.5}$ eV, and zenith angles of $\theta = [0, 12, 22, 32, 38]^{\circ}$.

The strategy was applied to Phase I data, covering the years 2019, 2020, 2021, and 2022, resulting in calibration curves obtained for 83 modules. The coefficient A of the parametrisation, which relates the increase in the charge deposited per muon with the particle density, shows similarity between data and simulations, indicating that the effect of knock-on electrons in data is accurately replicated in simulations. The bias in the number of muons reconstructed between ADC and binary modes is shown to be flat up to $N_{\mu}^{\text{Bin}} = 70$, where the binary mode serves as a reliable estimator.

Moreover, calibration curves were obtained for 105 modules using Phase II data collected between 2023 and September 2024. A long-term performance effect was observed between Phase I and Phase II, with the average measured charge at r=450 m being approximately -5%. This effect is similar to the one reported in Ref. [90] for comparable scintillator detectors.

The calibration curves obtained in this study, for both simulations and data, were integrated into $\overline{\text{Off}}\underline{\text{line}}$ within the `MdADCMuonEstimator` module.

Chapter VIII

Muon lateral distribution function and iron-proton shower discrimination

There are several methods to reconstruct the muon lateral distribution function (MLDF) of the UMD. The ones based on the binary acquisition mode are described in Refs. [67, 65, 91]. A method to reconstruct the MLDF based on the ADC acquisition mode only is also developed and described in Ref. [92]. A combined method using both acquisition modes is developed in Refs. [92, 93]. In Ref. [92], the binary likelihood is used in the region of small and intermediate values of the estimated number of muons that hit a given muon detector and the ADC likelihood is used in the region of large values of the estimated number of muons, whereas in Ref. [93] the likelihood function found has the same expression regardless the values of the estimated number of muons that hit a given muon detector.

In the combined methods mentioned above, the following hypothesis is proposed: the ADC output is linear and can be expressed as the arithmetic sum of individual signals, so the overall charge Q associated with n muons can be represented as $Q = n \sum_{i=1} q_i$ where q_i represent the charge of a single muon. As shown in Chapter 6 and Chapter 7, this assumption is incorrect. The charge deposited by several muons is not linear with the charge of a single muon due to the increase in the energy deposition produced by the more energetic muons generating more knock-on electrons close to the shower axis.

In this chapter a combined likelihood method is presented using both binary and ADC acquisition modes of the UMD to reconstruct the MLDF, taking into account the effect of knock-on electrons in the ADC mode for high muon densities. The method is studied with full-detector simulations. In Section 8.1, the

biases of the binary and ADC mode are shown, along with the bias in the reconstructed distance to the shower core obtained by the SD. Section 8.2 introduces the likelihood method. In Section 8.3 the parameters of the MLDF are briefly reviewed, with particular emphasis on α due to its significance at short distances from the shower core. Finally, in Section 8.4, the muon estimator is obtained, along with the capability of the UMD to discriminate between proton and iron primary cosmic rays.

8.1. Bias and resolution of N_μ and r

The data set to validate the strategy in simulations contained proton and iron showers, simulated in Offline [73] using the hadronic interaction model EPOS-LHC, with energies $1{\times}10^{17.5}$ eV, $1{\times}10^{18}$ eV, $1{\times}10^{18.5}$ eV and $1{\times}10^{19}$ eV and zenith angles $\theta = [0, 12, 22, 32, 38]^\circ$.

The bias and resolution in muon reconstruction are illustrated in Fig. 8.1a as a function of the number of injected muons per 10 m^2 module and in Fig. 8.1b as a function of the true distance to the shower core. The figures were computed for showers of energy $1{\times}10^{18.5}$ eV constructed calculating the average across all zenith angle bins. The ADC mode is represented with orange squares, while the binary mode is presented with green dots. The region where the absolute value of the bias is below 5% is represented in the left panels with a light blue rectangle. In the binary mode, the infinite-window strategy was employed, whereas the corner-clipping corrections, detailed in Ref. [68], were applied. In the ADC mode, the number of muons was estimated employing the LG channel and taking into consideration the corrections produced by the effect of knock-on electrons, detailed in Chapter 7. Saturated modules were excluded from this analysis.

To estimate the MLDF measured by the UMD, each mode is employed in the regime where it performs best: binary mode for low muon densities and ADC mode for intermediate/high muon densities. The ADC mode is utilised if the number of muons reconstructed in the ADC mode is higher than 70 muons or if the binary mode is saturated. Otherwise, the binary mode is used to reconstruct the muon density. The cut proposed at $N_\mu^{\text{ADC}} = 70$ to switch between binary and ADC was selected observing the bias and resolution of both modes. The monte-carlo value of 70 muons is represented in Fig. 8.1a with a vertical dashed line. The distance to the shower core where the switch between binary-ADC is produced depends on the energy of the shower. For showers of energy $1{\times}10^{18.5}$ eV, the maximum true distance to switch between modes, illustrated with a vertical dashed curve in Fig. 8.1b, is approximately $r_{\text{True}} \sim 440$ m. For higher muon densities than 70 muons and smaller distances than $r_{\text{True}} \sim 440$ m., the bias in the number of muons reconstructed with the ADC mode remains flat, while the

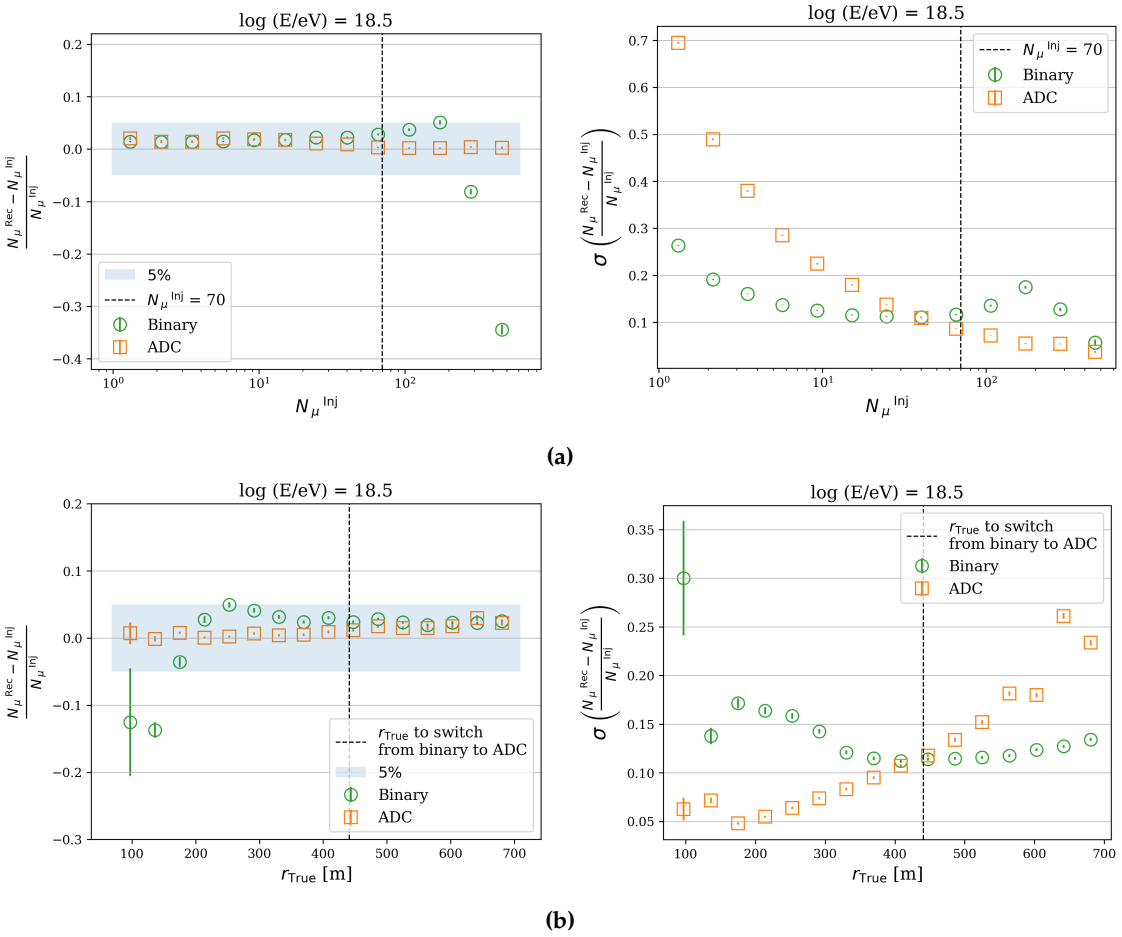

Figure 8.1: Bias (left panel) and resolution (right panel) in muon reconstruction for showers of energy $1{\times}10^{18.5}$ eV (a) as a function of the number of injected muons per 10 m^2 module and (b) as a function of the true distance to the shower core. The ADC mode is depicted in orange squares, whereas the binary mode is presented in green dots.

resolution in the estimator is much improved compared to the binary mode. The same conclusion can be reached from different energy bins. For the energies of $1{\times}10^{17.5}$ eV, $1{\times}10^{18}$ eV and $1{\times}10^{19}$ eV, the maximum true distance r_{True} to switch between modes are $\sim$ 185 m, $\sim$ 281 m and $\sim$ 706 m, respectively.

It is worth noting that applying the corrections to the ADC mode, detailed in Chapter 7, improves the muon reconstruction closer to the shower core. However, the reconstruction of the MLDF depends not only on the reconstructed number of muons but also on the reconstructed distance to the shower core obtained by the surface detector (SD). The bias of the latter is shown in Fig. 8.2 as a function of the true distance to the shower core for showers of energy $1{\times}10^{18.5}$ eV. For distances $r_{\text{True}} \lesssim 200$ m, the bias in the core reconstruction exceeds the 5% regime represented with a light blue rectangle. For this reason, the core reconstruction of events with stations near the shower core plays a key role in

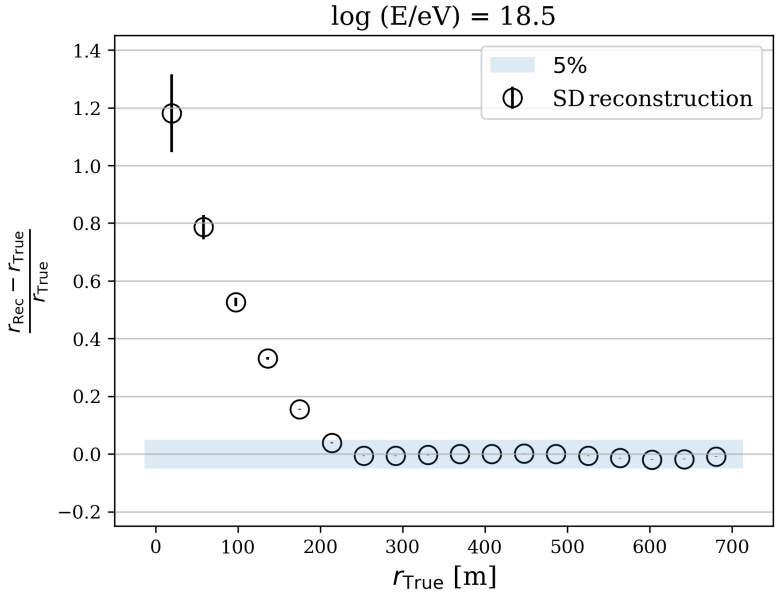

Figure 8.2: Bias in distance reconstruction from the SD as a function of the true distance to the shower core for showers of energy $1{\times}10^{18.5}$ eV.

the MLDF reconstruction and will therefore be accounted for in the proposed likelihood.

8.2. Likelihood proposed

The average number of muons expected in a detector (μ) depends on the muon density (ρ), the detector area (A) and the zenith angle (θ) according to

$$\mu = \rho A \cos\theta. \tag{8.1}$$

Stations are divided into three classes: stations where the ADC mode measured less than 70 muons, stations where it measured more or equal to 70 muons and stations where the ADC mode saturated. The likelihood function is given by

$$\begin{aligned}\mathcal{L}(\vec{p}) = &\prod_{i=1}^{N_\mu^{\text{Rec}}<70} \mathcal{L}_{binomial}(\mu(r_i;\vec{p}), k_i) \times \prod_{i=1}^{N_\mu^{\text{Rec}}\geq 70} \mathcal{L}_{gaussian}(\mu(r_i;\vec{p}), (N_\mu^{\text{Rec}})_i) \times \\ &\prod_{i=1}^{N_\mu^{\text{Saturated}}} \mathcal{L}_{sat}(\mu(r_i;\vec{p}), (N_\mu^{\text{Rec}})_i),\end{aligned} \tag{8.2}$$

where N_μ^{Rec} is the reconstructed number of muons with the ADC mode and k the number of scintillator bars where a muon pattern was identified (referred to as

the number of segments on), r_i is the distance of the i-th station to the shower core and and $\bar{p}$ is a vector related to the parameters of the MLDF (see following section). For conciseness, these two latter dependencies in the parameters will be omitted in the subsequent equations.

The likelihood function $\mathcal{L}_{binomial}$ proposed for low muon densities, as detailed in Ref. [65], relates the number of segments on to μ. The average number of muons in each segment is μ/n, with n the total number of segments. In turn the number of muons in a segment follows a Poisson distribution with parameter μ/n. A segment has a signal when one or more muons reaches it. Then the probability of a signal, derived from a Poisson distribution, is $p = 1 - e^{-\mu/n}$. Calling k the number of segments on, the probability of k as function of μ follows the binomial distribution

$$\mathcal{L}_{binomial}(\mu, k) = \binom{n}{k} p^k (1-p)^k = \binom{n}{k} e^{-\mu}(e^{\mu/n} - 1)^k. \tag{8.3}$$

In the UMD, the total number of segments is equal to the number of scintillator bars ($n = 64$), the number of segments on k is the number of scintillator bars where a muon pattern was identified and the probability p is modified to $p = 1 - e^{-\mu(1+p_{cc})/64}$ in order to include the corner-clipping corrections p_{cc} [68].

The likelihood function $\mathcal{L}_{gaussian}$ proposed for high muon densities is a Gaussian likelihood described by equations

$$\begin{aligned} \mathcal{L}_{gaussian}(\mu, N_\mu^{\text{Rec}}) &= \frac{1}{\sqrt{2\pi\sigma^2(\mu)}} e^{-\frac{1}{2}\left(\frac{N_\mu^{\text{Rec}} - \mu}{\sigma(\mu)}\right)^2} \\ \sigma^2(\mu) &= \sigma^2_{Poisson}(\mu) + \sigma^2_{Rec}(\mu). \end{aligned} \tag{8.4}$$

To show that the estimator $\frac{N_\mu^{\text{Rec}} - \mu}{\sigma(\mu)}$ is gaussianlly distributed, a Q-Q (quantile-quantile) plot is exhibited in the left panel of Fig. 8.3 for $N_\mu^{\text{Inj}} = 100$ muons. In a Q-Q plot the quantiles of the sample data are plotted against the corresponding quantiles of the theoretical distribution. Since the dataset, represented by blue dots, lies roughly along the straight 45-degree line, plotted in red, the dataset follows the theoretical normal distribution proposed within approximately ± 2 standard deviations. In the right panel of Fig. 8.3, the variance model used in Eq. (8.4) is depicted. In this model, the standard deviation of the Gaussian is a sum in quadrature of two terms. The first term, represented in red, is given by the poissonian fluctuations of an ideal detector. The second term is computed with a fit, presented as a black curve, from the detector fluctuations in the measured number of muons (blue dots).

Finally, for the saturated modules, the likelihood function $\mathcal{L}_{sat}$ is given by

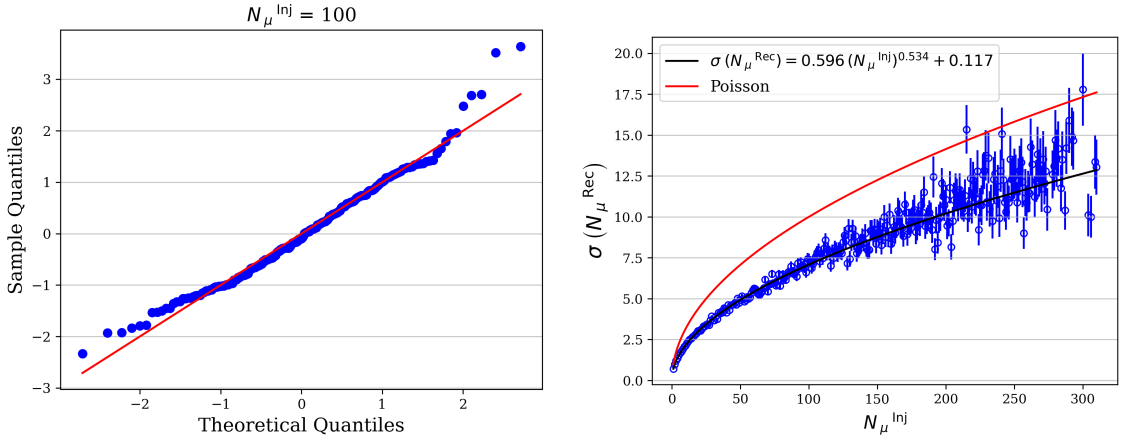

Figure 8.3: (left) Q-Q plot for $N_\mu^{\text{Inj}} = 100$ muons to show that $\frac{N_\mu^{\text{Rec}} - \mu}{\sigma(\mu)}$ is gaussianlly distributed. (right) Variance model developed for N_μ^{Rec} taking into consideration the poissonian fluctuations of an ideal detector and the detector fluctuations of the reconstructed number of muons.

$$\mathcal{L}_{sat}(\mu, N_\mu^{\text{Rec}}) = \frac{1}{2}\left[1 - \text{Erf}\left(\frac{N_\mu^{\text{Rec}} - \mu}{\sqrt{2\sigma^2(\mu)}}\right)\right]. \tag{8.5}$$

The reconstruction of the MLDF relies on the estimated distance to the shower core, as determined by the SD. As shown in previous section, stations located near the shower core can exhibit a substantial bias in core reconstruction. When a shower lands close to a station, leaving the core reconstruction fixed to the SD can bias the fit of the MLDF. Ref. [94] shown that the MLDF fit can be improved by treating the core as a free parameter while incorporating a penalty term in the likelihood. This approach constrains the UMD core to remain close to the SD core, discouraging core positions that deviate too far from the SD reconstruction. The distribution of the UMD core (x, y) is modelled as a bivariate gaussian whose expected value corresponds to the SD core, and whose covariance matrix is given by the covariance matrix of the core coordinates obtained in the SD fit. When taking the logarithm of this factor, a χ^2 term is added to the final likelihood

$$\begin{aligned} -\ln\mathcal{L}(\bar{p}, x, y) = &- \sum_{i=1}^{N_\mu^{\text{Rec}}<70} \ln\mathcal{L}^i_{binomial}(\bar{p}, x, y) - \sum_{i=1}^{N_\mu^{\text{Rec}}\geq 70} \ln\mathcal{L}^i_{gaussian}(\bar{p}, x, y) \\ &- \sum_{i=1}^{N_\mu^{\text{Saturated}}} \ln\mathcal{L}^i_{sat}(\bar{p}, x, y) + \frac{1}{2}\chi^2(x, y), \end{aligned} \tag{8.6}$$

where the extra χ^2 term is given by

$$\chi^2(x,y) = \frac{1}{1-\rho_{\mathrm{SD}}^2}\left[\left(\frac{x-x_{\mathrm{SD}}}{\sigma_{x_{\mathrm{SD}}}}\right)^2 + \left(\frac{y-y_{\mathrm{SD}}}{\sigma_{y_{\mathrm{SD}}}}\right)^2 - 2\frac{\rho_{\mathrm{SD}}}{\sigma_{x_{\mathrm{SD}}}\sigma_{y_{\mathrm{SD}}}}(x-x_{\mathrm{SD}})(y-y_{\mathrm{SD}})\right]. \tag{8.7}$$

8.3. Muon lateral distribution function

The MLDF is a great tool for composition analyses, as both its size and slope carry information of the primary mass. Ref. [64] presents a detailed analysis of different MLDF models found in the literature. The study computes the average MLDF from UMD data and evaluates the goodness-of-fit of the multiple models with the observed data. The functional form proposed for the parametrisation of the MLDF is the modified NKG (Nishimura-Kamata-Greisen) or KASCADE-Grande [95], where the muon density expected in the detector, related by Eq. (8.1) to the number of expected muons $\mu(r)$, is given by

$$\rho^{\mathrm{mNKG}}(r) = \rho_{\mathrm{ref}}\left(\frac{r}{r_{\mathrm{ref}}}\right)^{-\alpha}\left(\frac{1+r/r_0}{1+r_{\mathrm{ref}}/r_0}\right)^{-\beta}\left(\frac{1+(r/10r_0)^2}{1+(r_{\mathrm{ref}}/10r_0)^2}\right)^{-\gamma}, \tag{8.8}$$

where r is the distance to the shower axis, ρ_{ref}, r_0, α, β and γ are parameters which define the shape and size of the MLDF. The parameter γ describes the behaviour of the MLDF at relatively large distances from the core, where only low statistics are available in general.

In Ref. [64], an in-depth study is presented to understand how the shape of the MLDF parametrisation depends on its parameters. The α term is shown to be a significant factor at short distances to the shower axis. However, in practice, α is usually fixed to a single value across a wide range of energies and zenith angles. This is normally done given that α and β are so strongly correlated that fitting both simultaneously would be extremely challenging. Nevertheless, Eq. (8.8) can still be well tuned at a fixed α by varying β. The fixed parameters r_0= 320 m, α=0.75, and γ=3.0 were found in Ref. [64] as optimal for fitting the average MLDF when reconstructing muon densities with the binary mode of the UMD. Fixing these parameters biases in less than ±2% the muon density at 450 m, demonstrating that choosing ρ_{ref} as ρ_{450} is optimal, as this distance minimises uncertainties in the MLDF. Since the muon densities from the ADC mode of the UMD complement the measurements of the binary mode reaching distances much closer to the core, the evaluation of fixing the parameter α to 0.75 is revisited in Section 8.4.

Finally, to fit the MLDF we minimise the likelihood function $-\ln\mathcal{L}(\bar{p})$ from Eq. (8.6) with respect to the free parameters $\bar{p} = (\rho_{450}, \beta)$ of the MLDF.

The parameter β is allowed to vary on an event-by-event basis and then it is

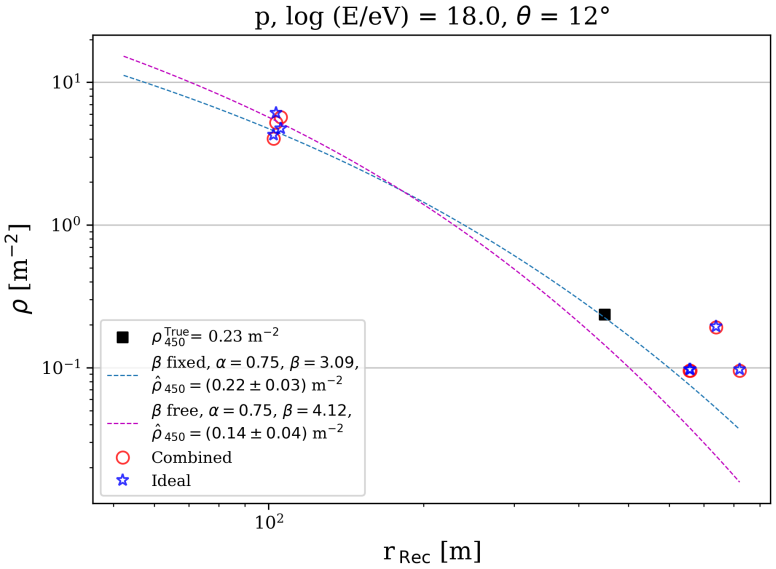

Figure 8.4: Same event reconstructed with a fixed β (blue curve) and a free β (pink curve) in the MLDF.

parametrised as a function of the zenith angle and the energy of the shower. The muon estimator $\hat{\rho}_{450}$ is then determined with β fixed in the MLDF. To illustrate the importance of parametrising β in the MLDF, the same event is reconstructed in Fig. 8.4 using both a fixed β (blue curve) and a free β (pink curve). The monte-carlo muon density at 450 m ρ_{450}^{True} is depicted with a dark square. The reconstructed muon densities from the combined strategy are exhibited with red circles, while the monte-carlo muon densities are represented by blue stars. When only a few stations are involved in the event, allowing β to remain free in the MLDF reconstruction significantly impacts the muon estimator. The effect of a free β on the computation of $\hat{\rho}_{450}$ is further analysed in the next section.

An example of the parametrisation of β is shown in Fig. 8.5 and Fig. 8.6 for the dataset generated using the standard UMD reconstruction with α=0.75. In Fig. 8.5, the average β is determined for each primary and energy bin as a function of sec θ. Each curve is fitted using the equation $\beta = A\,(\sec\theta - 1.2) + B$. The coefficients A and B obtained from the fit are exhibited in Fig. 8.6 for proton (red dots) and iron (blue dots) as a function of the shower energy. The mean value calculated from both primaries is represented by dark dots. Since the dependence of coefficient A on the energy of the shower is minimal, A is calculated as the average of the mean values for both primaries across all energy bins, as indicated by the dark line. The coefficient B is treated as energy-dependent, with the equation $B = B_1(\log(E/\text{eV}) - 18.25) + B_0$ (dark line) fitted to the mean of the primaries.

In Section 8.4, the parameter α was varied to 0.75, 0.9, and 1.05 to study its impact on the bias and resolution of the muon estimator $\hat{\rho}_{450}$. Given the

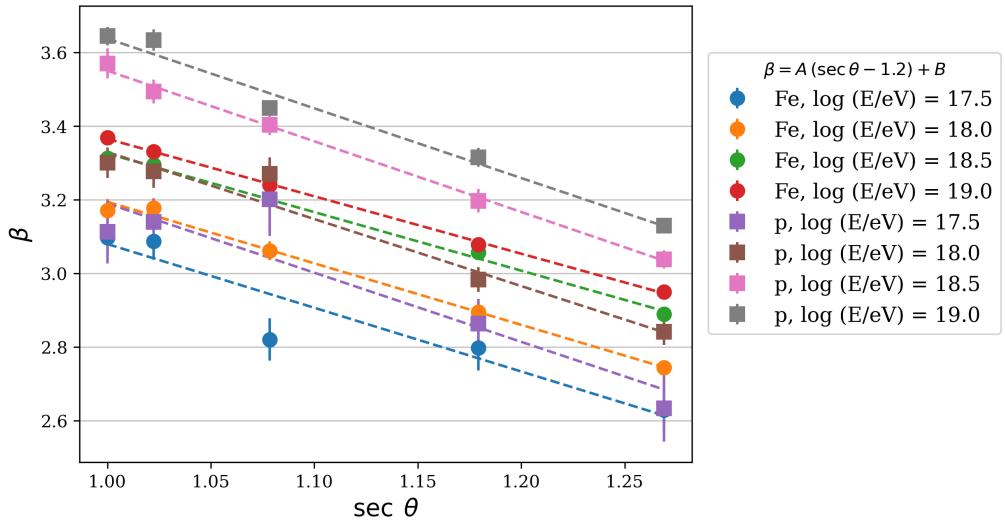

Figure 8.5: Average β for each primary and energy bin as a function of sec θ. The curves, obtained using α=0.75, are fitted with $\beta = A\,(\sec\theta - 1.2) + B$.

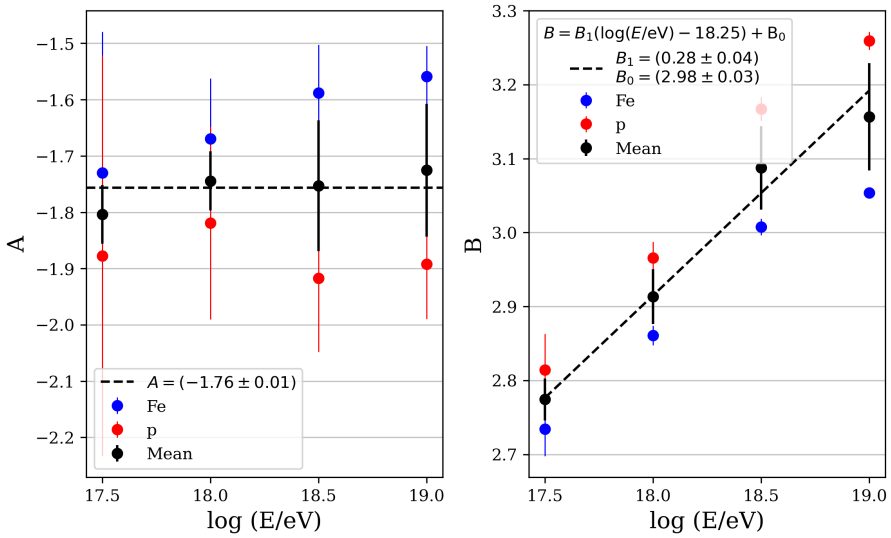

Figure 8.6: Coefficients A and B for proton (red dots) and iron (blue dots) as a function of the shower energy. The mean value calculated from both primaries is represented by dark dots, while the fits for A and B, computed from the mean, are indicated as black lines.

strong correlation between α and β, the parametrisation of β was carried out for each value of α individually. The effect of varying α on the estimation of the average β is shown in Fig. 8.7 for showers with an energy of $1{\times}10^{18}$ eV, where different primaries are represented by distinct colours and different zenith angles are indicated by various markers. An increase in the parameter α leads to a decrease in the parameter β, showing the correlation between both parameters of the MLDF.

Two examples of MLDFs are exhibited in Fig. 8.8 for an iron shower with

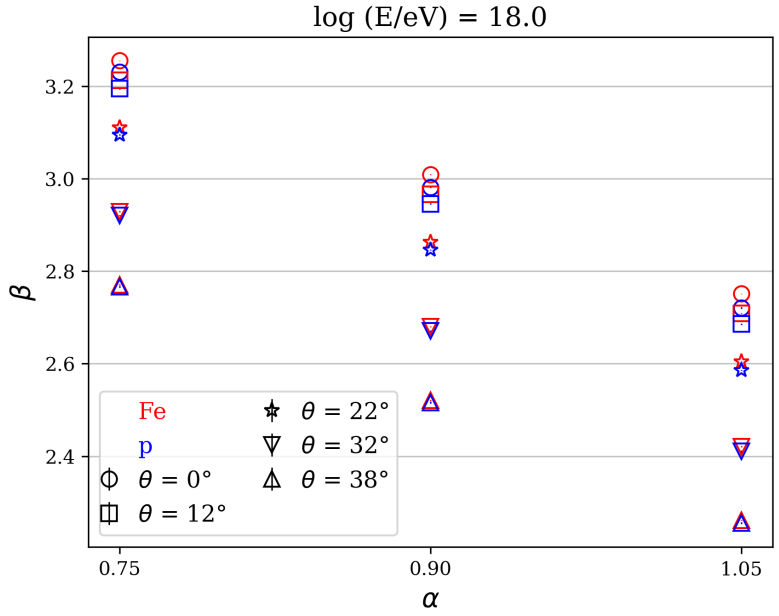

Figure 8.7: Average β as a function of the α parameter used in the MLDF.

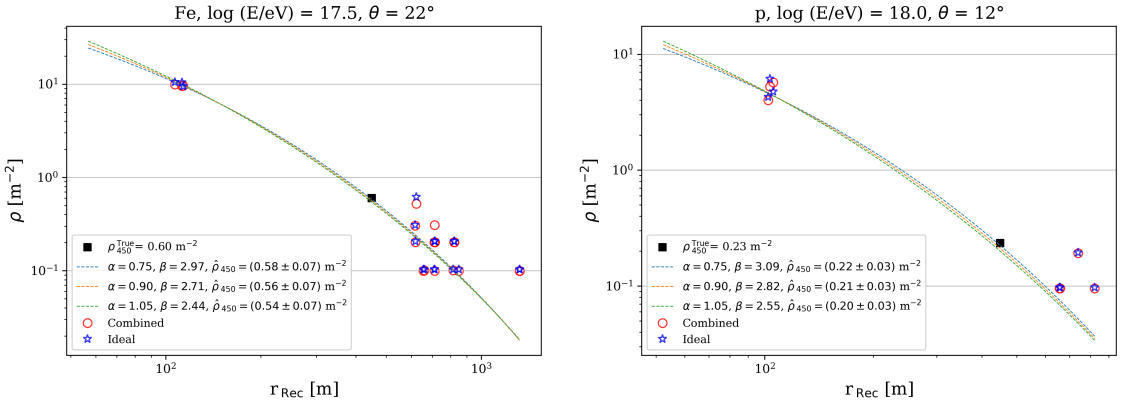

Figure 8.8: Two examples of MLDF reconstructions for α=0.75 (blue curve), α=0.9 (orange curve) and α=1.05 (green curve).

energy $1{\times}10^{17.5}$ eV and $\theta = 22°$ (left panel), and a proton shower with energy $1{\times}10^{18}$ eV and $\theta = 12°$ (right panel). The reconstructed muon densities from the combined strategy are represented by red circles, while the monte-carlo muon densities are shown as blue stars and the monte-carlo muon density at 450 m ρ_{450}^{True} as a dark square. The MLDFs obtained for α=0.75 are presented in blue, for α=0.9 in orange and for α=1.05 in green, respectively. It can be noted that all three MLDFs perform reasonably well and that the reconstructed muon densities from the combined strategy provide good estimators of the monte-carlo muon densities, even at 100 m from the shower core.

In Fig. 8.9, the dependence of the MLDF shape on its parameters is illustrated

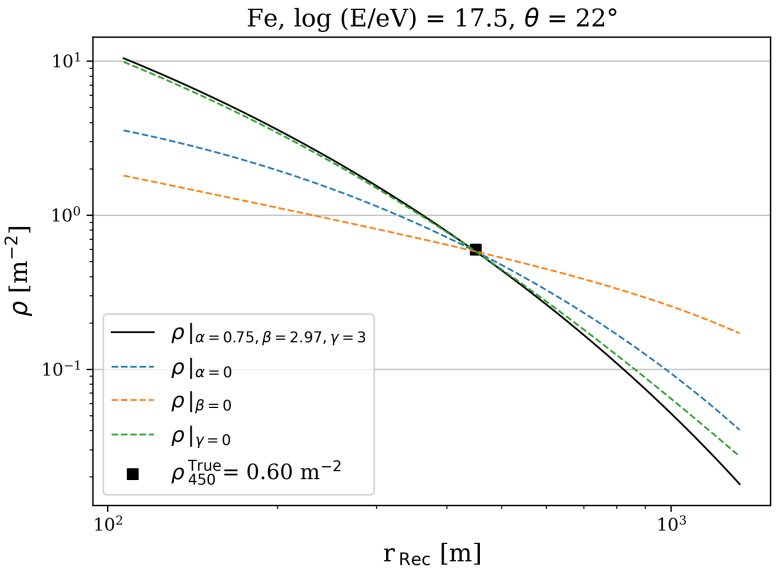

Figure 8.9: Example of a MLDF reconstruction (black curve) compared to the MLDF evaluated at $\alpha = 0$ (blue curve), $\beta = 0$ (orange curve) and $\gamma = 0$ (green curve).

using the event from the left panel of Fig. 8.8 as an example. The MLDF from this event, reconstructed with $\alpha = 0.75$, is shown with a black curve. The MLDF is also evaluated for $\alpha = 0$ (blue curve), $\beta = 0$ (orange curve), and $\gamma = 0$ (green curve). As previously explained, removing the parameter γ impacts the behaviour of the MLDF at relatively large distances from the core, while α plays a significant role at short distances. The MLDF is most significantly affected by removing β, especially at short and intermediate distances.

In Fig. 8.10, the residuals are displayed for showers with energies of $1{\times}10^{17.5}$ eV (left panel) and $1{\times}10^{19}$ eV (right panel) as a function of the reconstructed distance to the shower core. The residuals are calculated for each event by comparing the MLDF reconstruction with the reconstructed muon density, and then averaging the results across all zenith angle bins and primary masses. The reference distance at 450 m is represented with a pink vertical line. At this reference distance, the residuals are approximately 1% for $1{\times}10^{17.5}$ eV showers and 0.3% for $1{\times}10^{19}$ eV showers. The three MLDFs perform reasonably well, with $\alpha = 0.75$ yielding the smallest residual at $1{\times}10^{17.5}$ eV. Residuals increase closer to the shower core as modules saturate, leading to a less accurate reconstruction of the muon density.

8.4. MUON ESTIMATOR $\hat{\rho}_{450}$ AND MERIT FACTORS

To compute the bias and resolution of the muon estimator $\hat{\rho}_{450}$, 11 stations were located at r_{ref}= 450 m to obtain the true value ρ_{450}^{True} of the muon density at 450 m, using the average monte-carlo number of injected muons across the 11 stations.

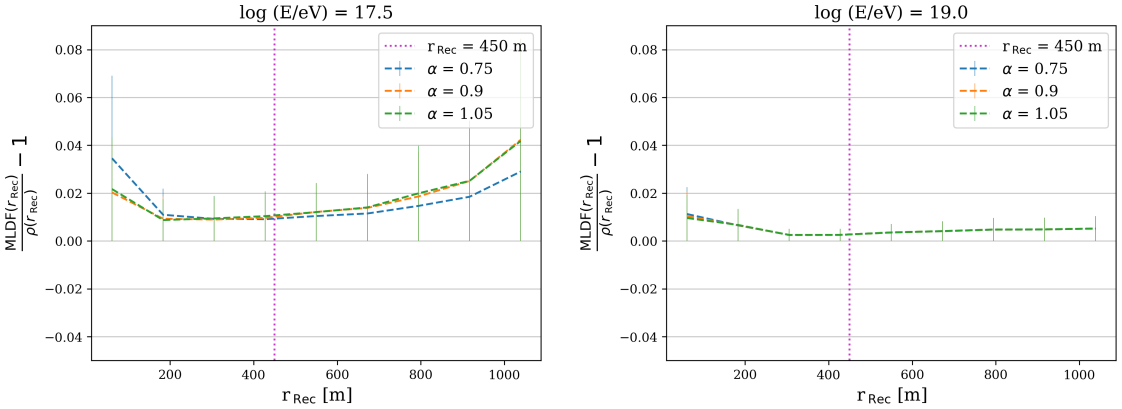

Figure 8.10: Residuals of the MLDF reconstruction compare to the reconstructed muon density as a function of the reconstructed distance to the shower core.

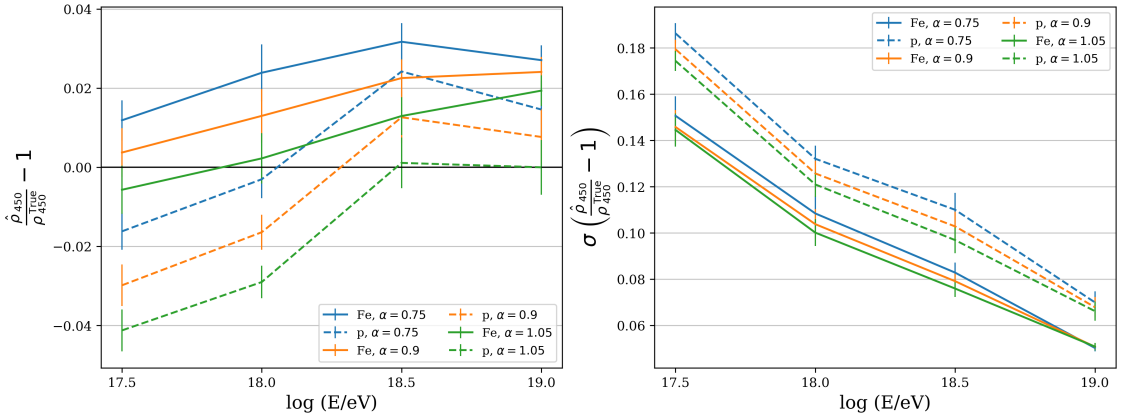

Figure 8.11: Average bias and resolution of muon estimator $\hat{\rho}_{450}$ for showers of primary mass iron (solid lines) and proton (dashed lines). The parameter α was fixed to α=0.75 (blue), α=0.9 (orange) and α=1.05 (green).

In Fig. 8.11, the bias and resolution of the muon estimator $\hat{\rho}_{450}$ are exhibited, constructed computing the average across all zenith angle bins. The solid lines represent the values obtained for iron showers, whereas for proton showers the values are presented with dashed lines. The parameter α was fixed to three different parameters: α=0.75 (blue), α=0.9 (orange) and α=1.05 (green). The usual UMD reconstruction α=0.75, indicated with blue curves, biases in less than ±3% the muon density at 450 m. Increasing α to 1.05 enhances the resolution of the estimator $\hat{\rho}_{450}$ by approximately 1%. While this parameter reduces the bias for high-energy showers, it comes at the cost of increasing the bias for low-energy showers.

The merit factor for proton-iron discrimination is given by

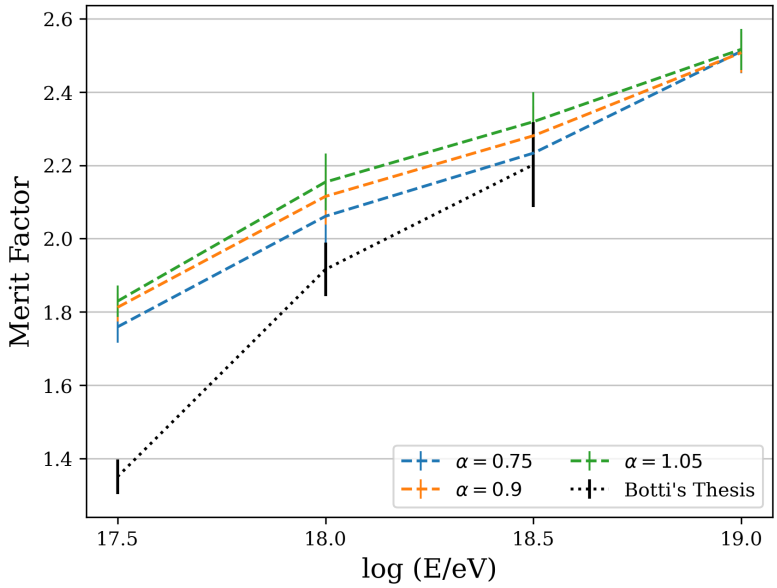

Figure 8.12: Average merit factors for α=0.75 (blue), α=0.9 (orange) and α=1.05 (green). The dark dotted curve illustrates the merit factor obtained with the ADC mode in previous works [63].

$$MF = \frac{\left|\bar{\rho}^{\mathrm{Fe}}_{450} - \bar{\rho}^{\mathrm{p}}_{450}\right|}{\sqrt{\sigma^2_{\rho^{\mathrm{Fe}}_{450}} + \sigma^2_{\rho^{\mathrm{p}}_{450}}}}, \tag{8.9}$$

where Fe refers to iron and p to proton. In Fig. 8.12, the merit factor was computed, calculating the average across all zenith angle bins. The usual UMD reconstruction α=0.75 is indicated with blue, while α=0.9 and α=1.05 with orange and green, respectively. For comparison, the merit factor computed in Ref. [63], employing the ADC mode and full-detector simulations, is illustrated with a dark dotted line. Firstly, the merit factor to discriminate proton and iron is improved from previous works approximately 20% on low energy showers. Secondly, the merit factor is improved by 5% when increasing α. The merit factor, as shown in Eq. (8.9), can be maximised by increasing the separation between the means of $\hat{\rho}_{450}$ for protons and iron nuclei. For instance, this occurs when α=1.05 at low-energy showers, even though the biases of the estimators are not optimal. Therefore, the primary goal is to enhance both the bias and resolution of the estimators, rather than solely focusing on maximising the merit factor.

No significant improvements were observed in the bias and resolution of $\hat{\rho}_{450}$ when varying α from its standard UMD reconstruction value of 0.75. To maintain consistency with analyses conducted using UMD data, the standard parameter will be applied to the data.

In Fig. 8.13, the bias and resolution of the muon estimator $\hat{\rho}_{450}$ are exhibited

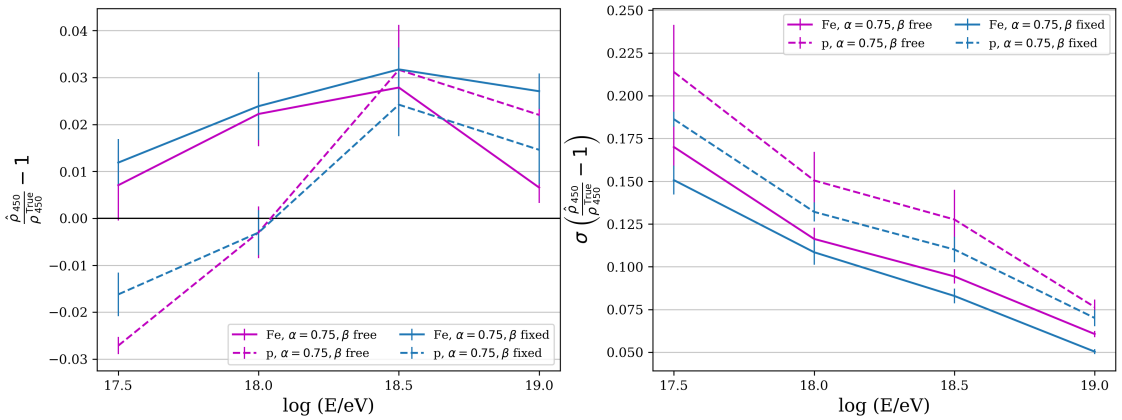

Figure 8.13: Average bias and resolution of muon estimator $\hat{\rho}_{450}$ obtained with β fixed (blue curve) and β free (pink curve). The two primary mass iron and proton are represented with solid and dashed lines, respectively.

for α=0.75, comparing results obtained with β fixed (blue curve) and β free (pink curve) in the MLDF. Allowing the parameter β to vary on an event-by-event basis, affects the resolution of the muon estimator, particularly for low-energy showers. This effect arises due to the limited number of stations involved in low-energy events. For high-energy showers, the impact is less pronounced. The increase in the resolution of the muon estimator leads to a degradation of the merit factor used for proton and iron discrimination.

Finally, the likelihood proposed was also studied with the hadronic interaction model QGSJII-04, considering the same primary mass, energy and zenith angle bins. Similar results were obtained for α=0.75 when computing the bias and resolution of the muon estimator $\hat{\rho}_{450}$, resulting in biases of less than ±2.5%.

8.5. Summary

A combined likelihood method was developed for the UMD, utilising the reconstructed number of muons from the ADC mode and the number of segments on (the number of scintillator bars where a muon pattern was identified). Since stations located near the shower core were found to exhibit a significant bias in core reconstruction, an additional penalty term was incorporated into the likelihood to treat the core as a free parameter. The final likelihood was evaluated using full-detector simulations.

The parameters β and α of the MLDF were briefly reviewed. It was shown that allowing the parameter β to vary on an event-by-event basis, increased the resolution of the muon estimator $\hat{\rho}_{450}$ and reduced therefore the merit factor to discriminate proton and iron, particularly for low-energy showers due to the limited number of stations involved. The parameter α was varied to three different

fixed parameters: α=0.75, α=0.9 and α=1.05. The standard UMD reconstruction with α=0.75 was shown to introduce a bias of less than ±3% in the muon density at 450 m. Since no significant improvements were observed in the bias and resolution of $\hat{\rho}_{450}$ when varying α, the standard UMD reconstruction value of 0.75 will be used for consistency with UMD data analyses.

Finally, the merit factor was shown to improve by approximately 20% over previous works [63] for showers with an energy of $1{\times}10^{17.5}$ eV.

Chapter IX

Muon content in data

In Chapter 7, the method proposed to calibrate the ADC mode, shown to improve the bias in muon reconstruction, was applied to Phase I and Phase II data. In Chapter 8, a combined likelihood method, utilizing the reconstructed number of muons from the ADC mode, was developed for the UMD to obtain the muon estimator ρ_{450}[1]. In this chapter, we report the first measurement of the muon content in EASs obtained using the information of the ADC mode of the UMD to analyse Phase I and Phase II data. In Refs. [96, 97, 98], measurements of the muon content were presented but using solely the information of the binary mode. The comparison with these studies will be further analysed in Section 9.7.

It is well established that current air-shower simulations fail to reproduce the muon content observed in data (see Section 1.4). As detailed in Ref. [40], muon measurements seem to be consistent with simulations based on the models tuned to LHC data, such as EPOS-LHC and QGSJII-04, up to about $1{\times}10^{16}$ eV. At higher energies, a growing muon deficit in the simulations is observed. In this chapter, the muon content is compared in data to the model expectations from simulations to assess whether UMD data is consistent with a muon deficit in air-shower simulations. Proton and iron primaries were considered, for the high-energy hadronic interaction models EPOS-LHC and QGSJII-04.

In Section 9.1, we present the quality cuts applied in the data selection. The parametrisation of the parameter β in the MLDF is detailed in Section 9.2. The muon estimator ρ_{450} is then determined with β fixed in the MLDF and subsequently converted into the zenith-independent muon estimator ρ_{35} in Section 9.3. The evolution of ρ_{35} with energy is illustrated using simulations in Section 9.4 and data in Section 9.5. Systematic uncertainties considered in the data analysis are discussed in Section 9.6. To mitigate the strong energy dependence of the muon estimator ρ_{35}, it is normalised by energy in Section 9.7, where the muon content

[1]For consistency in notation, the muon estimator ρ_{450} in Chapter 8 was written as $\hat{\rho}_{450}$ to emphasize the difference from the monte-carlo muon density at 450 m ρ_{450}^{True}.

in data is compared to model predictions from simulations. In Section 9.8, we compute the z-scale and $\ln A$, as defined in Ref. [40], to facilitate comparisons of muon density measurements across different experiments and analyses. Finally, in Section 9.9, we report the muon deficit observed in simulations.

9.1. Data selection

The muon content of EASs was studied using Phase I data, acquired with the former electronics (UB) from 2018 to 2022, and Phase II data, collected with the new electronics (UUB) between 2023 and September 2024 (see Section 2.1).

As is customary for the UMD, the reconstructed EASs were required to have energies larger than $1{\times}10^{17.3}$ eV and zenith angles smaller than 45°. Requesting these energy and zenith angle cuts ensures a T4 efficiency above 98% [99]. Since the UMD trigger depends on the SD trigger, events were selected based on full SD trigger efficiency to minimise biases from upward fluctuations.

Quality cuts were also applied to the SD and UMD reconstruction. Periods of unreliable data, referred to as "bad periods", were excluded. Only events in which the "hottest" SD station, defined as the station nearest to the shower core, was paired with a functioning UMD module were considered. Additionally, a 6T5 trigger was required for an event to be included in the analysis, ensuring that the six SD stations closest to the "hottest" station were operating properly.

9.2. Parametrisation of β

As explained in Section 8.3, the parameter β is allowed to vary on an event-by-event basis and is then parametrised as a function of the zenith angle and the energy of the shower. The muon estimator ρ_{450} is subsequently determined with β fixed in the MLDF. The events to parametrise β are selected based on the number of counters that triggered within a distance around 450 m. In this analysis, a minimum of five triggered counters was required.

The parametrisation of β for Phase I data is presented in Fig. 9.1 and Fig. 9.2. In Fig. 9.1, the average β is calculated for each energy bin as a function of sec θ. Each curve is fitted using the equation $\beta = A\,(\sec\theta - 1.2) + B$. To ensure sufficient data for the fit in sec θ, the highest energy bin considered is $1{\times}10^{18.3}$ eV. The coefficients A and B obtained from the fit are exhibited in Fig. 9.2 as a function of the shower energy. The coefficient A is calculated as the average across all energy bins, as indicated by the dark line. The coefficient B is treated as energy-dependent and parametrised as $B = B_1(\log(E/\text{eV}) - 17.8) + B_0$ (dark line). The same analysis was performed to estimate β for Phase II data.

An example of a reconstructed event is shown in Fig. 9.3, where the muon

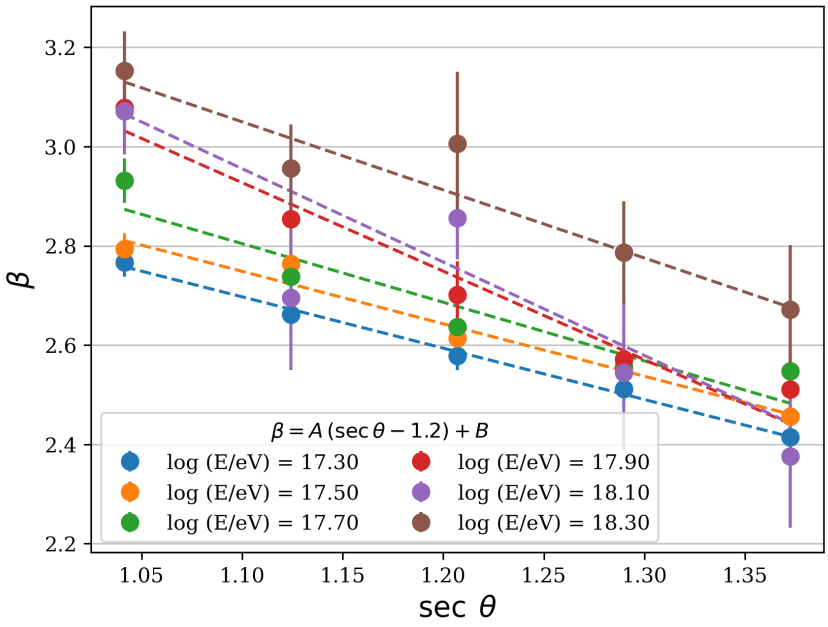

Figure 9.1: Phase I average β for each energy bin as a function of sec θ. The curves are fitted with $\beta = A\,(\sec\theta - 1.2) + B$.

estimator ρ_{450}, indicated by a dark star, was determined with β fixed in the MLDF. This event corresponds to one of the most energetic showers measured with the UMD, with an energy of approximately 10^{19} eV. The reconstructed muon densities, derived from the combined strategy, are displayed as empty markers, with each UMD acquisition mode applied in the regime where it yields the best performance, as discussed in Section 8.1.

9.3. CONSTANT INTENSITY CUT

The aim is to obtain a zenith-independent muon estimator by combining the measurements of ρ_{450} at different zenith angles. Given that showers arriving at larger zenith angles have to go through more atmosphere before reaching the detectors, the Constant Intensity Cut (CIC) method [100] is used to correct for this geometrical effect.

The CIC method relies on the assumption that cosmic rays arrive isotropically, which is consistent with observations in the energy range considered [101]. After correcting for the attenuation of the atmosphere, the isotropy assumption implies that the number of events in a detector $\mathrm{d}N/\mathrm{d}\sin^2\theta$ is expected to be constant in an energy region where the detector is fully efficient. By forcing the expected number of events in equal-sized $\sin^2\theta$ bins to be constant, the attenuation curve $f_{\mathrm{att}}(\theta)$ is determined from the CIC method to infer a zenith-independent muon estimator $\rho_{\mathrm{ref}}(E)$, for the reference zenith angle θ_{ref}, as $\rho_{\mathrm{ref}}(E) = \frac{\rho_{450}(E,\theta)}{f_{\mathrm{att}}(\theta)}$. The

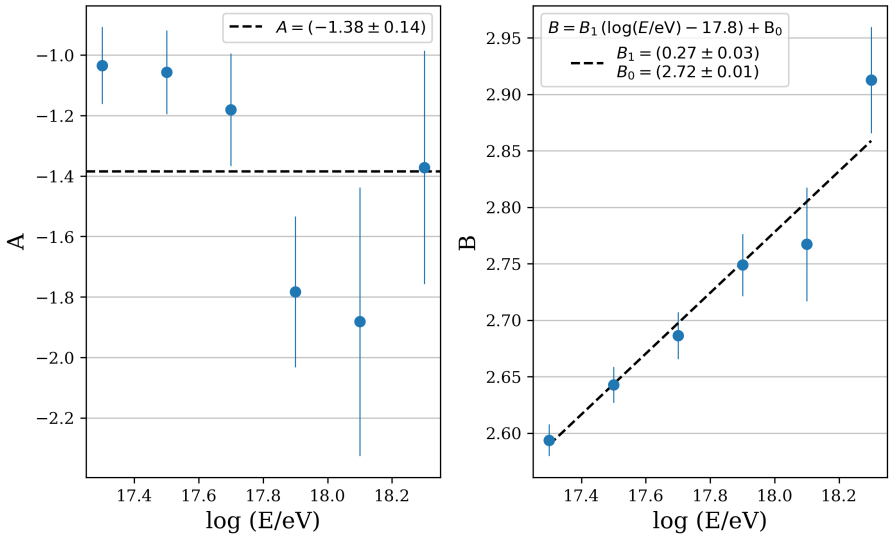

Figure 9.2: Coefficients A and B of the β parametrisation as a function of the shower energy.

reference zenith angle θ_{ref} is usually chosen as the median of the measured zenith angles. However, $\theta_{\text{ref}} = 35°$ was chosen as in previous studies [96] for comparison, resulting in $\rho_{35}(E) f_{\text{att}}(\theta) = \rho_{450}(E, \theta)$.

The functional form chosen empirically [102] to describe the relative amount of attenuation of the air shower is

$$f_{\text{att}}(\theta) = 1 + ax + bx^2, \tag{9.1}$$

where $x = \sin^2\theta - \sin^2\theta_{\text{ref}}$, a and b are the parameters to be found by minimising, for a fixed cut intensity n_{cut}, the following expression

$$\text{LS}(a, b) = \sum_{i=1}^{N_\theta} \frac{1}{\sigma_i^2} (\rho_{450,i}^{\text{cut}} - \rho_{35}^{\text{cut}} f_{\text{att}}(\theta_i, a, b))^2, \tag{9.2}$$

where ρ_{35}^{cut} is a fit parameter, N_θ is the number of $\sin^2\theta$ bins considered, $\rho_{450,i}^{\text{cut}}$ is the muon density in the i-th $\sin^2\theta$ bin and $\sigma_i = \sqrt{n_{\text{cut}}}$ the Poissonian error.

The shape of $f_{\text{att}}(\theta)$ is dependent on both the energy and the average mass of the primary particles at that energy, given that the attenuation that a shower undergoes before being detected is related to the depth of shower maximum and the particle content. This implies that a single choice of n_{cut} could introduce a mass and/or energy bias [102]. Therefore, the attenuation function is obtained from a global fit using different n_{cut}. The attenuation curve parameters were obtained using the code provided by Ref. [103], for both data and simulations.

To illustrate the significance of computing the attenuation correction, Fig. 9.4 presents the ratio between vertical and inclined events for Phase I data, compar-

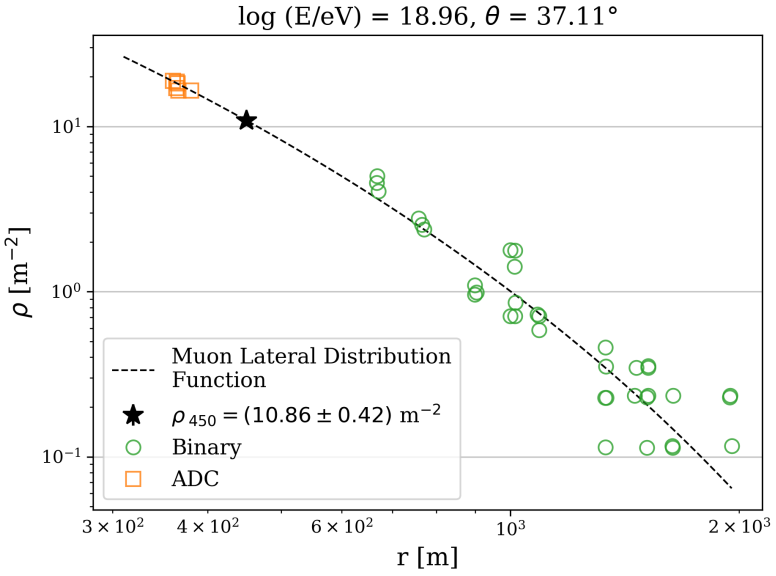

Figure 9.3: Example of a MLDF reconstruction (black curve) determined with β fixed. The event, with an energy of approximately 10^{19} eV, corresponds to one of the most energetic showers recorded by the UMD.

ing ρ_{450} (blue triangles) to ρ_{35} (light blue circles). Vertical events are selected within a zenith angle range of $\theta = [0, 30]°$, while inclined events correspond to $\theta = [30, 45]°$. After applying the attenuation correction, ρ_{35} serves as a zenith-independent muon estimator.

9.4. ρ_{35} IN SIMULATIONS

The muon content measured in data is compared in Section 9.7 to Monte-Carlo simulations of proton and iron showers using two hadronic interaction models: EPOS-LHC and QGSJII-04. The showers were simulated in Offline [73] with full-detector simulations, using discrete energies of $1{\times}10^{17.5}$, $1{\times}10^{18}$, $1{\times}10^{18.5}$, and $1{\times}10^{19}$ eV and zenith angles $\theta = [0, 12, 22, 32, 38]°$.

The average muon estimator $\langle\rho_{35}\rangle$ and the average of its natural logarithm $\langle\ln(\rho_{35})\rangle$ were calculated as functions of shower energy in Fig. 9.5 for the hadronic interaction models EPOS-LHC (top panel) and QGSJII-04 (bottom panel). Proton showers are represented by red markers, while iron showers are indicated by blue markers. The fitted curves, shown as dashed lines, follow the relations $\langle\rho_{35}\rangle = a\,(E/10^{18}\text{eV})^b$ with a power-law index $b \sim 0.9$ (see Eq. (9.3)) and $\langle\ln(\rho_{35})\rangle = A\,(\log(E/\text{eV}) - 17.8) + B$.

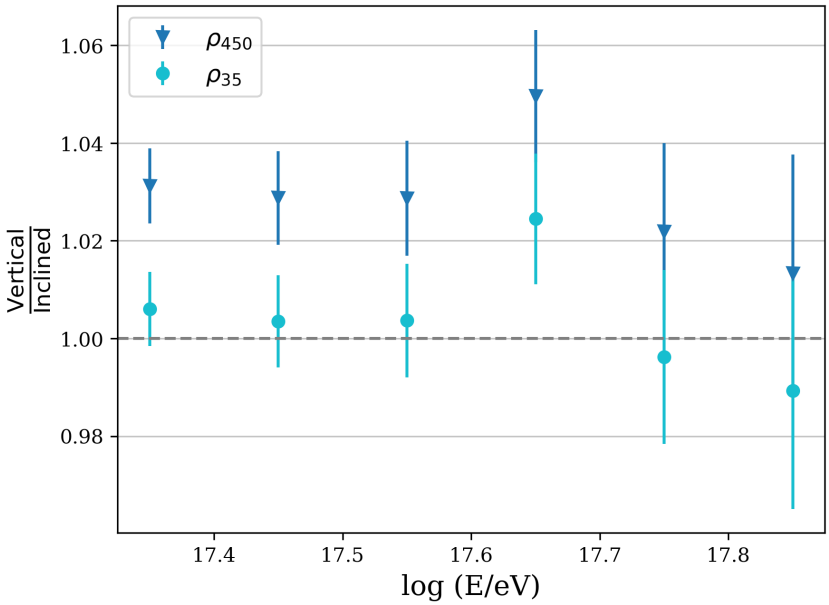

Figure 9.4: Ratio between vertical and inclined events for Phase I data, comparing ρ_{450} (blue triangles) to ρ_{35} (light blue circles).

9.5. ρ_{35} in data

In Section 8.2, we showed that to obtain the muon estimator ρ_{450} using the combined likelihood method, the ADC mode is employed in an event if there is at least one UMD module where the ADC mode measured more or equal to 70 muons. In Fig. 9.6, the fraction of events using the ADC mode is exhibited for Phase I (left panel) and Phase II data (right panel). The ADC mode is more useful when high muon densities are measured, so for low energy showers, the influence of the ADC mode on the total number of reconstructed events is small. For energies greater than $1{\times}10^{18.2}$ eV, more than half of the events were reconstructed with at least one UMD module in the MLDF using the ADC mode, while for energies above $1{\times}10^{18.6}$ eV, all events employed the ADC mode.

In Fig. 9.7, the muon estimator ρ_{35} is shown as a function of the shower energy for Phase I (left panel) and Phase II (right panel), with the average values represented by red stars.

9.6. Systematic uncertainties

The following systematic uncertainties were considered in the data reconstruction: the calibration of the ADC mode, the MLDF shape, and the energy reconstruction. While the systematic uncertainties presented in this section were accounted for in the Phase I data reconstruction, the same analysis was also

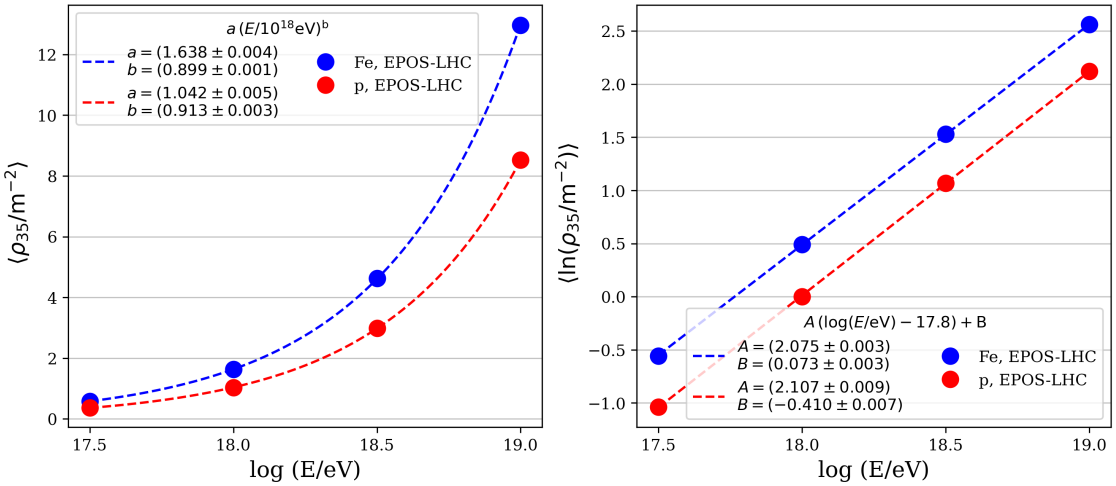

(a) Simulated with the hadronic interaction model EPOS-LHC.

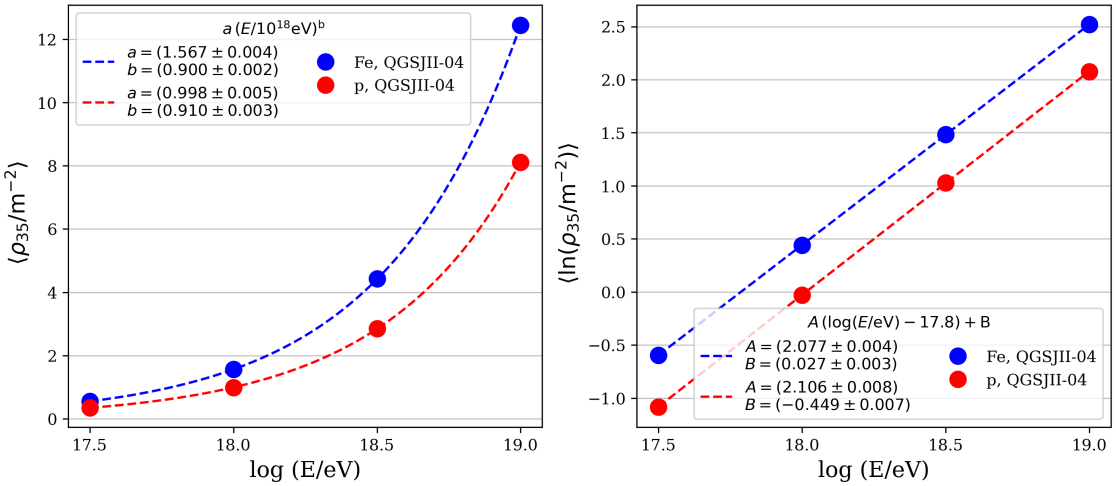

(b) Simulated with the hadronic interaction model QGSJII-04.

Figure 9.5: Average muon estimator $\langle \rho_{35} \rangle$ (left) and average of its natural logarithm $\langle \ln(\rho_{35}) \rangle$ (right) as a function of the shower energy.

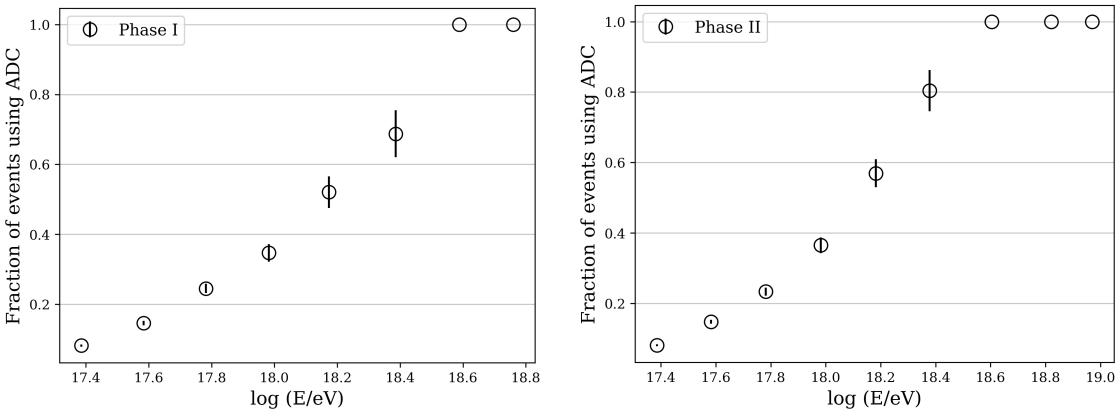

Figure 9.6: Fraction of events using the ADC mode as a function of the shower energy.

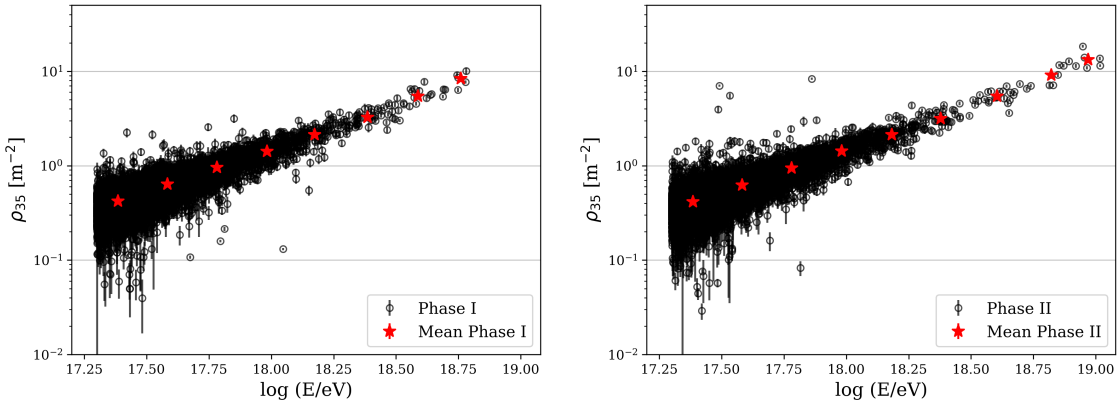

Figure 9.7: Muon estimator ρ_{35} for Phase I (left) and Phase II (right) as a function of the shower energy.

conducted for Phase II data.

The first systematic uncertainty arises from the long-term performance effects observed in the calibration of the ADC mode for Phase I, as detailed in Section 7.2.1. To account for this aging rate, the calibration curves of all detectors were modified by ±2.5%, and the corresponding muon estimator $\rho_{35}^{\pm\text{cal. sys.}}$ was computed.

The second systematic uncertainty is caused by the unknown MLDF shape. To assess the impact of parametrising the parameter β in the MLDF, the bias and resolution of β are computed in Fig. 9.8 for events where β was allowed to vary on an event-by-event basis and compared to the fixed value from the parametrisation β_{param}. The events selected to allow β as a free parameter required a minimum of five triggered counters within a distance around 450 m, as detailed in Section 9.2. The bias of β in Fig. 9.8, illustrated as blue dots, remains flat and approximately zero, as expected from parametrising the parameter β properly in Section 9.2. The resolution of β, represented by orange dots, is fitted as a function of shower energy using the equation $\sigma = a\, e^{-b\,(\log(E/\text{eV})-17.8)} + c$. To account for the uncertainty due to the unknown MLDF shape, $\rho_{35}^{\pm\beta\text{ sys.}}$ was calculated by varying β by $\pm\sigma$.

The third and most significant systematic uncertainty is associated with the energy reconstruction of the Pierre Auger Observatory. The total systematic uncertainty of the energy scale is 14% [104], dominated by effects such as the calibration of the FD telescopes, atmospheric effects, and several reconstruction uncertainties related to the shower profile. The effect of the energy-scale uncertainty is examined by shifting the reconstructed energy in the dataset by ±14% and computing $\rho_{35}^{\pm E\text{ sys.}}$.

The bias of the systematic uncertainties $\rho_{35}^{\text{sys.}}$ is shown in Fig. 9.9 for Phase I. The calibration systematics are represented by light blue triangles, whereas the systematics due to the MLDF shape are displayed by violet triangles. As observed,

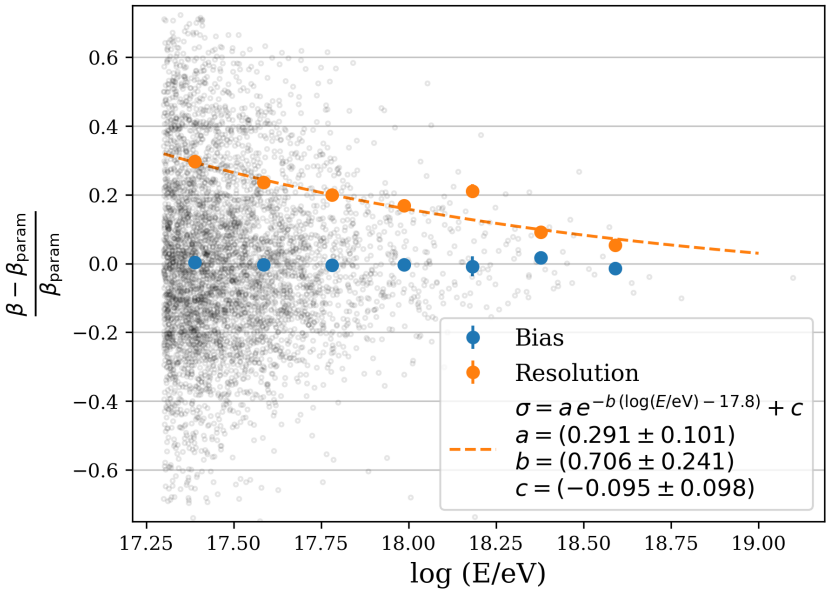

Figure 9.8: Bias and resolution of β for Phase I data as a function of the shower energy, comparing events where β was allowed to vary on an event-by-event basis to events where β_{param} was fixed from the parametrization.

the systematic uncertainties related to the MLDF shape are more significant for low energy showers, where fewer stations are involved in the MLDF reconstruction, while the systematic uncertainties from the calibration of the ADC mode have more impact at high energy showers, as more muons are measured and the ADC mode is consequently used more. It is worth noting that the most important systematic uncertainty arises from the energy reconstruction, with an impact of approximately -10% and 15% in $\rho_{35}^{\text{sys.}}$, as indicated by the black triangles. The total systematics are computed by summing all the systematic uncertainties in quadrature. The total systematic uncertainties are taken as the average across all energy bins, represented by the green dashed lines, while the systematics associated to the UMD are shown with red solid lines.

9.7. MUON CONTENT OF DATA COMPARED TO SIMULATIONS

To soften the strong energy dependence in the muon estimator ρ_{35} (see Fig. 9.7), the muon estimator is normalised by energy. The normalised values $\frac{\rho_{35}}{(E/10^{18}\text{eV})^{0.9}}$ are exhibited in Fig. 9.10 for Phase I (top panel) and Phase II (bottom panel) as a function of the shower energy. The average values are displayed by round black markers, where the energy position of the marker corresponds to the mean of the energy bin. The energy bins considered are indicated as light grey vertical lines. Error bars denote the statistical uncertainties, while the total systematics are represented as dark horizontal dashes. The systematic uncertainties are dominant

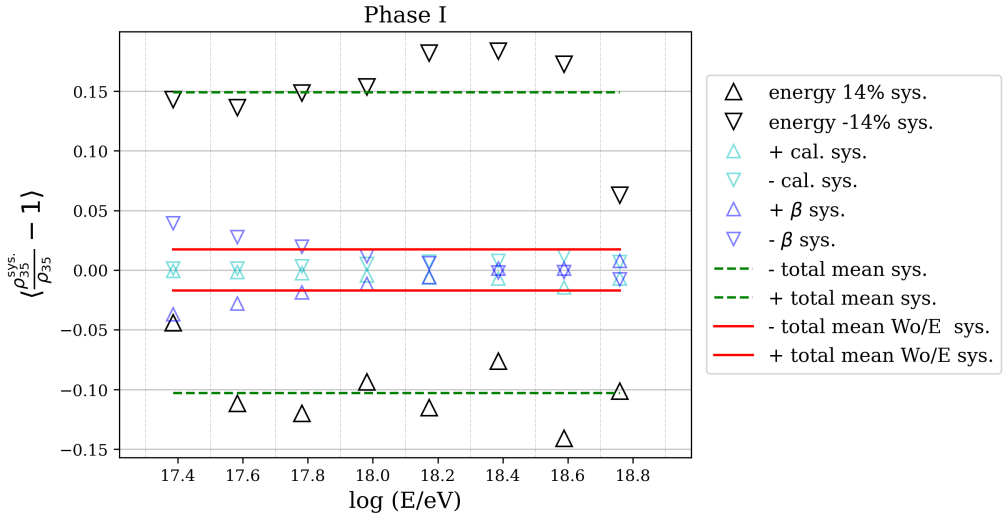

Figure 9.9: Bias of the systematic uncertainties $\rho_{35}^{\text{sys.}}$ for Phase I.

with respect to the statistical ones. The dashed and dotted lines in red and blue colours show the expectations for proton and iron primaries from the hadronic interaction models EPOS-LHC and QGSJII-04, respectively.

The average normalised values $\frac{\rho_{35}}{(E/10^{18}\text{eV})^{0.9}}$ from Fig. 9.10 are illustrated in Fig. 9.11 for Phase I (blue squares) and Phase II (black circles) with its corresponding error bars from the statistical uncertainties. The total systematic uncertainties are represented as light bands and the systematics purely from the UMD (without the energy-scale dominant systematic) are presented as darker bands. The number of events in each energy bin is indicated in brackets for each data-set. The data from Phase I and Phase II is consistent within statistical errors. More events were measured in Phase II than in Phase I due to the deployment of new UMD stations during Phase II. The muon content is compared to the one in simulations, where the expectations for proton and iron primaries are illustrated as red and blue lines. For the three highest energy bins the muon estimator shows a trend towards a heavier composition.

The UMD engineering array results, obtained using standard PMTs instead of SiPMs as photodetectors, published in Ref. [96], are shown in Fig. 9.11 as orange triangles. The engineering array of the UMD consisted of seven sets of scintillator detectors, each equipped with two 5 m^2 modules and two 10 m^2 modules, differing from the final design, which includes three 10 m^2 modules. The PMT-based results were obtained using the binary mode of the UMD to identify muon patterns, applying corner-clipping corrections and accounting for the effective efficiency in counting individual muons due to light attenuation along the module fibers. These results were computed over a one-year period, starting in October 2015, using approximately 10 times fewer events than those

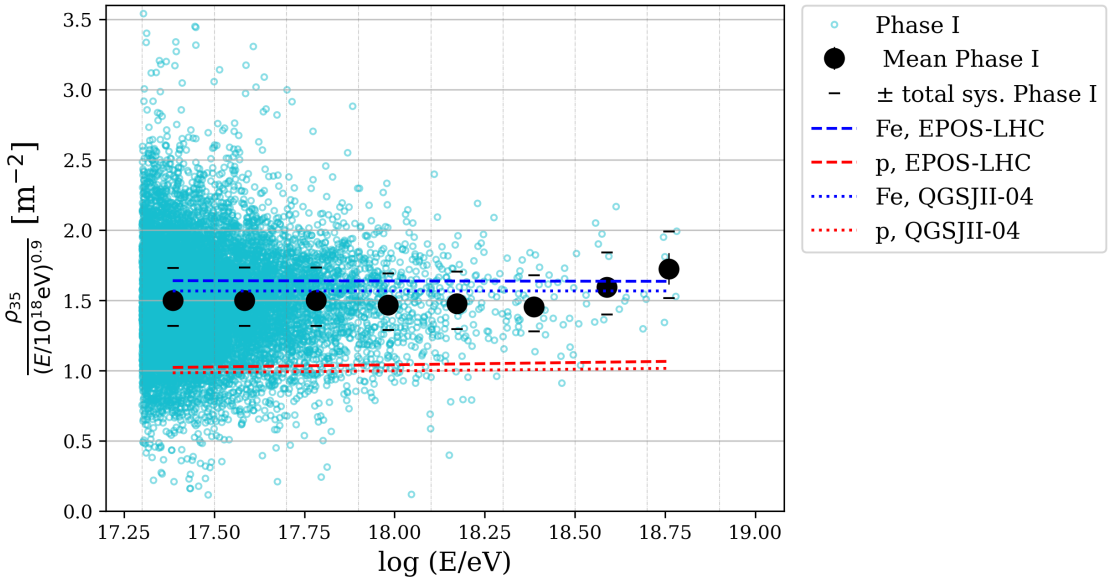

(a) Phase I data.

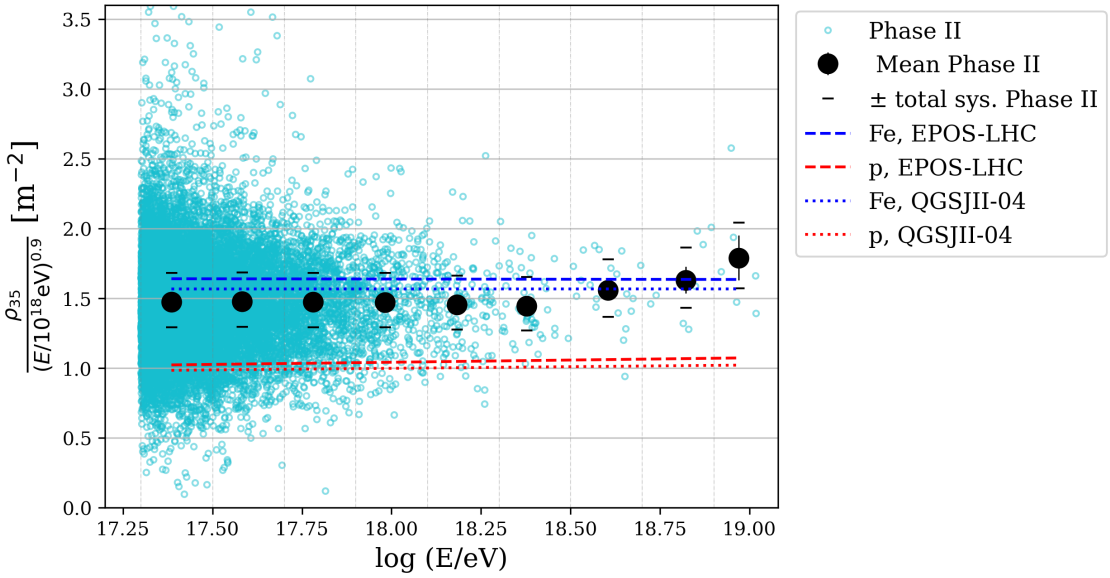

(b) Phase II data.

Figure 9.10: Normalized values $\frac{\rho_{35}}{(E/10^{18}\text{eV})^{0.9}}$ for Phase I (top) and Phase II (bottom) as a function of the shower energy.

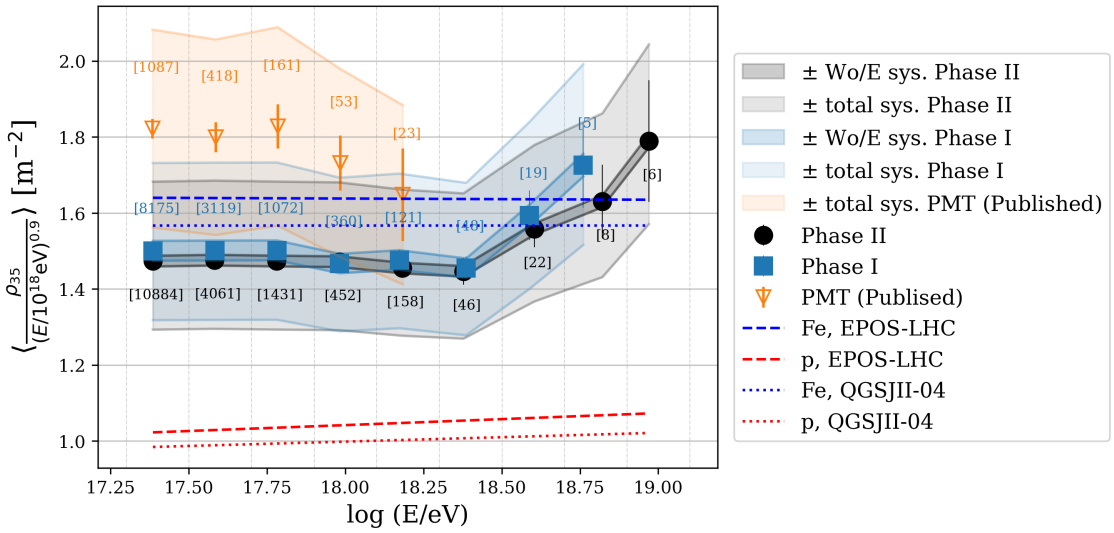

Figure 9.11: Average normalized values $\frac{\rho_{35}}{(E/10^{18}\text{eV})^{0.9}}$ for both Phases as a function of the energy of the shower. The results, reconstructed with SiPMs as photodetectors, are compared to the PMT analysis published in Ref. [96].

measured in this work for Phase II. While clear differences exist between the data obtained in this study using SiPMs and the PMT-based analysis, they remain within the systematic uncertainties. It is important to mention that similar results to those presented here have been reported in Refs. [97, 98] for reconstructions performed with SiPMs using only binary mode information. For example, in Ref. [98] simulations of the UMD were used to train a deep-learning neural network (DNN) to reconstruct muon densities from binary traces. Although the differences between SiPM- and PMT-based data require further investigation to be fully understood, some remarks can still be made regarding the discrepancies between both analyses. In the SiPM analysis, a muon is defined if a pattern of at least 4 consecutive positive bits, i.e., "1111...", is found in the binary trace, whereas in the PMT analysis the strategy was "111" or "101" in three consecutive bits. The MLDF parameters in the PMT analysis were derived from simulation studies, while for SiPMs, they were investigated using both data [64] and simulations. Further investigation of the PMT results is needed to assess the influence of factors such as the 5 m^2 modules in the dataset, the impact of modifying the muon pattern for muon identification or modifying the parameters of the MLDF reconstructions, the corrections associated to corner-clipping and to effective efficiency.

It is worth noting that for the three highest energy bins in Fig. 9.11 the number of events is less than 40 per bin. In the following sections the results of the z-scale, ln A and muon deficit are presented for all energy bins, but it is important to emphasise that no definitive conclusions can be drawn due to the limited

statistical data for events with energies higher than $1{\times}10^{18.5}$ eV.

9.8. ESTIMATION OF z-SCALE AND $\ln A$

According to the Matthews-Heitler model of air showers (see Section 1.3.2), the muon number depends on the mass A and energy E of the cosmic ray following

$$N_\mu = A\left(\frac{E}{A\,C}\right)^\beta = A^{1-\beta}\left(\frac{E}{C}\right)^\beta, \tag{9.3}$$

with power-law index $\beta \sim 0.9$ and energy constant C. Moreover, taking the logarithm on both sides and computing the mean, the following linear equation can be obtained

$$\langle \ln N_\mu \rangle = (1-\beta)\langle \ln A \rangle + \beta \langle \ln\left(\frac{E}{C}\right)\rangle. \tag{9.4}$$

To compare the measurements of the muon density between different experiments and analyses, a z-scale was defined in Ref. [40] as

$$z := \frac{\ln(N^{\text{data}}_{\mu,\,\text{det}}) - \ln(N^{\text{p}}_{\mu,\,\text{det}})}{\ln(N^{\text{Fe}}_{\mu,\,\text{det}}) - \ln(N^{\text{p}}_{\mu,\,\text{det}})} \tag{9.5}$$

where $N^{\text{data}}_{\mu,\,\text{det}}$ is the measured muon density by the detector, while $N^{\text{p}}_{\mu,\,\text{det}}$ and $N^{\text{Fe}}_{\mu,\,\text{det}}$ are the proton and iron muon densities derived from full-detector simulations. Since muon measurements are performed in each experiment under very different conditions and using different techniques, each experiment is compared to air shower simulations. Consequently, the z-scale adopts air shower simulations as a universal reference frame, where $z = 0$ corresponds to pure proton showers and $z = 1$ to pure iron showers, assuming there are no discrepancies between real and simulated air showers. The advantage of the z-scale is that biases of the form $\ln(N_{\mu,\,\text{det}}) = A + B\ln(N_{\mu,\,\text{true}})$ in the measured muon density with respect to the true muon density are cancelled in Eq. (9.5) [40].

To estimate the muon scale z using the muon density ρ_{35} from the UMD, it is necessary to introduce the mean within a given energy bin, expressed as

$$z = \frac{\ln(\langle \rho^{\text{data}}_{35}\rangle) - \ln(\langle \rho^{\text{p}}_{35}\rangle)}{\ln(\langle \rho^{\text{Fe}}_{35}\rangle) - \ln(\langle \rho^{\text{p}}_{35}\rangle)}. \tag{9.6}$$

Since the z-scale is computed relative to simulations, different results are obtained for each hadronic interaction model. The z-scale is exhibited in Fig. 9.12 for EPOS-LHC and for QGSJII-04 in the top and bottom panels, respectively. It is worth noting that the z-scale can varied up to $\sim \pm 0.25$ due to the systematic

uncertainties, represented as light bands, mainly from the energy-scale. If there are no discrepancies between real and simulated air showers, the data suggest an energy-dependent trend. The z values rise above the iron line for EPOS-LHC and for QGSJII-04 beyond the energies of $\sim 1{\times}10^{18.75}$ eV and $\sim 1{\times}10^{18.6}$ eV, respectively. The z-scale results are consistent at the highest energies with previous measurements reported by the Pierre Auger Observatory (red band), obtained using the SD and the FD, and with AGASA (orange band). In contrast, they show tension with Yakutsk (violet band) and, as mentioned earlier, with the PMT-based results from the UMD (green band). The comparison data was extracted from Ref. [105].

In Ref. [40], the mass composition estimator, z_{mass}, is introduced as $z_{\text{mass}} = \frac{\langle \ln A \rangle}{\ln(56)}$, derived from Eq. (9.4) and Eq. (9.5). The estimator $\langle \ln A \rangle$ can thus be calculated using the muon density ρ_{35} from the UMD, by binning in energy the following equation

$$\langle \ln A \rangle = \ln(56)\, z_{\text{mass}} = \ln(56)\, \frac{\langle \ln(\rho_{35}^{\text{data}}) \rangle - \langle \ln(\rho_{35}^{\text{p}}) \rangle}{\langle \ln(\rho_{35}^{\text{Fe}}) \rangle - \langle \ln(\rho_{35}^{\text{p}}) \rangle}. \tag{9.7}$$

It is important to note that the estimators z and z_{mass} are in principle different, as computing the logarithm of the mean muon content is not equivalent to taking the mean of the logarithm. A detailed explanation of the differences between z and z_{mass} can be found in Refs. [64, 40]. Both estimators of the muon scale can be biased if the detector simulations mismodel the real detector effects or if there is a composition bias in the reconstructed muon density. In particular, a poor detector resolution or using wide energy bins can also introduce biases in z_{mass} [106].

In Fig. 9.13, $\langle \ln A \rangle$ is computed for EPOS-LHC (top panel) and for QGSJII-04 (bottom panel). Assuming there are no discrepancies between real and simulated air showers, the data suggest an energy-dependent trend for both hadronic interaction models, going from a lighter to a heavier mass composition beyond the energies of $\sim 1{\times}10^{18.5}$ eV. The $\langle \ln A \rangle$ results reported by the Pierre Auger Observatory using the maximum shower depth, X_{max}, are illustrated as a light blue band. Although both measurements exhibit an energy-dependent trend, clear inconsistencies are observed between the mass composition measurements derived from the two leading observables (X_{max} and N_{μ}) suggesting that the hadronic interaction models fail to fully describe all aspects of hadronic physics in air showers. Assuming the correctness of the maximum shower depth results, the number of muons must therefore be adjusted to achieve consistency, as will be addressed in the following section.

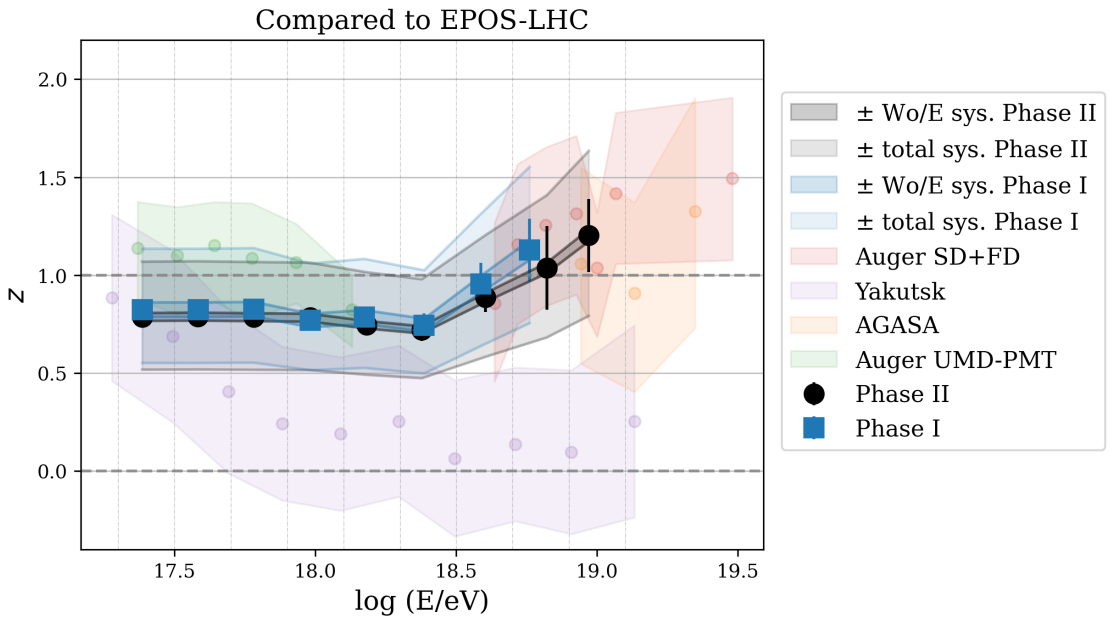

(a)

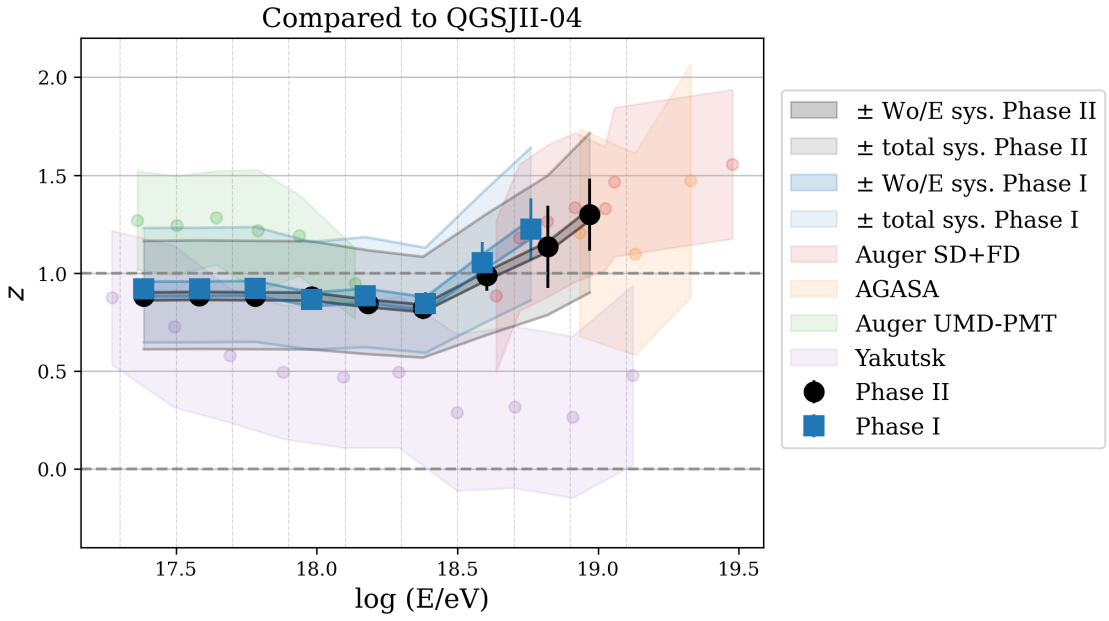

(b)

Figure 9.12: z-scale between data and simulations with the hadronic interaction models EPOS-LHC (top) and QGSJII-04 (bottom).

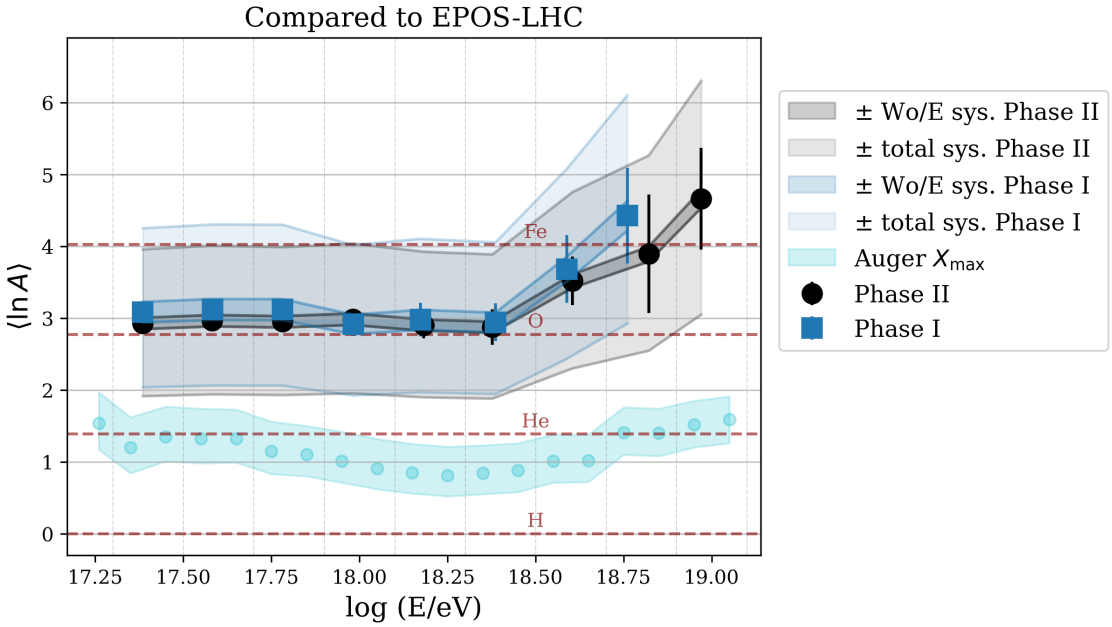

(a)

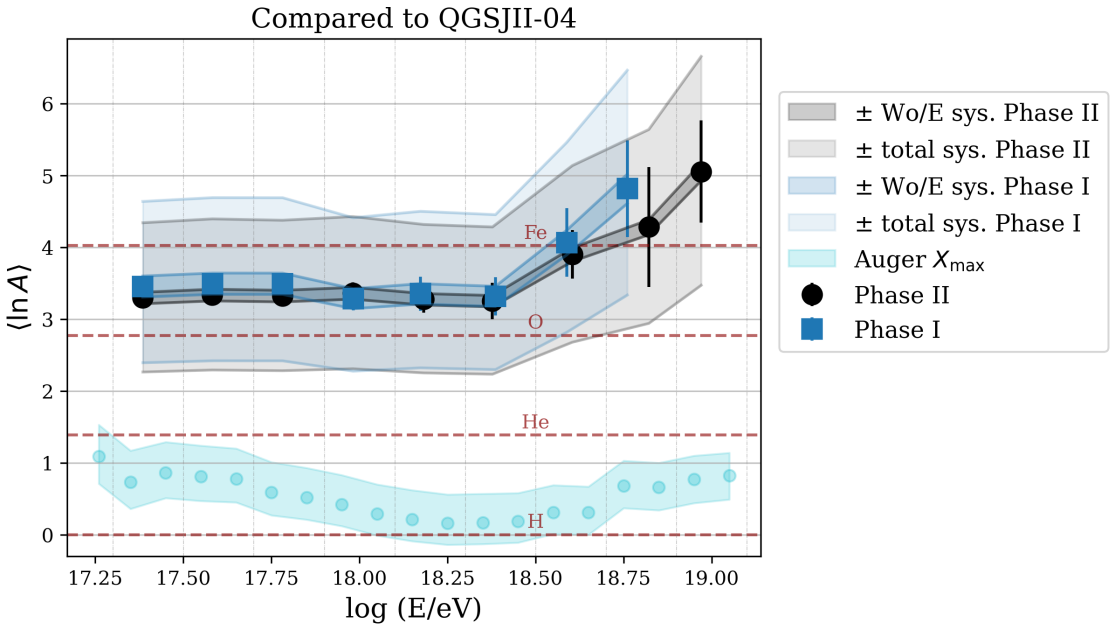

(b)

Figure 9.13: $\langle \ln A \rangle$ between data and simulations with the hadronic interaction models EPOS-LHC (top) and QGSJII-04 (bottom).

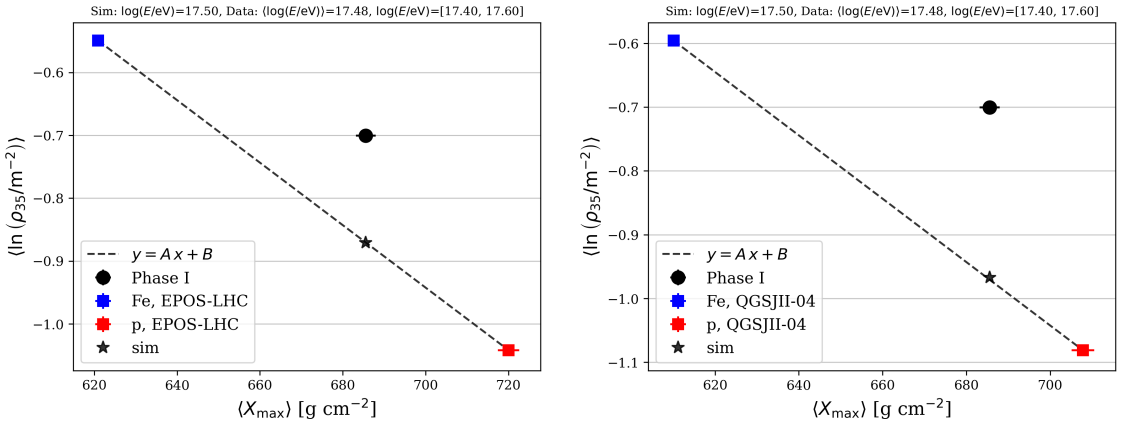

Figure 9.14: $\langle \ln(\rho_{35}) \rangle$ as a function of $\langle X_{\max} \rangle$ for the energy bin of $\log(E/\text{eV})$= 17.5, comparing Phase I data to the hadronic interaction models EPOS-LHC (left panel) and QGSJII-04 (right panel).

9.9. MUON DEFICIT

The muon deficit f between data and simulations [107] is calculated as

$$f = e^{\langle \ln(\rho_{35}^{\text{data}}) \rangle - \langle \ln(\rho_{35}^{\text{sim}}) \rangle}, \tag{9.8}$$

where $f = 1$ indicates agreement between the muon content of simulations and data, $f > 1$ indicates there is a muon deficit in simulations and $f < 1$ indicates a muon excess in simulations.

To estimate $\langle \ln(\rho_{35}^{\text{sim}}) \rangle$, $\langle \ln(\rho_{35}) \rangle$ is computed as a function of the maximum shower depth, $\langle X_{\max} \rangle$, using the values of $\langle \ln(\rho_{35}^{\text{p}}) \rangle$, $\langle \ln(\rho_{35}^{\text{Fe}}) \rangle$, $\langle X_{\max}^{\text{p}} \rangle$, and $\langle X_{\max}^{\text{Fe}} \rangle$, extracted from the simulated showers. In Fig. 9.14, this procedure is demonstrated for the energy bin of $\log(E/\text{eV}) = 17.5$, comparing Phase I data to the hadronic interaction models EPOS-LHC (left panel) and QGSJII-04 (right panel). A linear fit of the form $y = Ax + B$ is performed, indicated by the dark dashed line, between the proton and iron estimators, represented by red and blue squares, respectively. Assuming the correctness of the maximum shower depth measurements, $\langle \ln(\rho_{35}^{\text{sim}}) \rangle$, denoted by the dark star, is obtained by evaluating the fit at the measured maximum depth, extracted from Ref. [108].

The same procedure is applied to each of the simulated energy bins, yielding energy-dependent coefficients A and B, which are fitted with the equations: $A(E) = A_0 \, (\log(E/\text{eV}) - 17.8) + A_1$, and $B(E) = B_0 \, (\log(E/\text{eV}) - 17.8) + B_1$. Using the measured values of $\langle X_{\max} \rangle$ from Ref. [108] along with the parametrisations for $A(E)$ and $B(E)$, $\langle \ln(\rho_{35}^{\text{sim}}) \rangle$ is estimated for all the energy bins of the measured data.

The muon deficit f is calculated in Fig. 9.15 for EPOS-LHC and QGSJII-

04, shown in the top and bottom panels, respectively. A muon deficit is observed in simulations for both hadronic interaction models, suggesting an energy-dependent trend in the muon deficit. Due to the systematic uncertainties, primarily arising from the energy scale, the muon deficit varies up to $\sim \pm 20\%$. It is important to note that even when considering the lower bound of the systematic uncertainties, a muon deficit remains apparent. The muon deficit ranges from $\sim$ 22% ± 1(stat.) ± 24(sys.) at the lowest energy to $\sim$ 40% ± 11(stat.) ± 24(sys.) at the highest energy for EPOS-LHC, and from $\sim$ 36% ± 1(stat.) ± 24(sys.) to $\sim$ 55% ± 11(stat.) ± 24(sys.) for QGSJII-04.

As detailed in Ref. [40], muon measurements seem to be consistent with simulations based on the models tuned to LHC data, such as EPOS-LHC and QGSJII-04, up to about $1{\times}10^{16}$ eV. At higher energies, a growing muon deficit in the simulations is observed.

The significance of the slope in a linear regression is determined using a t-test, calculating the t-statistic and the p-value to test whether the slope is significantly different from zero. We compute the t-statistic defined as $t = \frac{\hat{\beta}}{SE(\hat{\beta})}$, where $\hat{\beta}$ is the estimated slope from the sample data in Fig. 9.15 and $SE(\hat{\beta})$ is the standard error of the slope. The p-value is then the probability of measuring a slope $\hat{\beta}$, assuming that the true slope was zero. The null hypothesis being tested is that the slope is zero and it will be rejected if the p-value is small. The p-value is computed from the t-statistic, assuming a t-distribution with $n-2$ degrees of freedom (n number of data points considered), as the probability of getting a t-statistic T greater than the observed value $|t|$ defined by equation $p = 2\,P(T > |t|) = 2\,(1 - P(T \leq |t|))$. The factor two accounts for the two-tailed test and $P(T \leq |t|)$ is the Cumulative Distribution Function (CDF).

The two estimators t-statistic and p-value are illustrated in Table 9.1, where the significance of the slope from Fig. 9.15 was computed taking into account the statistical error bars of the data-set. The systematic uncertainties were not considered since they are independent of the shower energy. The data is compared to EPOS-LHC (top panel) and QGSJII-04 (bottom panel), including also the results when computed the analysis using data up to $1{\times}10^{18.5}$ eV, given that for higher energy bins the number of events is less than 40 per bin (see Fig. 9.11). For Phase II data and both hadronic models, given that t is large and the p-value is small (less than 0.05), the slope is statistically significant, indicating that the energy of the shower affects the muon deficit. For Phase I data, the same conclusion can be drawn except for the hadronic model EPOS-LHC when using data up to $1{\times}10^{18.5}$ eV, given that the p-value is larger than 0.05 and t is small. In that particular case, the slope is not statistically significant thus there is no strong evidence that the muon deficit depends on the energy of the shower.

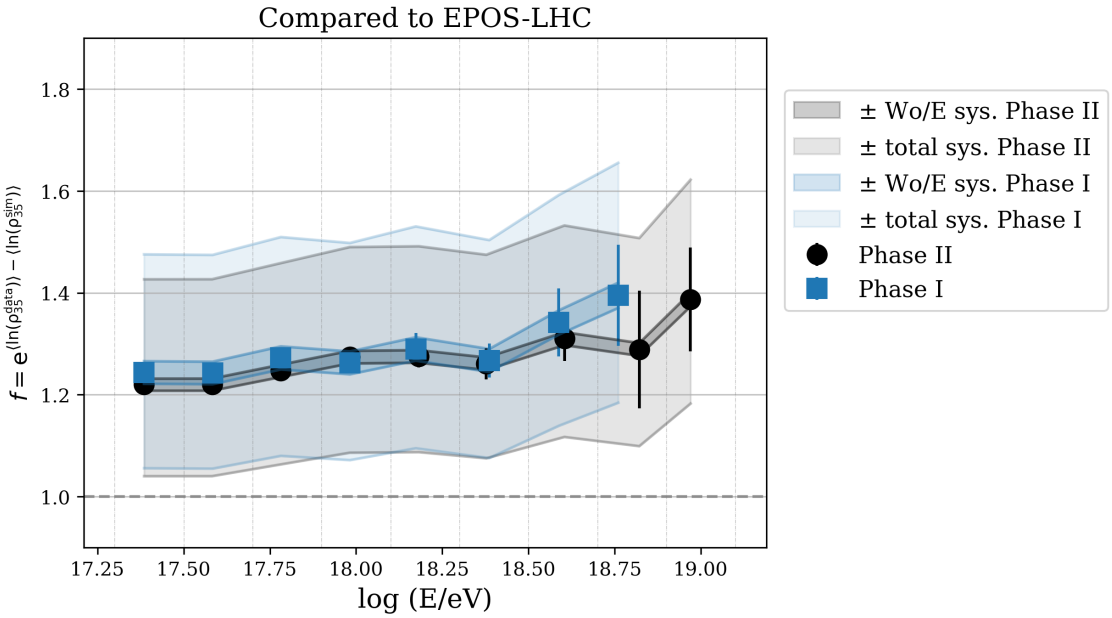

(a)

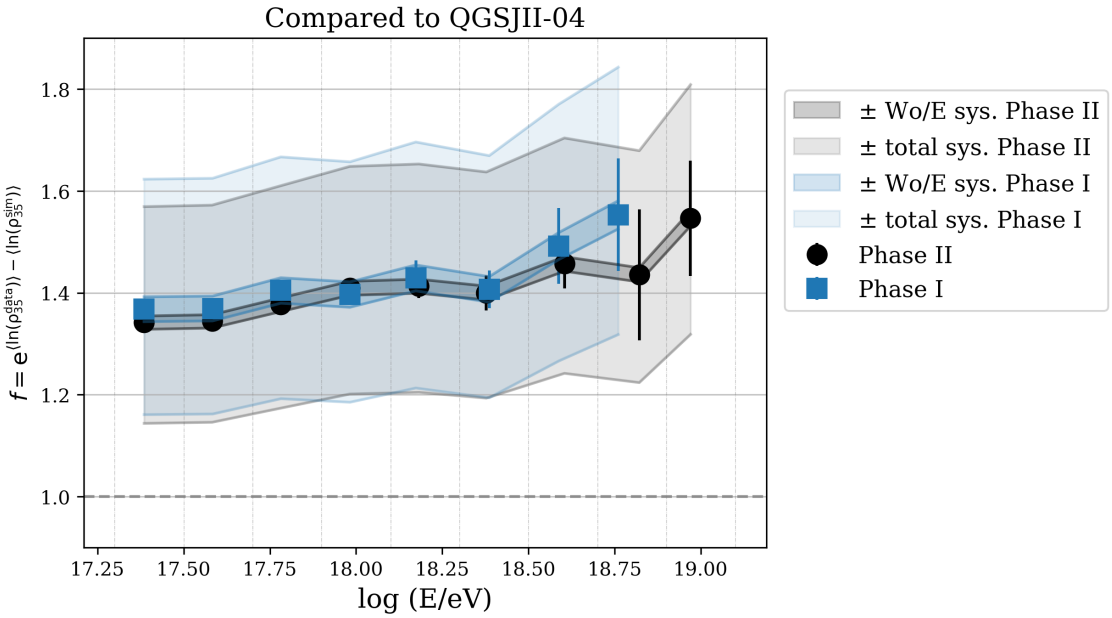

(b)

Figure 9.15: Muon deficit between data and simulations with the hadronic interaction models EPOS-LHC (top) and QGSJII-04 (bottom).

EPOS-LHC	t-statistic	p-value
Phase I	2.953	0.026
Phase II	5.135	0.001
Phase I up to $1\times10^{18.5}$ eV	2.427	0.072
Phase II up to $1\times10^{18.5}$ eV	4.512	0.011
QGSJII-04	**t-statistic**	**p-value**
Phase I	3.695	0.010
Phase II	6.037	0.001
Phase I up to $1\times10^{18.5}$ eV	3.136	0.035
Phase II up to $1\times10^{18.5}$ eV	5.350	0.006

Table 9.1: Significance of the slope in the muon deficit with the shower energy, compared to EPOS-LHC (top) and QGSJII-04 (bottom).

9.10. Summary

In this chapter, we have presented the first measurement of the muon content in EASs obtained using the information of the ADC mode of the UMD. The analysis was conducted using Phase I data, acquired with the former electronics (UB) from 2018 to 2022, and Phase II data, collected with the new electronics (UUB) between 2023 and September 2024. More events were measured in Phase II than in Phase I due to the deployment of new UMD stations during Phase II.

To soften the strong energy dependence in the muon estimator ρ_{35}, the muon estimator was normalised by energy. The normalised values $\frac{\rho_{35}}{(E/10^{18}\text{eV})^{0.9}}$ were shown to be consistent within statistical errors between Phase I and Phase II data. Moreover, the normalised values obtained using the ADC mode were consistent with other results reported in Refs. [97, 98] using solely the information of the binary mode of the UMD. All these results were reconstructed using SiPMs as photodetectors and showed differences with the PMT-based results published in Ref. [96], which were derived from a dataset with lower statistical significance acquired with the UMD engineering array. The observed differences between the two photodetector technologies require further investigation to elucidate the underlying causes.

The muon content in data was compared to the model expectations from simulations based on the hadronic interaction models of EPOS-LHC and QGSJII-04 that are tuned to LHC data. Proton and iron primaries were considered. We computed the z-scale and $\ln A$, as defined in Ref. [40], to facilitate comparisons of muon density measurements across different experiments and analyses, adopting air shower simulations as a universal reference frame. The data suggested an energy-dependent trend for both hadronic interaction models, going from a lighter to a heavier mass composition beyond the energies of $\sim 1\times10^{18.5}$ eV, assuming there are no discrepancies between real and simulated air showers. However,

it is important to emphasise that no definitive conclusions can be drawn due to the limited statistical data, since there were only 60 events with energies higher than $1{\times}10^{18.5}$ eV.

The UMD data is consistent with a muon deficit in air-shower simulations for both hadronic interaction models, as established by other muon measurements [40]. The muon deficit f in simulations ranged from $\sim 22\% \pm 1(\text{stat.}) \pm 24(\text{sys.})$ at the lowest energy to $\sim 40\% \pm 11(\text{stat.}) \pm 24(\text{sys.})$ at the highest energy for EPOS-LHC, and from $\sim 36\% \pm 1(\text{stat.}) \pm 24(\text{sys.})$ to $\sim 55\% \pm 11(\text{stat.}) \pm 24(\text{sys.})$ for QGSJII-04. Since an energy-dependent trend was observed in the muon deficit, the significance of the slope was computed. Given the limited statistical data for high energy events, we studied also the implications of considering the data up to $1{\times}10^{18.5}$ eV. For Phase II data and both hadronic models, we found that the slope was statistically significant, even when removing the high energy events, indicating that the muon deficit is energy-dependent. For Phase I data, the same conclusion can be drawn except for the hadronic model EPOS-LHC when using data up to $1{\times}10^{18.5}$ eV.

It is worth noting that for the normalised values of ρ_{35}, the z-scale and $\ln A$, and the muon deficit f, the systematic uncertainties were dominant with respect to the statistical ones. The most significant systematic uncertainty arose from the energy reconstruction of the Pierre Auger Observatory, whose systematic uncertainty is 14% [104], with an impact of approximately -10% and 15% in $\rho_{35}^{\text{sys.}}$.

Chapter X

Final remarks

The Underground Muon Detector (UMD) plays a crucial role in the AugerPrime upgrade of the Pierre Auger Observatory, as it allows the direct measurement of a mass composition sensitive observable: the muonic component of the air shower. Identifying the masses of ultra-high-energy cosmic rays could help us solve the mysteries regarding their origin. Moreover, ultra-high-energy cosmic rays offer a unique opportunity to explore particle physics beyond the energy scales accessible by modern colliders.

The UMD is equipped with scintillation modules buried at 2.3 m, providing two complementary methods for muon estimation: binary mode for low particle densities and ADC mode for high particle densities. While the binary mode relies on the amplitude of the signals, the ADC mode depends on the charge of the signal determined by the energy deposited by muons in the detector.

The aim of this thesis was to improve the muon reconstruction for high particle densities estimated with the ADC mode and to use this information to accurately determine the muon content in air showers. Before any conclusion can be drawn from the comparison of the muon content between data and simulations, the ADC mode signal calculation, its calibration and reconstruction techniques had to be fully understand to enhance the data reconstruction and provide an unbiased muon estimator close to the shower core.

For an improved data reconstruction of the signals measured by the detector, two modules were developed and implemented in Offline after a comprehensive analysis of three years of data. The new algorithms, implemented in `MdADCGlitchCleaner` and `MdADCChargeCalculator`, improved the charge estimation of the ADC mode from the previous existing algorithm, by minimising the appearance of outliers and by enhancing the data quality. Additionally, during this development, we found periods of bad data to ensure high quality data for any subsequent analyses.

We provided a comprehensive analysis of the existing calibration strategy [60], known as 'online calibration' and implemented in the so-called 'ADCT1 files', designed to estimate the charge deposited by individual atmospheric muons using the T1 trigger from the associated WCD. From the calibration files, we developed a set of new monitoring tools that have been integrated into the UMD shifts to inspect the detector performance and to examine the quality of the data acquired on a daily basis. However, we showed that the online calibration introduces a bias favouring inclined, high-energy muons due to the trigger condition, which generates a significant bias in muon reconstruction.

First, we studied the ADC mode calibration using single muon simulations, showing the stronger dependence on muon energy and muon zenith angle of the ADC mode compared to the binary mode. Simulations were performed for omnidirectional atmospheric muons, those without knock-on electrons/positrons, and vertical muons to compare with the online calibration, validate agreement with UMD laboratory data, and analyse the reconstruction bias of the ADC mode.

Analysis of the ADCT1 files revealed that the T1 trigger requested from the associated WCD generated asymmetries between the halves of modules, in both charge and number of events. Additionally, the ADC and binary modes from the online calibration did not align with laboratory measurements, single muon simulations, or shower events. To investigate this, we conducted three studies: (i) simulations of muons detected in coincidence by the WCD and UMD, which reproduced observed data patterns; (ii) estimates showing that inclined muons in coincidence are an order of magnitude more frequent than vertical ones reaching the UMD after a WCD trigger; and (iii) an alternative ADC calibration using T3 shower events, revealing that the bias in muon reconstruction between binary and ADC modes can reach 45% with the online calibration but only 10% with the T3 shower events, though both methods showed a non-uniform bias increasing by $\sim$ 10% with the muon density, within the studied range of up to 100 muons.

We have shown that calibrating underground muon detectors based on plastic scintillators requires careful consideration of the interactions of penetrating particles through matter. Using the average charge from single vertical muons to calibrate the ADC mode, as originally proposed for the ADC mode reconstruction [63], introduces a bias in the reconstructed muon density, that can reach up to 20% for densities of $\sim$30 μ/m^2 in proton showers of $10^{17.5}$ eV. The bias is attributed to the increased energy deposition per muon, especially near shower axis, where higher-energy muons produce more knock-on electrons. We studied the energy deposition of the particles alongside the muons, and particularly whether the arriving electrons at the UMD were primarily knock-on or punch-through electrons, by comparing simulations where all particles were injected on ground with simulations where only muons were injected on ground and propagated through

the soil. Within the range where the detector is not saturated, besides muons, knock-on electrons dominate the energy deposition, although protons and other particles like π^+ and K^+ can also contribute slightly. The largest contribution of these particles to the energy deposition was observed for the lowest energy showers of $10^{17.5}$ eV and at the highest muon density of $\sim$30 μ/m^2, where 23% of the total energy is deposited by knock-on electrons and 8% by protons and other particles, mainly π^+ and K^+.

Calibration methods of underground muon detectors based on plastic scintillators should account for variations in the charge with the energy of the incoming muons, or any other related observable. To cope with this issue, a new calibration method in the ADC mode was presented, which consisted in parametrising the charge deposited per muon per vertical path-length using the binary mode and the distance to the shower core for low muon densities. This parametrised curve can then be used to calculate the charge per muon per vertical path-length at high muon densities by extrapolation. The method was shown to improve the bias in muon reconstruction, reducing it to less than 5%. The improved calibration strategy was applied to Phase I data, covering the years 2019, 2020, 2021, and 2022, and to Phase II data collected between 2023 and September 2024, resulting in calibration curves obtained for 105 modules. The bias in the number of muons reconstructed in data between ADC and binary modes was shown to be flat up to $N_\mu^{\text{Bin}} = 70$, where the binary mode serves as a reliable estimator. A long-term performance effect was observed between Phase I and Phase II, similar to the one reported in comparable scintillator detectors, and it was taken into account as a systematic uncertainty in the final results. Finally, the calibration curves, for both simulations and data, were integrated to the `MdADCMuonEstimator` module in Offline, thus the muon reconstruction of the ADC mode was finally complete.

After significantly improving the muon reconstruction for high particle densities, a combined likelihood method was developed that integrated both binary and ADC acquisition modes to reconstruct the Muon Lateral Distribution Function (MLDF). Since stations located near the shower core were found to exhibit a significant bias in core reconstruction, an additional penalty term was incorporated into the likelihood to treat the shower core as a free parameter. The final likelihood was evaluated using full-detector simulations. The parameters β and α of the MLDF were briefly reviewed, showing the importance of parametrising β, particularly for low-energy showers due to the limited number of stations involved. The standard UMD reconstruction with α=0.75 was shown to introduce a bias of less than ±3% in the muon density at the reference distance of 450 m. Finally, the merit factor to discriminate proton and iron showers was shown to improve by approximately 20% over previous works [63] for showers with an energy of $1\times10^{17.5}$ eV.

Finally, we have presented the first measurement of the muon content in EASs obtained using the information of the ADC mode of the UMD, covering a six-year period. The muon content of Phase I and Phase II data were shown to be consistent within statistical errors, and additionally, consistent with other results reported in Refs. [97, 98] using solely the information of the binary mode of the UMD. The most significant systematic uncertainty arose from the energy reconstruction of the Pierre Auger Observatory with an impact of approximately -10% and 15% in the muon content. Despite the observed differences between the SiPM-based results (this work and Refs. [97, 98]) and the PMT-based results (Ref. [96]) being within systematic uncertainties, their potential implications make further investigation necessary for a comprehensive understanding.

The muon content in data was compared to the model expectations from simulations of proton and iron primaries, based on the hadronic interaction models of EPOS-LHC and QGSJII-04 that are tuned to LHC data. As introduced in Ref. [40] to compare the measurements of the muon density between different experiments and analyses, we calculated the z-scale and $\ln A$. Assuming there are no discrepancies between real and simulated air showers, the data suggested an energy-dependent trend for both hadronic interaction models, going from a lighter to a heavier mass composition beyond the energies of $\sim 1{\times}10^{18.5}$ eV. Since there were only 60 events with energies higher than $1{\times}10^{18.5}$ eV, it is important to emphasise that no definitive conclusions can be drawn due to the limited statistical data.

The UMD data is consistent with a muon deficit in air-shower simulations for both hadronic interaction models, as established by other muon measurements [40], ranging from $\sim$ 22% ± 1(stat.) ± 24(sys.) at the lowest energy to $\sim$ 40% ± 11(stat.) ± 24(sys.) at the highest energy for EPOS-LHC, and from $\sim$ 36% ± 1(stat.) ± 24(sys.) to $\sim$ 55% ± 11(stat.) ± 24(sys.) for QGSJII-04. We showed that the muon deficit was observed to have an energy-dependent trend. We found that the slope was statistically significant for Phase II data and both hadronic models, even when removing the high energy events, indicating that the muon deficit is energy-dependent. The same conclusion can be drawn for Phase I data, except for the hadronic model EPOS-LHC when using data up to $1{\times}10^{18.5}$ eV. These conclusions provide a valuable input for improving the high-energy hadronic interaction models to ensure they accurately reproduce the observed muon content. Achieving this level of agreement would not only enhance the reliability of these models but also allow for a reduction in the systematic uncertainties associated with mass composition analyses. Consequently, this could lead to a deeper understanding of the origin of cosmic rays.

Chapter XI

Acknowledgements

I would like to thank first my supervisors Professor Doctor Juan Manuel Figueira and Professor Doctor Ralph Engel for giving me the opportunity to participate in the DDAp programme and for their guidance and constructive feedback during the development of this work. I would also like to acknowledge Professor Doctor Federico Sánchez, since his expertise in the UMD has been very helpful throughout this thesis, and Doctor Darko Veberič for his continuous advice in Offline and thoughtful reviews. I extend my gratitude to all the people in the Pierre Auger Collaboration who contributed to this thesis by constructive suggestions. I would also like to thank Sabine Bucher and Marie-Christine Mundt for their support with organisational matters during my two stays at KIT in Germany.

This experience has been incredibly enriching, both professionally and personally. My sincere thanks go to all my colleagues and friends in both Germany and Argentina. There are many people I would like to mention, and I hope not to forget anyone. The German side: Tobias, Steffen, Emily, Allan, Fabio, Álvaro, Alex, Paul, Fabian. The Argentinian side: Martina, Nicolás, Luciano, Joaquin, Varada, Carmina, Ezequiel, Rolando, Belén, Fernando, Manuel, Gabriel. Thanks for all the fruitful science discussions, for the patient encouragement to finish this PhD thesis and for all the memorable fun times together, including our Tuesday Malbec tastings and Friday Beer Time gatherings.

Special thanks to my family and friends outside the office for their patience and support. I am eternally grateful to my grandparents, Tito and Ilda, for having taught me the meaning of hard work. Last but not least, I would like to thank my 'rock' Romina, whose constant support and motivation was my source of strength. I couldn't have finish without your love and understanding. A special thanks to my beloved cats, whose cozy naps by my side made every late hour of writing the thesis more bearable.

Chapter 11. Acknowledgements

Bibliography

[1] L. Evans and P. Bryant, "LHC machine," *Journal of Instrumentation*, vol. 3, no. 08, p. S08001, 2008.

[2] T. K. Gaisser, R. Engel, and E. Resconi, *Cosmic rays and particle physics*. Cambridge University Press, 2016.

[3] V. F. Hess, "Über Beobachtungen der durchdringenden Strahlung bei sieben Freiballonfahrten," *Zeitschrift für Physik*, vol. 13, p. 1084, 1912.

[4] R. A. Millikan, "High frequency rays of cosmic origin," *Science*, vol. 62, no. 1612, pp. 445–448, 1925.

[5] B. Rossi, "On the magnetic deflection of cosmic rays," *Physical Review*, vol. 36, no. 3, p. 606, 1930.

[6] B. Rossi, "Über die eigenschaften der durchdringenden korpuskularstrahlung im meeresniveau," *Zeitschrift für Physik*, vol. 82, no. 3, pp. 151–178, 1933.

[7] S. H. Neddermeyer and C. D. Anderson, "Note on the nature of cosmic-ray particles," *Physical Review*, vol. 51, no. 10, p. 884, 1937.

[8] P. Auger, R. Maze, and A. Robley, "Extension et pouvoir pénétrant des grandes gerbes de rayons cosmiques," *Comptes rendus*, vol. 208, p. 1641, 1939.

[9] K.-H. Kampert and A. A. Watson, "Extensive air showers and ultra high-energy cosmic rays: a historical review," *The European Physical Journal H*, vol. 37, no. 3, pp. 359–412, 2012.

[10] Pierre Auger Collaboration, "The Pierre Auger Observatory and its upgrade," *Science Reviews From The End Of The World*, vol. 1, no. 4, pp. 1–26, 2020.

[11] C. Evoli, "The cosmic-ray energy spectrum," Zenodo, 2020.

[12] T. Antoni, W. Apel, A. Badea, K. Bekk, A. Bercuci, J. Blümer, H. Bozdog, I. Brancus, A. Chilingarian, K. Daumiller, *et al.*, "KASCADE measurements of energy spectra for elemental groups of cosmic rays: results and open problems," *Astroparticle Physics*, vol. 24, no. 1-2, pp. 1–25, 2005.

[13] W. Apel, J. Arteaga-Velázquez, K. Bekk, M. Bertaina, J. Blümer, H. Bozdog, I. Brancus, P. Buchholz, E. Cantoni, A. Chiavassa, *et al.*, "Kneelike structure in the spectrum of the heavy component of cosmic rays observed with KASCADE-Grande," *Physical Review Letters*, vol. 107, no. 17, p. 171104, 2011.

[14] M. Unger, G. R. Farrar, and L. A. Anchordoqui, "Origin of the ankle in the ultrahigh energy cosmic ray spectrum, and of the extragalactic protons below it," *Physical Review D*, vol. 92, no. 12, p. 123001, 2015.

[15] K. Greisen, "End to the cosmic-ray spectrum?," *Physical Review Letters*, vol. 16, no. 17, p. 748, 1966.

[16] G. T. Zatsepin and V. A. Kuz'min, "Upper limit of the spectrum of cosmic rays," *Soviet Journal of Experimental and Theoretical Physics Letters*, vol. 4, p. 78, 1966.

[17] A. A. Penzias and R. W. Wilson, "A measurement of excess antenna temperature at 4080 MHz," in *A Source Book in Astronomy and Astrophysics, 1900–1975*, pp. 873–876, Harvard University Press, 1979.

[18] F. W. Stecker and M. Salamon, "Photodisintegration of ultra-high-energy cosmic rays: A new determination," *The Astrophysical Journal*, vol. 512, no. 2, p. 521, 1999.

[19] L. N. Epele and E. Roulet, "Comment on "on the origin of the highest energy cosmic rays"," *Physical Review Letters*, vol. 81, no. 15, p. 3295, 1998.

[20] R. Tennent, "The Haverah Park extensive air shower array," *Proceedings of the Physical Society*, vol. 92, no. 3, p. 622, 1967.

[21] A. Ivanov, S. Knurenko, and I. Y. Sleptsov, "Measuring extensive air showers with Cherenkov light detectors of the Yakutsk array: the energy spectrum of cosmic rays," *New Journal of Physics*, vol. 11, no. 6, p. 065008, 2009.

[22] E. Apel, J. Arteaga, A. Badea, K. Bekk, M. Bertaina, J. Blümer, H. Bozdog, I. Brancus, P. Buchholz, E. Cantoni, *et al.*, "The KASCADE-grande experiment," *Nuclear Instruments and Methods in Physics Research Section A*, vol. 620, no. 2-3, pp. 202–216, 2010.

[23] N. Hayashida, K. Honda, N. Inoue, K. Kadota, F. Kakimoto, S. Kakizawa, K. Kamata, S. Kawaguchi, Y. Kawasaki, N. Kawasumi, *et al.*, "The AGASA Collaboration," *Astroparticle Physics*, vol. 10, p. 303, 1999.

[24] R. Baltrusaitis, R. Cady, G. Cassiday, R. Cooperv, J. Elbert, P. Gerhardy, S. Ko, E. Loh, M. Salamon, D. Steck, *et al.*, "The Utah Fly's eye detector," *Nuclear Instruments and Methods in Physics Research Section A*, vol. 240, no. 2, pp. 410–428, 1985.

[25] J. H. Boyer, B. C. Knapp, E. J. Mannel, and M. Seman, "FADC-based DAQ for HiRes Fly's Eye," *Nuclear Instruments and Methods in Physics Research Section A*, vol. 482, no. 1-2, pp. 457–474, 2002.

[26] E. Fermi, "On the origin of the cosmic radiation," *Physical Review*, vol. 75, no. 8, p. 1169, 1949.

[27] R. Protheroe, "Acceleration and interaction of ultra high energy cosmic rays," *arXiv preprint astro-ph/9812055*, 1998.

[28] E. Fermi, "Galactic magnetic fields and the origin of cosmic radiation," in *A Source Book in Astronomy and Astrophysics, 1900–1975*, pp. 671–676, Harvard University Press, 1979.

[29] A. Achterberg, Y. A. Gallant, J. G. Kirk, and A. W. Guthmann, "Particle acceleration by ultrarelativistic shocks: theory and simulations," *Monthly Notices of the Royal Astronomical Society*, vol. 328, no. 2, pp. 393–408, 2001.

[30] A. M. Hillas, "The origin of ultra-high-energy cosmic rays," *Annual Review of Astronomy and Astrophysics*, vol. 22, pp. 425–444, 1984.

[31] Pierre Auger Collaboration, "Large-scale cosmic-ray anisotropies above 4 EeV measured by the Pierre Auger Observatory," *The Astrophysical Journal*, vol. 868, no. 1, p. 4, 2018.

[32] M. Aartsen, M. Ackermann, J. Adams, J. A. Aguilar, M. Ahlers, M. Ahrens, D. Altmann, K. Andeen, T. Anderson, I. Ansseau, *et al.*, "Astrophysical neutrinos and cosmic rays observed by IceCube," *Advances in Space Research*, vol. 62, no. 10, pp. 2902–2930, 2018.

[33] Pierre Auger Collaboration, "Upper limit on the cosmic-ray photon fraction at EeV energies from the Pierre Auger Observatory," *Astroparticle Physics*, vol. 31, no. 6, pp. 399–406, 2009.

[34] Pierre Auger Collaboration, "Upper limit on the diffuse flux of UHE tau neutrinos from the Pierre Auger Observatory," *arXiv preprint arXiv:0712.1909*, 2007.

[35] W. Heitler, *The quantum theory of radiation*. Courier Corporation, 1984.

[36] J. Matthews, "A heitler model of extensive air showers," *Astroparticle Physics*, vol. 22, no. 5-6, pp. 387–397, 2005.

[37] A. Haungs, J. Blumer, B. Fuchs, D. Kang, S. Schoo, D. Wochele, J. Wochele, W. Apel, J. Arteaga-Velázquez, K. Bekk, *et al.*, "Kcdc—the kascade cosmic-ray data centre," *Journal of Physics: Conference Series*, vol. 632, no. 1, 2015.

[38] T. Pierog, I. Karpenko, J. M. Katzy, E. Yatsenko, and K. Werner, "EPOS LHC: Test of collective hadronization with data measured at the CERN Large Hadron Collider," *Physical Review C*, vol. 92, p. 034906, Sep 2015.

[39] S. Ostapchenko, "QGSJET-III model: physics and preliminary results," *EPJ Web of Conferences*, vol. 208, 2013.

[40] H. Dembinski, J. Arteaga-Velázquez, L. Cazon, R. Conceição, J. Gonzalez, Y. Itow, D. Ivanov, N. Kalmykov, I. Karpikov, S. Müller, *et al.*, "Report on tests and measurements of hadronic interaction properties with air showers," *EPJ Web of Conferences*, vol. 210, 2019.

[41] K.-H. Kampert and M. Unger, "Measurements of the cosmic ray composition with air shower experiments," *Astroparticle Physics*, vol. 35, no. 10, pp. 660–678, 2012.

[42] J. R. Hoerandel, "On the knee in the energy spectrum of cosmic rays," *Astroparticle Physics*, vol. 19, no. 2, pp. 193–220, 2003.

[43] H. Dembinski, R. Engel, A. Fedynitch, T. Gaisser, F. Riehn, and T. Stanev, "Data-driven model of the cosmic-ray flux and mass composition from 10 GeV to 10^{11} GeV," *arXiv preprint arXiv:1711.11432*, 2017.

[44] Pierre Auger Collaboration, "Testing hadronic interactions at ultrahigh energies with air showers measured by the Pierre Auger Observatory," *Physical Review Letters*, vol. 117, no. 19, p. 192001, 2016.

[45] D. Veberič[2] , Link provided, 2025.

[46] Pierre Auger Collaboration, "The Pierre Auger cosmic ray Observatory," *Nuclear Instruments and Methods in Physics Research Section A*, vol. 798, pp. 172–213, 2015.

[47] Pierre Auger Collaboration, "The surface detector system of the Pierre Auger Observatory," *Nuclear Instruments and Methods in Physics Research Section A*, vol. 586, no. 3, pp. 409–420, 2008.

[48] B. G. Keilhauer, "Investigation of atmospheric effects on the development of extensive air showers and their detection with the Pierre Auger Observatory," Ph.D. thesis, Karlsruhe Institute of Technology, 2004.

[49] Pierre Auger Collaboration, "Reconstruction of events recorded with the surface detector of the Pierre Auger Observatory," *Journal of Instrumentation*, vol. 15, no. 10, p. P10021, 2020.

[50] Pierre Auger Collaboration, "The Pierre Auger Observatory upgrade-preliminary design report," *arXiv preprint arXiv:1604.03637*, 2016.

[51] Pierre Auger Collaboration, "Calibration of the surface array of the Pierre Auger Observatory," *Nuclear Instruments and Methods in Physics Research Section A*, vol. 568, no. 2, pp. 839–846, 2006.

[52] Pierre Auger Collaboration, "Trigger and aperture of the surface detector array of the Pierre Auger Observatory," *Nuclear Instruments and Methods in Physics Research Section A*, vol. 613, no. 1, pp. 29–39, 2010.

[53] Pierre Auger Collaboration, "The fluorescence detector of the Pierre Auger Observatory," *Nuclear Instruments and Methods in Physics Research Section A*, vol. 620, no. 2-3, pp. 227–251, 2010.

[54] H. Klages, "HEAT–enhancement telescopes for the Pierre Auger Southern Observatory," in *30th International Cosmic Ray Conference (ICRC2007)*, vol. 5, 2007.

[55] Pierre Auger Collaboration, "The Pierre Auger Observatory: Contributions to the 36th International Cosmic Ray Conference (ICRC2019)," *arXiv preprint arXiv:1909.09073*, 2019.

[56] Pierre Auger Collaboration, "Radio detection of cosmic rays with the Auger Engineering Radio Array," *EPJ Web of Conferences*, vol. 210, 2019.

[57] Pierre Auger Collaboration, "Muon counting using silicon photomultipliers in the AMIGA detector of the Pierre Auger Observatory," *Journal of Instrumentation*, vol. 12, no. 03, p. P03002, 2017.

[58] Pierre Auger Collaboration, "Design, upgrade and characterization of the silicon photomultiplier front-end for the AMIGA detector at the Pierre Auger Observatory," *Journal of Instrumentation*, vol. 16, no. 01, p. P01026, 2021.

[59] Pierre Auger Collaboration, "Design and implementation of the AMIGA embedded system for data acquisition," *Journal of Instrumentation*, vol. 16, no. 07, p. T07008, 2021.

[60] Pierre Auger Collaboration, "Calibration of the underground muon detector of the Pierre Auger Observatory," *Journal of Instrumentation*, vol. 16, no. 04, p. P04003, 2021.

[61] A. Botti *et al.*, "Simulation of the AMIGA underground muon detector: SiPM and electronics," Auger internal notes GAP-2019-063, 2019.

[62] A. M. Botti, F. Sánchez, M. Roth, and A. Etchegoyen, "Development and validation of the signal simulation for the underground muon detector of the Pierre Auger Observatory," *Journal of Instrumentation*, vol. 16, no. 07, p. P07059, 2021.

[63] A. Botti, "Determination of the chemical composition of cosmic rays in the energy region of 5 EeV with the AMIGA upgrade of the Pierre Auger Observatory," Ph.D. thesis, Karlsruhe Institute of Technology, 2020.

[64] F. Gesualdi, "The muon content of atmospheric air showers and the mass composition of cosmic rays," Ph.D. thesis, Karlsruhe Institute of Technology, 2022.

[65] D. Ravignani and A. D. Supanitsky, "A new method for reconstructing the muon lateral distribution with an array of segmented counters," *Astroparticle Physics*, vol. 65, pp. 1–10, 2015.

[66] F. Gesualdi and A. D. Supanitsky, "Estimation of the number of counts on a particle counter detector with full time resolution," *The European Physical Journal C*, vol. 82, no. 10, p. 925, 2022.

[67] A. Supanitsky, A. Etchegoyen, G. Medina-Tanco, I. Allekotte, M. G. Berisso, and M. C. Medina, "Underground muon counters as a tool for composition analyses," *Astroparticle Physics*, vol. 29, no. 6, pp. 461–470, 2008.

[68] J. de Jesús et al., "Data-driven method to quantify and correct the corner-clipping effect in segmented muon counters," *Proceedings of Science UHECR2024*, vol. 078, 2024.

[69] C. P. Bertolli *et al.*, "Towards the development of a Protocol for UMD Shifts," Auger internal notes GAP-2022-043, 2022.

[70] MACRO Collaboration, "Seasonal variations in the underground muon intensity as seen by MACRO," *Astroparticle Physics*, vol. 7, no. 1-2, pp. 109–124, 1997.

[71] A. Dmitrieva, R. Kokoulin, A. Petrukhin, and D. Timashkov, "Corrections for temperature effect for ground-based muon hodoscopes," *Astroparticle Physics*, vol. 34, no. 6, pp. 401–411, 2011.

[72] A. Botti *et al.*, "Characterization of AMIGA ADC signals with SiPMs," Auger internal notes GAP-2019-016, 2019.

[73] S. Argiro, S. Barroso, J. Gonzalez, L. Nellen, T. Paul, T. Porter, L. Prado Jr, M. Roth, R. Ulrich, and D. Veberič, "The offline software framework of the Pierre Auger Observatory," *Nuclear Instruments and Methods in Physics Research Section A*, vol. 580, no. 3, pp. 1485–1496, 2007.

[74] A. Botti *et al.*, "Calibration of the AMIGA ADC channel with T1 background events," Auger internal notes GAP-2019-046, 2019.

[75] D. E. Groom, N. V. Mokhov, and S. I. Striganov, "Muon stopping power and range tables 10 MeV–100 TeV," *Atomic Data and Nuclear Data Tables*, vol. 78, no. 2, pp. 183–356, 2001.

[76] P. K. Grieder, *Cosmic rays at Earth*. Elsevier, 2001.

[77] LAGO Collaboration, "The ARTI framework: cosmic rays atmospheric background simulations," *The European Physical Journal C*, vol. 82, no. 11, p. 1019, 2022.

[78] A. Botti *et al.*, "The ADC channel of the underground muon detector: calibration parameters, data, and monitoring variables," Auger internal notes GAP-2021-015, 2021.

[79] J. de Jesús *et al.*, "Study on the optical fiber attenuation of the UMD using the integrator channel," Auger internal notes GAP-2021-052, 2021.

[80] A. Botti *et al.*, "The ADC channel of the underground muon detector: calibration parameters, data, and monitoring variables," Auger internal notes GAP-2021-015, 2021.

[81] J. Blümer *et al.*, "On the influence of accidental muons on air shower detection," Auger internal notes GAP-2008-110, 2008.

[82] J. Smith and N. Duller, "Effects of pi meson decay-absorption phenomena on the high-energy mu meson zenithal variation near sea level," *Journal of Geophysical Research*, vol. 64, no. 12, pp. 2297–2305, 1959.

[83] L. Dedenko, T. Roganova, and G. Fedorova, "Signals in the underground scintillation detectors of the Yakutsk array from muons of extensive air showers," *Moscow University Physics Bulletin*, vol. 66, pp. 358–362, 2011.

[84] C. Anderson, G. McKinney, J. Tutt, and M. James, "Delta-ray production in MCNP 6.2.0," *Physics Procedia*, vol. 90, pp. 229–236, 2017.

[85] P. Stoker, C. Hofmeyr, and C. Bornman, "Knock-on electrons and direct electron pair production by cosmic-ray muons," *Proceedings of the Physical Society*, vol. 78, no. 5, p. 650, 1961.

[86] N. Chaudhuri and M. Sinha, "Production of knock-on electrons by cosmic-ray muons underground (148 m we)," *Il Nuovo Cimento (1955-1965)*, vol. 35, pp. 13–22, 1965.

[87] Geant4 Collaboration, "GEANT4—a simulation toolkit," *Nuclear Instruments and Methods in Physics Research Section A*, vol. 506, no. 3, pp. 250–303, 2003.

[88] Particle Data Group, "Review of particle physics," *Progress of Theoretical and Experimental Physics*, vol. 2020, no. 8, p. 083C01, 2020.

[89] Pierre Auger Collaboration, "Status and performance of the Underground Muon Detector of the Pierre Auger Observatory," *Proceedings of Science ICRC2023*, vol. 267, 2023.

[90] MINOS Collaboration, "Long term performance of the MINOS calibration procedure and stability of the MINOS detectors," *Journal of Physics: Conference Series*, vol. 404, no. 1, 2012.

[91] D. Ravignani, A. D. Supanitsky, and D. Melo, "Reconstruction of air shower muon densities using segmented counters with time resolution," *Astroparticle Physics*, vol. 82, pp. 108–116, 2016.

[92] V. K. Covilakam, A. Supanitsky, and D. Ravignani, "Reconstruction of air shower muon lateral distribution functions using integrator and binary modes of underground muon detectors," *The European Physical Journal C*, vol. 83, no. 12, p. 1157, 2023.

[93] D. R. A.D. Supanitsky and V. K. Covilakam, "A likelihood function based on the binary and ADC acquisition modes of the underground muon detectors," Auger internal notes GAP-2023-025, 2023.

[94] J. de Jesús, "Current status of reconstruction of the binary mode of the UMD," talk presented at Auger Collaboration Meeting, 2024.

[95] T. Antoni, J. Blümer, J. Hörandel, M. Roth, M. Sumpert, J. Van Buren, W. Apel, F. Badea, K. Bekk, H. Bozdog, *et al.*, "Muon size spectrum measured by KASCADE-Grande," in *29th International Cosmic Ray Conference (ICRC2005)*, vol. 6, 2005.

[96] Pierre Auger Collaboration, "Direct measurement of the muonic content of extensive air showers between 2 $\times 10^{17}$ and 2 $\times 10^{18}$ eV at the Pierre Auger Observatory," *The European Physical Journal C*, vol. 80, pp. 1–19, 2020.

[97] J. de Jesús, "Muon content of air showers measured by the UMDs," talk presented at Auger Collaboration Meeting, 2024.

[98] A. Poctarev, "Deep learning reconstruction of muon densities using the underground muon detector of the Pierre Auger Observatory," Auger internal notes GAP-2024-055, 2024.

[99] A. Coleman, "Measurement of the cosmic ray flux above 100 PeV at the Pierre Auger Observatory," Auger internal notes GAP-2018-045, 2018.

[100] J. Hersil, I. Escobar, D. Scott, G. Clark, and S. Olbert, "Observations of extensive air showers near the maximum of their longitudinal development," *Physical Review Letters*, vol. 6, no. 1, p. 22, 1961.

[101] Pierre Auger Collaboration, "Cosmic-ray anisotropies in right ascension measured by the Pierre Auger Observatory," *The Astrophysical Journal*, vol. 891, no. 2, p. 142, 2020.

[102] Pierre Auger Collaboration, "The energy spectrum of cosmic rays beyond the turn-down around 10^{17} eV as measured with the surface detector of the Pierre Auger Observatory," *The European Physical Journal C*, vol. 81, pp. 1–25, 2021.

[103] D. Ravignani , Code provided, 2024.

[104] Pierre Auger Collaboration, "The energy scale of the Pierre Auger Observatory," *Proceedings of Science ICRC2019*, vol. 358, 2019.

[105] J. Arteaga Velazquez, "A report by the WHISP working group on the combined analysis of muon data at cosmic-ray energies above 1 PeV," *Proceedings of Science ICRC2023*, vol. 466, 2023.

[106] H. P. Dembinski, "Computing mean logarithmic mass from muon counts in air shower experiments," *Astroparticle Physics*, vol. 102, pp. 89–94, 2018.

[107] S. N. Müller, "Measurement of the cosmic ray composition with air showers detected by the amiga extension at the Pierre Auger Observatory," Ph.D. thesis, Karlsruhe Institute of Technology, 2019.

[108] Pierre Auger Collaboration, "Mass composition of cosmic rays with energies above $10^{17.2}$ eV from the hybrid data of the Pierre Auger Observatory," *Proceedings of Science ICRC2019*, vol. 358, 2019.